



HAL
open science

Experimental and numerical study of the hydromechanical behaviour of bentonite pellet-powder mixtures

Benjamin Dardé

► **To cite this version:**

Benjamin Dardé. Experimental and numerical study of the hydromechanical behaviour of bentonite pellet-powder mixtures. Géotechnique. Université Paris-Est, 2019. English. NNT : 2019PESC1030 . tel-02884083

HAL Id: tel-02884083

<https://pastel.hal.science/tel-02884083>

Submitted on 29 Jun 2020

HAL is a multi-disciplinary open access archive for the deposit and dissemination of scientific research documents, whether they are published or not. The documents may come from teaching and research institutions in France or abroad, or from public or private research centers.

L'archive ouverte pluridisciplinaire **HAL**, est destinée au dépôt et à la diffusion de documents scientifiques de niveau recherche, publiés ou non, émanant des établissements d'enseignement et de recherche français ou étrangers, des laboratoires publics ou privés.

Thèse

soumise pour l'obtention du grade de
Docteur de l'Université Paris-Est
Ecole Doctorale Sciences, Ingénierie et Environnement (SIE)

par

Benjamin Dardé

**Experimental and numerical study of the hydromechanical
behaviour of bentonite pellet-powder mixtures**

Spécialité : *Géotechnique*

Préparée à l'École des Ponts ParisTech, laboratoire Navier, équipe Géotechnique

Soutenue le 5 décembre 2019 devant un jury composé de :

Prof. François Chevoir	Ifsttar	Président
Prof. Antonio Gens	Universitat Politècnica de Catalunya	Rapporteur
Dr. Vincent Richefeu	Université Grenoble Alpes	Rapporteur
Prof. Robert Charlier	Université de Liège	Examineur
Dr. Jean Talandier	Andra	Examineur
Dr. Patrick Dangla	Ifsttar	Examineur
Dr. Jean-Noël Roux	Ifsttar	Examineur
Prof. Jean-Michel Pereira	École des Ponts ParisTech	Invité
Dr. Minh Ngoc Vu	Andra	Invité
Dr. Anh Minh Tang	École des Ponts ParisTech	Directeur de thèse

Thèse

soumise pour l'obtention du grade de
Docteur de l'Université Paris-Est
Ecole Doctorale Sciences, Ingénierie et Environnement (SIE)

par

Benjamin Dardé

**Experimental and numerical study of the hydromechanical
behaviour of bentonite pellet-powder mixtures**

Spécialité : *Géotechnique*

REMERCIEMENTS

Ce travail de thèse a été réalisé au laboratoire Navier à l'École des Ponts ParisTech et financé par l'Andra. Je souhaite remercier sincèrement toutes les personnes qui, par leur aide, leurs conseils ou leur soutien, ont contribué à l'aboutissement de ce travail.

Je remercie les membres du jury pour l'intérêt porté à mon travail et le temps accordé à la lecture du manuscrit. J'ai beaucoup apprécié l'ensemble de nos discussions, qui m'ont permis de réfléchir sur le sujet avec différentes approches et m'ont donné des idées pour continuer à développer certains points dans le futur. Je remercie vivement Antonio Gens et Vincent Richefeu qui m'ont fait l'honneur d'accepter d'être rapporteurs de ma thèse. Je les remercie pour leurs commentaires détaillés et leurs suggestions pertinentes concernant les différentes parties de mon mémoire. Je remercie Robert Chaliier d'avoir accepté d'examiner mon travail de thèse. Je le remercie aussi pour nos agréables échanges, scientifiques et non scientifiques, lors des réunions du projet Beacon. Je remercie François Chevoir d'avoir accepté d'être examinateur de la thèse et d'avoir présidé le jury le jour de la soutenance.

Je remercie l'Andra pour le financement de mes travaux de recherche. Je remercie particulièrement Jean Talandier et Minh Ngoc Vu qui ont suivi mes travaux au cours des trois années et m'ont régulièrement conseillé. Jean Talandier m'a également donné la chance de participer au projet Beacon, je l'en remercie. La participation à ce projet m'a beaucoup apporté. Chaque réunion m'a permis de présenter l'avancée de mon travail, d'avoir un aperçu des différents travaux menés sur la bentonite par diverses institutions européennes, et de mieux en comprendre les enjeux, les problématiques et les applications.

Je remercie chaleureusement l'ensemble des membres du laboratoire Navier pour leur accueil. Je remercie particulièrement mes encadrants de thèse, Anh Minh Tang, Patrick Dangla, Jean-Michel Pereira et Jean-Noël Roux. Je les remercie pour leur disponibilité tout au long de la thèse. J'ai apprécié chacune de nos nombreuses discussions, qui m'ont permis d'apprendre énormément au cours de ces trois années, dans des domaines très variés. Au-delà de connaissances scientifiques, ils ont su me transmettre leur passion pour la recherche et c'est sans aucun doute grâce à eux si je souhaite aujourd'hui poursuivre dans cette voie.

Je souhaite exprimer mon immense gratitude à mon directeur de thèse, Anh Minh Tang, pour m'avoir donné l'opportunité de réaliser cette thèse. Je le remercie infiniment pour la confiance qu'il m'a accordée depuis le début de la thèse. Je le remercie pour tous ses conseils, pour toutes ses suggestions concernant l'orientation des travaux. J'ai toujours quitté son bureau avec les idées plus claires et mes éventuels doutes dissipés. Je le remercie aussi pour ses encouragements, qui ont permis de garder ma motivation intacte durant trois ans.

Je remercie l'équipe technique du laboratoire, Emmanuel de Laure, Xavier Boulay, Loïc Lesueur, et particulièrement Baptiste Chabot et Marine Lemaire pour leur aide inestimable dans la partie expérimentale de mon travail.

Je remercie les doctorants pour tous les moments agréables passés ensemble, au laboratoire ou à l'extérieur. J'ai passé trois belles années en votre compagnie. L'ambiance conviviale, l'entraide, le soutien entre doctorants étaient pour moi des conditions idéales pour réaliser la thèse.

Je remercie enfin mes amis et ma famille pour leurs encouragements et leur soutien permanent.

ABSTRACT

Bentonite-based materials are considered as a sealing material in radioactive waste disposal concepts because of their low permeability, radionuclide retention capacity and ability to swell upon hydration, thus filling technological gaps. Within this context, bentonite pellet mixtures have been studied owing to operational convenience. Pellets are laid in the galleries in a dry state as a granular assembly. The mixture progressively becomes homogeneous upon hydration by the pore water of the host rock. Before homogenisation, the granular structure of the material controls the macroscopic behaviour of the mixture.

The present work focuses on the experimental characterisation and numerical modelling of a mixture of bentonite pellet and crushed pellet (powder), in proportion 70/30 in dry mass, a candidate sealing material in the French concept of radioactive waste disposal. The proposition, implementation and validation of a modelling framework, considering features such as the initial granular structure of the material or local heterogeneities of densities, is the main objective of this PhD work.

The influence of the initial granular structure is evidenced by performing suction-controlled swelling pressure tests in the laboratory, using samples of various powder contents. A simple model describing the hydromechanical behaviour of a pellet is proposed from grain-level experimental characterisation, and implemented in a Discrete Element Method (DEM) code. Using DEM and the proposed model, aforementioned swelling pressure tests performed on samples containing no powder are simulated to validate the model. The same method is used to model large pellet assemblies of various pellet densities. Relevant parameters involved in the macroscopic behaviour of pellet mixtures in “granular” state are identified from simulation results and constitutive laws are proposed to describe the hydromechanical behaviour of these materials using a continuum mechanics approach.

The transition from a “granular” state to a “continuous” state is described by criteria involving suction and relative volume fractions of pellet and powder. A modified version of the Barcelona Basic Model is proposed to model the material behaviour following the transition. The proposed model is implemented in the Finite Element Method (FEM) code Bil. Using a single set of parameters, all swelling pressure tests performed in the laboratory are satisfactorily reproduced in FEM simulations along the entire hydration path.

The material behaviour upon hydration in constant volume condition is finally studied at a larger scale by performing mock-up imbibition tests, using various powder contents. Cells have a square section. A glass side and a camera allow the texture of the mixture to be observed during hydration. The dominance of vapour transfer in the saturation process of the material, the influence and evolution of the granular structure upon hydration, and the influence of the powder content on the macroscopic response are notably identified. Transfer laws are proposed to describe the observed material behaviour in the mock-up tests and implemented in Bil.

Performing larger-scale simulations using the proposed hydromechanical model is a perspective arising from this PhD work. Predictive simulations can be performed at the structure scale, considering relevant features such as the initial granular structure and local heterogeneities of density in the sealing material.

RÉSUMÉ

Les matériaux à base de bentonite sont envisagés pour la réalisation des ouvrages de fermeture dans les concepts de stockage de déchets radioactifs afin de tirer profit de leur faible perméabilité, leur capacité de rétention de radionucléides et leur potentiel de gonflement lors de l'humidification, qui permet de combler les vides technologiques. Dans ce contexte, les matériaux mis en place sous forme de mélanges de granules (« pellets ») de bentonite sont étudiés car ils présentent moins de contraintes d'installation comparés aux blocs préfabriqués. Les pellets sont disposés dans les galeries à l'état sec et forment un matériau granulaire. Le matériau est humidifié par l'eau issue de la roche encaissante et acquiert une texture homogène. Avant homogénéisation, le caractère granulaire du matériau contrôle son comportement.

Ce travail se concentre sur la caractérisation expérimentale et la modélisation numérique d'un mélange de pellets et pellets concassés (« poudre ») de bentonite en proportion 70/30 en masse sèche, matériau envisagé pour réaliser les ouvrages de fermeture dans le concept français de stockage de déchets radioactifs. La proposition, l'implémentation et la validation d'un modèle de comportement tenant compte de la nature granulaire initiale et d'éventuelles hétérogénéités locales de densité sont les objectifs principaux de ce travail.

L'influence de la nature granulaire initiale est mise en évidence par l'intermédiaire d'essais de pression de gonflement à succion contrôlée au laboratoire. Les essais sont réalisés sur des échantillons préparés à différentes teneurs en poudre. A partir d'une caractérisation expérimentale à l'échelle du pellet, un modèle simple décrivant le comportement hydromécanique du pellet est proposé et implémenté dans un code de calcul utilisant la méthode des Éléments Discrets (DEM). Les essais réalisés au laboratoire sur les échantillons sans poudre sont simulés par la DEM pour valider le modèle proposé. Cette méthode est utilisée pour simuler de larges assemblages granulaires de densités variées soumis à des sollicitations hydromécaniques. Les paramètres influençant le comportement macroscopique des assemblages de pellets à l'état « granulaire » sont identifiés à partir de ces simulations. Une loi de comportement est proposée pour modéliser le matériau comme un milieu continu.

La transition d'un état « granulaire » à un état « continu » est décrite par des critères faisant intervenir la succion et les fractions volumiques relatives des pellets et de la poudre. Une version modifiée du Barcelona Basic Model est proposée pour modéliser le comportement du matériau à l'état « continu », après la transition. Le modèle est implémenté dans le code de calcul par Éléments Finis (FEM) BIL. Les essais de pression de gonflement réalisés au laboratoire sur des échantillons contenant différentes teneurs en poudre sont simulés par FEM de manière satisfaisante, sur l'ensemble du chemin d'humidification, en utilisant un unique jeu de paramètres.

Le comportement du matériau au cours de l'humidification en conditions de volume constant est finalement étudié à plus grande échelle par la réalisation d'essais d'imbibition en modèle réduit au laboratoire, à différentes teneurs en poudre. Les cellules sont de section carrée avec une face vitrée. Une caméra permet l'observation de l'évolution de la texture du matériau au cours de l'humidification. La prédominance des transferts en phase vapeur dans le processus de saturation du matériau, l'influence et l'évolution de la structure granulaire au cours de l'humidification et l'influence de la teneur en poudre sur la réponse macroscopique du mélange sont mis en évidence. Des lois de transferts hydriques sont proposées à partir des résultats et observations expérimentales et implémentées dans le code BIL.

La perspective principale de ce travail est la réalisation de simulations FEM à plus grande échelle en utilisant le modèle développé. Ainsi, des problématiques inhérentes à l'utilisation des mélanges de pellets et poudre, notamment la nature granulaire initiale et les hétérogénéités locales de densité, pourront être prises en compte.

CONTENTS

List of Tables.....	xiii
List of Figures.....	xv
List of Notations.....	xxv
List of Symbols.....	xxvii
1 Introduction.....	1
1.1 General context.....	1
1.2 Problem statement and objectives of the present work.....	3
1.3 Outline of the thesis.....	4
2 Literature review.....	7
2.1 Introduction.....	7
2.2 Microstructure of compacted bentonites.....	7
2.2.1 Structure of montmorillonite clay minerals.....	8
2.2.2 Fabric of compacted bentonites.....	8
2.2.3 Suction in unsaturated soils.....	11
2.2.4 Fabric evolution upon hydration.....	15
2.3 Macroscopic response under hydromechanical loading.....	22
2.3.1 Hydraulic loading of compacted bentonite.....	23
2.3.2 Mechanical loading at constant suction.....	27
2.3.3 Influence of the stress path.....	30
2.3.4 Swelling pressure development upon hydration in confined conditions.....	32
2.3.5 Water saturation of compacted bentonites.....	37
2.3.6 Water transfer in compacted bentonites.....	40
2.4 Particular features of bentonite pellet mixtures.....	44
2.4.1 Characteristics of high density bentonite pellet.....	44

2.4.2	Heterogeneities and homogenisation of pellet mixtures	46
2.4.3	Influence of the granular structure	51
2.5	Modelling the behaviour of compacted bentonite on hydration	56
2.5.1	Stress variables	56
2.5.2	Barcelona Basic Model	58
2.5.3	Description of water retention behaviour and transfer laws	63
2.6	Perspectives regarding the modelling of pellet-powder mixtures	64
2.6.1	Overview of pellet-powder mixtures characteristics	64
2.6.2	Limitations of the existing models	65
2.6.3	Proposition of an experimental and numerical program	66
3	Suction-controlled swelling pressure tests	67
3.1	Introduction	67
3.2	Material	68
3.2.1	Bentonite pellets	68
3.2.2	Bentonite powder	69
3.2.3	Pellet-powder mixtures	69
3.3	Suction-controlled swelling pressure tests	70
3.3.1	Isochoric cell	70
3.3.2	Preparation of the samples	72
3.3.3	Suction-controlled hydration at constant room temperature	74
3.4	Experimental results	75
3.4.1	Evolution of swelling pressure as a function of elapsed time	75
3.4.2	Suction-swelling pressure relationship	80
3.4.3	Evolution of the granular structure	84
3.5	Discussion	86
3.5.1	Final swelling pressure	86
3.5.2	Influence of the powder content	87
3.5.3	Influence of the initial granular structure	89
3.5.4	Influence of the sample preparation	90
3.5.5	Hydration mechanisms	91
3.5.6	Conceptual interpretation of the macroscopic response of tested samples	91

3.6	Concluding remarks and perspectives	93
3.6.1	Similitudes and differences between continuous and granular bentonite materials	93
3.6.2	Limitations of the testing procedure.....	93
3.6.3	Modelling the particular features of pellet-powder mixtures.....	95
4	Proposition and validation of a DEM-based numerical approach providing insight into the mechanical behaviour of pellet assemblies.....	97
4.1	Introduction	97
4.2	Hydromechanical behaviour of a pellet upon partial hydration	97
4.2.1	Introduction	97
4.2.2	Material	98
4.2.3	Experimental methods.....	99
4.2.4	Experimental results.....	103
4.2.5	Model describing the hydromechanical behaviour of a pellet.....	115
4.3	Simulations of swelling pressure tests using DEM	118
4.3.1	Introduction	118
4.3.2	Description of the proposed simulation method.....	119
4.3.3	Numerical simulation results.....	125
4.4	Discussion.....	130
4.4.1	Hydromechanical behaviour of a single pellet	131
4.4.2	Validity of the DEM model.....	132
4.4.3	Modelling at low suction.....	133
4.4.4	Influence of the walls on the measured response	134
4.4.5	Contribution of DEM to laboratory testing	135
4.4.6	Contribution of DEM to constitutive modelling of pellet materials.....	136
4.5	Conclusions and perspectives	137
4.5.1	Behaviour of a single pellet upon partial hydration in free-swelling conditions.....	137
4.5.2	Behaviour of pellet assemblies upon partial hydration in constant-volume conditions	137
4.5.3	Differences between measured response in the laboratory and intrinsic behaviour.....	138
4.5.4	Determination of constitutive laws describing the mechanical behaviour of pellet assemblies	138

5	Modelling the hydromechanical behaviour of pellet-based bentonite materials	139
5.1	Introduction	139
5.2	Conceptual approach	139
5.2.1	Description of the material phases	139
5.2.2	Main notations.....	140
5.2.3	Main hypotheses.....	143
5.3	DEM simulation of large pellet assemblies.....	145
5.3.1	Objectives.....	145
5.3.2	Method	145
5.3.3	Numerical simulation results and discussion	150
5.3.4	Proposition of a model for the “granular” state.....	159
5.4	Transition from “granular” to “continuous” state.....	162
5.4.1	Identified parameters.....	162
5.4.2	Description of DEM simulations of binary granular mixtures.....	164
5.4.3	Results of DEM simulations	165
5.4.4	Conclusions	168
5.5	Modelling the “continuous” material mechanical behaviour	168
5.5.1	Objectives.....	168
5.5.2	Modification of the Barcelona Basic Model	168
5.5.3	Constitutive equations	169
5.6	Implementation of the model.....	171
5.6.1	Introduction	171
5.6.2	Summary of the model features	172
5.6.3	Calculation of stress state from total volumetric strain	174
5.6.4	Microstructural strains.....	181
5.7	Validation against experimental results.....	182
5.7.1	Determination of the model parameters	183
5.7.2	Mechanical loading at constant suction in oedometer conditions	186
5.7.3	Simulation of the swelling pressure tests along the entire hydration path	188
5.8	Conclusions and perspectives	193
5.8.1	DEM simulations of large granular assemblies.....	194
5.8.2	DEM simulations of binary granular mixtures.....	194

5.8.3	Modification of the Barcelona Basic Model	194
5.8.4	Differences between experimental and numerical responses	195
5.8.5	Transition from granular to continuous state	195
5.8.6	Water transfer	196
6	Mock-up imbibition tests and water transfer laws	197
6.1	Introduction	197
6.2	Mock-up imbibition tests in the laboratory	197
6.2.1	Objectives.....	197
6.2.2	Material and methods.....	197
6.2.3	Experimental results.....	203
6.2.4	Discussion	216
6.2.5	Conclusions and perspectives.....	223
6.3	Proposition of transfer laws.....	224
6.3.1	Apparent permeability of the microstructure	224
6.3.2	Pellet-matrix transfer law	227
6.3.3	Water transfer within the matrix	233
6.4	Implementation of pellet-matrix transfer law	236
6.4.1	Implementation in Bil.....	236
6.4.2	Simulation of swelling pressure tests	237
6.5	Conclusion and perspectives	242
6.5.1	Mock-up imbibition tests	242
6.5.2	Proposition of transfer laws.....	243
6.5.3	Large scale modelling	243
7	General conclusion	245
7.1	Overview of the context	245
7.2	Contributions of the present work	245
7.2.1	Overview of the thesis.....	245
7.2.2	Limitations of the proposed model.....	247
7.3	Perspectives for future work.....	247
7.3.1	Large-scale modelling	247

Contents

7.3.2	Macrostructural swelling dependency on the dry density	248
7.3.3	Water retention behaviour and water transfer	248
7.3.4	Characterisation of the state transition	248
	List of references	251

LIST OF TABLES

Table 2-1: Main physical properties of MX80, Febex and FoCa7 bentonites	9
Table 2-2: Main initial characteristics of Lloret et al. (2003) and Villar (1999) samples.....	30
Table 2-3: Stress paths followed by Lloret et al. (2003) and Villar (1999) samples.....	31
Table 2-4: Values of parameters a_s and β_s of equation 2-6 for three types of bentonite (Wang et al., 2012).....	35
Table 2-5: Estimated water density of adsorbed water layers in Na-montmorillonite and Febex bentonite (Jacinto et al., 2012).	40
Table 2-6: Overview of the modelling approach for pellet mixtures in the literature.....	63
Table 2-7: Overview of the behaviour of pellet-powder mixtures	65
Table 3-1: Pellet geometrical properties at initial state.....	68
Table 3-2: Pellet physical properties at initial state.....	69
Table 3-3: Dimensions of the cell and sensor used in swelling pressure tests.	71
Table 3-4: Pellet and powder mass laid in the cell to prepare the samples.	73
Table 3-5: Summary of the characteristics of the suction-controlled swelling pressure tests performed in the laboratory.....	73
Table 3-6: Salt solutions used for vapour equilibrium technique.....	74
Table 3-7: Hydration paths followed by the samples.....	74
Table 3-8: Summary of the swelling pressure at equilibrium upon suction-controlled hydration for all swelling pressure tests.	84
Table 3-9: Final measured suction and water content of samples SP0a and SP15a.....	86
Table 3-10: Comparison between estimated final swelling pressure (Wang et al., 2012) and measured swelling pressure.	87
Table 4-1: 32-mm pellet geometrical properties at initial state.....	98
Table 4-2: 32-mm pellet physical properties at initial state.	98
Table 4-3: Salt solutions used for vapour equilibrium technique.....	100
Table 4-4: Parameters proposed to describe the hydromechanical behaviour of single MX80 pellets, determined from compression tests.	118
Table 4-5: Friction values used during preparation and hydration steps in DEM01, DEM02 and DEM03 simulations. 100 simulations are performed for each type of simulation.	120
Table 5-1: Overview of the phases and levels of structure describing the material in the model. ..	140
Table 5-2: Overview of the different notations used to describe the different phases in the model.....	140

Table 5-3: Initial state properties of the numerical samples. All samples are cubic and contain 4000 beads.....	148
Table 5-4: Proposed values for the dimensionless parameters describing the behaviour of pellet assemblies.....	158
Table 5-5: Criteria describing the transition from granular to continuous states.	172
Table 5-6: List of the main equations of the model.	173
Table 5-7: Main properties of the different MX80 pellet-powder mixtures simulated in the present Chapter.	183
Table 5-8: Model parameters for the granular state used in the simulations.....	183
Table 5-9: Model parameters for the continuous state used in the simulations	185
Table 5-10: Model parameters for plasticity and hardening	186
Table 6-1: Dimensions of the cell and sensor used in swelling pressure tests.	198
Table 6-2: Main features of MU30, MU15, and MU0 samples.	203
Table 6-3: Elapsed time from the start of imbibition at which pictures are taken in Figure 6-22; Figure 6-23 and Figure 6-24.	215
Table 6-4: Summary of the five types of FEM simulations performed. $k_{int 1}$ is given in m^2	231

LIST OF FIGURES

Figure 1-1: Location of Bure on a geological map of the Paris basin and 3D block diagram presenting the geological context of the Bure underground research laboratory.....	2
Figure 1-2: Expansive clays plugs in drift in the French concept of radioactive waste disposal.	3
Figure 2-1: Structure of montmorillonite clay minerals. Two “TOT” unit layers with hydrated interlamellar cations are represented (modified after Pusch and Yong, 2006).....	8
Figure 2-2: Schema of a bentonite particle (modified after Pusch and Yong, 2006).	9
Figure 2-3: Pore size distribution of a MX80 bentonite-sand mixture compacted at two dry densities (left, Wang et al., 2013a) and a MX80 granule at a dry density of 2.12 Mg/m ³ (right, Molinero-Guerra et al., 2017).	10
Figure 2-4: ESEM micrographs of the Černý vrch bentonite equilibrated at a suction of 290.75 MPa. The sample dry densities are 1.27 Mg/m ³ (left) and 1.90 Mg/m ³ (right) (Sun et al., 2019).	11
Figure 2-5: The axis-translation method (Delage and Cui, 2000).	13
Figure 2-6: The osmotic method (Delage and Cui, 2000).	14
Figure 2-7: The vapour equilibrium technique.	14
Figure 2-8: Probability distribution of the number of water layers adsorbed in interlamellar space in MX80 bentonite (Saiyouri et al., 2004).	16
Figure 2-9: Evolution of the average interlayer distance and number of layers per particle in MX80 bentonite upon suction decrease (Saiyouri et al., 2004).	16
Figure 2-10: Total water content compared to crystalline water content and number of layers per particle as a function of decreasing suction (Saiyouri et al., 2004).	17
Figure 2-11: Water retention curve of MX80 bentonite materials under different hydration conditions and at different dry densities, upon suction decrease. CV = constant volume, FS = free-swelling, ρ_{d0} = initial dry density.	18
Figure 2-12: Pore size distributions of a MX80 bentonite-sand mixture upon hydration in constant-volume conditions (Wang et al., 2013b).	19
Figure 2-13: Mercury intrusion porosimeter test results performed on a MX80 granular bentonite compacted at 1.80 Mg/m ³ upon hydration in constant-volume conditions (Seiphoori et al., 2014). Left: cumulative void ratio, right: pore size distribution. Dashed line: as compacted state, solid line: saturated.	20
Figure 2-14: Profile of inter-aggregate porosity deduced from X-ray computed tomography images obtained at different times (left) and initial and final state images of the sample with average inter-aggregate porosity (right). t1 = 7.1 days, t2 = 8.8 days, t3 = 15.8 days, t4 = 19.7 days, t5 = 39.8 days. The initial inter-aggregate porosity was 38 % and decreased to 0 % upon wetting (Massat et al., 2016).	20
Figure 2-15: SEM micrographs of a sample of granular bentonite compacted at a dry density of 1.80 Mg/m ³ characterised by a bimodal pore size distribution (left, as compacted state) and a monomodal pore size distribution (right) (Seiphoori et al., 2014).	21

Figure 2-16: Honeycomb structure filling inter-aggregate porosity as a result of aggregate exfoliation during hydration (Keller et al., 2014).....	22
Figure 2-17: SEM micrographs of the sample compacted at a dry density of 1.7 Mg/m ³ and water content of 0.125 at 1 day (left) and 90 days (right). Picture width is 40 μm (Delage et al., 2006).	22
Figure 2-18: Maximum swelling strain of Kunigel bentonite under zero stress as a function of initial dry density (left) and as a function of vertical stress at different initial dry density (right) (Komine and Ogata, 2003).	23
Figure 2-19: Final swelling strain of Febex bentonite upon wetting under constant vertical stress at different initial dry densities (Villar and Lloret, 2008).	24
Figure 2-20: Slope of the void ratio-logarithm of suction relationship of Febex bentonite upon hydration (right) (Lloret et al., 2003) and evolution of void ratio upon suction decrease of MX80 bentonite-sand mixtures at initial dry density of 1.96 Mg/m ³ and free-swelling conditions (Gatabin et al., 2016) and at initial dry density of 1.67 Mg/m ³ and vertical stress of 0.1 MPa (Wang et al., 2013a).....	24
Figure 2-21: Evolution of void ratio during wetting of FoCa7 bentonite samples under their respective compaction stress (Cui et al., 2002a).	25
Figure 2-22: Influence of a wetting-drying path on Febex bentonite at high suction under low vertical stress. White symbols represent initial states (Lloret et al., 2003).	26
Figure 2-23: Evolution of swelling and shrinkage of a Febex bentonite-sand mixture (initial dry density of 1.50 Mg/m ³) with the number of wetting-drying cycles under constant vertical stress of 396 kPa (Alonso et al., 2005).	27
Figure 2-24: Loading of compacted Febex bentonite under constant suction in oedometer tests (Lloret et al., 2003). Grey solid lines aim at delimiting elastic and elastic-plastic loadings.	28
Figure 2-25: Apparent preconsolidation pressure at various suction values for three types of compacted expansive soils: compacted Febex bentonite (initial dry density ~1.70 Mg/m ³ ; Lloret et al., 2003), compacted MX80 bentonite-sand mixture in proportions 70/30 (initial dry density 1.67 Mg/m ³ ; Wang et al., 2013a), compacted bentonite-silt mixture in proportions 60/40 (initial dry density 1.27 Mg/m ³ ; Cuisinier and Masrouri, 2005). Saturated conditions are plotted as 0.1 MPa of suction.	29
Figure 2-26: Apparent preconsolidation pressure at saturation for MX80 bentonite materials at various void ratios. After experimental data from Marcial (2003), Villar (2005), Molinero-Guerra et al. (2019b). The dashed blue line corresponds to equation 2-5 with $p^*_o = 110$ MPa and $n_p = 3.7$	30
Figure 2-27: Stress paths followed by Lloret et al. (2003) and Villar (1999) samples.	31
Figure 2-28: Evolution of the void ratio of Febex samples in Lloret et al. (2003) and Villar (1999).	31
Figure 2-29: Suction controlled swelling pressure tests performed on compacted Febex bentonite. Initial dry densities and suction for SP1, SP2, SP3, and SP4 are: 1.65 Mg/m ³ and 424 MPa, 1.63 Mg/m ³ and 146 MPa, 1.57 Mg/m ³ and 70 MPa, and 1.50 Mg/m ³ and 39 MPa, respectively. The two black dashed lines crossing test results are delimiting the three identified zones (Lloret et al., 2003).....	34
Figure 2-30: Evolution of inter-aggregate porosity and swelling pressure as a function of elapsed time during wetting under constant-volume conditions (Massat et al., 2016).....	34
Figure 2-31: Relationship between dry density and swelling pressure for three different bentonites and estimation using equation 2-6 (Wang et al., 2012).	35

Figure 2-32: Relationship between swelling pressure and bentonite dry density (equation 2-7) for MX80 based materials (Wang et al., 2012).....	36
Figure 2-33: Influence of the ionic strength of the wetting fluid on the swelling potential of Febex bentonite compacted to a dry density of 1.65 Mg/m ³ (Castellanos et al., 2006).....	37
Figure 2-34: Evolution of the degree of saturation of a bentonite-sand mixture (70/30 in dry mass proportions) compacted at an initial dry density of 2.01 Mg/m ³ upon hydration in constant-volume and free-swelling conditions (Gatabin et al., 2016).....	38
Figure 2-35: Suction-degree of saturation relationship for MX80 bentonite in constant-volume conditions.....	39
Figure 2-36: Suction-degree of saturation relationship for MX80 bentonite in free-swelling conditions.....	39
Figure 2-37: Water content (left) and dry density (right) profiles in the EB experiment following dismantling (Wieczorek et al., 2017).....	42
Figure 2-38: Unsaturated apparent hydraulic conductivity of a MX80-sand (70/30 in proportions) mixture as a function of decreasing suction (Wang et al., 2013b).....	43
Figure 2-39: Intrinsic permeability of MX80 bentonite in saturated conditions as a function of dry density.....	44
Figure 2-40: 3D reconstruction of a bentonite pellet from X-ray computed tomography images. A crack network is identified and associated to the macroporosity (Molinero-Guerra et al., 2017).....	45
Figure 2-41: Saturated porosity in MX80 bentonite pellet deduced from saturation and MIP test results of Molinero-Guerra et al. (2019a), at different suction: 135.5 MPa (a); 9 MPa (b); 4.2 MPa (c); 1 MPa (d).....	46
Figure 2-42: Pore size distribution of a pelletised Febex bentonite (Hoffmann et al., 2007).....	47
Figure 2-43: Distribution of density in a bentonite pellet-powder mixture at dry state, obtained from X-ray computed tomography results (van Geet et al., 2005).....	47
Figure 2-44: Grain size distribution before and after compaction to a dry density of 1.50 Mg/m ³ (Hoffmann et al., 2007).....	48
Figure 2-45: Evolution of a pelletised Febex bentonite sample upon hydration, at four degrees of saturation (Sr) (Hoffmann et al., 2007).....	49
Figure 2-46: Evolution of the granular structure of a MX80 bentonite pellet-powder mixture during hydration (Molinero-Guerra et al., 2018a).....	49
Figure 2-47: Permeability of a pelletised Febex bentonite compacted at a dry density of 1.3 Mg/m ³ as a function of the degree of saturation (Hoffmann et al., 2007).....	50
Figure 2-48: MX80 pellet-powder mixture prepared for hydration test, at initial state. Local heterogeneities of density are clearly observable. SP xx labels correspond to the position of pressure sensors, xx being the elevation in mm (Molinero-Guerra et al., 2018b).....	51
Figure 2-49: Evolution of the void ratio of an ideal binary mixtures with $d_L \gg d_s$. The blue area corresponds to the behaviour mainly controlled by large particles. The red area corresponds to the behaviour mainly controlled by small particles.....	53

Figure 2-50: Reasons for underestimation of void ratio using equations 2-12 and 2-13: insertion of particles not small enough (left and centre) and wall effect inducing a low density zone near large particles (right).	53
Figure 2-51: Results of suction-controlled oedometer tests performed by Molinero-Guerra et al. (2019b) on a pellet-powder mixture: void ratio-vertical stress relationship (left) and volumetric strain-elapsed time relationship following loading. Negative volumetric strains indicate swelling.	54
Figure 2-52: Swelling pressure test results performed on pelletised Febex bentonite (Hoffmann et al., 2007).....	55
Figure 2-53: Example of stress path in the s-p plane and coupling between SI and LC.	61
Figure 3-1: Diagram of the pellets used in the present work.	68
Figure 3-2: Assembly of the MX80 pellets used in the present work.	69
Figure 3-3: Diagram of the isochoric cell designed for swelling pressure tests.....	71
Figure 3-4: Picture of the isochoric cell used for swelling pressure tests.	71
Figure 3-5: Sketch of the suction-controlled system. Red arrows represents humid air circulation. 75	
Figure 3-6: Swelling pressure as a function of elapsed time for test SP30a. The dots on the solid line are the values considered at equilibrium.	76
Figure 3-7: Swelling pressure as a function of elapsed time for test SP15a. The dots on the solid line are the values considered at equilibrium.	77
Figure 3-8: Swelling pressure as a function of elapsed time for test SP15b. The dots on the solid line are the values considered at equilibrium.	78
Figure 3-9: Swelling pressure as a function of elapsed time for test SP0a. The dots on the solid line are the values considered at equilibrium.	79
Figure 3-10: Swelling pressure as a function of elapsed time for test SP0b. The dots on the solid line are the values considered at equilibrium.	79
Figure 3-11: Swelling pressure as a function of decreasing suction for test SP30a.	81
Figure 3-12: Swelling pressure as a function of decreasing suction for test SP15a.	81
Figure 3-13: Swelling pressure as a function of decreasing suction for test SP15b.....	82
Figure 3-14: Swelling pressure as a function of decreasing suction for test SP0a.	83
Figure 3-15: Swelling pressure as a function of decreasing suction for test SP0b.....	83
Figure 3-16: Picture of samples SP0a and SP0b after dismantling. a: SP0a equilibrated at 9 MPa of suction; b: SP0b equilibrated at 4 MPa of suction; c: SP0a removed from the isochoric cell.	85
Figure 3-17: Picture of SP15a sample after dismantling. Left: Top of the sample in the cell, right: sample removed from the isochoric cell. The sample lost its integrity.	86
Figure 3-18: Comparison of SP15b; SP0a and SP0b test results.	88
Figure 3-19: Comparison of SP30a; SP15b; SP0a and SP0b test results. Left: semi-logarithmic plot, right: logarithmic-logarithmic plot.	88

Figure 3-20: Comparison of SP0a and SP0b test results. The vertical dashed line correspond to the suction at which the material has been observed to be granular.	89
Figure 3-21: Comparison of SP15a and SP15b test results.	90
Figure 3-22: Interpretation of the experimental results in terms of involved mechanisms. It is not clear if a “granular-continuous” transition occurred in “dense” powder samples or if only the “continuous” behaviour was observed.	92
Figure 4-1: Picture of an assembly of 32-mm pellet.	99
Figure 4-2: Desiccator used for the vapour equilibrium technique.	100
Figure 4-3: Picture of a 32-mm pellet following equilibrium at a controlled suction of 9 MPa. Left: Pellet height; Right: Pellet diameter.	101
Figure 4-4: Load frame used for the compression test. Left: Picture; Right: Diagram.	101
Figure 4-5: Compression directions. Left: Axial tests; Right: Radial tests.	102
Figure 4-6: Evolution of 7-mm pellet water content upon hydration at controlled relative humidity in the desiccators.	103
Figure 4-7: Evolution of water content upon suction decrease for three MX80 pellets in free-swelling conditions.	104
Figure 4-8: Evolution of the degree of saturation upon suction decrease for three MX80 pellets.	105
Figure 4-9: Experimental results for axial strain and radial strain of 7-mm pellets.	105
Figure 4-10: Evolution of mean radial strain, mean axial strain, and corresponding volumetric strain of 7-mm pellet upon suction decrease. The red dashed line is the model prediction (see 4.2.5).	106
Figure 4-11: Evolution of mean radial strain, mean axial strain, and corresponding volumetric strain of 32-mm pellet upon suction decrease. The red dashed line is the model prediction (see 4.2.5).	106
Figure 4-12: Evolution of total void ratio of pellets upon suction decrease.	107
Figure 4-13: Pictures of 32-mm pellets at equilibrium at different suctions. Left: 59 MPa; Centre: 40 MPa; Right: 13 MPa.	107
Figure 4-14: Picture of 7-mm pellets at equilibrium at 9 MPa suction.	107
Figure 4-15: Axial test results for 7-mm pellets. Solid black lines are the experimental force-displacement relationships. The dashed red lines are the relationship obtained through equation 4-5 for a given value of E . Tests are performed at different suctions: a) 89 MPa; b) 82 MPa; c) 59 MPa; d) 57 MPa; e) 40 MPa; f) 38 MPa; g) 25 MPa; h) 13 MPa; i) 9 MPa.	109
Figure 4-16: Axial test results for 32-mm pellets. Solid black lines are the experimental force-displacement relationships. The dashed red lines are the relationship obtained through equation 4-5 for a given value of E . Tests are performed at different suctions: a) 107 MPa (equilibrium with laboratory conditions); b) 82 MPa; c) 59 MPa; d) 40 MPa; e) 25 MPa; f) 13 MPa; g) 9 MPa.	110
Figure 4-17: Determination of E in radial tests using equation 4-6.	111
Figure 4-18: Radial test results for 7-mm pellets. Solid black lines are the experimental force-displacement relationships. Tests are performed at different suctions: a) 89 MPa; b) 82 MPa; c) 59 MPa; d) 57 MPa; e) 40 MPa; f) 38 MPa; g) 25 MPa; h) 13 MPa; i) 9 MPa.	113
Figure 4-19: Radial test results for 32-mm pellets.	113

Figure 4-20: Evolution of the experimental results for E in axial and radial tests for the 7-mm pellet.	114
Figure 4-21: Evolution of the experimental results for E in axial and radial tests for the 32-mm pellet.	114
Figure 4-22: Experimental results for pellet (7 mm) strength upon suction decrease in axial and radial directions. Red dashed lines represent the model predictions for $R_A(s)$ and $R_R(s)$	115
Figure 4-23: Experimental results for pellet (32 mm) strength upon suction decrease in axial and radial directions. Red dashed lines represent the model predictions for $R_A(s)$ and $R_R(s)$	115
Figure 4-24: Relationship between pellet strength and pellet Young modulus. Experimental results for 7-mm pellet. The red dashed lines represent the model predictions.	116
Figure 4-25: Relationship between pellet strength and pellet Young modulus. Experimental results for 32-mm pellet. The red dashed lines represent the model predictions.	117
Figure 4-26: Sketch of two spheres in contact in DEM simulations.	121
Figure 4-27: Normal force-normal deflection relationship in DEM simulations.	122
Figure 4-28: Diagram representing the tangential reaction-tangential displacement relationship in DEM simulations.	123
Figure 4-29: Preparation step in DEM simulations.	124
Figure 4-30: Dimensions of the simulated cell.	124
Figure 4-31: Evolution of the apparent swelling pressure in DEM01, DEM02 and DEM03 numerical samples and SP0a and SP0b experimental samples upon suction decrease. The mean values determined over 100 simulations are plotted for numerical results.	125
Figure 4-32: Evolution of the apparent swelling pressure and contact plasticity in DEM01 numerical samples upon suction decrease. The mean values determined over 100 simulations are plotted.	126
Figure 4-33: Evolution of the apparent swelling pressure and contact plasticity in DEM02 numerical samples upon suction decrease. The mean values determined over 100 simulations are plotted.	126
Figure 4-34: Evolution of the apparent swelling pressure and contact plasticity in DEM03 numerical samples upon suction decrease. The mean values determined over 100 simulations are plotted.	127
Figure 4-35: Evolution of the coordination number in numerical samples upon suction decrease. The mean values determined over 100 simulations are plotted.	128
Figure 4-36: Evolution of the coefficient of variation of some features of DEM01 numerical samples during hydration: a) swelling pressure; b) coordination number; c) proportion of plastic contacts.	129
Figure 4-37: Evolution of apparent swelling pressure in DEM01 numerical samples upon suction decrease for two diameter ratios.	130
Figure 4-38: Variability of the calculated swelling pressure as a function of the diameter ratio (D_{sensor} / a_{eq0}). Left: overview, right: zoom on diameter ratio between 3 and 6.	130
Figure 4-39: Evolution of the bulk modulus and volumetric strain of a MX80 aggregate, 7-mm pellet, and 32-mm pellet from values of α_m and β_m determined by Tang and Cui (2009) and in the present study.	131

Figure 4-40: Mean elastic normal deflection increment as a function of radius increment for particles-upper wall contacts in simulations DEM01, DEM02, DEM03. The mean values, determined over 100 simulations, are plotted. The coloured dots correspond to the occurrence of the peak of swelling pressure. The black dashed line correspond to a “1:1” line, i.e. each radius increment induces a similar increment in mean elastic normal deflection, thus no rearrangement of the granular structure, provided that contacts are elastic.....	134
Figure 4-41: Evolution and variability of apparent swelling pressure ($D_{sensor} / a_{eq 0} = 4$) and mean stress upon suction decrease in DEM01 simulations.....	135
Figure 5-1: Representation of the initial states of all numerical samples, along with DEM01 initial state for comparison.	148
Figure 5-2: Evolution of the granular assembly volumetric strain as a function of the dimensionless pressure parameter during isotropic compression in A-samples.	151
Figure 5-3: Evolution of the granular assembly volumetric strain as a function of the dimensionless pressure parameter during isotropic compression in B-samples.	151
Figure 5-4: Evolution of the granular assembly volumetric strain as a function of the dimensionless pressure parameter during isotropic compression in C-samples.	151
Figure 5-5: Evolution of the granular assembly volumetric strain as a function of the dimensionless pressure parameter during isotropic compression in D-samples.	152
Figure 5-6: Evolution of the granular assembly volumetric strain as a function of the dimensionless pressure parameter during isotropic compression in J-samples.	152
Figure 5-7: Evolution of the proportion of plastic contacts in the granular assembly as a function of the dimensionless pressure parameter during isotropic compression in A-samples.....	153
Figure 5-8: Evolution of the proportion of plastic contacts in the granular assembly as a function of the dimensionless pressure parameter during isotropic compression in B-samples.....	154
Figure 5-9: Evolution of the proportion of plastic contacts in the granular assembly as a function of the dimensionless pressure parameter during isotropic compression in C-samples.....	154
Figure 5-10: Evolution of the proportion of plastic contacts in the granular assembly as a function of the dimensionless pressure parameter during isotropic compression in D-samples.....	154
Figure 5-11: Evolution of the proportion of plastic contacts in the granular assembly as a function of the dimensionless pressure parameter during isotropic compression in J-samples.....	155
Figure 5-12: Evolution of the coordination number as a function of the dimensionless pressure parameter in A- and B-samples.	156
Figure 5-13: Evolution of the granular assembly volumetric strain as a function of the dimensionless pressure parameter during isotropic compression in A1- and B1-samples.	156
Figure 5-14: Comparison of the volumetric strains calculated upon isotropic compression for A1, B1, C1, D1, and J1 samples. The red dashed line corresponds to the model predictions for elastic contacts.....	157
Figure 5-15: Relationship between m_{g^*} and Φ_{10} for all simulation results.	158
Figure 5-16: Relationship between f_{Mm} obtained for all types of samples (dots) and ε_{vI} (dashed line) determined by swelling-shrinkage simulations using DEM. m_g is taken equal to $\sim 10^{-3}$	159

Figure 5-17: Evolution of mean stress as a function of decreasing suction in the simulation of binary granular mixtures using DEM. Dots represent the mean value for five samples while dashed lines represent the interval defined by two standard deviations.165

Figure 5-18: Contribution of the pellet assembly without powder grains and of the powder grain assembly without pellets to the total mean stress developed in the samples upon suction decrease. Mean values for the five samples are plotted.166

Figure 5-19: Evolution of r_{vf} and r_{ms} as functions of decreasing suction in the five samples. Mean values are plotted.....167

Figure 5-20: Values of κ_s used in the simulations as functions of the material initial dry density. 185

Figure 5-21: Mesh and displacement boundary conditions used in the simulation of the oedometer test.187

Figure 5-22: Comparison between experimental results of a constant suction mechanical loading in oedometer and numerical modelling of these latter. Left: comparison of results at identical vertical stress; right: evolution of void ratio in the simulation and transition across three domains: granular and “elastic contacts”, granular and “plastic contacts”, continuous.....188

Figure 5-23: Mesh and displacement boundary conditions used in the simulation of the swelling pressure tests.....189

Figure 5-24: Comparison between swelling pressure test results and numerical simulation of these latter for the 70/0 mixture.....191

Figure 5-25: Comparison between swelling pressure test results and numerical simulation of these latter for the 70/15 mixture.....191

Figure 5-26: Comparison between swelling pressure test results and numerical simulation of these latter for the 70/30 mixture.....192

Figure 5-27: Comparison of all experimental and numerical results of swelling pressure tests.193

Figure 6-1: Diagram of the imbibition cell.198

Figure 6-2: Picture of the imbibition cell.199

Figure 6-3: MU0 sample during the preparation step.200

Figure 6-4: Picture of the MU0 sample following the preparation step.....201

Figure 6-5: Picture of the MU15 sample following the preparation step.....201

Figure 6-6: Picture of the MU30 sample following the preparation step.....202

Figure 6-7: Picture of the three cells and the framework of the black box following the preparation step.202

Figure 6-8: Picture of the three samples at initial state.203

Figure 6-9: Evolution of the infiltrated volume of water as a function of elapsed time for the three imbibition tests (left) and zoom after 300 days of imbibition (right).204

Figure 6-10: Evolution of relative humidity in MU0 imbibition test as a function of elapsed time, at four different elevations.205

Figure 6-11: Relative humidity in MU0 imbibition test as a function of elevation, at five different elapsed times.205

Figure 6-12: Evolution of relative humidity in MU15 imbibition test as a function of elapsed time, at four different elevations.	206
Figure 6-13: Relative humidity in MU15 imbibition test as a function of elevation, at six different elapsed times.	206
Figure 6-14: Evolution of relative humidity in MU30 imbibition test as a function of elapsed time, at four different elevations.	207
Figure 6-15: Relative humidity in MU30 imbibition test as a function of elevation, at five different elapsed times.	207
Figure 6-16: Swelling pressure as a function of elapsed time at different elevations in MU0 test.	208
Figure 6-17: Profile of swelling pressure at different elapsed times in MU0 test.	208
Figure 6-18: Swelling pressure as a function of elapsed time at different elevations in MU15 test.	209
Figure 6-19: Profile of swelling pressure at different elapsed times in MU15 test.	210
Figure 6-20: Swelling pressure as a function of elapsed time at different elevations in MU30 test.	210
Figure 6-21: Profile of swelling pressure at different elapsed times in MU30 test.	211
Figure 6-22: Pictures of the 70/0 sample at different elapsed time during imbibition.	212
Figure 6-23: Pictures of the 70/15 sample at different elapsed time during imbibition.	213
Figure 6-24: Pictures of the 70/30 sample at different elapsed time during imbibition.	214
Figure 6-25: Estimation of pellet vertical displacements in MU0 test.	215
Figure 6-26: Peak swelling pressure as a function of relative humidity in MU0, MU15, and MU30 tests.	217
Figure 6-27: Peak swelling pressure as a function of (macrostructural) suction in MU0, MU15, and MU30 tests.	217
Figure 6-28: Identified dry inter-pellet voids in MU0 test after 1.5 year of imbibition.	218
Figure 6-29: Water fluxes at the bottom of the cell in MU0, MU15 and MU30 tests.	219
Figure 6-30: Picture of the 70/30 mixtures following MU30 dismantling after 235 days: a) $z = \sim 60$ mm; b) $z = \sim 80$ mm; c) $z = \sim 110$ mm.	221
Figure 6-31: Measured suction and water content as functions of elevation in dismantled MU30 test.	222
Figure 6-32: Corrected suction, swelling pressure, and measured relative humidity as functions of elevation in dismantled MU30 test.	222
Figure 6-33: Water retention curve of the 70/30 mixture in the dismantled MU30 test compared with free-swelling pellets. Mixture values are obtained at different elevations. The dashed blue line represents the theoretical final water content.	223
Figure 6-34: Mesh used for the FEM simulations of a single pellet hydration to determine microstructural permeability.	225

Figure 6-35: Numerical results of the evolution of microstructural suction in the pellet as a function of elapsed time, under boundary conditions of MU30 tests and with $k_{int 1} = 10^{-23} \text{ m}^2$, compared with experimental results.....	226
Figure 6-36: Characteristic time of transfer as a function of suction for two values of $k_{int 1}$	228
Figure 6-37: Mesh used for the FEM simulations of the hydration of a single pellet to determine the transfer coefficient.....	229
Figure 6-38: Evolution of the profile of suction in the pellet with time. The profile is homogeneous at $t = \tau$ (4756300 s).....	230
Figure 6-39: Mass exchange as a function of time during a step of suction decrease. It is highlighted that the equilibrium can be reached before $t = \tau$	230
Figure 6-40: Evolution of β_{Mm} as a function of suction for varying l_c/r (a), varying $k_{int 1}$ (b), and varying N (c).	232
Figure 6-41: Comparison of β_{Mm} obtained in FEM simulations and values obtained from equation 6-8.....	232
Figure 6 42: Sketch of water transfer in pellet-powder mixtures described in the present section. Red arrows represent vapour transfer, Green arrows represent liquid transfer, blue arrows represent pellet-matrix exchanges, and yellow arrow represents powder-macropores transfer (equilibrium). Left: mixture scale; Centre: pellet scale; Right: powder grain scale.	233
Figure 6-43: Comparison of experimental data for bentonite intrinsic permeability and model prediction for the matrix using $k_{int 1} = 10^{-23} \text{ m}^2$; $k_A = 7 \text{ m}^3/\text{Mg}$ and $k_B = 7.5 \times 10^7$. Dashed line represents model predictions.	235
Figure 6-44: Comparison of FEM results and experimental results for the 70/0 material and two values of β_H	238
Figure 6-45: Comparison of FEM results and experimental results in the swelling pressure-suction (s_2) plane for $\beta_H = 5 \times 10^5 \text{ kg}^{-1} \text{ Pa}^{-0.5}$, $\beta_H = 5 \times 10^6 \text{ kg}^{-1} \text{ Pa}^{-0.5}$, and $\beta_H \rightarrow \infty$ for the 70/0 material.	239
Figure 6-46: Evolution of pellet suction as a function of elapsed time in the simulation for $\beta_H = 5 \times 10^6 \text{ kg}^{-1} \text{ Pa}^{-0.5}$; $\beta_H = 5 \times 10^5 \text{ kg}^{-1} \text{ Pa}^{-0.5}$ and $\beta_H \rightarrow \infty$ for the 70/0 material.	239
Figure 6-47: Comparison of FEM results and experimental results for the 70/15 material and two values of β_H	240
Figure 6-48: Comparison of FEM results and experimental results in the swelling pressure-suction (s_2) plane for $\beta_H = 5 \times 10^5 \text{ kg}^{-1} \text{ Pa}^{-0.5}$, $\beta_H = 5 \times 10^6 \text{ kg}^{-1} \text{ Pa}^{-0.5}$, and $\beta_H \rightarrow \infty$ for the 70/15 material.	240
Figure 6-49: Evolution of pellet suction as a function of elapsed time in the simulation for $\beta_H = 5 \times 10^6 \text{ kg}^{-1} \text{ Pa}^{-0.5}$; $\beta_H = 5 \times 10^5 \text{ kg}^{-1} \text{ Pa}^{-0.5}$ and $\beta_H \rightarrow \infty$ for the 70/15 material.	240
Figure 6-50: Comparison of FEM results and experimental results for the 70/30 material and two values of β_H	241
Figure 6-51: Comparison of FEM results and experimental results in the swelling pressure-suction (s_2) plane for $\beta_H = 5 \times 10^5 \text{ kg}^{-1} \text{ Pa}^{-0.5}$, $\beta_H = 5 \times 10^6 \text{ kg}^{-1} \text{ Pa}^{-0.5}$, and $\beta_H \rightarrow \infty$ for the 70/30 material.	241
Figure 6-52: Evolution of pellet suction as a function of elapsed time in the simulation for $\beta_H = 5 \times 10^6 \text{ kg}^{-1} \text{ Pa}^{-0.5}$; $\beta_H = 5 \times 10^5 \text{ kg}^{-1} \text{ Pa}^{-0.5}$ and $\beta_H \rightarrow \infty$ for the 70/30 material.	242

LIST OF NOTATIONS

BBM: Barcelona Basic Model
BExM: Barcelona Expansive Model
Ca: Calcium
CEC: Cation exchange capacity
CV: Constant-volume
DEM: Discrete Element Method
EB: Engineered Barrier experiment
EDS: Energy-Dispersive Xray Spectroscopy
ESEM: Environmental scanning electron microscope
FEBEX: Full scale high level waste Engineered Barrier experiment
FEM: Finite Element Method
FIB-nt: Cryo-Focused Ion Beam nanotomography
FS: Free-swelling
LC: Loading-Collapse (BBM)
LVDT: Linear variable differential transformer
Mg: Magnesium
MIP: Mercury intrusion porosimetry
Na: Sodium
PEG: Polyethylene glycol
PSD: Pore size distribution
REV: Representative Elementary Volume
SD: Suction Decrease (BBM)
SEM: Scanning electron microscope
SI: Suction Increase (BBM)
 S_{sa} : Specific surface area
URL: Underground research laboratory
WRC: Water retention curve

LIST OF SYMBOLS

$\overline{(\quad)}$: Mean value

A : Water retention parameter

a_{eq} : Equivalent diameter of modelled pellets

a_{eq0} : Initial equivalent diameter of modelled pellets

a_{eqf} : Final equivalent diameter of modelled pellets

a_{eqi} : Equivalent diameter of modelled pellets at step i

a_S : Model parameter relating final swelling pressure to dry density

B : Bentonite proportion in mixture

C : Constitutive tensor

C : Transfer coefficient

C_A : Model parameter relating pellet axial strength to pellet Young modulus

C_C : Virgin compression stiffness parameter

C_R : Model parameter relating pellet radial strength to pellet Young modulus

C_S : Unloading/reloading stiffness parameter

C_{tr} : Micro-macro transfer coefficient

CV : Coefficient of variation

D : Pellet diameter

D : Damage coefficient

d_L : Diameter of large particles

d_S : Diameter of small particles

D_{sensor} : Sensor diameter

D_{vap} : Diffusion coefficient of vapour in air

E : Young modulus

E^* : Equivalent Young modulus

e : Void ratio

e_0 : Void ratio at initial state

e_1 : Pellet void ratio in FEM

e_2 : Powder void ratio in FEM

e_{ins} : Void ratio obtained by insertion mechanism

- e_L : Void ratio of the assembly of large particles
- e_M : Macrostructural void ratio
- e_m : Microstructural void ratio
- e_{min} : Theoretical minimum void ratio
- e_s : Void ratio of the assembly of small particles
- e_{sub} : Void ratio obtained by substitution mechanism
- f : BExM interaction function
- F : Yield surface in the BBM
- \bar{F} : Mean value of the contact force in a granular assembly
- F_{ij} : Contact force between two particles i and j
- f_{mA} : Model parameter
- F_{max} : Maximum force applied on a particle in DEM
- f_{mB} : Model parameter
- f_{Mm} : Ratio of granular assembly volumetric strain to particle volumetric strain
- F_{net} : Net force applied on a particle in DEM
- f_{NR} : Test function in the Newton-Raphson procedure
- F_T : Tangential reaction vector
- F_T : Norm of the tangential reaction vector
- f_e : Parameter describing the compressibility of the granular assembly
- f_{eA} : Model parameter
- f_{eB} : Model parameter
- G : Plastic potential
- G_s : Specific gravity of secondary material in mixture
- h : height of the cylinder part of the pellet
- H_{cell} : Height of the cell
- $H_{cell 0}$: Initial height of the cell
- h_w : Water head
- I : Identity matrix
- I : Dimensionless inertia parameter in DEM simulation
- i : Iteration
- i_{vap} : Diffusive flux vector for vapour in air
- $K^{(e)}$: Material bulk modulus
-

-
- K : Apparent hydraulic conductivity
- k_A : Matrix permeability parameter
- k_B : Matrix permeability parameter
- k_{int} : Intrinsic permeability
- $k_{int\ 1}$: Intrinsic permeability of the pellet phase in FEM
- K_m : Microstructural bulk modulus
- k_r : Relative permeability
- k_s : Parameter describing the increase of cohesion with suction
- l_c : Characteristic length of the mesh in FEM
- M : Slope of the critical state line in the modified Cam Clay model
- m : Water retention parameter
- m_I : Mass of the pellet phase in FEM
- m_g : Dimensionless pressure parameter
- m_g^* : Dimensionless pressure parameter at pellet strength
- m_l : Liquid water mass
- m_p : Mass of a particle in DEM
- m_{pel} : Pellet mass
- m_{pow} : Powder mass
- m_{vap} : Vapour mass
- M_w : Molecular mass of water
- m_w : Water mass
- N : In FEM simulations, number of suction decrease steps
- N : Elastic normal force at contact in DEM
- n : Water retention parameter
- N_c : Number of contacts
- $N_{c\ 1}$: Number of particle-particle contacts
- $N_{c\ 2}$: Number of particle-wall contacts
- n_p : Model parameter
- N_p : Number of particles
- N^v : Viscous component of the contact force
- p : Mean stress
- \bar{p} : Net stress
-

- p' : Effective mean stress
- p'_m : Microstructural effective mean stress
- $p_0(s)$: Apparent preconsolidation pressure at suction s
- p_0 : Saturated apparent preconsolidation pressure
- p_0^* : Model parameter
- p_1' : Effective mean stress in pellets in FEM
- p_2' : Effective mean stress in powder in FEM
- p_{atm} : Atmospheric pressure
- p_c : BBM reference stress
- pF : Potential of free energy
- p_g : Gas pressure
- p_m : Microstructural mean stress
- $p_s(s)$: Intersection of the yield surface and p axis in the BBM at suction s
- P_S^* : Computed swelling pressure at equilibrium in DEM simulations
- p_{vap} : Partial pressure of vapour
- p_w : Water pressure
- \mathbf{q} : Advective flux vector
- q : Deviatoric stress
- \mathbf{q}_l : Advective flux vector for liquid water
- R : Ideal gas constant
- R^* : Equivalent radius in contact law
- r : Constant related to the ratio of $\lambda(s \rightarrow \infty)$ to $\lambda(0)$ in the BBM
- r : Equivalent radius of a pellet in FEM
- \bar{r} : Average distance between two particle centres in DEM
- r_0 : Initial equivalent radius in FEM
- r_0 : Initial distance between two particle centres in DEM
- R_A : Axial strength of pellet
- r_c : Curvature radius
- RH : Relative humidity
- \mathbf{r}_{ij} : Vector joining the centres of two particles i and j in contact in DEM
- r_{ms} : Ratio of mean stress in DEM simulations of binary mixtures
- R_R : Radial strength of pellet
-

-
- r_{vf} : Ratio of volume fraction in DEM simulations of binary mixtures
- r_{vf}^* : Threshold ratio of volume fraction in the granular-continuous transition
- s : Soil suction
- s^* : Threshold soil suction in the granular-continuous transition
- s_0 : Suction yield locus in the BBM
- s_1 : Suction in pellets in FEM
- s_2 : Suction in matrix in FEM
- S_g : Degree of saturation of the gas phase
- s_i : Suction measured in pellets at initial state
- $s_{i\ pow}$: Suction measured in powder at initial state
- s_m : Matric suction
- s_m : Microstructural suction
- $s_{m\ 0}$: Microstructural suction at initial state
- s_o : Osmotic suction
- S_l : Degree of saturation of liquid water
- s_t : Total suction
- T : Thermodynamic temperature
- t : time
- \mathbf{u} : Displacement field
- u_N : Normal displacement in compression tests
- w : Gravimetric water content
- w_a : Gravimetric water content of secondary material
- w_i : Gravimetric water content measured in pellet at initial state pellet
- $w_{i\ pow}$: Gravimetric water content measured in powder at initial state
- w_m : Gravimetric water content of mixture
- $x_{c\ sup}^P$: Proportion of plastic contact between pellets and upper wall in numerical samples
- $x_{c\ tot}^P$: Proportion of plastic contact in a numerical sample
- x_L : Volumetric proportion of large particles
- x_S : Volumetric proportion of small particles
- $x_{S\ 0}$: Mass proportion of powder in the sample
- $x_{S\ crit}$: Critical volumetric proportion of small particles
- Z : Coordination number
-

z : Elevation

α_L : Volume fraction of large particles

α_L^* : Maximum volume fraction of large particles

α_m : Microstructural elastic stiffness parameter

α_S : Volume fraction of small particles

α_S^* : Maximum volume fraction of small particles

α_v : Damping parameter in DEM

β : BBM parameter

β_H : Model parameter describing micro-macro water transfers

β_m : Microstructural elastic stiffness parameter

β_{Mm} : Coefficient describing micro-macro water transfers

β_S : Model parameter

Γ_{max} : Maximum moment applied on a particle

Γ_{net} : Net moment applied on a particle

γ : Parameter of the model, set to 1.5

δ_N : Normal deflection at contact

δ_T : Relative tangential displacement vector

$\boldsymbol{\varepsilon}$: Strain tensor

ϵ : Tolerance value for equilibrium in DEM

ϵ_0 : Parameter describing the initial diameter increment in DEM

ϵ_a : Axial strain

ϵ_f : Parameter describing the final diameter increment in DEM

ϵ_i : Parameter describing the diameter increment at calculation step i in DEM

$\dot{\epsilon}$: Strain rate

ϵ_r : Radial strain

ϵ_V : Volumetric strain

ϵ_{V1} : Pellet volumetric strain in FEM

ϵ_{V2} : Powder volumetric strain in FEM

$\epsilon_{VA}^{(e)}$: Elastic volumetric strain associated to variation of m_g

$\epsilon_{VB}^{(e)}$: Elastic volumetric strain associated to variation of ϵ_{V1}

$\epsilon_{VC}^{(e)}$: Elastic volumetric strain in pellets associated to variation of suction

$\epsilon_{VD}^{(e)}$: Elastic volumetric strain in powder associated to variation of suction

-
- $\varepsilon_{VE}^{(e)}$: Elastic volumetric strain associated to variation of p
 ε_V^e : Elastic volumetric strain
 ε_{VM} : Macrostructural volumetric strain
 ε_{Vm} : Microstructural volumetric strain
 ε_{Vm}^e : Microstructural elastic volumetric strain
 ε_V^P : Plastic volumetric strain
 $\varepsilon_V^{P_{LC}}$: Plastic volumetric strain induced by LC mechanism
 $\varepsilon_V^P_M$: Macrostructural plastic volumetric strain
 ζ : Relative permeability parameter
 Θ : Volumetric water content
 Θ_r : Residual volumetric water content
 Θ_{sat} : Saturated volumetric water content
 κ : Unloading/reloading (elastic) stiffness parameter
 κ_{eq} : Equivalent dimensionless stiffness parameter
 κ_g : Dimensionless stiffness parameter for granular assemblies
 κ_m : Microstructure elastic stiffness parameter
 κ_s : Elastic stiffness parameter for change in suction
 λ : Virgin compression stiffness parameter
 $\lambda(s)$: Elastoplastic stiffness parameter for net stress change, at suction s
 λ_m : Microstructure elastoplastic stiffness parameter
 λ_p : Plastic multiplier
 λ_s : Elastoplastic stiffness parameter for suction increase
 μ : Friction coefficient
 μ_f : Fluid dynamic viscosity
 μ_w : Water dynamic viscosity
 ν : Poisson ratio
 ρ_d : Dry density
 ρ_d^* : Average dry density of the pellet-powder mixture
 ρ_{d0} : Initial dry density
 ρ_{d1} : Pellet dry density
 ρ_{db} : Bentonite dry density
 ρ_{dmat} : Apparent dry density of the matrix
-

List of Symbols

- ρ_f : Fluid density
 ρ_m : Mixture density
 ρ_s : Density of solid particles
 ρ_{vap} : Vapour density
 ρ_w : Water density
 σ : Total stress tensor
 $\sigma^{(e)}$: Total trial stress tensor
 σ' : Effective stress tensor
 σ_S : Estimated final swelling pressure
 σ_V' : Effective vertical stress
 τ : Characteristic time of water transfers
 τ_g : Tortuosity
 Φ_I : Pellet volume fraction
 Φ_{I0} : Pellet initial volume fraction
 Φ_2 : Powder volume fraction
 Φ_M : Macropore volume fraction
 Φ_{mat} : Matrix volume fraction
 ϕ : Porosity
 ϕ_I : Porosity of the pellet phase in FEM
 ϕ_{im} : Inter-pellet porosity
 χ : Bishop parameter
 ψ_g : Gravitational potential
 ψ_m : matrix potential
 ψ_o : Osmotic potential
 ψ_p : Pressure potential
 ψ_i : Total water potential
 Ω : Total volume
 Ω_0 : Total volume at initial state
 Ω_I : Pellet volume in FEM
 Ω_2 : Powder volume in FEM
 Ω_L : Volume of large particles
 Ω_M : Macropore volume in FEM

Ω_p : Pellet volume

Ω_s : Volume of small particles

Ω_{s1} : Volume of solid in pellets in FEM

Ω_{s2} : Volume of solid in powder in FEM

Ω_v : Void volume

Ω_w : Water volume

1 INTRODUCTION

1.1 GENERAL CONTEXT

Deep geological repository is considered worldwide as the safest option for radioactive waste disposal, allowing waste to remain isolated from biosphere over long periods of time. Concepts of radioactive waste disposals vary depending on countries, but a general feature of these concepts is the reliance on the multi-barrier principle.

The multi-barrier principle consists in containing waste using a combination of natural and engineered materials which purposes are to isolate the waste and to impede water flow within the repository, thus enhancing the robustness of the concept. In most concepts, the multi-barrier system relies on (Sellin and Leupin, 2013; Andra, 2005):

- A canister containing and isolating waste, resisting to corrosion and retaining radionuclides;
- A natural geological barrier, *i.e.* a low permeability host rock, able to prevent the release of radionuclides for very long periods of time, allowing the level of radioactivity to decrease to a negligible level;
- An engineered barrier system, either surrounding and isolating the canister or installed as sealing plugs in the disposal galleries to prevent fluid migration through these latter.

The natural geological barrier considered in repository concepts varies between countries. For instance, crystalline rock such as granite is envisaged as host rock in Finland and Sweden; claystone is envisaged as host rock in Switzerland and France.

Engineered barriers concepts consist in the installation of a buffer composed of compacted bentonite-based materials, owing to their favourable properties regarding waste disposal. Bentonite-based materials are characterised by low permeability, good radionuclide retention capacity, and high swelling potential upon hydration. These properties would allow the engineered barrier to prevent fluid migration in the repository, fill technological voids upon hydration and subsequent swelling, and apply a swelling pressure against the gallery walls.

Engineered barrier performances are set in terms of permeability, required to be low enough to fulfil isolation requirements, and swelling pressure, required to be high enough to contribute to the sealing of fractures in the excavation damaged zone but limited to avoid damage of the host rock or the concrete abutments. These properties are related to the material dry density and, in this respect, the target dry density of engineered barrier is a key parameter of their installation.

The present work mainly focuses on the French concept of radioactive waste disposal, managed by Andra (the French national radioactive waste management agency). In the French concept of radioactive waste disposal (Cigéo), the Bure Callovo-Oxfordian claystone formation is a candidate host rock for deep geological repository (Figure 1-1). This formation is ~130 m thick, ~500 m deep, characterised by a low permeability and self-sealing abilities (Andra, 2005).

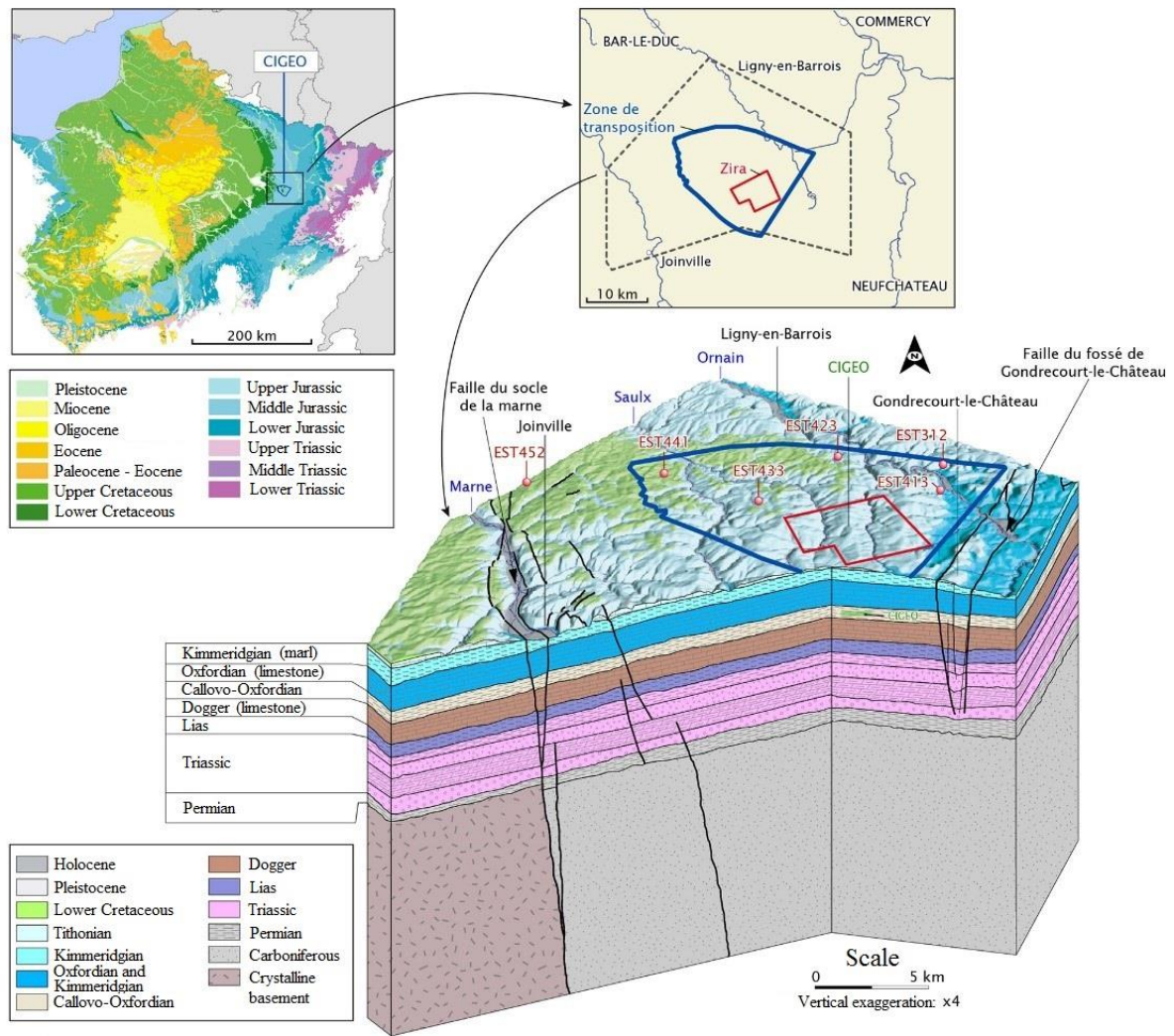


Figure 1-1: Location of Bure on a geological map of the Paris basin and 3D block diagram presenting the geological context of the Bure underground research laboratory.

The present work in particular focuses on the hydromechanical behaviour of the bentonite-based sealing plugs in the framework of the French concept. Engineered barriers in Cigéo are not directly surrounding canisters. Bentonite buffers are installed at several locations in the disposal galleries and are confined between concrete abutments (Figure 1-2). The buffer material is installed in a dry state in the galleries and progressively undergoes hydration as water flows from the host rock.

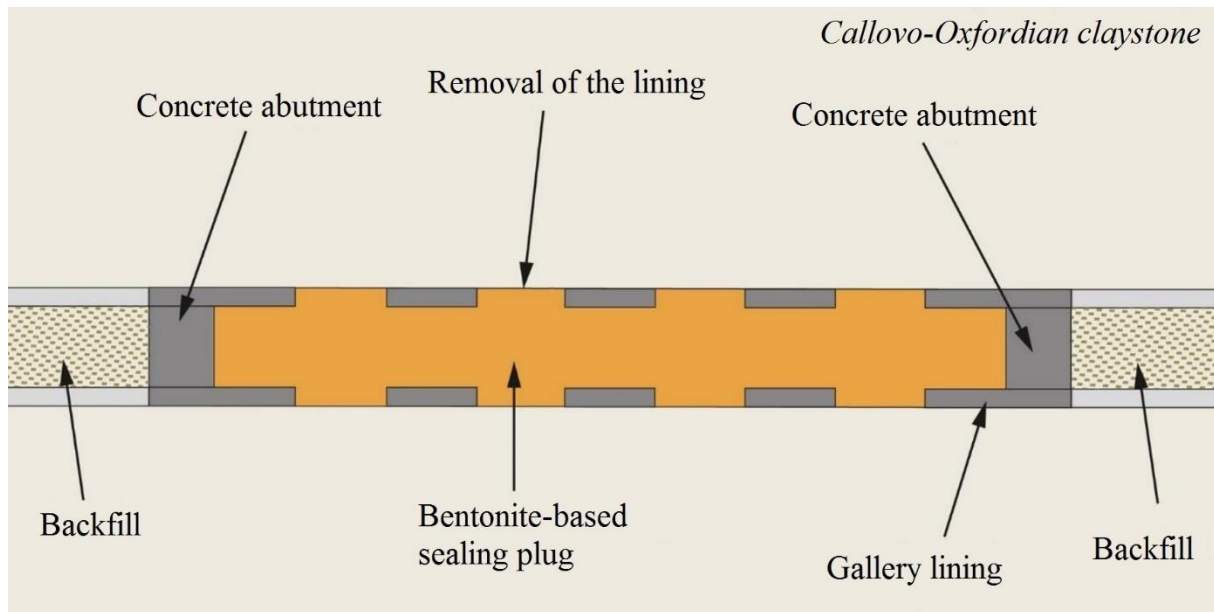


Figure 1-2: Expansive clays plugs in drift in the French concept of radioactive waste disposal.

The long-term assessment of the engineered barrier performance requires a deep knowledge of the hydromechanical behaviour of compacted bentonite. In this respect, this latter has been widely addressed over the last decades (*e.g.* Saiyouri et al., 2000; Blatz et al., 2002; Lloret et al., 2003; Komine and Ogata, 2003; Cuisinier and Masrouri, 2005; Agus and Schanz, 2005; Delage et al., 2006; Villar 2007; Tang et al., 2008; Karnland et al., 2008; Wang et al., 2012; Saba et al., 2014a; Seiphoori et al., 2014; Keller et al., 2014; Massat et al., 2016; Sun et al., 2019).

1.2 PROBLEM STATEMENT AND OBJECTIVES OF THE PRESENT WORK

Bentonite granular mixtures have been envisaged for the engineered barriers owing to operational convenience and reduction of technological voids (*e.g.* Volckaert et al., 1996; van Geet et al., 2005; Imbert and Villar, 2006; Hoffmann et al., 2007; Alonso et al., 2011; Gens et al., 2011; Molinero-Guerra et al., 2017; Mokni et al., 2019).

In the French concept of radioactive waste disposal, a bentonite pellet-powder mixture is a candidate material for the sealing of galleries. Pellets are high-density subspherical bentonite granules. Powder is a fine-grained material basically obtained by crushing pellets. Owing to performance requirement, a dry density of 1.50 Mg/m^3 and relative proportions of 70 % pellet and 30 % powder are envisaged for the mixture.

In repository conditions, the mixture is laid in dry state as a granular assembly. In fully-saturated conditions, bentonite granular mixtures are characterised by a homogenised state and behave as traditional compacted blocks. Before a homogenised state is reached, the initial granular structure of the mixture is likely to influence the hydromechanical behaviour of the buffer. Yet, this latter is neither clearly known nor explicitly accounted for in numerical models. During the installation of granular bentonite materials in repository conditions, local heterogeneities of pellet/powder content are likely to arise. In some zones within the buffer, initial state can thus be characterised by inter-pellet voids filled with a dense powder phase, a loose powder phase, or even no powder phase. In this respect, the

characterisation of the influence of the granular structure with respect to powder content seems a requirement to assess the performance of engineered barriers made of pellet mixtures.

To this purpose, the objectives of the present work are:

- the experimental characterisation of pellet-based bentonite materials upon hydration, from pellet scale to large scale;
- a numerical investigation using discrete simulations, to assess the relationship between the behaviour of the pellet and that of the pellet assembly;
- the proposition of a modelling framework able to consider the particular features of pellet-powder mixtures;
- the implementation and validation against experiments of the proposed model.

1.3 OUTLINE OF THE THESIS

The objectives of the thesis are addressed in five Chapters.

In Chapter 2, a literature review is presented. Bentonite-based materials have been studied for several decades in the framework of radioactive waste disposal, and an overview of the state of knowledge resulting from these studies is provided. In particular, the microstructure of bentonite materials and its evolution upon hydration; the macroscopic response of bentonite materials under hydromechanical loadings; particular features related to granular mixtures; and the presentation of a commonly used modelling framework are presented in this review.

In Chapter 3, the experimental evidence of the influence of the initial granular structure on the macroscopic response upon hydration is provided. Suction-controlled swelling pressure tests are performed on three different pellet-powder mixtures, all of them characterised by the exact same mass of pellet and different powder contents.

Chapter 4, following the results of Chapter 3, aims at validating a modelling approach based on discrete element method. The hydromechanical behaviour of a single pellet at high suction is characterised in the laboratory. A simple model is proposed to describe its behaviour. Discrete simulations of swelling pressure tests of Chapter 3 are performed by modelling pellets as spheres and providing each sphere with the behaviour of a pellet. Simulation results provide an insight into the influence of the granular structure on the material response in swelling pressure tests. Variability of the measured response in the laboratory is also addressed.

Chapter 5 presents the realisation of discrete simulation of the isotropic compression of large pellet assemblies at different initial densities. The influence of pellet swelling on the swelling of the pellet assembly is also addressed. A model describing the hydromechanical behaviour of pellet-powder mixtures before homogenisation is proposed from simulation results. From experimental works available in the literature and, to some extent, from discrete simulations of binary granular mixtures, a criterion is proposed to describe the transition from a mechanical behaviour controlled by the pellet assembly to the behaviour of a continuous material. A modification of the Barcelona Basic Model (Alonso et al., 1990) is proposed to consider different levels of structure to describe the behaviour of pellet-powder mixtures in the “continuous” domain. The model is implemented in the finite element method (FEM) code Bil. Swelling pressure tests presented in Chapter 3 are then simulated by imposing a suction decrease, using a single set of parameters, along the entire hydration path.

Chapter 6 presents the realisation of mock-up imbibition tests on the three mixtures already tested in Chapter 3. In this experimental study, a glass side is considered in the cell design to allow pictures to be taken using a camera. This special design along with traditional measurements of relative humidity and swelling pressure profiles provide valuable information regarding the mixture hydration. Transfer laws are proposed following the experimental study to describe water transfer in pellet-powder mixtures, in the light of experimental results, simulation results at the pellet scale, and data available in the literature. A simplified transfer law describing pellet-macroporosity water exchanges in particular is implemented in Bil and swelling pressure tests of Chapter 3 are simulated, imposing the same suction-elapsed time relationship as in experiments.

General conclusions along with identified perspectives arising from the present work finally constitute Chapter 7.

2 LITERATURE REVIEW

2.1 INTRODUCTION

Bentonite based materials have been considered as sealing materials in radioactive waste disposal concepts for more than thirty years owing to their low permeability, good radionuclide retention capacity and ability to swell upon hydration, an important property allowing the material to fill technological voids in the galleries (*e.g.* Pusch 1979; Delage et al., 1998; Saiyouri et al., 2000; Vaunat and Gens, 2005; Villar 2008; Mokni et al., 2016; Molinero-Guerra et al., 2019a).

While many studies on the behaviour of bentonite-based materials in repository conditions focused on compacted blocks, pellet mixtures have been considered as an interesting alternative because of operational convenience (*e.g.* Volckaert et al., 1996; van Geet et al., 2005; Hoffmann et al., 2007; Alonso et al., 2011; Gens et al., 2011; Molinero-Guerra et al., 2017). In this case, dry pellets are laid in the galleries as a granular assembly. The material loses its initial granular structure upon wetting from the host rock pore water, then behaves as traditional compacted blocks near saturation.

The hydromechanical behaviour of bentonite materials is known to involve strong multi-scale couplings, making it challenging to perform quantitative long term predictive simulations at the structure scale. A significant amount of studies about experimental characterisation of the material and numerical modelling of its behaviour under various conditions can be found in the literature. This chapter aims at providing the reader with an overview of the state of knowledge concerning the hydromechanical behaviour of bentonite-based materials used as engineered barriers.

The microstructural features of bentonite materials are first described in 2.2. The macroscopic response of compacted bentonite under various hydromechanical loadings is then presented in 2.3. Bentonite pellet mixtures are characterised by some particular features induced by the initial granular structure. These aspects are underlined in 2.4. An overview of modelling approaches commonly used to perform simulations of the hydromechanical behaviour of engineered clayey barriers then constitutes section 2.5. Finally, section 2.6 is a conclusion of the literature review. This final section suggests some needed contributions to better understand and model the behaviour of pellet mixtures in repository conditions, which is the main objective of the present work.

2.2 MICROSTRUCTURE OF COMPACTED BENTONITES

In this section, the microstructure of compacted bentonites is addressed. Bentonites are clay materials characterised by a significant montmorillonite clay minerals content. The structure of montmorillonite minerals has a significant influence on bentonite hydromechanical behaviour. Its description constitutes part 2.2.1.

In the framework of nuclear waste disposal, bentonite materials are compacted to a high dry density on the dry side of their optimum water content. The arrangement of montmorillonite particles in this context defines the bentonite double structure fabric. Its description constitutes part 2.2.2.

Suction in bentonite materials has a significant importance in the hydromechanical behaviour. Its definition and relationship with microstructural features as well as method to control its value in the laboratory constitute part 2.2.3.

Bentonites fabric controls its macroscopic response under hydromechanical loading. Hydration mechanisms and influence of hydration on the double structure constitute part 2.2.4.

2.2.1 Structure of montmorillonite clay minerals

Some relevant features of bentonite materials such as the significant swelling potential or water retention behaviour are direct consequences of the montmorillonite structure. The montmorillonite structure consists of the succession of one sheet of silicon tetrahedron, one sheet of hydroxyl and aluminium octahedron, and one sheet of silicon tetrahedron. It is often referred to as the “TOT” or “2:1” unit layer (Figure 2-1).

Cations substitutions affect this ideal structure, mostly Al^{3+} for Si^{4+} in tetrahedron sheets and a divalent cation for the trivalent cation in the octahedron sheet. The positive charge deficit is balanced by the presence of additional cations in the interlamellar space. The thickness of the “TOT”/“2:1” unit layer is 1 nm, the thickness of the interlamellar space depends on the hydration state (Pusch and Yong, 2006; Meunier, 2005). The positive charge deficit and presence of cation in interlamellar space is a key feature of bentonite hydration mechanisms and is discussed in the following parts.

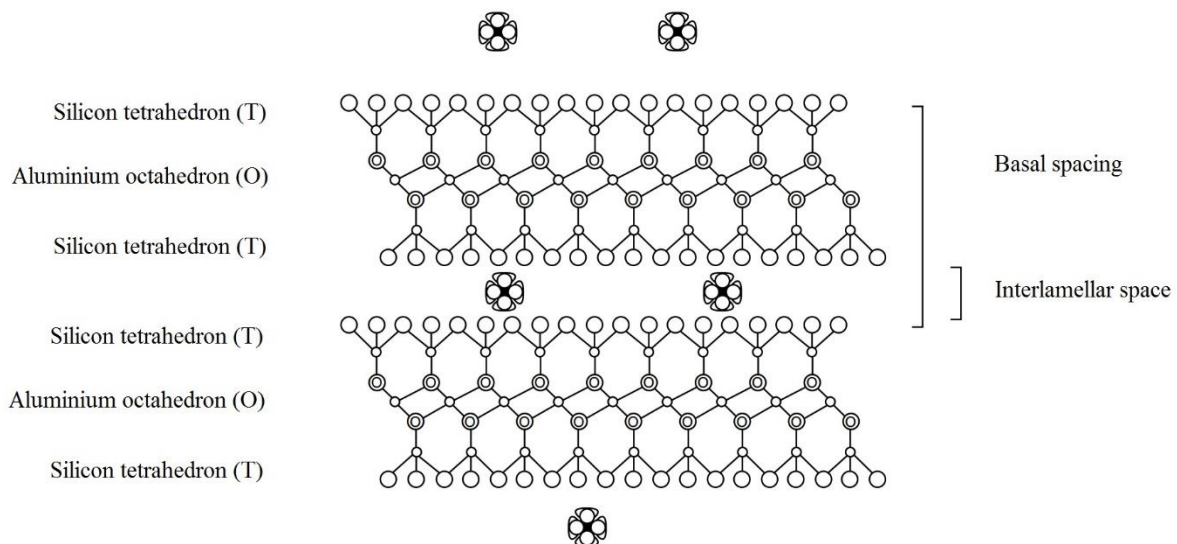


Figure 2-1: Structure of montmorillonite clay minerals. Two “TOT” unit layers with hydrated interlamellar cations are represented (modified after Pusch and Yong, 2006).

2.2.2 Fabric of compacted bentonites

2.2.2.1 Description of bentonite particles

Clay particles are stacks of clay mineral unit layers. In bentonites, most of the clay minerals are montmorillonite, which structure has been previously described. A typical bentonite particle is a stack of 1 nm thick “TOT” unit layers (Figure 2-1) with exchangeable cations in the interlamellar space. Depending on the main exchangeable cation, bentonites can be referred to as “sodium (Na)-bentonite”, “calcium (Ca)-bentonite”, or “magnesium (Mg)-bentonite”.

Febex, MX80 and FoCa bentonites are among the most frequently studied bentonites in the framework of radioactive waste disposal. Their Na^+ , Ca^{2+} and Mg^{2+} exchangeable cation contents as well as cation exchange capacity (CEC) and specific surface area (S_{sa}) are presented in Table 2-1.

Table 2-1: Main physical properties of MX80, Febex and FoCa7 bentonites

Bentonite	CEC	S_{sa}	Na^+	Ca^{2+}	Mg^{2+}
	meq/100 g	m^2/g	meq/100 g	meq/100 g	meq/100 g
Febex	111 ^a	725 ^a	25 ^a	47 ^a	36 ^a
MX80	82.3 ^b	522 ^b	80 ^b	5 ^b	-
FoCa7	69 ^b	454 ^b	3 ^b	63 ^b	-

^a:Lloret and Villar (2007); ^b: Saiyouri et al., 2004;

The CEC is defined as the number of positive charges per dry mass of clay that can be exchanged. The S_{sa} is defined as the total surface area (interlayer surface area and external surface area of particles) per dry mass of clay. These parameters and the nature of exchangeable cations influence the material water retention and swelling behaviour, which will be addressed in a further part.

The number of “TOT” unit layers per particle in bentonite depends on the hydration state. For instance, it ranges from ~ 350 at dry state to ~ 10 at wet state for MX80 bentonite, from ~ 100 to ~ 10 for FoCa7 bentonite (Saiyouri et al., 2004). This decrease is related to hydration mechanisms, discussed in a following part. A schema of a bentonite particle is provided in Figure 2-2. Bentonite particles can aggregate as a result of Coulomb force (Meunier, 2005). The size of an aggregate is in the $\sim 10 - \sim 100 \mu\text{m}$ order of magnitude and obviously depends on the hydration state.

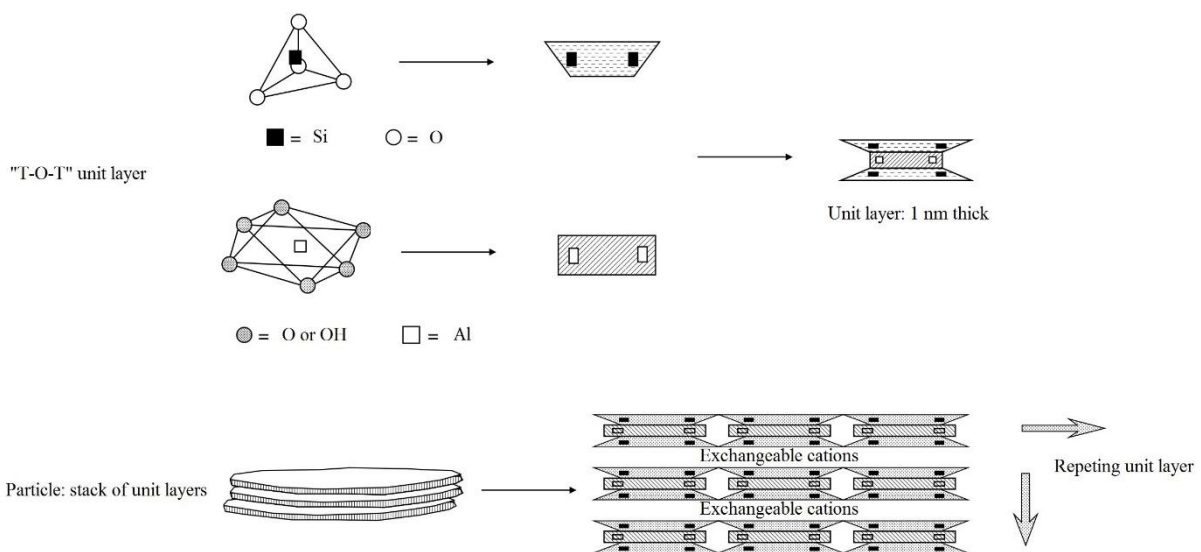


Figure 2-2: Schema of a bentonite particle (modified after Pusch and Yong, 2006).

2.2.2.2 A double porosity material

The pore structure of unsaturated clay sample can be studied using Mercury Intrusion Porosimetry (MIP) tests. The sample is freeze-dried and undergoes mercury injection. Mercury is a non-wetting fluid and therefore requires a pressure to be applied in order to wet the sample. Pores are assumed to be cylindrical. The Laplace law relates the mercury pressure to the entrance diameter of pores (Delage and Lefebvre, 1984). Samples are considered not to be altered by the experimental protocol (Lawrence, 1978; Delage and Pellerin, 1984). The sample pore size distribution (PSD) is obtained from the injected volume of mercury-applied pressure relationship. Additional details concerning the MIP test procedure and result interpretation can be found in Delage and Lefebvre (1984), Cuisinier and Laloui (2004), Romero and Simms (2008)

Clayey materials compacted on the dry side of the optimum water content are known to exhibit an aggregated structure (Delage et al., 1996). The aggregated structure is evidenced by the presence of two peaks on PSD (Romero and Simms, 2008). These two peaks correspond to two distinct families of pores, referred to as “micropores” and “macropores”.

Micropores are the voids inside clay aggregates, between particles and in particles (interlamellar space). Macropores are inter-aggregates voids. Experimental results available on various clayey materials suggest that micropores are not impacted by mechanical loading, whereas macropores diameter and proportion decrease with increasing dry density (*e.g.* Delage et al., 1996; 2006; Romero et al., 2005; Romero and Simms, 2008). Aggregated soils at high dry density may have negligible macroporosity as a result. It is highlighted in Figure 2-3 which presents MIP results for a MX80 bentonite-sand mixture compacted at dry densities 1.67 Mg/m³ and 1.97 Mg/m³ and a highly compacted MX80 bentonite granule. Similar trend can be found in Lloret et al. (2003) and Lloret and Villar (2007) on Febex bentonite.

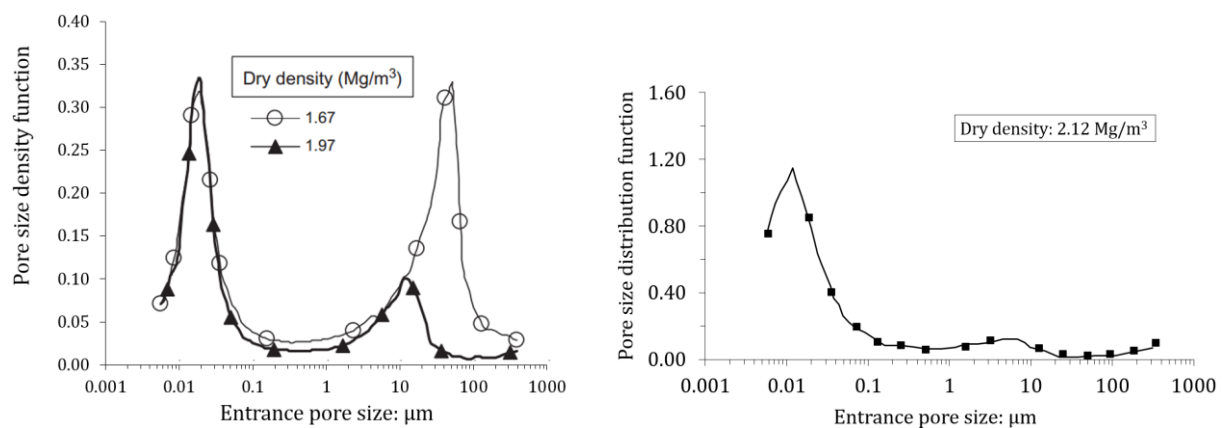


Figure 2-3: Pore size distribution of a MX80 bentonite-sand mixture compacted at two dry densities (left, Wang et al., 2013a) and a MX80 granule at a dry density of 2.12 Mg/m³ (right, Molinero-Guerra et al., 2017).

The double structure of bentonite materials can be directly observed using scanning electron microscopy techniques. Environmental scanning electron microscope (ESEM) is particularly adapted for the observation of unsaturated compacted bentonites. It allows a gaseous environment in the chamber, which allows humid samples to be observed which is not possible in scanning electron microscope (SEM) (Romero and Simms, 2008). Figure 2-4 presents a micrograph of two samples of a

bentonite from Černý vrch deposit, Czech Republic. Both samples are equilibrated at a suction of 290.75 MPa. The dry densities of the samples are 1.27 Mg/m³ and 1.90 Mg/m³. Aggregates of comparable size can be easily identified on both micrographs. Macroporosity is clearly identified on the micrograph of the 1.27 Mg/m³ sample whereas no clear macroporosity is visible on the micrograph of the 1.90 Mg/m³ sample (Sun et al., 2019).

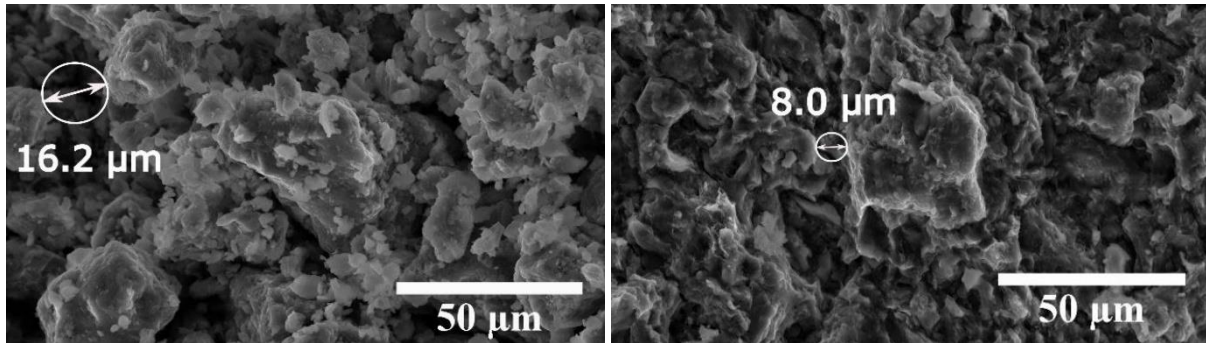


Figure 2-4: ESEM micrographs of the Černý vrch bentonite equilibrated at a suction of 290.75 MPa. The sample dry densities are 1.27 Mg/m³ (left) and 1.90 Mg/m³ (right) (Sun et al., 2019).

2.2.3 Suction in unsaturated soils

Soil water interactions in highly active clayey soils have a significant influence on the soil water retention behaviour, mechanical behaviour and water flow. These interactions can be related to the soil water potential or to suction. In this part, soil water potential and suction are first defined. Then, methods allowing to control suction in soils in the laboratory are presented.

2.2.3.1 Definition of soil water potential and suction

The water potential is defined as the work amount per unit mass of pure water required to transport reversibly and isothermally an infinitesimal quantity of water from a pool of pure water, at specified elevation and gas pressure, to the soil water, at the point under consideration (Aitchison et al., 1965).

The notation ψ_t is usually adopted for the total water potential. ψ_t is usually divided into four distinct parts. The sum of these four partial water potentials is equal to ψ_t :

$$\psi_t = \psi_g + \psi_p + \psi_o + \psi_m \quad 2-1$$

Where ψ_g is the gravitational potential. It is related to differences of elevation. It certainly affects water flow but has a limited effect on the soil mechanical behaviour. ψ_p is the pressure potential, related to applied pressure. ψ_p affects water flow. Its influence on the soil mechanical behaviour is however limited if the soil skeleton is considered incompressible. ψ_o is the osmotic potential, related to osmotic phenomena and dependent on the fluid chemistry. It is likely to have negligible effects in non-active soils (Gens, 2010). ψ_m is the matric, or internal, potential. It is related to capillary and adsorption

phenomena and is a negative value. In active clayey materials, only ψ_m and ψ_o have effect on the mechanical behaviour.

In terms of units, in Aitchison et al. (1965) definition, ψ_t is expressed in J.kg^{-1} . In soils, it is convenient to express the water potential in terms of water height or as a pressure:

- The first one introduces the “potential of free energy”, p_F , defined as

$$p_F = \log h_w \quad 2-2$$

Where h_w is the water height corresponding to the water potential, in cm (Schofield, 1935; Tessier, 1984).

- The second one can be defined as a work amount per unit volume instead of unit mass, thus expressed in J.m^{-3} (thus equivalent to a pressure unit) and introduces the concept of “total suction”. It is usually considered as a positive value, thus a sign change is required.

The total suction, s_t , is the sum of matric suction, s_m , and osmotic suction, s_o , analogous to matric potential and osmotic potential, respectively. s_t is related to relative humidity, RH , by the Kelvin law:

$$s_t = \frac{R T \rho_w}{M_w} \ln RH \quad 2-3$$

Where R is the ideal gas constant, T is the thermodynamic temperature, ρ_w is the water density, and M_w is the molecular mass of water.

Matric suction is usually considered to be equal to the sum of a capillary component and an adsorption component (Tuller et al., 1999; Baker and Frydman, 2009). Depending on the type of soil considered, capillary or adsorptive phenomena dominate. In granular soils, capillary potential tends to be dominant. In clayey soils, adsorptive potential tends to be dominant (Baker and Frydman, 2009; Gens, 2010).

Matric suction is sometimes referred to as *capillary pressure* or as a *negative pressure* and has traditionally been written as:

$$s_m = p_g - p_w \quad 2-4$$

Where p_g is the gas pressure and p_w is the water pressure. This is equivalent to considering that matric suction is only defined by capillary phenomena. Although this is not the case in compacted bentonites, where suction at unsaturated state can reach several tens to hundreds of MPa, this “*negative water pressure*” can be regarded as a way of quantifying the degree of attachment of water to the clay particle (Gens, 2010).

2.2.3.2 Control of soil suction in the laboratory

Since suction is directly related to the internal component of the water potential in soils, controlling suction in the laboratory allows the material to be studied upon controlled stages of hydration. An overview of four methods used to control soil suction in the laboratory is provided hereafter:

- The tensiometric plate method (Croney et al., 1958; Delage and Cui, 2000)
A soil sample is isolated from ambient air in a chamber. It is placed on a saturated, high air-entry value, ceramic disc which is connected to a water reservoir. A vacuum pump allows a negative pressure to be applied to the system, as described in equation 2-4. This latter is measured by a manometer. This system is limited by the cavitation phenomenon, which occurs at a pressure of -80 kPa in natural water (Delage and Cui, 2000).

- The axis translation method (Richards, 1941)
A soil sample is isolated from ambient air in a chamber. It is placed on a saturated, high air-entry value, ceramic disc which is connected to a water reservoir. The reservoir is maintained at atmospheric pressure. An air overpressure is applied in the chamber (Figure 2-5). Using equation 2-4, the controlled air overpressure and water pressure (ensured by the saturated porous stone) allows the matric suction to be controlled. The limit of this value is determined by the air-entry value of the porous ceramic disk. This technique has been criticised, mostly because: *i*) in natural soils air overpressure conditions are usually not encountered; *ii*) equation 2-4 does not exactly describe matric suction, water would undergo cavitation under high tension; *iii*) it is not clear how the air overpressure affects the soil sample in nearly saturated conditions where the gas phase continuity is not ensured (Delage et al., 2008; Baker and Frydman, 2009). However, good continuity has been found with vapour equilibrium technique (described hereafter) (Romero et al., 1999; Hoffmann et al., 2007; Delage et al., 2008; Tarantino et al., 2011).

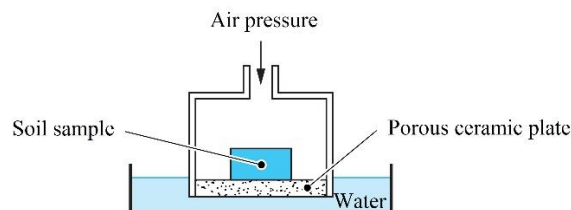


Figure 2-5: The axis-translation method (Delage and Cui, 2000).

- The osmotic method
A soil sample is placed inside a semipermeable membrane and plunged in a polyethylene glycol (PEG) solution. The concentration of the PEG solution induces an osmotic potential which makes water flow from the soil to the PEG solution across the membrane. The PEG reservoir should be large enough to consider its concentration constant when water crosses the membrane. Water transfer occurs until equilibrium is reached between the soil and the solution. The matric suction is therefore controlled by controlling the solution concentration (Delage et al., 1998; Williams and Shaykewich, 1969; Blatz et al., 2009). Matric suction up to ~10 MPa can be applied with reasonable accuracy using this method. The calibration of the suction-concentration relationship may be influenced by the type of membrane used for the test (Delage and Cui, 2008).

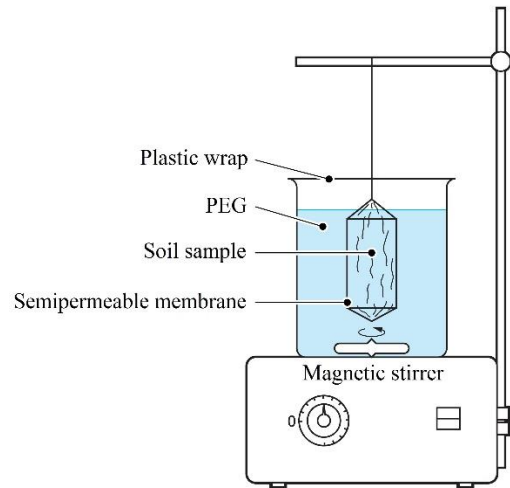


Figure 2-6: The osmotic method (Delage and Cui, 2000).

- The vapour equilibrium technique

The soil sample is isolated from ambient air in a desiccator. A solution is placed at the bottom of the desiccator. Depending on the chemical composition and concentration of the solution, air within the desiccator is equilibrated at a given relative humidity (Figure 2-7). Water exchanges occur in vapour phase between the soil sample and humid air of the desiccator. Solution in the desiccator are often oversaturated, to ensure that the concentration remains constant during water exchanges. Relative humidity values imposed in the desiccator can be found in the literature for a large number of salts (O'Brien 1948; Schneider 1960; Delage et al., 1998). Using equation 2-3, these values can be converted into total suction (Tang and Cui, 2005; Blatz et al., 2009). The vapour equilibrium technique is suitable for a wide range of suction, from zero suction (liquid water), up to several hundreds of MPa. It is therefore considered a very adapted method for compacted bentonites and has been extensively used in studies related to these materials (*e.g.* Saiyouri et al., 2000; Blatz et al., 2002; Lloret et al., 2003; Tang and Cui, 2005; Alonso et al., 2005; Agus and Schanz, 2005; Villar 2007; Wang et al., 2013a; Gatabin et al., 2016; Molinero-Guerra et al., 2019a).

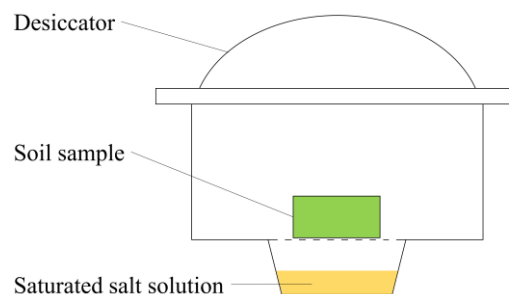


Figure 2-7: The vapour equilibrium technique.

A comparison between the four techniques presented in this part can be found in Fleureau et al. (1993). A kaolinite slurry is wet and dried over a wide range of suctions (0.4 – 180 MPa). A good correlation is found between the four techniques. In more active clays, experimental data from Marcial (2003) and Yigzaw et al. (2016) suggest that wetting using the osmotic technique can induce higher swelling strains or pressures at the same suction compared to the vapour equilibrium technique.

Finally, liquid water wetting is usually performed to impose a zero suction value to a soil sample. Further description and discussion related to suction control method in the laboratory can be found in Delage and Cui (2000); Delage et al. (2008); Delage and Cui (2008); Blatz et al. (2009); Romero et al. (2011).

2.2.4 Fabric evolution upon hydration

In the previous parts, the microstructure of compacted bentonites has been described. The material is characterised by a double structure fabric and its microstructure is mostly constituted by highly active montmorillonite minerals. High activity is reflected in considerable values of CEC and S_{SA} and induces high suction values of several tens to hundreds of MPa. These features have an influence on the hydration mechanisms of bentonites, which in turn affect the fabric described in 2.2.2. In this part, hydration mechanisms, water retention domains and double structure evolution upon hydration are presented.

2.2.4.1 Hydration mechanisms

The microstructure of the montmorillonite mineral (see Figure 2-1) has been shown to be characterised by a stack of the “TOT” unit layer and the presence of interlamellar cations to balance a positive charge deficit arising from substitutions within the mineral structure. These particular features influence the hydration mechanism of bentonites. Two main mechanisms have been described in the literature, described hereafter:

- “Crystalline” hydration

Crystalline hydration mechanism occurs at low relative humidity. Water molecules enter the interlamellar space of the clay mineral and first hydrate counterions, forming hydration spheres around the cations and hydrogen-bonding with the oxygen at the clay mineral surface (Norrish, 1954; Sposito and Prost, 1982). Upon further hydration, the solvation of exchangeable cations continues and water molecules organise in distinct layers, the maximum number of which mainly depends on the type of clay and nature of exchangeable cation. Water in interlamellar space can be denser and more viscous than bulk water (*e.g.* Langmuir 1917; Low, 1979; Villar, 2000; Bourg et al., 2003; Jacinto et al., 2012) and is not considered mobile under ordinary hydraulic gradients (Pusch and Yong, 2006).

Successive insertions of layers of water molecules in interlamellar space induce an increase of the interlayer spacing, referred to as crystalline swelling. In this respect, crystalline swelling, at the interlamellar space scale, can occur as a discrete phenomenon (Meunier, 2005). Using X-ray diffraction, the evolution of the interlamellar space upon hydration can be measured (*e.g.* Bradley et al., 1937; Hendricks et al., 1940; Saiyouri et al., 2000; 2004). For instance, in MX80 bentonite, Saiyouri et al. (2004) found that up to four layers of crystalline water are inserted upon hydration in free-swelling conditions. As a result, the interlamellar space increased from 9.6 Å (no water) to 12.6 Å (one layer), 15.6 Å (two layers), 18.6 Å (three layers), 21.6 Å (four layers). Figure 2-8

presents the probability distribution of the number of water layers inserted in interlayer space for three different suction values (Saiyouri et al., 2004).

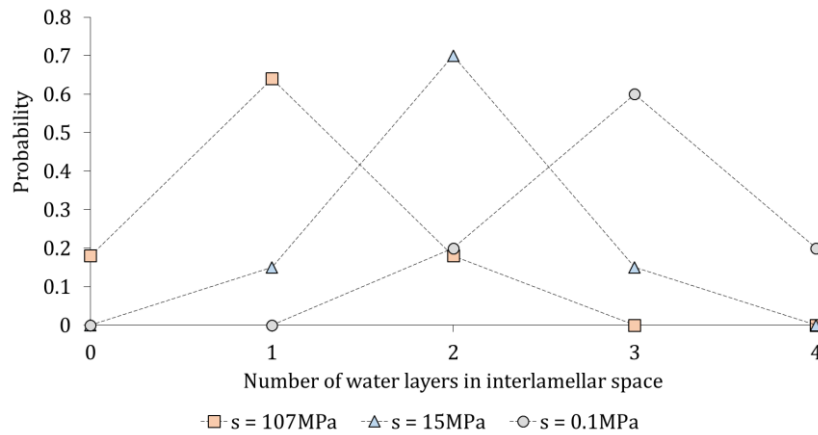


Figure 2-8: Probability distribution of the number of water layers adsorbed in interlamellar space in MX80 bentonite (Saiyouri et al., 2004).

The increase in interlayer space is accompanied by a decrease of the size of a particle resulting of a subdivision of clay particles (Saiyouri et al., 2000; 2004). Figure 2-9 presents the average number of layers per particle and the average interlayer distance for MX80 bentonite, as functions of decreasing suction. The subdivision of particles increases the proportion of inter-particle porosity as well as the distance between montmorillonite mineral surfaces allowing diffuse double layers to develop (Saiyouri et al., 2000). The second hydration phenomenon is related to this phenomenon.

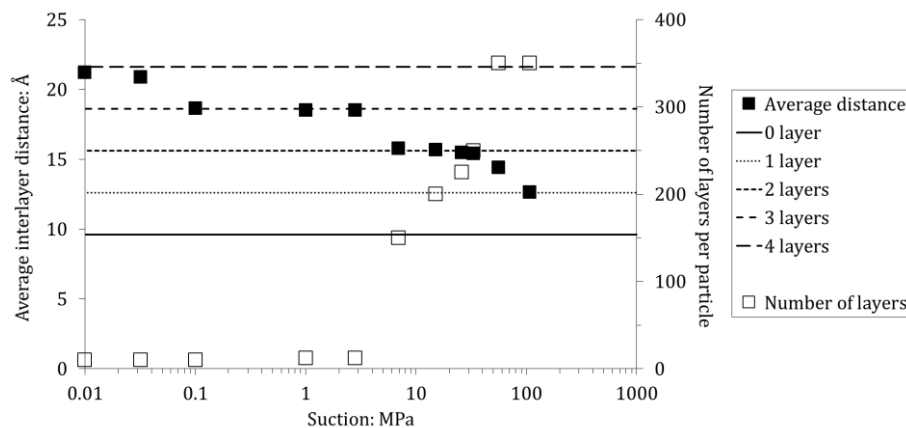


Figure 2-9: Evolution of the average interlayer distance and number of layers per particle in MX80 bentonite upon suction decrease (Saiyouri et al., 2004).

- “Osmotic” hydration

The osmotic hydration mechanism occurs as a consequence of large differences of concentration between the pore water and the surface of clay layers. Since cations are not free at the surface of the particle because of the negative charges, water from the solution migrates between the particle surfaces. Diffuse double layers (Gouy, 1910) develop at the surface of particles and repel each other (Madsen and Vanmoos, 1989). The swelling resulting from this phenomenon is

referred to as osmotic swelling and is associated with the change from electrostatic attractive forces to osmotic repulsive forces (Langmuir 1938; Norrish, 1954). Osmotic swelling is not limited as crystalline swelling is and larger strains can develop as a result. It is underlined by the analysis of the water retention curve (WRC) of a MX80 sample in free-swelling conditions performed by Saiyouri et al. (2004). Using X-ray diffraction, they determined the number of water layers in interlamellar space and deduced from the S_{SA} the gravimetric water content associated to crystalline hydration. Comparison between the WRC and the crystalline hydration contribution is presented in Figure 2-10. Below 3 MPa of suction, crystalline water remains nearly constant whereas a significant amount of water continues to be stored in inter-particle porosity, through osmotic phenomena, as the number of layers per particle has significantly decreased (Figure 2-9).

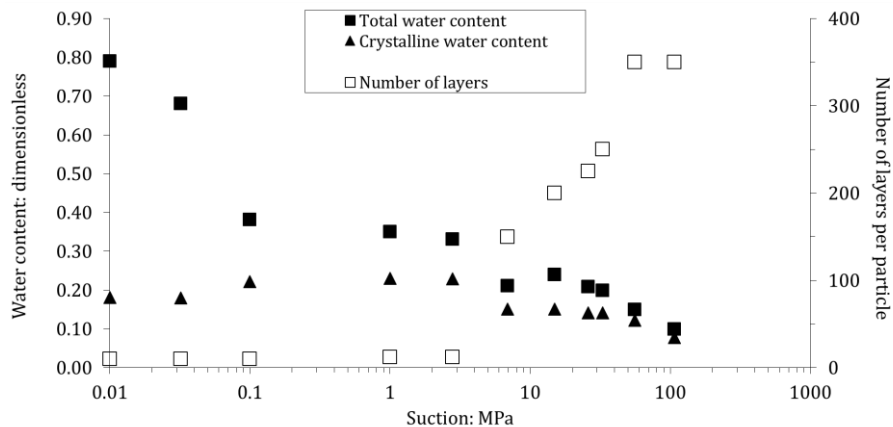


Figure 2-10: Total water content compared to crystalline water content and number of layers per particle as a function of decreasing suction (Saiyouri et al., 2004).

2.2.4.2 Identification of water retention domains

In expansive clayey soils characterised by an aggregated microstructure, the soil water retention behaviour is shown to be divided into two distinct domains: “intra-aggregate” or “microstructural” domain and “inter-aggregate” or “macrostructural” domain. These two water retention domains are directly related to the two levels of porosity identified in double structure unsaturated soils.

Romero et al. (1999) performed static compaction on unsaturated Boom Clay samples, a moderately expansive clay from Mol, Belgium. Results highlighted that up to a suction of 3 MPa, suction and water content are not affected by the dry density. Only the degree of saturation is affected by the dry density in this suction range (> 3 MPa). Similar trend is obtained on MX80 bentonite (Figure 2-11). At suction higher than ~7-10 MPa, a unique suction-water content relationship is observed regardless of dry density and hydration conditions. In the range ~3 to ~7 MPa of suction, differences in the water retention behaviour can be observed. Below a suction of ~3 MPa, significant differences are observed between samples hydrated in different conditions or at different dry densities. Samples allowed to swell store more water than samples prevented to swell. In constant-volume conditions, the water content was found to be higher at lower dry density. Comparable results have been obtained on Febex bentonite, either on compacted powder (Lloret et al., 2003) or granular samples (Hoffman et al., 2007) and Černý vrch bentonite (Sun et al., 2019).

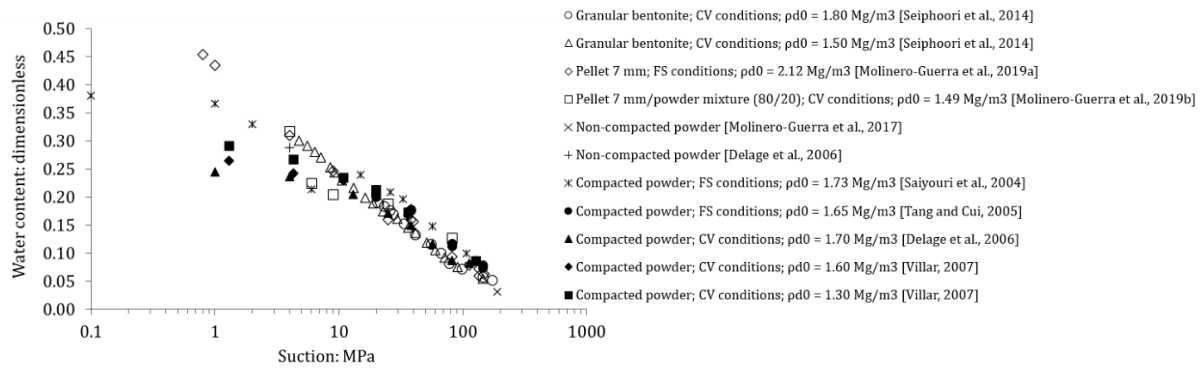


Figure 2-11: Water retention curve of MX80 bentonite materials under different hydration conditions and at different dry densities, upon suction decrease. CV = constant-volume, FS = free-swelling, ρ_{d0} = initial dry density.

The unicity of the suction-water content relationship with varying dry density basically means that, in this suction range, regardless of the volume fraction of voids in the soil, water is stored through adsorption mechanisms at the surface of clay particles, following the “crystalline hydration” mechanism described in 2.2.4.1. At lower suction, the adsorption phenomenon is no longer the dominant hydration mechanism. It is consistent with the observation that transition from “microstructural” to “macrostructural” domain is simultaneous to the sharp increase in number of clay particles and decrease of layers per particles.

Using ESEM, Sun et al. (2019) could observe that macropores remained mostly dry upon hydration of Černý vrch bentonite. Water menisci were identified only in high-dry density sample (1.90 Mg/m^3) at 3.3 MPa of suction, which is somewhat consistent with the transition previously described.

The “microstructural” domain is thus governed by adsorption mechanisms and is unaffected by compaction. The “macrostructural” domain seems governed by osmotic swelling within the microstructure and progressive rise of capillary phenomena within the macrostructure and is affected by volume constraint and compaction.

2.2.4.3 Microstructure evolution upon hydration

Fabric evolution upon hydration is highlighted in the literature by MIP tests, ESEM/SEM observations, Cryo-Focused Ion Beam nanotomography (FIB-nt) observations and X-ray computed tomography observations.

Agus and Schanz (2005) performed MIP tests on a Calcigel bentonite-sand mixture at suction values of 22.7 MPa and 0 MPa (water vapour was used in the vapour equilibrium technique), in free-swelling conditions, at initial dry density of 2 Mg/m^3 . The material at a suction of 22.7 MPa had a clear bimodal porosity with peaks identified at $\sim 15 \text{ nm}$ and $\sim 10 \text{ }\mu\text{m}$. The volume of both levels of pores increased during hydration. At a suction of 0 MPa, a monomodal PSD is observed with a single peak identified at $\sim 0.6 \text{ }\mu\text{m}$, and a notable increase in non-intruded microporosity is measured.

In constant-volume conditions, Wang et al. (2013b) performed MIP tests on a MX80 bentonite-sand mixture at different hydration stages during a wetting path, at a dry density of 1.67 Mg/m^3 . Suction was controlled using the vapour equilibrium technique. Macroporosity slightly decreased from 65 MPa of suction (initial state) to 12.6 MPa of suction while no significant changes in the micropores was detected using MIP. Upon further suction decrease, the macroporosity was significantly decreased and the proportion of $\sim 15 \text{ nm}$ micropores also decreased while a new family of $\sim 0.5 \text{ }\mu\text{m}$ pores appeared (Figure

2-12). It is consistent with the exfoliation of swelling aggregate in the macropores. The third pore family observed near saturation developed at the expense of initial micro- and macropores, which is also consistent with a porosity reorganisation toward a monomodal distribution (Agus and Schanz, 2005). Bian et al. (2018) also observed the development of the third pore family on a MX80 sample compacted at a dry density of 1.34 Mg/m^3 .

Seiphoori et al. (2014) reached a monomodal PSD upon hydration of a granular MX80 bentonite at higher dry density (1.80 Mg/m^3) in constant-volume conditions. However, the single pore family was comparable to the initial micropore family and the proportion of non-intruded porosity increased during hydration (Figure 2-13). The clogging of macroporosity induced by particle exfoliation was not reversible and the PSD remained monomodal upon drying. These observations suggest that the development of the new pore family requires available space and can be prevented at high dry density. Adsorption mechanisms induce the increase in non-intruded porosity. It is consistent with the description of the hydration mechanisms presented in 2.2.4.1. The subdivision of particles (Figure 2-10) arising upon wetting is likely to be an irreversible phenomenon.

Comparable trends have been reported on MIP tests performed on other materials, for instance on Febex bentonite (Lloret and Villar, 2007), Kunigel bentonite-sand mixture (Cui et al., 2002b), Boom Clay (Romero et al., 2011), illitic-kaolinitic clay (Romero 2013).

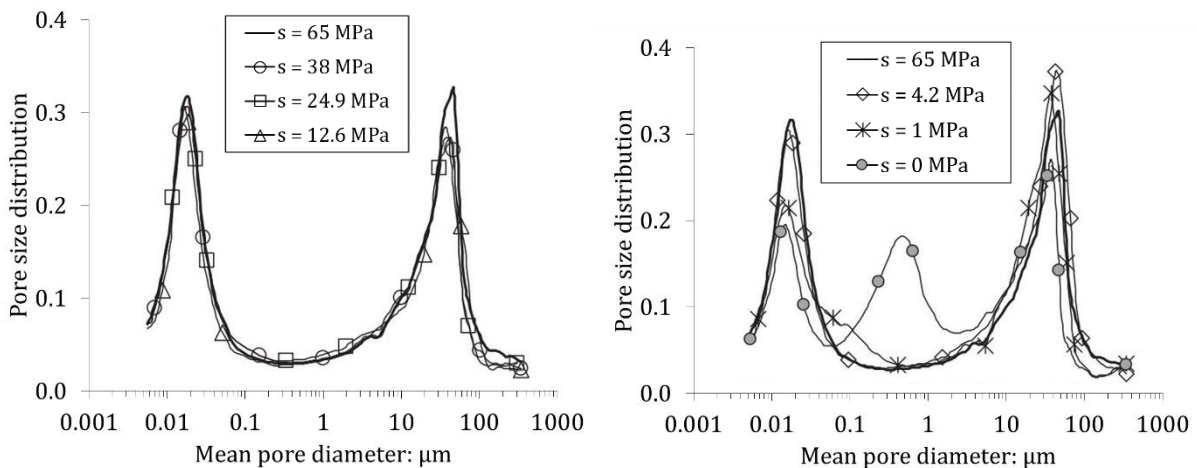


Figure 2-12: Pore size distributions of a MX80 bentonite-sand mixture upon hydration in constant-volume conditions (Wang et al., 2013b).

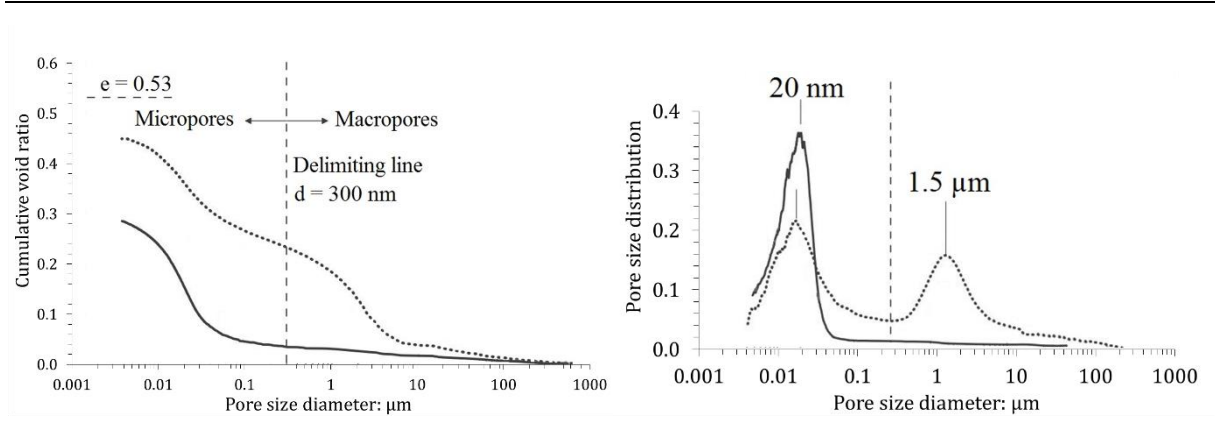


Figure 2-13: Mercury intrusion porosimeter test results performed on a MX80 granular bentonite compacted at 1.80 Mg/m^3 upon hydration in constant-volume conditions (Seiphoori et al., 2014). Left: cumulative void ratio, right: pore size distribution. Dashed line: as compacted state, solid line: saturated.

Using X-ray computed tomography, Massat et al. (2016) determined the evolution of inter-aggregate porosity in a sample of Kunipia-G bentonite, compacted at a dry density of 1.40 Mg/m^3 , upon hydration in constant-volume conditions. Starting from the water injection point, the inter-aggregate porosity decreased progressively in the sample during hydration, consistently with MIP results previously presented (Figure 2-14).

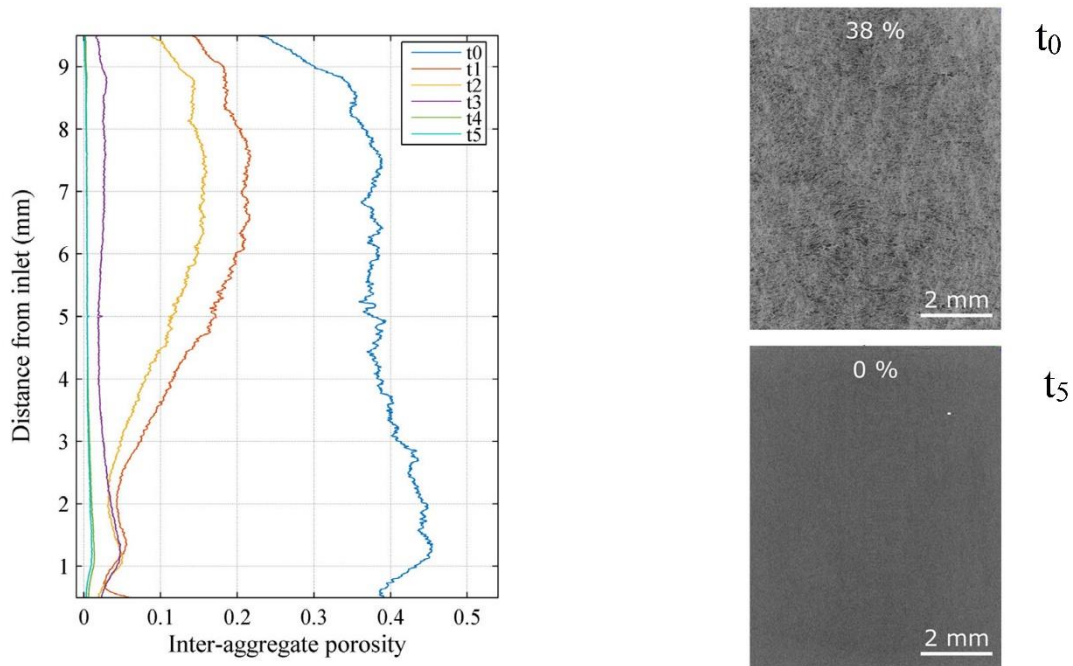


Figure 2-14: Profile of inter-aggregate porosity deduced from X-ray computed tomography images obtained at different times (left) and initial and final state images of the sample with average inter-aggregate porosity (right). $t_1 = 7.1$ days, $t_2 = 8.8$ days, $t_3 = 15.8$ days, $t_4 = 19.7$ days, $t_5 = 39.8$ days. The initial inter-aggregate porosity was 38 % and decreased to 0 % upon wetting (Massat et al., 2016).

The evolution of the material microstructure can be studied using imaging methods such as ESEM or SEM. Using these tools allows the material fabric to be directly observed at the aggregate scale. Montes-Hernandez et al. (2003) obtained ESEM micrographs of MX80 aggregates upon swelling on free-swelling conditions. Through digital image analyses, they quantified the swelling strain of the aggregates. At relative humidity higher than 95 %, a different swelling kinetics was identified. Aggregate would swell more than expected from trends identified at lower relative humidity. Using equation 2-3, this value corresponds to a suction of ~ 7 MPa at a temperature of 20°C , a value which has been shown to separate different hydration mechanisms in 2.2.4.1.

Seiphoori et al. (2014) obtained SEM micrographs of the granular MX80 bentonite equilibrated at different hydration states. Microstructure changes suggested from their MIP results is evidenced. At initial state, the aggregated structure is clearly observable, aggregate and inter-aggregate voids are easily identified. Following saturation, the PSD becomes monomodal and remains identical after drying. A micrograph obtained after wetting and drying of the sample evidences the loss of the initial aggregated structure (Figure 2-15).

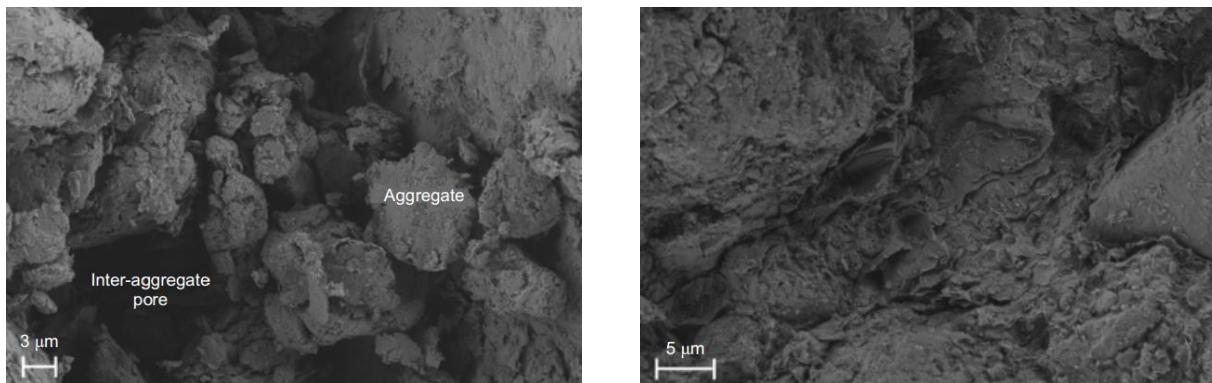


Figure 2-15: SEM micrographs of a sample of granular bentonite compacted at a dry density of 1.80 Mg/m^3 characterised by a bimodal pore size distribution (left, as compacted state) and a monomodal pore size distribution (right) (Seiphoori et al., 2014).

Using FIB-nt, Keller et al. (2014) observed the pore space of MX80 powder compacted to three dry densities: 1.23 Mg/m^3 ; 1.46 Mg/m^3 ; 1.67 Mg/m^3 . The inter-aggregate porosity appeared to be filled with clay particles exfoliated from swelling aggregates in the course of hydration. Particles form a clay gel (Pusch and Yong, 2006) and are organised in a mesh-like honeycomb-shaped structure (Figure 2-16). The walls of the honeycomb structure are made of stacked clay particles. The cores of the honeycomb structure are filled with a low density colloid formed by clay particles. Interestingly, this structure was found to partially fill the inter-aggregate porosity at low dry density (1.23 Mg/m^3); entirely fill the inter-aggregate porosity at intermediate dry density (1.46 Mg/m^3) and was not observed at high dry density (1.67 Mg/m^3). Keller et al. (2014) suggested that the gel could not form at high density because inter-aggregate porosity is not developed enough for the honeycomb-structure to form, which is consistent with MIP test results obtained at different dry densities.

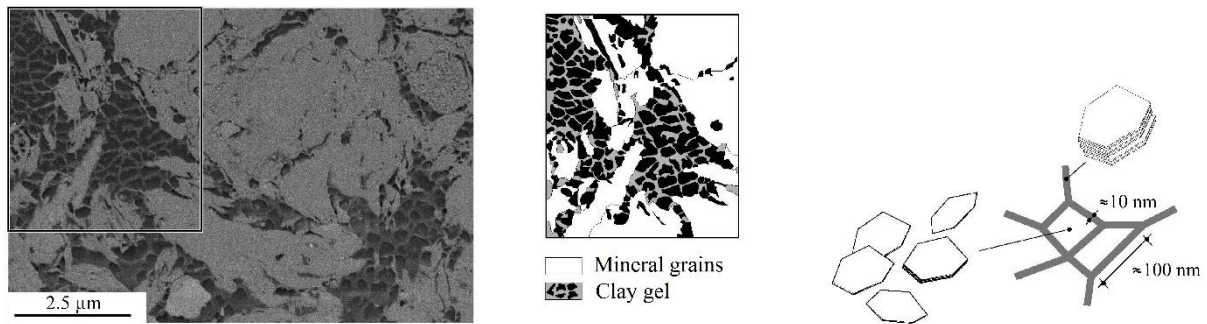


Figure 2-16: Honeycomb structure filling inter-aggregate porosity as a result of aggregate exfoliation during hydration (Keller et al., 2014).

The mechanisms affecting the material fabric has been shown by Delage et al. (2006) to be time-dependent. Using MIP and SEM micrographs, it was evidenced that microstructural rearrangement still occurs 90 days following compaction, in samples maintained in constant-volume and water content conditions (Figure 2-17). Inter-aggregate porosity would decrease and inter-particle porosity would increase with time. It is interpreted as a consequence of internal water redistribution, thus considering that compaction is an undrained process. Microstructural evolution observed with time following compaction can be related to the subdivision of particles and clogging of the macroporosity as a result of water redistribution in the samples.

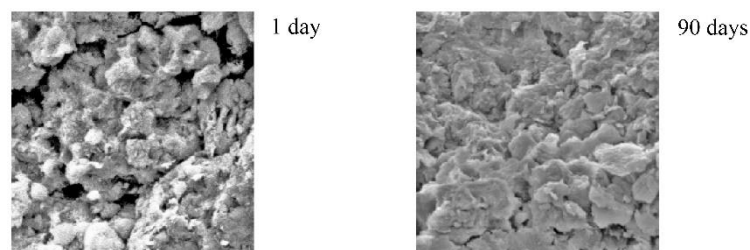


Figure 2-17: SEM micrographs of the sample compacted at a dry density of 1.7 Mg/m³ and water content of 0.125 at 1 day (left) and 90 days (right). Picture width is 40 μm (Delage et al., 2006).

2.3 MACROSCOPIC RESPONSE UNDER HYDROMECHANICAL LOADING

In this section, the macroscopic response of the material upon hydromechanical loadings at laboratory and larger scales is addressed.

The first three parts of this section present the main features of the material behaviour observed in the laboratory. The material response upon wetting at constant stress and drying constitutes part 2.3.1. The material response under mechanical loading at constant suction constitutes part 2.3.2. Experimental evidences concerning stress path dependency are discussed in 2.3.3. The following three parts, 2.3.4, 2.3.5 and 2.3.6, discuss hydration in constant-volume conditions and swelling pressure development, the saturation process of compacted expansive soils, and water transfer in the material, respectively.

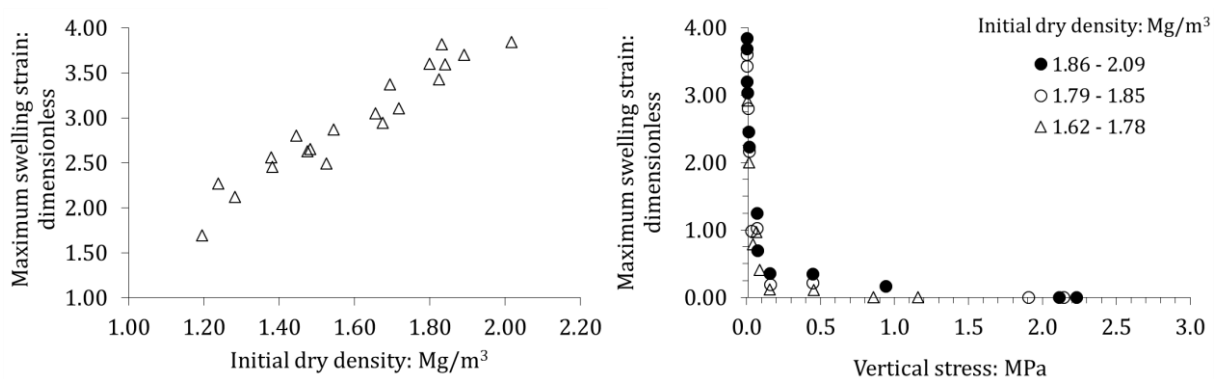
2.3.1 Hydraulic loading of compacted bentonite

Hydraulic loadings refers to suction decrease (hydration) or increase (drying). In the laboratory, suction-controlled oedometer tests are frequently carried out to study the influence of hydraulic loadings under constant mechanical loading. The macroscopic response of the material under these conditions is mostly characterised by the evolution of volumetric strain or void ratio upon suction variations. Their evolution, based on previous discussions, is likely to be influenced by the presence/absence of a developed macroporosity and its eventual ability to either swell or contract under the applied stress. The behaviour of the material under a wetting path, a drying path, and wetting-drying cycles is presented in this part.

2.3.1.1 Material response upon wetting

Hydration of compacted bentonites induces a swelling of particles and aggregates. Depending on the stress applied on the sample, the influence of microstructural swelling on macroporosity (directly affected by compaction) will vary. Relevant experimental results available in the literature related to hydration under constant stress are first presented.

The swelling potential (*i.e.* the volumetric strain of the sample upon wetting under zero stress) is directly related to the sample dry density. It is highlighted in Figure 2-18 which presents the swelling potential of a Kunigel bentonite, determined by Komine and Ogata (2003). In the light of the hydration mechanisms presented in 2.2.4.1, the increase of swelling potential with increasing dry density can be related to the higher amount of clay particles in the same initial volume, thus an increase in the amount of water stored in the sample microstructure. Besides, swelling is significantly decreased (compared to the swelling potential) under a vertical stress, even at low vertical stress. Regardless of the dry density, the maximum swelling strain decreases with increasing vertical stress. Villar and Lloret (2008) present comparable results on Febex bentonite. The final swelling strain of samples wetted under constant stress decreases with increasing vertical stress and decreasing dry density (Figure 2-19).



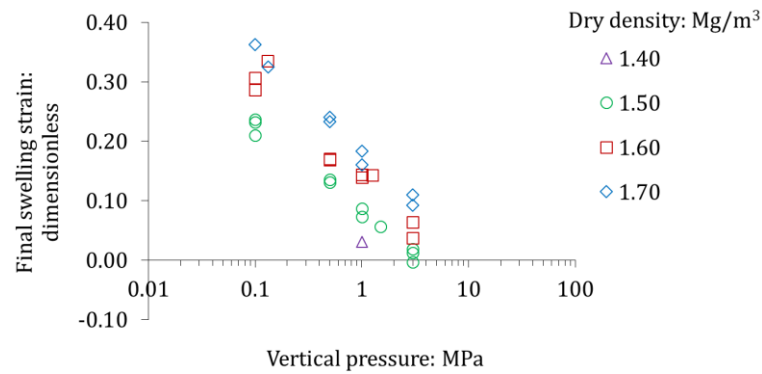


Figure 2-19: Final swelling strain of Febex bentonite upon wetting under constant vertical stress at different initial dry densities (Villar and Lloret, 2008).

In the course of hydration, the evolution of volumetric strain can be characterised by performing suction-controlled oedometer tests. Lloret et al. (2003) performed suction-controlled oedometer tests on Febex bentonite. Upon hydration, the variation of the sample void ratio (e) was nearly linear in the $e - \ln s$ plane. The final swelling strain was significant under low vertical stress and much smaller under high stress. Slopes ($-\Delta e / \Delta \ln s$) obtained are presented in Figure 2-20 as a function of the applied vertical stress. Comparable results have been obtained by Gatabin et al. (2016) and Wang et al. (2013a) on a MX80 bentonite-sand mixture (70/30 proportions in dry mass) upon hydration.

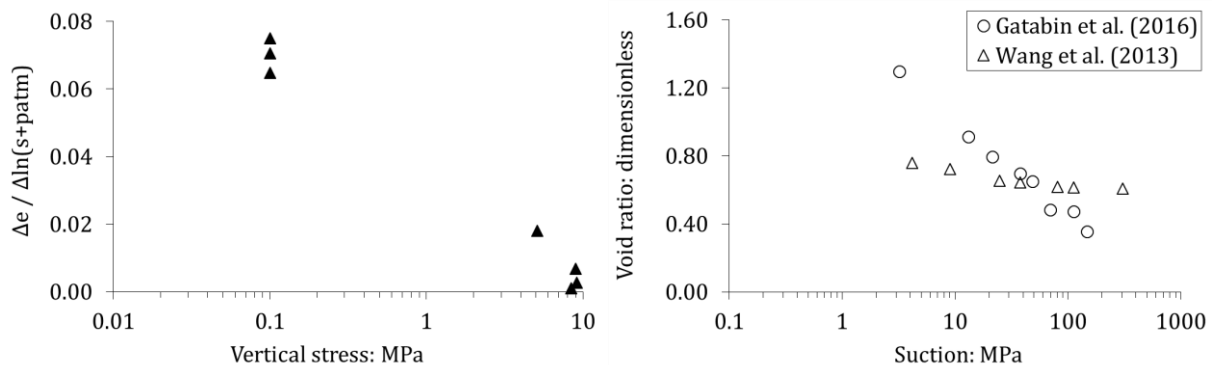


Figure 2-20: Slope of the void ratio-logarithm of suction relationship of Febex bentonite upon hydration (left) (Lloret et al., 2003) and evolution of void ratio upon suction decrease of MX80 bentonite-sand mixtures at initial dry density of 1.96 Mg/m³ and free-swelling conditions (Gatabin et al., 2016) and at initial dry density of 1.67 Mg/m³ and vertical stress of 0.1 MPa (Wang et al., 2013a) (right).

Cuisinier and Masrouri (2005) studied the hydromechanical behaviour of a bentonite-silt mixture (60/40 in proportions), compacted under a vertical pressure to a dry density of 1.27 Mg/m³. Upon hydration from initial suction (in the range ~20-25 MPa) to 0 MPa, two swelling phases were identified: a low swelling phase at suction higher than 4 MPa and a high swelling phase at suction lower than 4 MPa. This observation is somewhat consistent with the threshold identified in the hydration mechanisms presented in 2.2.4.1.

Influence of the microstructure evolution on the macroscopic response upon suction decrease is also evidenced by the collapse phenomenon. Collapse occurs as a result of the invasion of macropores by clay particles. For instance, Villar (1999) performed suction-controlled oedometer tests on Febex bentonite (from Cortijo de Archidona deposit, Spain). Wetting of samples under a low vertical stress

was characterised by a significant and monotonous swelling, as obtained in Lloret et al. (2003) for Febex bentonite, whereas wetting under a vertical stress of 9 MPa was characterised by a swelling then a collapse.

The collapse phenomenon and the influence of applied stress on this latter was also identified by Bernier et al. (1997) and Romero et al. (2003) on Boom Clay and Cui et al. (2002a) on FoCa7 bentonite (Figure 2-21). Results of hydration upon constant stress from Al Mukhtar et al. (2009) suggest that over-consolidated samples are less prone to the collapse phenomenon.

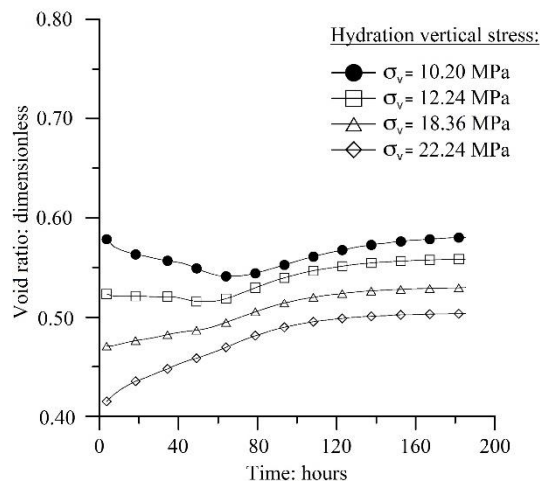


Figure 2-21: Evolution of void ratio during wetting of FoCa7 bentonite samples under their respective compaction stress (Cui et al., 2002a).

2.3.1.2 Material response upon drying and influence of successive wetting-drying cycles

Drying of the material induces a progressive decrease in the amount of water stored in the material. Macroporosity desaturates first, then microporosity, from the less bonded water layers to the most bonded water layers.

At high suction, water is stored in the sample as adsorbed layers at the surface of clay particles. Seiphoori et al. (2014) performed a wetting and a subsequent drying on granular MX80 bentonite compacted to a dry density of 1.80 Mg/m^3 . In constant-volume conditions, suction was decreased from ~ 180 MPa (initial state) to ~ 90 MPa, then dried and wetted to ~ 150 MPa and ~ 90 MPa. At this suction, only one water layer is adsorbed at the surface of particles and particle subdivision is not significant yet. A reversible path on the WRC was observed. Drying and subsequent wetting was however characterised by a hysteresis on the WRC for the same material previously wetted at ~ 50 MPa; ~ 25 MPa; ~ 20.6 MPa (saturated state). From Figure 2-9, it can be considered that the subdivision of particle starts becoming significant as a second layer of water is adsorbed, below ~ 56 MPa of suction. As this phenomenon induces an increase in inter-particle porosity compared to initial state, it can be suggested that hysteresis observed on drying paths at high suction is related to fabric changes. Interestingly, the drying path performed from the saturated state, characterised by a monomodal porosity (Figure 2-13), induced a hysteresis while the PSD was not affected. It can be explained, for instance, by parallel connections of pores of different sizes, series connection of “bottleneck shaped” pores, or “ink-bottle shaped” pores, as described in Delage and Lefebvre (1984) or Delage and Cui (2000).

Results consistent with Seiphoori et al. (2014) observation at high suction have been obtained by Villar (1999) on a drying path performed on a Febex bentonite. A sample dried under low vertical stress

(0.1 MPa) from ~138 MPa (initial state) to ~530 MPa of suction then wetted exhibited very low and reversible strain. Lloret et al. (2003) also obtained comparable results on Febex bentonite under low vertical stress (0.1 MPa). In addition, volumetric strain upon subsequent hydration was comparable to samples which only underwent hydration (Figure 2-22). It can be suggested from these results that the volumetric behaviour upon wetting is not affected by drying at high suction.

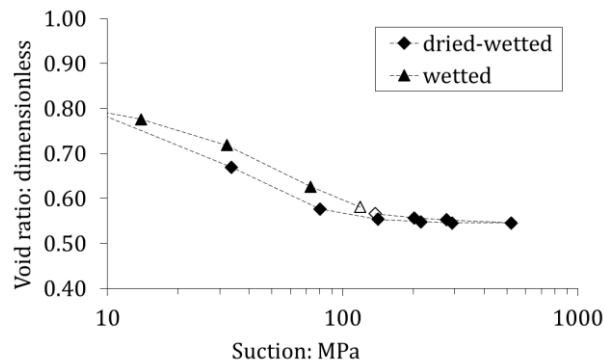


Figure 2-22: Influence of a wetting-drying path on Febex bentonite at high suction under low vertical stress. White symbols represent initial states (Lloret et al., 2003).

At lower suction, as particle subdivision induces irreversible changes in the material microstructure, the behaviour of expansive soils upon drying is more affected by dry density and applied stress. For instance, Romero et al. (2003) carried out drying tests on Boom Clay, initially compacted to dry densities of 1.37 Mg/m³ and 1.67 Mg/m³. Samples were wetted to a suction of 0.01 MPa and subsequently dried, under different constant vertical stresses. Shrinkage during drying was found to be less important than the previous swelling. Irreversible strains were less significant under higher vertical stress, which highlights the influence of macrostructural rearrangement and interaction between micro- and macroporosity in the wetting and drying processes of low and intermediate dry density samples.

Conversely, highly compacted expansive soils exhibit a nearly reversible behaviour even under low stress and low suction. Delage et al. (1998) performed wetting and drying paths on FoCa7 bentonite samples compacted at a dry density of 1.85-1.87 Mg/m³. Regardless of the suction and under free-swelling conditions, nearly no hysteresis were observed neither on the WRC nor on the measured volumetric strains. Wetting and drying paths were carried out in suction-controlled oedometers by Cui et al. (2002a), on the same material. The material volumetric strain was reversible under constant vertical stresses of 10 MPa and 20 MPa. Interestingly, Delage et al. (1998) highlighted that, for these high dry densities, the total volume change of the sample coincided with the water volume change. In the light of previous discussion, it is reasonable to consider that in this case water was mostly stored in microporosity, providing further evidence that irreversible strains in compacted expansive soils are mainly related to macroporosity.

It is also suggested by the large accumulation of shrinkage strains observed upon successive wetting-drying cycles on low dry density samples. On Boom clay, Romero et al. (2003) obtained significant shrinkage on wetting-drying cycles on samples compacted at initial dry density of 1.37 Mg/m³ whereas no shrinkage accumulated on samples compacted at initial dry density of 1.67 Mg/m³. For low density samples, accumulation of shrinkage decreased during successive cycles under constant vertical stress, until a reversible behaviour was obtained. Equilibrium (*i.e.* no more accumulation of irreversible strain) was reached after a few cycles. Larger shrinkage was obtained under higher vertical stress. The same behaviour was observed on other materials, for instance a compacted bentonite-silt mixture (Nowamooz and Masrouri, 2008) and Febex bentonite-sand mixture (80/20 in proportion) (Alonso et al., 2005). This

latter was cyclically wetted-dried between $\sim 4\text{-}6$ MPa and $\sim 120\text{-}135$ MPa of suction (initial suction of 80 MPa). Figure 2-23 compares swelling strain and shrinkage strain at each cycle, under a constant vertical stress of 396 kPa, and illustrates the decrease of irreversible strain and tendency to reach equilibrium.

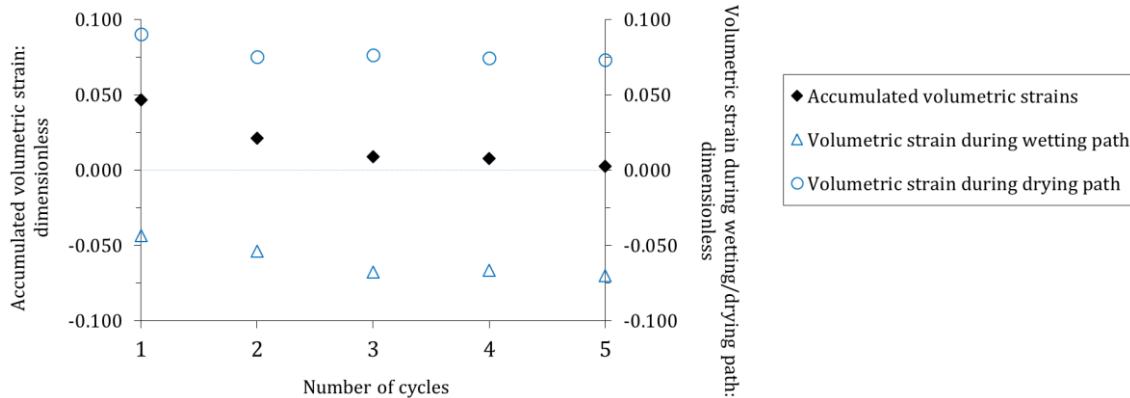


Figure 2-23: Evolution of swelling and shrinkage of a Febex bentonite-sand mixture (initial dry density of 1.50 Mg/m^3) with the number of wetting-drying cycles under constant vertical stress of 396 kPa (Alonso et al., 2005).

2.3.2 Mechanical loading at constant suction

Suction has been shown to affect the material fabric by inducing aggregate exfoliation and modify the balance of attraction/repulsion forces at micro-scale. Consequently, the material response under mechanical loading is significantly affected by suction. The material response under mechanical loading at controlled suction is mainly studied in the laboratory through oedometer tests. Information such as the soil compressibility and the apparent preconsolidation pressure can be determined by carrying out suction-controlled oedometer tests. Typical results available in the literature concerning the suction-dependency of compressibility and apparent preconsolidation pressure are presented and discussed in this part.

2.3.2.1 Suction dependency of the compressibility

In oedometer tests, radial strains are prevented, so the sample volumetric strain corresponds to the vertical strain. Measuring height variations allows the volumetric strain and void ratio to be calculated. Normally consolidated samples are characterised by a linear decrease of the void ratio with respect to the logarithm of stress while the void ratio of over-consolidated samples is characterised by a bilinear decrease.

In this respect, the soil compressibility is defined by the slopes in the “ $e\text{-log } \sigma_v$ ” semi-logarithmic plane. C_c characterises the virgin compression of the sample: $C_c = -\Delta e / \Delta \log \sigma_v'$, and C_s characterises the unloading/reloading of the sample: $C_s = -\Delta e / \Delta \log \sigma_v'$, where e denotes the sample void ratio and σ_v' denotes the effective vertical stress.

Models describing the mechanical behaviour of soils usually use isotropic compression parameters, where λ characterises the virgin compression of the sample: $\lambda = -\Delta e / \Delta \ln p'$, and κ characterises the unloading/reloading of the sample: $\kappa = -\Delta e / \Delta \ln p'$, where p' is the effective mean stress.

Since measurement of radial stresses is not often performed, only σ_v' is usually known in experiments. It is common to consider that $\lambda = C_c / \ln(10)$ and $\kappa = C_s / \ln(10)$ when interpreting experimental results for modelling purpose.

At constant suction, the same overall behaviour as at saturated state is observed: mechanical loading at stresses below the preconsolidation pressure induces reversible (elastic) strains while irreversible strains arise during virgin compression (elastic-plastic). However, compressibility is affected by suction.

Lloret et al. (2003) performed suction-controlled oedometer tests on compacted Febex bentonite. Results highlight that compressibility at over-consolidated state slightly increases with decreasing suction. Virgin compression however is significantly affected by suction (Figure 2-24). Similar conclusions were obtained by Cuisinier and Masroui (2005) for a bentonite-silt mixture (60/40 in proportions), Romero et al. (2003) for compacted Boom Clay, Al-Mukthar et al. (2009) on Na-laponite and Na-hectorite (two clays belonging to the smectite family). On compacted MX80 bentonite and compacted bentonite-sand mixture, Marcial (2003) and Wang et al. (2013a) obtained an increasing compressibility coefficient with decreasing suction at suction higher than 12.6 MPa, then a slight increase at suction lower than 12.6 MPa. It was interpreted as a consequence of the collapse of macrostructure: above this threshold, compressibility is associated to the closing of a nearly dry macroporosity, below this threshold, compressibility is associated to the expulsion of adsorbed water from inter-aggregate porosity (Wang et al., 2013a).

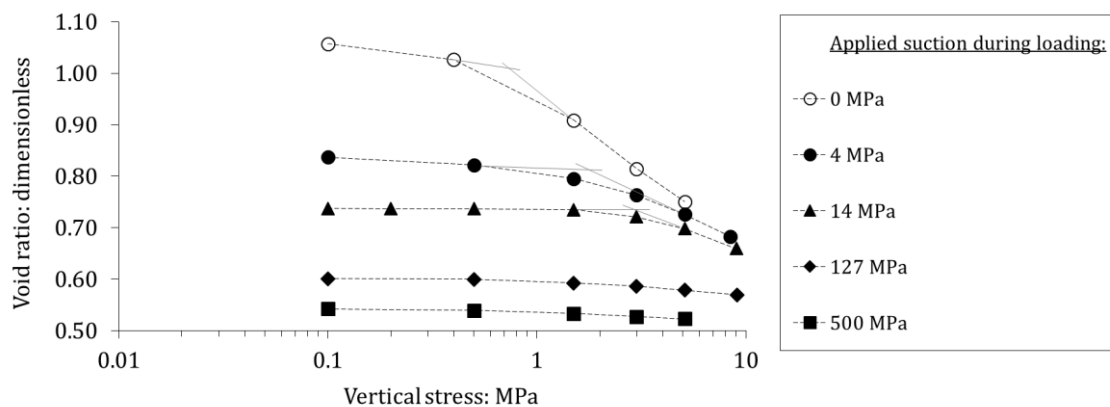


Figure 2-24: Loading of compacted Febex bentonite under constant suction in oedometer tests (Lloret et al., 2003). Grey solid lines aim at delimiting elastic and elastic-plastic loadings.

2.3.2.2 Apparent preconsolidation pressure

The apparent preconsolidation pressure is the stress delimiting pseudo-elastic and elastic-plastic behaviours in oedometer tests. As seen in Lloret et al. (2003) test results (Figure 2-24), this value is affected by suction (Figure 2-25). This trend is typical of unsaturated soils. It has been observed in other compacted expansive materials, either pure or mixed with silt or sand (*e.g.* Cuisinier and Masroui, 2005; Wang et al., 2013a; Marcial, 2003).

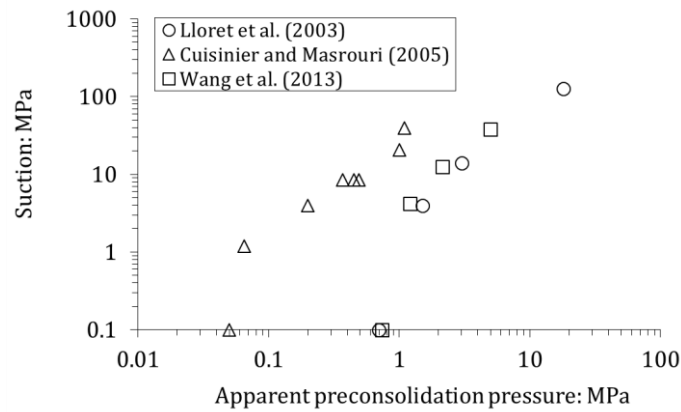


Figure 2-25: Apparent preconsolidation pressure at various suction values for three types of compacted expansive soils: compacted Febex bentonite (initial dry density $\sim 1.70 \text{ Mg/m}^3$; Lloret et al., 2003), compacted MX80 bentonite-sand mixture in proportions 70/30 (initial dry density 1.67 Mg/m^3 ; Wang et al., 2013a), compacted bentonite-silt mixture in proportions 60/40 (initial dry density 1.27 Mg/m^3 ; Cuisinier and Masrouri, 2005). Saturated conditions are plotted as 0.1 MPa of suction.

Preconsolidation is a result of compaction and apparent preconsolidation pressure is found to be dry density dependent. For instance, Nowamooz and Masrouri (2009) found that the apparent preconsolidation pressure of a compacted bentonite-silt (60/40 in proportions) increased with increasing dry density, at constant suction. Comparable results were obtained by Wang et al. (2013a) on a MX80 bentonite-sand mixture. On “pure” compacted MX80 bentonite, comparison of experimental results from different authors allows the relationship between the initial void ratio and preconsolidation pressure at saturated state to be determined. Figure 2-26 presents the preconsolidation pressure at saturated state obtained by Marcial (2003) and Villar (2005) on pure compacted MX80 bentonite and Molinero-Guerra et al. (2019b) on a MX80 bentonite pellet-powder mixture (80/20 in proportions), considered homogeneous at saturated state, as a function of void ratio. The preconsolidation pressure appears related to the void ratio, consistently with Nowamooz and Masrouri (2009) observation. The following fitting curve is proposed for MX80 bentonite:

$$p_0 = p_0^* \exp(-n_p e) \quad 2-5$$

Where p_0 is the saturated apparent preconsolidation pressure (in MPa); p_0^* is a parameter expressed in MPa; e is the total void ratio; n_p is a dimensionless parameter.

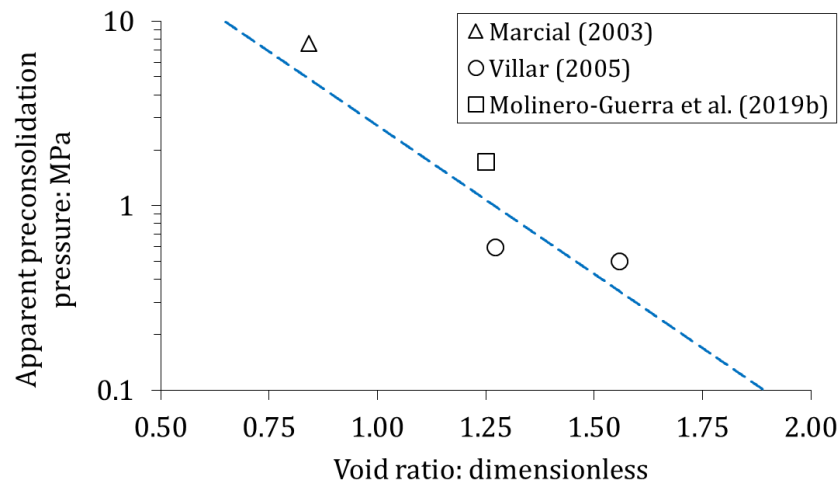


Figure 2-26: Apparent preconsolidation pressure at saturation for MX80 bentonite materials at various void ratios. Experimental data from Marcial (2003), Villar (2005), Molinero-Guerra et al. (2019b). The dashed blue line corresponds to equation 2-5 with $p^*_0 = 110$ MPa and $n_p = 3.7$.

2.3.3 Influence of the stress path

It was evidenced in the previous parts that irreversible strains may arise as a consequence of wetting and loading. Wetting and loading paths both can induce irreversible strain. Still, it was shown that they affect the material in different ways. Therefore, compacted bentonite based materials characterised by the same initial state and under the same mechanical stress and suction may have different fabric and void ratio depending on the stress path they experienced.

Lloret et al. (2003) and Villar (1999) performed suction-controlled oedometer tests on Febex bentonite. Initial state and stress paths are summarised in Figure 2-27, Table 2-2 and Table 2-3. Initial and final states are comparable, but stress paths are different.

Table 2-2: Main initial characteristics of Lloret et al. (2003) and Villar (1999) samples.

Reference	Sample	Initial conditions	
		Dry density: Mg/m ³	Suction: MPa
Lloret et al. (2003)	1	1.72	138
	2	1.72	138
Villar (1999)	1	1.70	130
	2	1.70	130

Table 2-3: Stress paths followed by Lloret et al. (2003) and Villar (1999) samples.

Reference	Sample	Stress path				
		I σ_v : MPa s : MPa	II σ_v : MPa s : MPa	III σ_v : MPa s : MPa	IV σ_v : MPa s : MPa	V σ_v : MPa s : MPa
Lloret et al. (2003)	1	0.1 138	0.1 550	5.1 460	5.1 0	-
	2	0.1 138	0.1 520	0.1 0	5.0 0	-
Villar (1999)	1	0.1 130	0.1 14	0.5 14	0.5 0	5.0 0
	2	0.1 130	0.1 14	5.0 14	5.0 0	-

In both cases, samples wetted under lower stress systematically exhibited higher final void ratios (Figure 2-28). Other tests reported in Lloret et al. (2003) share this trend. The following explanation is suggested. High mechanical stresses prevent the free expansion and rearrangement of the microstructural level upon wetting. On the other hand, hydration mechanisms described in 2.2.4.1 strongly affect the material fabric. Higher stress would be required to decrease the void ratio after wetting, since the proportion of macroporosity, significantly more affected by mechanical loading, is reduced.

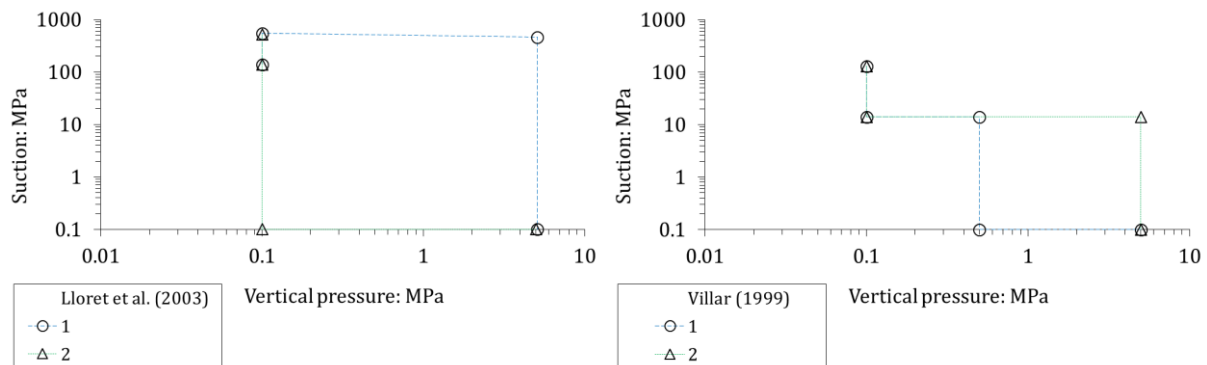


Figure 2-27: Stress paths followed by Lloret et al. (2003) and Villar (1999) samples.

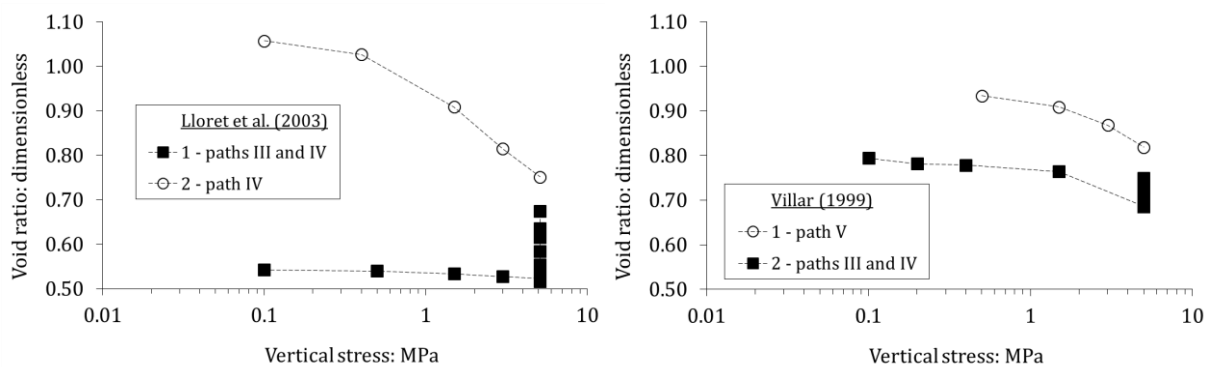


Figure 2-28: Evolution of the void ratio of Febex samples in Lloret et al. (2003) and Villar (1999).

2.3.4 Swelling pressure development upon hydration in confined conditions

Hydration of expansive clays results in a macroscopic swelling. If swelling is prevented, hydration induces the development of a swelling pressure. In repository conditions, swelling of the bentonite buffer will progressively close technological voids then, as expansion will be prevented, swelling pressure will increase upon hydration. In radioactive waste disposal concepts, swelling pressure development upon wetting is a key feature of engineered barriers performance. On the one hand it should be high enough to participate in the sealing of the host rock damaged by excavation. On the other hand, it should not reach excessive value since it would induce further damage in the host rock, thus providing preferential paths for radionuclides.

In this part, methods commonly used to study swelling pressure in the laboratory are first presented and discussed. Then, the behaviour of compacted expansive soils upon hydration in constant-volume conditions is discussed in the light of experimental results available in the literature. Relevant parameters influencing the swelling pressure are highlighted.

2.3.4.1 Definition of the swelling pressure and determination methods in the laboratory

Swelling pressure in the laboratory is usually determined using one of the following methods (Basma et al., 1995; Wang et al., 2012; Yigzaw et al., 2016):

- The swell-consolidation method:
This method consists in two steps. First, the sample is wetted in free-swelling conditions in an oedometer ring. Then, the sample is incrementally loaded until the void ratio has reached its initial value.
- The zero-swell method:
This method consists in incrementally increasing the applied load simultaneously to wetting in an oedometer ring, so that the swelling induced by hydration is instantly cancelled by the load increment.
- The constant-volume hydration method:
This method consists in wetting the sample in a constant-volume cell and measuring the stress using a pressure sensor.
- The restrained-swelling method:
This method consists in loading several samples. Samples are then wetted under different applied stress. Samples wetted under low applied stress swell while samples wetted under high applied stress shrink. The stress corresponding to no swelling as well as no shrinkage is determined and assumed to be the swelling pressure.

In previous discussions, the stress path dependency of compacted expansive soils was highlighted. Indeed, the swelling pressure determined using the four aforementioned methods is different. Yigzaw et al. (2016) determined the swelling pressure of Georgia-bentonite and MX80 bentonite samples using the swell-consolidation method, the constant-volume hydration method and the restrained-swelling method (“load-swell” method in their study). It was evidenced that the apparent swelling pressure was the highest using the swell-consolidation method, intermediate using the constant-volume hydration and the lowest using the restrained-swelling method. It is a consequence of the stress path dependency discussed in the previous part. In the restrained-swelling method, the applied load inhibits the swelling

potential. Inversely, fabric changes resulting from free-swelling require higher load to be applied to recover the initial void ratio (Lloret et al., 2003; Villar, 1999; Yigzaw et al., 2016; Basma et al., 1995; Wang et al., 2012). Constant-volume conditions are somewhat intermediate between these two test conditions. In addition, constant-volume conditions are closer to repository conditions in which expansion is prevented by the gallery wall. Consequently, this method is frequently used to determine the swelling pressure in studies carried out in the context of radioactive waste disposal.

In constant-volume swelling pressure tests, the swelling pressure is most often measured by a pressure sensor in axial position. In the other methods, loads are applied vertically in oedometer rings. Most of the time, samples are uniaxially compacted, which can lead to preferential orientation of the microstructure and anisotropic swelling behaviour (Gatabin et al., 2016; Molinero-Guerra et al., 2019a). Still, following the fabric rearrangement upon hydration, anisotropy might be decreased. It is suggested by Saba et al. (2014a) who measured both radial and axial stress during constant-volume hydration of a bentonite-sand mixture. It is also suggested by swelling pressure test results from Imbert and Villar (2006) who obtained the same final swelling pressure for uniaxially compacted FoCa bentonite and pellet-powder mixture (50/50 in proportions) of the same bentonite at the same average dry density.

2.3.4.2 Hydration in constant-volume conditions

In constant-volume conditions, the macroscopic swelling induced by hydration is prevented which results in the increase of swelling pressure to maintain the confined conditions. Hydration of the material still is characterised by the fabric changes previously described, associated with a pressure increase. As discussed in previous parts, pressure increase affects the material macrostructure. In swelling pressure tests, the macroscopic response of the material (*i.e.* the evolution of the apparent swelling pressure in these conditions) is thus influenced by the progressive loss of aggregated structure and the importance of the macroporosity.

The swelling pressure evolves in three stages upon suction decrease. First, at high suction and low pressure, the swelling pressure increases upon suction decrease. Second, as suction decreases further and pressure continues to increase, the fabric undergoes rearrangement as aggregates collapse and fill the macroporosity. This stage is characterised by a decrease of the swelling pressure. Third, at low suction, swelling strains overcome shrinkage and the swelling pressure increases again to maintain constant-volume conditions (*e.g.* Lloret et al., 2003; Imbert and Villar, 2006; Baille et al., 2010; Saba et al., 2014a; Massat et al., 2016; Yigzaw et al., 2016).

The relative importance of these three stages depends on the macrostructure of the sample. The presence of a developed macroporosity is required for collapse to occur. On the other hand, significant macroporosity may lead to a low and monotonous increase of the swelling pressure with no transient decrease. The macroscopic response upon hydration is thus related to the sample dry density. Figure 2-29 presents the results of suction-controlled swelling pressure tests performed by Lloret et al. (2003) on Febex bentonite compacted to different dry densities and initial suctions. The three stages and relative importance of each for higher/lower dry densities are clearly observable.

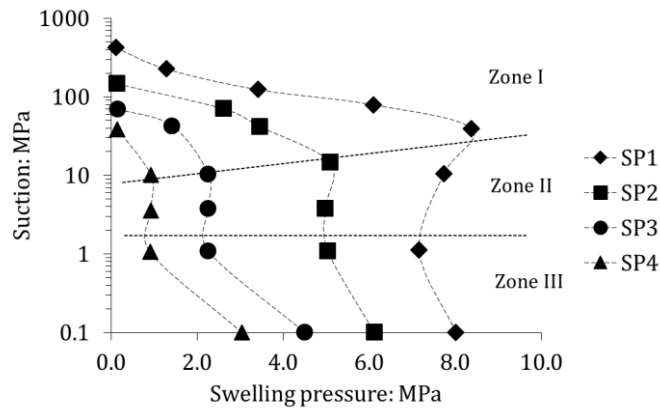


Figure 2-29: Suction controlled swelling pressure tests performed on compacted Febex bentonite. Initial dry densities and suction for SP1, SP2, SP3, and SP4 are: 1.65 Mg/m³ and 424 MPa, 1.63 Mg/m³ and 146 MPa, 1.57 Mg/m³ and 70 MPa, and 1.50 Mg/m³ and 39 MPa, respectively. The two black dashed lines crossing test results are delimiting the three identified zones (Lloret et al., 2003).

The influence of fabric changes on the swelling pressure development and most notably the occurrence of a transient peak is highlighted by Massat et al. (2016) experimental study. Using X-ray computed tomography, Massat et al. (2016) determined the evolution of inter-aggregate porosity in a sample of Kunipia-G bentonite, compacted at a dry density of 1.40 Mg/m³, upon hydration in constant-volume conditions. Swelling pressure evolution was characterised by the three stages previously described. Comparing the evolutions of inter-aggregate porosity and swelling pressure, they concluded that the transient drop in swelling pressure coincides with the closure of macroporosity (Figure 2-30).

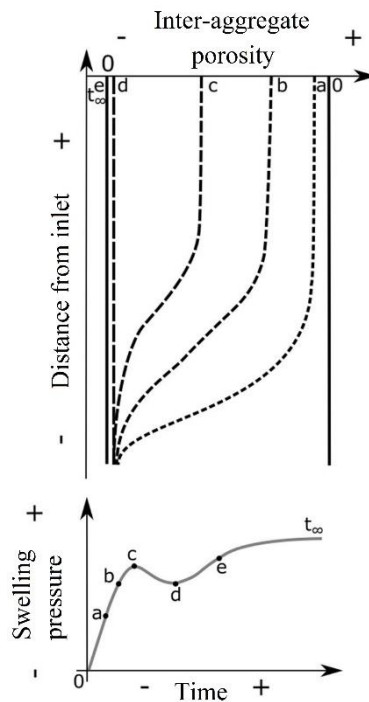


Figure 2-30: Evolution of inter-aggregate porosity and swelling pressure as a function of elapsed time during wetting under constant-volume conditions (Massat et al., 2016).

For a given wetting fluid and initial suction, the final swelling pressure of compacted expansive soils is directly related to the dry density of the sample (*e.g.* Basma et al., 1995; Borgesson et al., 1996; Lloret et al., 2003; Villar and Lloret, 2008; Baille et al., 2010; Wang et al., 2012; Agus et al., 2013; Kaufhold et al., 2015; Yigzaw et al., 2016; Cui, 2017). For various type of bentonites, Figure 2-31 presents experimental results obtained by different authors. An exponential relationship between the material dry density and the final swelling pressure is suggested from these results. In the context of radioactive waste disposal, the exponential relationship is of importance since a dry density variation can lead to significant change in the final swelling pressure of the buffer material. For instance, Wang et al. (2012) proposed the following estimation of the final swelling pressure:

$$\sigma_s = a_s \exp(\beta_s \rho_d) \quad 2-6$$

Where σ_s is the final swelling pressure (MPa), a_s and β_s are parameters (MPa and m^3/Mg , respectively), ρ_d is the effective dry density (Mg/m^3). Values of parameters a_s and β_s are given in Table 2-4 for different bentonite materials (Wang et al., 2012).

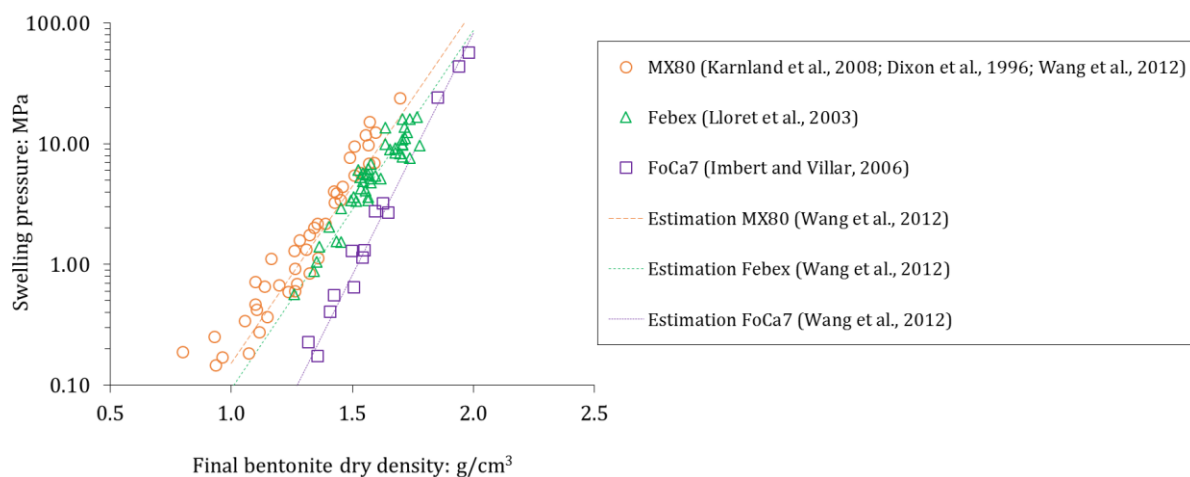


Figure 2-31: Relationship between dry density and swelling pressure for three different bentonites and estimation using equation 2-6 (Wang et al., 2012).

Table 2-4: Values of parameters a_s and β_s of equation 2-6 for three types of bentonite (Wang et al., 2012).

Bentonite	a_s : MPa	β_s : m^3/Mg
MX80	1.78×10^{-4}	6.75
Febex	9.80×10^{-5}	6.85
FoCa	7.83×10^{-7}	3.32

In some studies, a mixture of bentonite with other materials such as sand or crushed claystone is envisaged as sealing material. In this respect, the secondary component can be considered inert

compared to the bentonite large swelling potential, as suggested by Wang et al. (2012), Saba et al. (2014a), Cui (2017). The “effective” bentonite dry density can be introduced:

$$\rho_{db} = \frac{B \rho_m G_s}{G_s (1 + w_m) - \rho_m (1 - B) (1 + w_a)} \quad 2-7$$

Where ρ_{db} is the bentonite dry density (Mg/m^3), B is the bentonite content in dry mass (dimensionless), ρ_m is the mixture density (Mg/m^3); w_m is the mixture gravimetric water content (dimensionless), w_a is the secondary material gravimetric water content (dimensionless), G_s is the specific gravity of the secondary material (dimensionless) (Wang et al., 2012).

Using this concept of effective dry density, swelling pressures obtained on mixtures follow the same trend as pure bentonite materials (Figure 2-32).

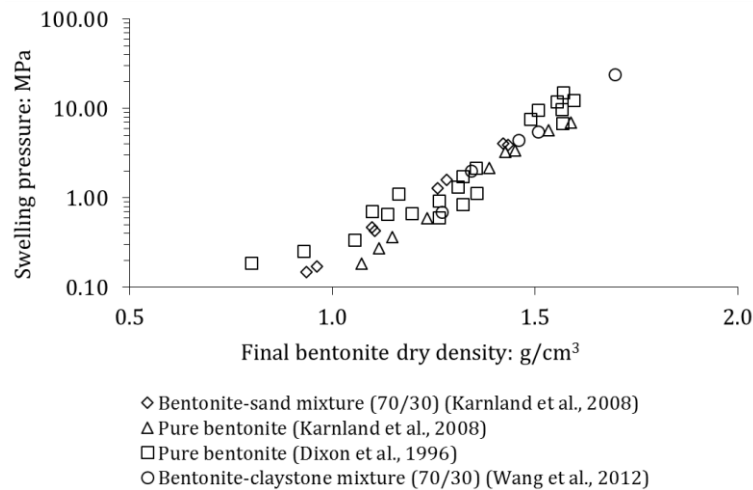


Figure 2-32: Relationship between swelling pressure and bentonite dry density (equation 2-7) for MX80 based materials (Wang et al., 2012).

For a given dry density and initial suction, the salinity of the wetting fluid influences the final swelling pressure. The higher the ion concentration in the wetting fluid the lower the final swelling pressure (*e.g.* Komine and Ogata, 2003; Castellanos et al., 2006; 2008; Warr and Berger, 2007; Lloret and Villar, 2007; Sun et al., 2015; Massat et al., 2016). It is considered that the salt concentration can interact at the diffuse double layer level and reduce the swelling potential through osmotic phenomena. For high dry density materials, the influence of the wetting fluid is reduced in constant-volume conditions (Pusch and Yong, 2006). In such conditions, diffuse double layers are thought to be less developed since less voids are available for the diffuse double layers to develop. Figure 2-33 presents swelling pressure test results performed by Castellanos et al., 2006 on Febex bentonite, wetted with fluids of different ionic strength.

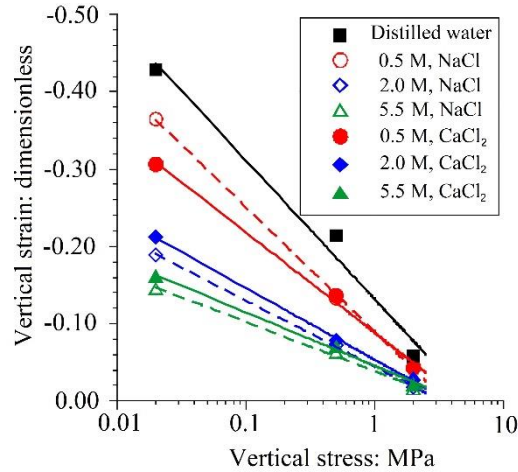


Figure 2-33: Influence of the ionic strength of the wetting fluid on the swelling potential of Febex bentonite compacted to a dry density of 1.65 Mg/m^3 (Castellanos et al., 2006).

2.3.5 Water saturation of compacted bentonites

2.3.5.1 Definition of the degree of saturation

The degree of saturation in porous materials is the ratio of the water volume to the void volume:

$$S_r = \frac{\Omega_w}{\Omega_v} \quad 2-8$$

Where S_r is the degree of saturation, Ω_w and Ω_v are the volume of pore water and the volume of pores, respectively.

Equation 2-8 is equivalent to:

$$S_r = \frac{\rho_s w}{\rho_w e} \quad 2-9$$

Where ρ_s is the density of the solid particles, ρ_w is the water density, w is the gravimetric water content and e is the material void ratio.

As highlighted by equations 2-8 and 2-9, the degree of saturation can be modified in different ways: increase/decrease of the water volume (*i.e.* “pore invasion”); increase/decrease of the void volume (*i.e.* “pore deformation”); combination of pore invasion and pore deformation (Tarantino, 2009; Coussy et al., 2010; Vaunat and Casini, 2017).

2.3.5.2 Influence of the wetting conditions

In compacted expansive soils, wetting is associated to swelling. Therefore, change in the water volume induces change in the void volume. In this respect, saturation of compacted expansive soils is dependent on the wetting conditions as well as the swelling potential of the material (Figure 2-34, Gatabin et al., 2016).

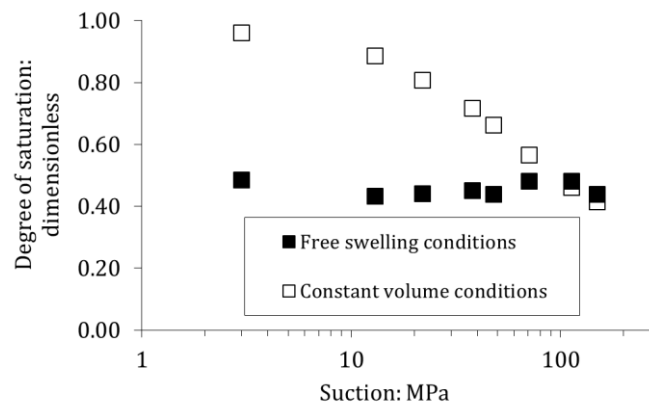


Figure 2-34: Evolution of the degree of saturation of a bentonite-sand mixture (70/30 in dry mass proportions) compacted at an initial dry density of 2.01 Mg/m^3 upon hydration in constant-volume and free-swelling conditions (Gatabin et al., 2016).

In constant-volume conditions, the void ratio is kept constant and water uptake invariably induces an increase of the degree of saturation. The suction-degree of saturation relationship in these conditions is dry density dependent. The higher the dry density, the lower the void ratio. Since the first stage of hydration is characterised by a suction-water content relationship intrinsic to the bentonite type (see 2.2.4.1), it is highlighted by equation 2-9 that the degree of saturation must increase faster upon hydration at higher dry density. For instance, Figure 2-35 presents experimental results of hydration in constant-volume conditions obtained on MX80 bentonite materials (pellet and powder mixture, Molinero-Guerra et al., 2019b; compacted powder, Delage et al., 2006; granular bentonite, Seiphoori et al., 2014) compacted at different dry densities ρ_d . The dry density dependence of the evolution of the degree of saturation is clearly observable. The dry density dependence of the material air-entry value (highest suction at which the material remains fully saturated) is also highlighted by these results.

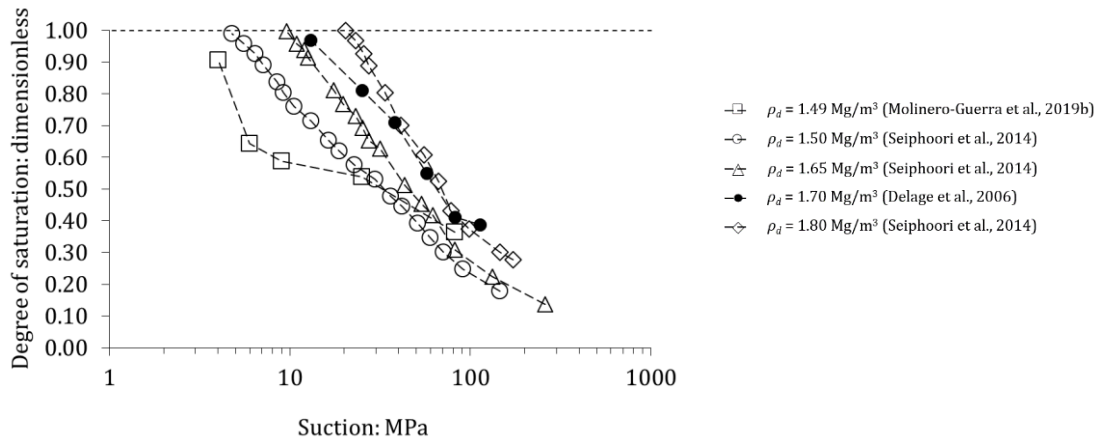


Figure 2-35: Suction-degree of saturation relationship for MX80 bentonite in constant-volume conditions.

In free-swelling conditions, the suction-degree of saturation relationship is influenced by the evolution of the material void ratio upon swelling, which occurs simultaneously to water uptake. Figure 2-36 presents experimental results of hydration in free-swelling conditions obtained on MX80 bentonite materials (compacted powder, Saiyouri et al., 2004; highly compacted pellet, Molinero-Guerra et al., 2019b; compacted bentonite-sand (70/30 in proportions) mixture, Gatabin et al., 2016) compacted at different initial dry densities ρ_{d0} . A nearly constant trend is obtained for the three materials in the investigated suction range (at suction below 0.032 MPa, the degree of saturation of Saiyouri et al., 2004 samples started to increase). A constant value basically means that the pore deformation phenomenon compensates the pore invasion phenomenon. A similar trend was obtained, in free-swelling conditions, by Villar (2000) on bentonite from Cabo de Gata (Spain) compacted at initial dry density of 1.60 Mg/m³, 1.67 Mg/m³, 1.75 Mg/m³. On hydration, the degree of saturation increased for suction higher than ~100 MPa, then remained unchanged as suction decreased to ~0.5 MPa. The first increase of the degree of saturation was interpreted as the influence of the microstructure saturation. Results from Molinero-Guerra et al. (2019a) display a comparable trend at suction higher than ~100 MPa (Figure 2-36), suggesting that the microstructure in MX80 bentonite may desaturate above this value. It is the value estimated by Tessier et al. (1992) to be the air entry value of montmorillonite clay particles.

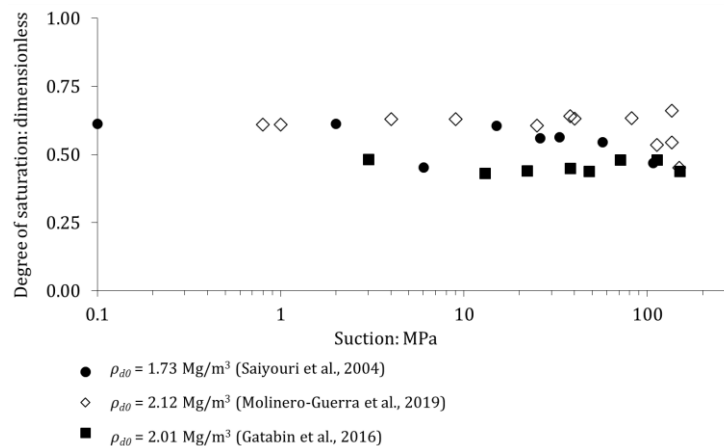


Figure 2-36: Suction-degree of saturation relationship for MX80 bentonite in free-swelling conditions.

2.3.5.3 Evolution of the water density

A significant part of the water stored in compacted expansive clays is adsorbed at the surface of clay mineral layers. Water in this state does not behave as free water and can reach density higher than 1.00 Mg/m^3 , the value of free water (*e.g.* Villar, 2000; Marcial, 2003; Lloret and Villar, 2007; Jacinto et al., 2012). Interpretation of experimental results can therefore lead to an overestimation of the degree of saturation (equation 2-9). Degree of saturation higher than 1 can be obtained if water density is taken equal to free water density.

Jacinto et al. (2012) determined the water density of each adsorbed layer for Na-montmorillonite (*e.g.* MX80) and Febex bentonite (Table 2-5). From the relationship between number of water layers and suction (Figure 2-8), a relationship between water density and suction/relative humidity can be determined to correct experimental values of the degree of saturation.

Table 2-5: Estimated water density of adsorbed water layers in Na-montmorillonite and Febex bentonite (Jacinto et al., 2012).

Water layer	Water density: Mg/m^3	
	Na-montmorillonite	Febex
1	1.32	1.51
2	1.17	1.23 - 1.13
3	1.16	1.11
4	1.14	-

2.3.6 Water transfer in compacted bentonites

In repository conditions, saturation of bentonite-based engineered barriers results from wetting by the pore water of the host rock. In these conditions, material in contact with the host rock is saturated first. Then, engineered barriers saturate owing to water transfer through the material porosity. Evolution of the buffer saturation, permeability, swelling pressure over time are key parameters to assess its performance and depend on the kinetics of water transfer in the material.

Water transfer in bentonite occurs in vapour and liquid phase and involve strong hydromechanical couplings. Their understanding and characterisation is not straightforward. Basically, wetting induces fabric changes which in turn affect water transfer kinetics.

In this part, water transfer processes in compacted bentonite are presented. Experimental evidences of the influence of water transfer on the macroscopic response of the material are first presented. Then, water transfer mechanisms in bentonites and parameters controlling the evolution of permeability are discussed, for unsaturated and saturated states.

2.3.6.1 Experimental evidence of the influence of water transfer on macroscopic response

Imbibition tests aim at hydrating a bentonite sample in conditions reproducing in-situ conditions of engineered barriers, at the laboratory scale. These tests usually consist of constant-volume cells of a tens centimetre high. Hydration is performed either from bottom or from both top and bottom (Wang et al., 2013b; Saba et al., 2014b). They differ from swelling pressure tests at the representative elementary volume scale (REV) because the cell length induces non-negligible gradient of suction.

Saba et al. (2014b) performed mock-up imbibition tests on a compacted bentonite-sand mixture in 120 mm height x 60 mm diameter cylindrical cells. The evolution of measured swelling pressures was shown to be significantly influenced by water transfer. The increase of swelling pressure was faster further from water inlet. The peak swelling pressure was higher and occurred at higher suction further from water inlet. It is interpreted as a consequence of the compression of the material far from the water inlet induced by the faster swelling of the material near the water inlet. Saba et al. (2014b) found that, for this material, hydration from both top and bottom ends does not affect the swelling pressure trend but accelerates its kinetics by a factor of 4. In these hydration conditions, air was found not to get trapped but was evacuated by diffusion.

The faster hydration and swelling near injection point and subsequent compaction further from this point can cause heterogeneities of density and water content at saturation. Wang et al. (2013b) obtained a higher water content and lower dry density near the injection face following saturation and a lower water content and higher dry density at the opposite end of the sample. They interpreted this distribution as a consequence of the pressure applied at the top to dismantle the test (12 MPa). While it is obvious that this pressure may have increased the dry density at the top, the lower dry density and higher water content near injection point have been observed in other infiltration tests on compacted MX80 bentonite (Kröhn, 2004; Villar et al., 2005a; Bian et al., 2018).

Heterogeneities arising as a consequence of hydromechanical couplings are also observed in large-scale hydration tests. The Full-scale high-level waste Engineered Barrier experiment (FEBEX) is a metric-scale infiltration test performed on compacted blocks of dry density 1.60 Mg/m^3 at Grimsel Test Site, Switzerland. A cylindrical gallery of diameter 2.3 m is excavated in the crystalline host rock and filled with bentonite blocks. The bentonite then undergoes hydration in natural conditions. Following the dismantling after five years, dry densities and water content heterogeneities were measured, ranging from $\sim 1.4 \text{ Mg/m}^3$ to $\sim 1.7 \text{ Mg/m}^3$ (dry density) and ~ 0.36 to ~ 0.14 (water content) from outer parts toward the axis of the cylindrical buffer (Villar et al., 2005b).

The Engineered Barrier (EB) experiment is also a metric-scale infiltration test carried out at Mont Terri, Switzerland (Mayor et al., 2007). A dummy canister (no heat production) is placed on compacted blocks of Ca-bentonite (dry density of 1.69 Mg/m^3) and surrounded by granular bentonite (average dry density of the mixture of 1.36 Mg/m^3), as presented in Figure 2-37. Hydration is artificially performed through a pipe system in the buffer for five years, then the buffer undergoes hydration in natural conditions (uptake from the surrounding Opalinus Clay) for five years. Following the dismantling after ten years, the contrast between blocks and pellets had vanished, but heterogeneities of dry density and water content were measured (Figure 2-37). From bottom to top, dry densities and water content were ranging from $\sim 1.24 \text{ Mg/m}^3$ to $\sim 1.42 \text{ Mg/m}^3$ and ~ 0.44 to ~ 0.33 , respectively (Palacios et al., 2013; Garcia-Siñeriz et al., 2015; Wiczorek et al., 2017).

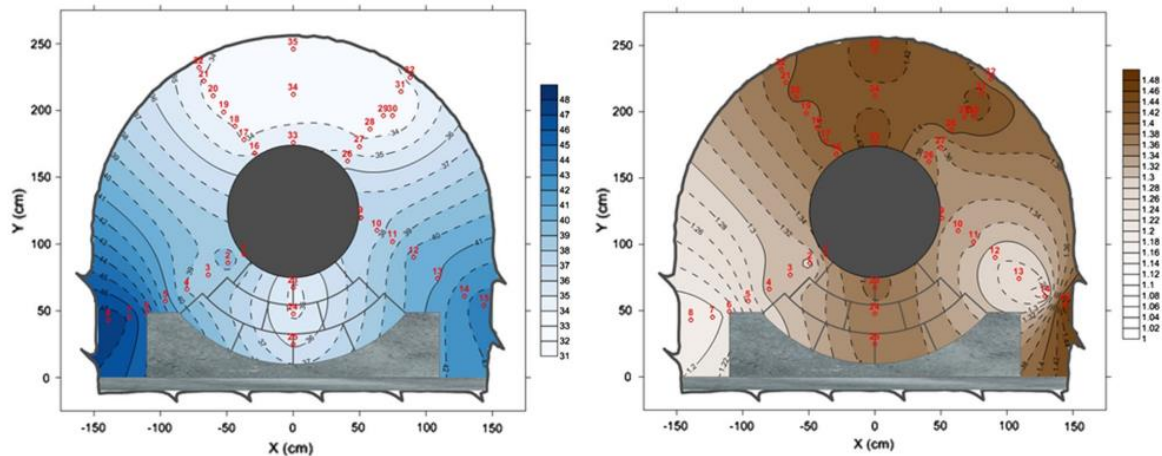


Figure 2-37: Water content (left) and dry density (right) profiles in the EB experiment following dismantling (Wieczorek et al., 2017).

2.3.6.2 Water transfer in unsaturated bentonite

In unsaturated materials, pores are generally considered partially filled with gas and liquid. In compacted bentonite, characterised by a double structure, it was shown that water is first adsorbed and strongly linked to the surface of clay particles while macropores remain dry at least until the change in hydration mechanisms (see 2.2.4.1). At suctions higher than this threshold, the progressive increase of relative humidity in macropores, measured experimentally using *RH* sensors (*e.g.* Krohn, 2004; Cui et al., 2008) can occur as a result of liquid water transfer within microstructure and vapour transfer within macroporosity.

Gas mobility in unsaturated bentonite is higher than water mobility (Olivella and Gens, 2000). At dry states, thus high suctions, gas permeability is found to be significantly higher than saturated liquid permeability (Olivella and Gens, 2000; Lloret and Villar, 2007). Krohn (2004; 2005) highlighted that the saturation process of bentonite materials wetted using liquid water can be explained by phase change and vapour transfer.

Vapour transfer in a low permeability media can occur through three main mechanisms: advective, diffusive, dispersive. Dispersive fluxes are usually neglected due to the high molecular diffusivity of vapour in air. In isothermal conditions and with no external pressure gradient applied, diffusive fluxes can be considered the dominant transfer mechanism (Croney et al., 1958; Olivella and Gens, 2000).

Vapour diffusion in porous materials is usually described using the Fick law, which is presented in a further section (2.5.3.3). In the course of isothermal hydration, vapour diffusive fluxes have been shown to depend on the mass fraction gradient, the gas degree of saturation (*i.e.* $1 - S_r$) and the porosity (Philip and de Vries, 1957).

Cui et al. (2008) determined the apparent unsaturated permeability of Kunigel bentonite-sand mixture (70/30 in dry mass proportions) upon hydration in constant-volume and free-swelling conditions using the instantaneous profile method (Delage and Cui, 2000). In free-swelling conditions, the apparent permeability was found to increase upon hydration. In constant-volume conditions, the apparent permeability was found to decrease upon hydration then increase after a threshold suction. Similar trend in constant-volume conditions are reported in the literature (Ye et al., 2009; Liu et al., 2012; Wang et al., 2013b, Figure 2-38). In free-swelling conditions, the macropore volume is known to increase upon

wetting, while in constant-volume conditions, expansion is prevented and macropores are progressively filled with exfoliated particles.

Results from Cui et al. (2008) are thus consistent with the dominance of vapour transfer in the saturation process of the bentonite. The increase of apparent permeability at low suction can be associated to the clogging of macropores. In this case, vapour diffusion would no longer be dominant and the increase of apparent permeability can be explained by a progressive increase in the influence of liquid transfer as suction decreases further.

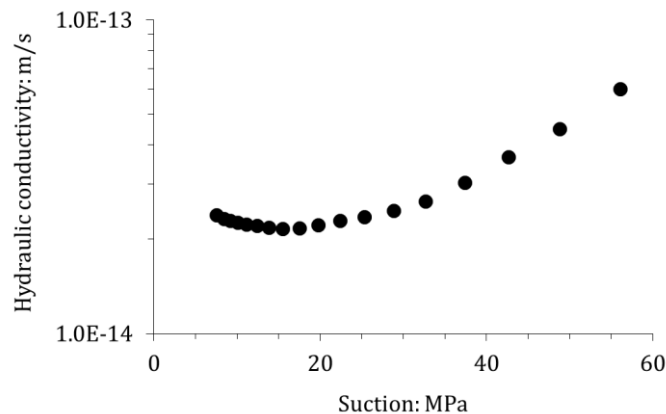


Figure 2-38: Unsaturated apparent hydraulic conductivity of a MX80-sand (70/30 in proportions) mixture as a function of decreasing suction (Wang et al., 2013b).

2.3.6.3 Water transfer in saturated bentonite

In saturated state, pores are fully filled with water. In these conditions, water transfer occurs in liquid phase and advective phenomena are dominant, assuming that no significant chemistry gradient exists in the saturating fluid (*i.e.* water in repository conditions).

Pressure and suction gradients govern the mass transfer in saturated bentonite. In saturated conditions, this latter is influenced by the soil fabric and the wetting fluid:

- Clay-water interactions affect water mobility in saturated bentonite. In this respect, some authors have suggested that water fluxes are likely not to be directly related to pressure gradient through Darcy's law (*e.g.* Bennethum et al., 1997; Dixon et al., 1999; Komine, 2008; 2010; Liu et al. 2012).
- The material dry density significantly affects the apparent water permeability (Figure 2-39). Studies evidence that the lower the dry density the higher the permeability (Dixon et al., 1999; Villar; 2005; Lloret and Villar, 2007; Karnland et al., 2006; 2008; Komine, 2008; 2010; Wang et al., 2013a; Cui, 2017; Xu et al., 2016). In a double porosity framework, if water transfer is considered to occur in both micro- and macrostructure, the macrostructure permeability is therefore likely to be higher than the microstructure permeability.
- The fluid salinity has been shown to influence the material apparent permeability. Fluids with higher salinity increase the permeability (Pusch, 2001; Villar, 2005).

- The relative proportion of bentonite/secondary material in mixtures affects the permeability. The higher the bentonite proportion, the lower the saturated permeability (Komine, 2004; 2008; Xu et al., 2016).

For a given material saturated using a given fluid, the most important parameter affecting the permeability is thus the dry density.

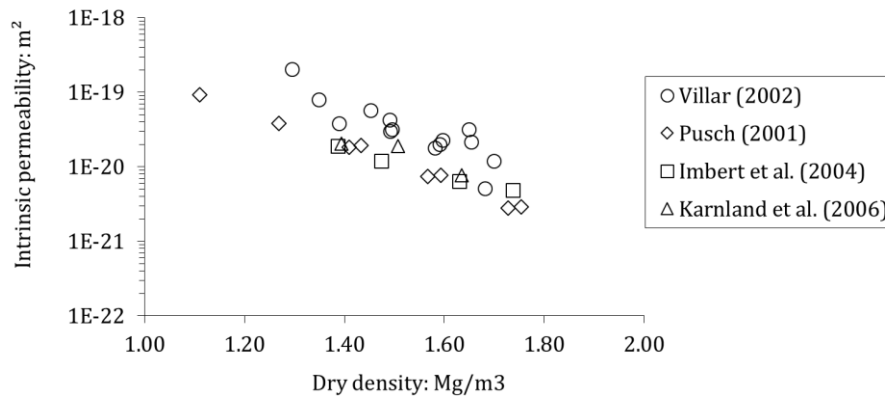


Figure 2-39: Intrinsic permeability of MX80 bentonite in saturated conditions as a function of dry density.

2.4 PARTICULAR FEATURES OF BENTONITE PELLET MIXTURES

In this section, particular features of pellet materials are highlighted. Main characteristics of a high density bentonite pellet constitutes the first part. Initial heterogeneities and final homogenisation of pellet mixtures are discussed in the second part. Influence of the initial granular structure on the material behaviour is highlighted in the third part.

2.4.1 Characteristics of high density bentonite pellet

Different materials have been referred to as “bentonite pellet”, “pelletised bentonite” or “granular bentonite” in the literature. For instance, Hoffmann et al. (2007), Alonso et al. (2010a), Alonso et al. (2011) focused on pelletised Febex bentonite of heterogeneous grain size, Karnland et al. (2008), Seiphoori et al. (2014) focused on a “granular” MX80 bentonite of heterogeneous grain size. Van Geet et al. (2005), Garcia-Gutierrez et al. (2004), Imbert and Villar (2006), Gens et al. (2011) focused on 25x25x15 mm FoCa pellets. Molinero-Guerra et al. (2017; 2018a; 2018b; 2019a; 2019b) focused on 7 mm sub-spherical MX80 pellets. Differences of shape and grain size distribution are likely to have an influence on the material response to hydromechanical solicitations. However, granular bentonite materials share some relevant features, described in the present part.

2.4.1.1 Characteristics at initial state

Pellets are obtained from compaction of bentonite powder at high dry density or pelletisation of compacted block of bentonite powder. In this respect, pellet initial characteristics are the same as high density compacted bentonite materials described in 2.2.2.

Molinero-Guerra et al. (2017) performed MIP test on a MX80 bentonite pellet (initial dry density 2.12 Mg/m^3). A traditional double porosity structure was identified, with microporosity corresponding to $\sim 95\%$ of the total porosity. Authors performed X-ray computed tomography on the pellet. From X-ray computed tomography results they reconstructed the pellet in 3D and identified that macroporosity was characterised by a crack network (Figure 2-40). Cracks were not homogeneously distributed inside the pellet. More cracks were identified at the top and bottom of the pellet. It was suggested that cracks appeared during swelling as a consequence of hydration in free-swelling conditions, during storage in the laboratory.

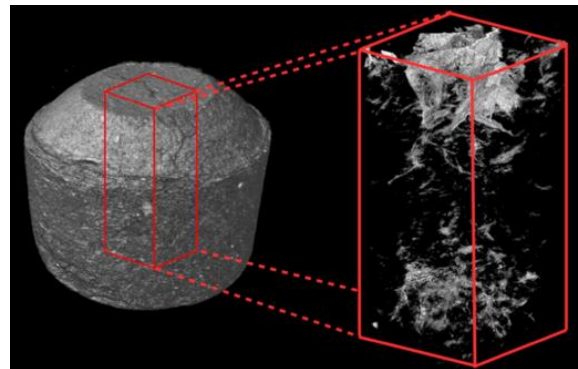


Figure 2-40: 3D reconstruction of a bentonite pellet from X-ray computed tomography images. A crack network is identified and associated to the macroporosity (Molinero-Guerra et al., 2017).

On SEM images of a pellet cross section, Molinero-Guerra et al. (2017) identified mineral inclusions in MX80 pellets and analysed these latter using Energy-Dispersive X-ray Spectroscopy (EDS). Analyses evidenced the presence of quartz, pyrite and calcite inclusions in pellets, the size of which sometimes appeared to be non-negligible in comparison to the pellet size (~ 10 to more than $130 \mu\text{m}$ for the inclusions, 7 mm for the pellet).

2.4.1.2 Influence of hydration on the pellet microstructure

Molinero-Guerra et al. (2019a) studied the evolution of a MX80 bentonite pellet pore size distribution upon hydration in free-swelling conditions using the vapour equilibrium technique and MIP. Using the vapour equilibrium technique, the time required for equilibrium at $\text{RH} = 100\%$ was in the range ~ 20 - 30 days. Water content, saturation and volumetric strain evolution were also determined. On MIP test results, both microporosity and macroporosity increased upon wetting. Macropores were associated to the development of crack networks identified using X-ray computed tomography. At suction below 4.2 MPa , a notable reorganisation of the material fabric was evidenced. This threshold coincides with the suction below which the water retention curves of a single pellet in free-swelling conditions and a pellet-powder mixture in constant-volume conditions exhibited different trends (Molinero-Guerra et al., 2019b), consistently with results obtained on other compacted bentonites.

In constant-volume conditions, Seiphoori et al. (2014) identified a progressive closure of macroporosity in a granular bentonite and no evidence of crack network development. In the light of these results, it can be suggested that crack network are a feature of pellet hydration in free-swelling conditions.

From suction-saturation relationship and MIP test results from Molinero-Guerra et al. (2019a) and assuming that smaller voids saturate first, the water ratio can be determined to evidence that macropores remain dry even at low suction (Figure 2-41), consistently with Sun et al. (2019) observation on the Černý vrch bentonite.

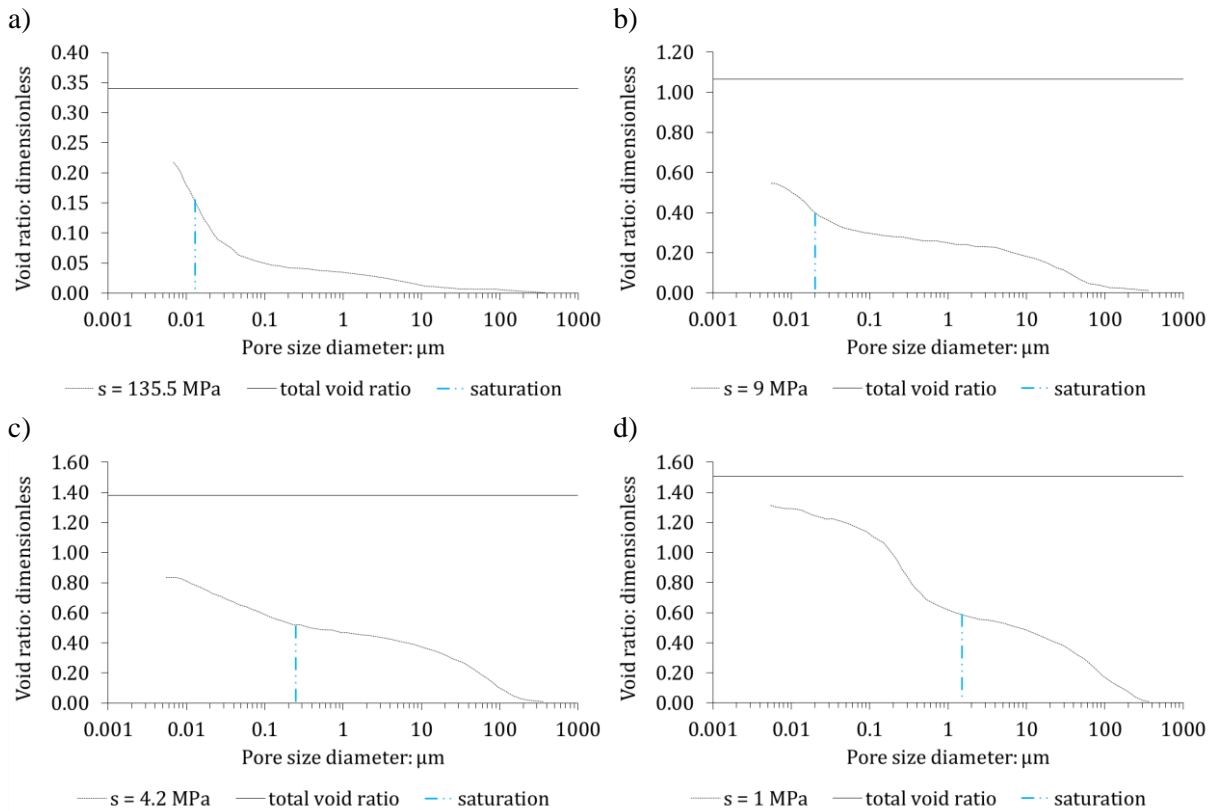


Figure 2-41: Saturated porosity in MX80 bentonite pellet deduced from saturation and MIP test results of Molinero-Guerra et al. (2019a), at different suction: 135.5 MPa (a); 9 MPa (b); 4.2 MPa (c); 1 MPa (d).

2.4.2 Heterogeneities and homogenisation of pellet mixtures

Bentonite pellet mixtures are composed of an assembly of bentonite pellets and eventually bentonite powder to fill inter-pellet voids. These materials are heterogeneous at initial state and homogenise upon wetting. Material heterogeneities and homogenisation at saturation are described in this part.

2.4.2.1 Triple porosity of pellet mixtures

It was presented in 2.4.1 that pellets have the same pore size distribution as traditional compacted bentonite materials. Pellet or pellet-powder mixtures are characterised by an initial triple porosity fabric: micropores and macropores in the pellets and eventually in the powder grains, and inter-pellet voids. The triple porosity fabric is observable on Figure 2-42, which presents MIP test results of a pelletised Febex bentonite, performed by Hoffmann et al. (2007).

The presence of inter-pellet voids provides the material with large and connected porosity, inducing a high permeability to water at initial state. The large inter-pellet pores are progressively reduced upon

pellet swelling and are the most affected by eventual compaction of the material (Hoffmann et al., 2007; Alonso et al., 2010a).

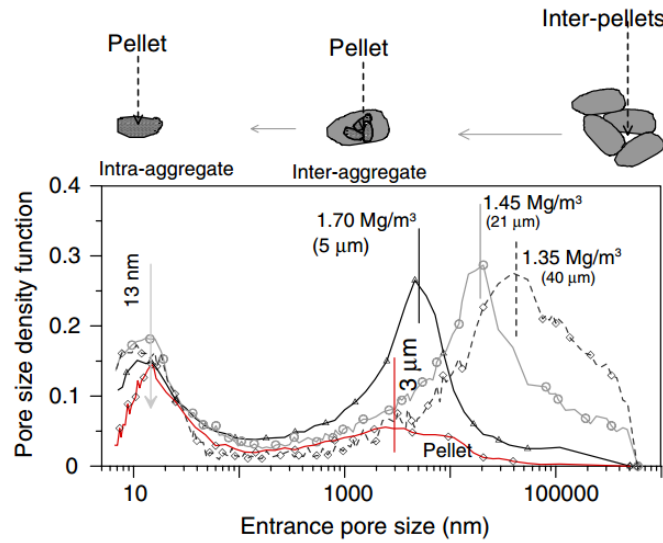


Figure 2-42: Pore size distribution of a pelletised Febex bentonite (Hoffmann et al., 2007).

2.4.2.2 Local heterogeneities of density

In addition to heterogeneities highlighted at the pellet scale and the discontinuous pore networks, pellet materials can be characterised by heterogeneities of density at initial state.

In a pellet mixture, initial state is characterised by an intrinsic heterogeneous distribution of dry densities. To reach a target swelling pressure, samples are prepared at a target average dry density. In this respect, pellet dry density is significantly higher than this value, while inter-pellet voids are filled with air or low density powder grain assembly. It is clearly observable on Figure 2-43, presenting interpreted results of X-ray computed tomography from Van Geet et al. (2005).

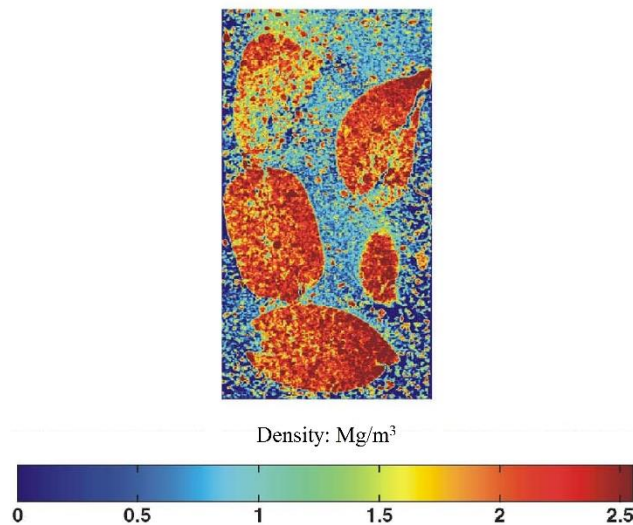


Figure 2-43: Distribution of density in a bentonite pellet-powder mixture at dry state, obtained from X-ray computed tomography results (van Geet et al., 2005).

Besides, Molinero-Guerra et al. (2017) evidenced that the preparation of a bentonite pellet-powder sample invariably induces a heterogeneous distribution of pellet and powder at laboratory scale. Therefore, because of difficulties in preparing the samples or as a result of fine grained material migration in pellet-powder mixture, the local dry density can vary within a sample at initial state.

In pellet mixtures compacted to reach a target average dry density, the pellet strength can be reached. Pellet breakage can lead to an increase of the proportion of fine-grained material (Figure 2-44, Hoffmann et al., 2007). Pellet breakage and associated increase of the proportion of fine-grained material are also likely to make the local dry density vary within a sample if fine-grained materials migrate through large inter-pellet voids as a result of gravity.

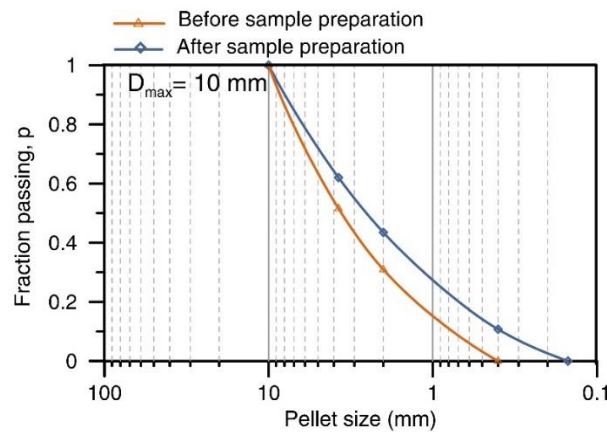


Figure 2-44: Grain size distribution before and after compaction to a dry density of 1.50 Mg/m^3 (Hoffmann et al., 2007).

2.4.2.3 Homogenisation upon hydration

Hydration at laboratory scale

Upon hydration at REV scale, pellet mixtures progressively homogenise. At full saturation, the material is no longer characterised by a granular structure and has a perfectly homogeneous appearance. Figure 2-45 presents the evolution of a sample of pelletised Febex bentonite during hydration (Hoffmann et al., 2007). A progressive closure of inter-pellet voids is observable.

Consistently with Hoffman et al. (2007) observations, Van Geet et al. (2005) and Molinero-Guerra et al. (2018a) evidenced through X-ray computed tomography that the initially heterogeneous pellet mixture progressively lost its initial granular structure to reach a final homogeneous state (Figure 2-46). Van Geet et al. (2005) computed the sample dry density and highlighted that the initial heterogeneous distribution of dry density was homogeneous at saturation.

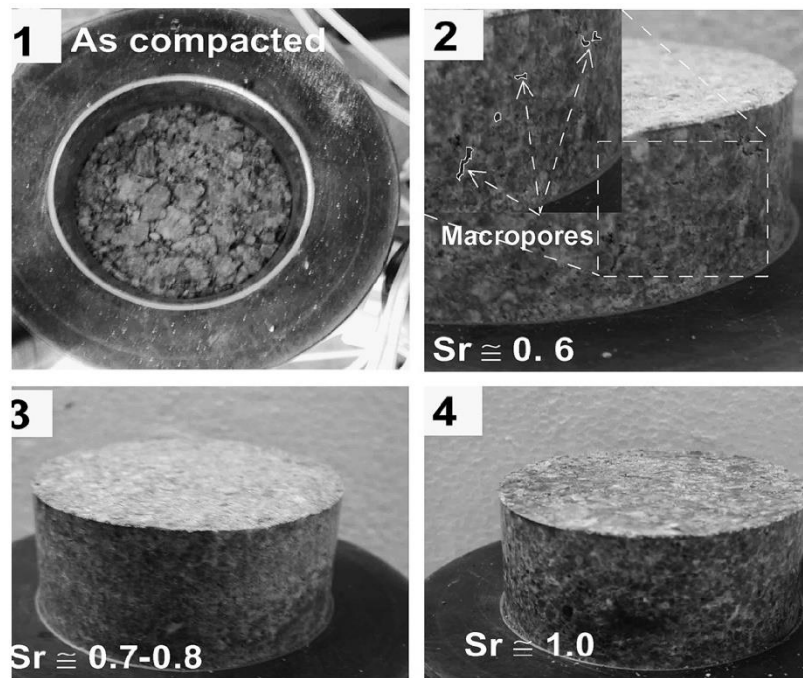


Figure 2-45: Evolution of a pelletised Febex bentonite sample upon hydration, at four degrees of saturation (S_r) (Hoffmann et al., 2007).

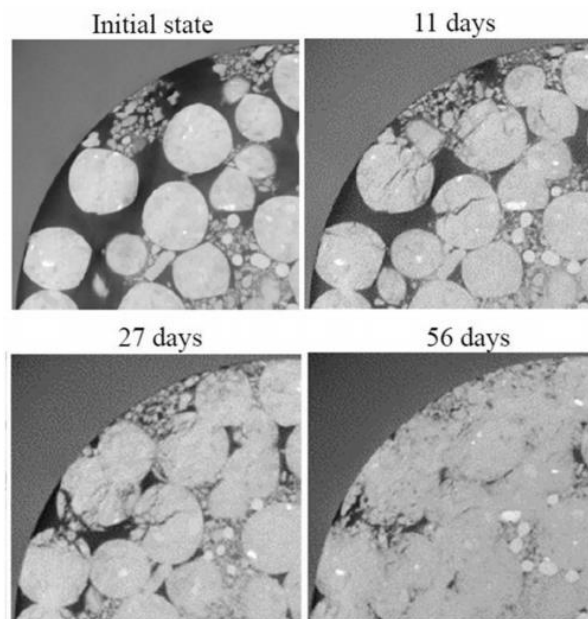


Figure 2-46: Evolution of the granular structure of a MX80 bentonite pellet-powder mixture during hydration (Molinero-Guerra et al., 2018a).

Hoffmann et al. (2007) and Alonso et al. (2010a) determined the evolution of a pelletised Febex bentonite sample permeability to water upon wetting. It was highlighted that the material is characterised by a high permeability at initial state, which is significantly reduced as the degree of saturation increases (Figure 2-47). At full saturation, the saturated permeability was found to be similar to other Febex materials on a permeability-dry density plane, suggesting that dry density had homogenised upon saturation. Karland et al. (2008) suggested similar conclusions for the saturated permeability of MX80

pelletised bentonite. In addition, Garcia-Gutierrez et al. (2004) studied the diffusion process in saturated pellet-powder mixture and compacted powder material at the same average dry density and concluded that the diffusion coefficient was similar in both materials.

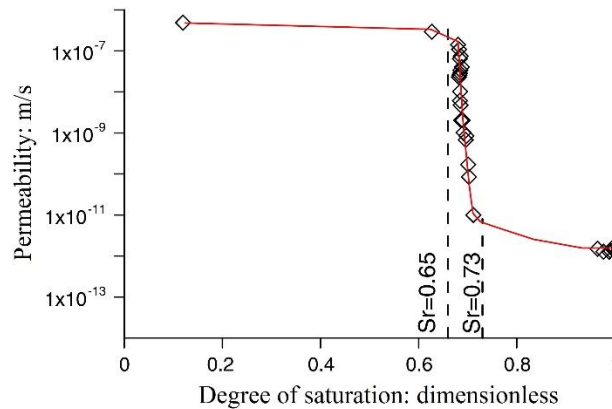


Figure 2-47: Permeability of a pelletised Febex bentonite compacted at a dry density of 1.3 Mg/m^3 as a function of the degree of saturation (Hoffmann et al., 2007).

The final swelling pressure in swelling pressure tests has been shown to be mostly a function of the final dry density. Karnland et al. (2008) and Imbert and Villar (2006) determined the swelling pressure of MX80 pellet bentonite and FoCa bentonite pellet-powder mixture. The final swelling pressure of pellet-based materials was found to be similar to the final swelling pressure of compacted powder at the same average dry density, evidencing that the initial heterogeneities of the material had no influence on the final swelling pressure, at the study scale (cylindrical samples of 35 mm diameter and 10 mm height, Karnland et al. (2008); cylindrical samples of 100-120 mm diameter and 30-100 mm height, Imbert and Villar (2006). Conversely, Molinero-Guerra et al. (2018b) performed hydration test in constant-volume cylindrical cell (60 mm diameter and 120 mm height) and suggested that initial heterogeneities of density could explain the heterogeneous radial pressure profile (Figure 2-48).

Large-scale hydration

At metric to multi-metric scale, experimental results available in the literature suggest that final distribution of water content and dry density in pellet-based bentonite buffers are not perfectly homogeneous (Gens et al., 2013; Palacios et al., 2013; Garcia-Siñeriz et al., 2015; Wieczorek et al., 2017). Still, it is worth mentioning that: *i*) even without pellets, hydration of bentonite materials at this scale can lead to a non-homogeneous distribution of dry densities and water content at final state, as highlighted in 2.3.6.1; and *ii*) initial heterogeneities between blocks and pellets are significantly reduced within the buffer, as highlighted by Gens et al. (2013) and Garcia-Siñeriz et al. (2015).

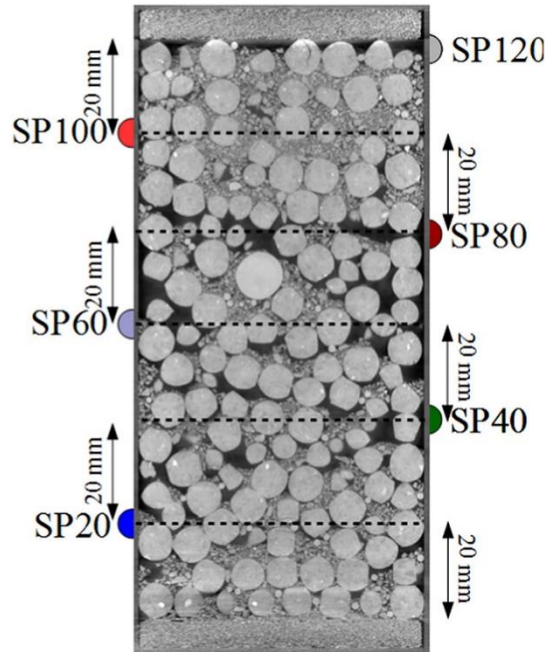


Figure 2-48: MX80 pellet-powder mixture prepared for hydration test, at initial state. Local heterogeneities of density are clearly observable. SP xx labels correspond to the position of pressure sensors, xx being the elevation in mm (Molinero-Guerra et al., 2018b).

2.4.3 Influence of the granular structure

Previous discussion mostly focused on the identification of initial heterogeneities and final homogenisation of granular bentonite materials. In this part, the influence of the granular structure in transient stages of hydration is highlighted. The concept of dominant phase in binary granular mixtures is first defined. Then, experimental evidences of the influence of granular structure on the material response during loading at constant suction and wetting at constant volume are highlighted from test results available in the literature.

2.4.3.1 Dominant phase in binary granular mixtures

Binary granular mixtures are granular materials composed of two families of grains of two different grain sizes. In the following, the case $d_L \gg d_S$, with d_L and d_S the diameter of the large and small particles respectively, will be considered. Depending on the relative proportion of large particles and small particles, two extreme cases can be defined. If the volumetric proportion of large and small particles are denoted x_L and x_S , the granular assembly behaviour is controlled by the assembly of large grains for $x_L \gg x_S$, with some particles filling the available voids. Conversely, for $x_S \gg x_L$, the mixture behaviour will be controlled by the assembly of small particles, forming a matrix in which some large particles are inserted but do not form a structured network.

In a granular assembly composed only of large particles, the material void ratio can be expressed as:

$$e = \frac{\Omega}{\Omega_L} - 1 = \frac{1}{\alpha_L} - 1 = e_L \quad 2-10$$

Where Ω is the total volume, Ω_L is the volume of large particles, α_L is the volume fraction of large particles and e_L is the void ratio of the large particle assembly.

Conversely, in a granular assembly composed only of small particles, the material void ratio is given by:

$$e = \frac{\Omega}{\Omega_S} - 1 = \frac{1}{\alpha_S} - 1 = e_S \quad 2-11$$

Where the subscript ‘‘S’’ denotes the small particles.

In the first case, where the large particles constitute the dominant phase, progressive insertion of small particles would reduce the void ratio. This phenomenon is referred to as the ‘‘insertion mechanism’’. In this case, the void ratio ‘‘ e_{ins} ’’ can be expressed as a function of x_S :

$$e_{ins}(x_S) = \frac{\Omega - (\Omega_L + \Omega_S)}{\Omega_L + \Omega_S} = e_L - (1 + e_L) x_S \quad 2-12$$

In the second case, where small particles constitute the dominant phase, x_L can be progressively increased by inclusion of large particles within the matrix, thus reducing x_S and substituting voids by large particles. This phenomenon is referred to as the ‘‘substitution mechanism’’. In this case, the void ratio ‘‘ e_{sub} ’’ can also be expressed as a function of x_S :

$$e_{sub}(x_S) = \frac{(\Omega - \Omega_L) - \Omega_S}{\Omega_L + \Omega_S} = e_S x_S \quad 2-13$$

Equations 2-12 and 2-13 describe two distinct lines in a plane e - x_S . If α_S and α_L both take the maximum value for the considered material (*i.e.* both granular materials are in their densest state), the coordinates of the intersection of e_{ins} and e_{sub} are the theoretical minimum void ratio e_{min} and critical fine proportion, $x_{S\ crit}$. The intersection is defined as:

$$e_{min} = \frac{\left(\frac{1}{\alpha_S^*} - 1\right) \left(\frac{1}{\alpha_L^*} - 1\right)}{\frac{1}{\alpha_S^*} + \frac{1}{\alpha_L^*} - 1} \quad 2-14$$

$$x_{S\ crit} = \frac{\frac{1}{\alpha_L^*} - 1}{\frac{1}{\alpha_S^*} + \frac{1}{\alpha_L^*} - 1} \quad 2-15$$

Where α_S^* and α_L^* are the maximum volume fraction for the granular assembly defined by small and large particles, respectively.

The intersection of these two lines split the e - x_S plane in two parts. For $x_S \ll x_{S\text{ crit}}$, large particles are considered the dominant phase. For $x_S \gg x_{S\text{ crit}}$, small particles are considered the dominant phase (Figure 2-49).

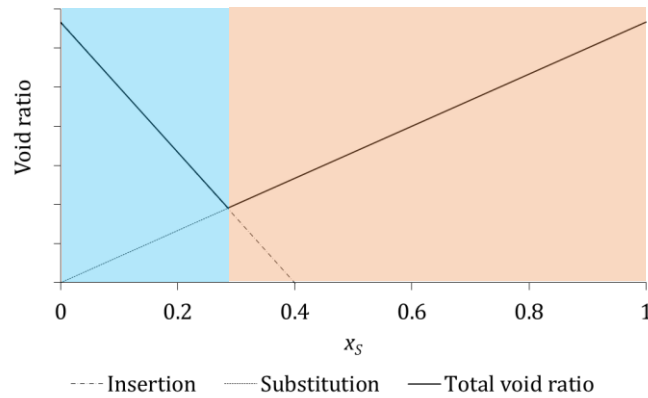


Figure 2-49: Evolution of the void ratio of an ideal binary mixture with $d_L \gg d_S$. The blue area corresponds to the behaviour controlled by large particles. The red area corresponds to the behaviour progressively controlled by small particles.

It is worth mentioning that for x_S close to $x_{S\text{ crit}}$, both particle families influence the material behaviour. In addition, equations 2-14 and 2-15 are likely to provide a rough estimation of x_S^* . Equations 2-12 and 2-13 indeed provide an ideal estimation of the void ratio. In cases where d_S/d_L does not approach zero, the void ratio will be higher than the value obtained through these equations. In the substitution mechanism, inclusion of large particles induces a “wall effect”: the matrix void ratio is higher in contacts with a large particle. In the insertion mechanism, addition of particles not small enough to fit in voids can induce an increase of the void ratio compared to the ideal one (Figure 2-50). In the extreme case where $d_S/d_L = 1$, the total void ratio would be a straight line from $e_{ins}(0)$ to $e_{sub}(1)$ in Figure 2-49.

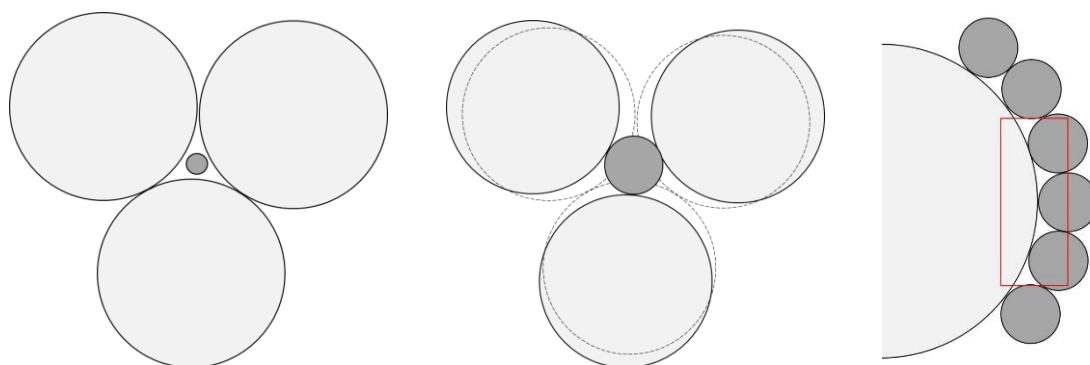


Figure 2-50: Reasons for underestimation of void ratio using equations 2-12 and 2-13: insertion of particles not small enough (left and centre) and wall effect inducing a lower density zone near large particles (right).

Further information and discussion concerning the dominant phase in binary granular mixtures can be found, for instance, in Westman and Hugill (1930); Yerazunis et al. (1965), de Larrard (2004); Roux et al. (2007); Ueda et al. (2011); Roquier (2015).

2.4.3.2 Mechanical loading at constant suction

The influence of the granular structure of the material upon loading at constant suction is suggested by suction-controlled oedometer tests performed by Hoffmann et al. (2007) on pelletised Febex bentonite. The variation of elastic compressibility of the material upon suction decrease was found to be non-negligible. On compacted Febex bentonite, Lloret et al. (2003) obtained only slight variations of this parameter upon suction decrease as well as smaller values of compressibility. It can be suggested that this observation is a consequence of the evolution of the granular structure of the pelletised bentonite upon wetting.

Molinero-Guerra et al. (2019b) also performed suction-controlled oedometer tests on a mixture of MX80 subspherical pellets and powder (80/20 in dry mass proportion, average dry density of 1.49 Mg/m^3 at initial state). The mixture was loaded in an oedometer at constant suction (138 MPa; 9 MPa; 0 MPa following wetting) (Figure 2-51). The authors observed that at zero suction, the volumetric strain-time relationship upon mechanical loading followed a standard trend of consolidation of fine-grained soils, highlighting that the material behaved as a continuous clayey material. Conversely, at 9 MPa and 138 MPa, instantaneous strains were observed following loading, which was interpreted as a consequence of rearrangement of the inter-pellet porosity as well as pellet failure. The apparent preconsolidation pressure was found to decrease with decreasing suction. However, it is highlighted that irreversible strains may arise as a result of totally distinct phenomena depending on the granular/continuous state of the material.

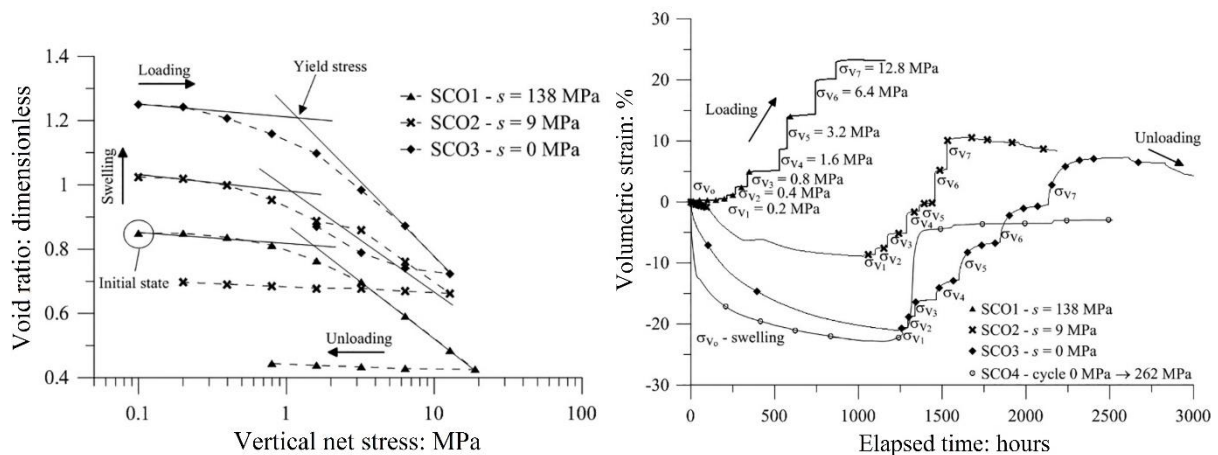


Figure 2-51: Results of suction-controlled oedometer tests performed by Molinero-Guerra et al. (2019b) on a pellet-powder mixture: void ratio-vertical stress relationship (left) and volumetric strain-elapsed time relationship following loading. Negative volumetric strains indicate swelling.

2.4.3.3 Hydration under constant-volume conditions

The influence of the granular structure can be highlighted during constant-volume hydration through suction-controlled swelling pressure tests. Hoffmann et al. (2007) performed this test on pelletised Febex bentonite compacted at dry densities of 1.3 Mg/m^3 and 1.5 Mg/m^3 . In both tests, the swelling pressure was found to increase during the first hydration step (decrease of suction from $\sim 300 \text{ MPa}$ to 90 MPa), then remained nearly constant or slightly decreased as suction was progressively decreased to zero (Figure 2-52). Authors interpreted this observation as a consequence of the progressive decrease of pellet strength and stiffness upon suction decrease which induced a decrease of the intergranular contact forces holding the granular assembly. Simultaneously, pellets would swell. As a result, macroscopic swelling and collapse occurred at the same time. Lloret et al. (2003) swelling pressure tests results on compacted Febex bentonite exhibited different trends (Figure 2-29).

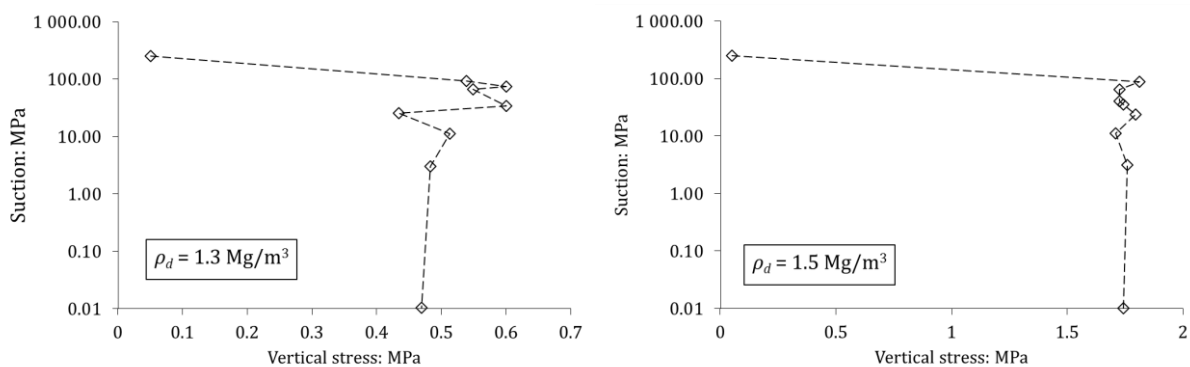


Figure 2-52: Swelling pressure test results performed on pelletised Febex bentonite (Hoffmann et al., 2007).

Imbert and Villar (2006) performed constant-volume hydration tests on a FoCa bentonite pellet-powder mixture (50/50 proportion in dry mass) and on compacted FoCa powder. Upon fast liquid water wetting, they evidenced that the trend followed by samples does not depend on the material initial state (*i.e.* continuous or granular). All samples exhibited the traditional “*increase-peak-decrease-increase*” trend of swelling pressure evolution. Pellet-powder mixture macroscopic response as a function of elapsed time was found to be identical to compacted powder macroscopic response.

The very different macroscopic response of Hoffmann et al. (2007) and Imbert and Villar (2006) and comparison to traditional trends observed on compacted materials suggest that the granular structure had no observable effects in Imbert and Villar (2006) tests. A notable difference between these studies is the wetting rate. The influence of the wetting rate on the macroscopic response of pellet-based materials is mentioned by Alonso et al. (2011). Upon liquid water saturation, water rapidly saturates inter-pellet porosity and the fabric rearrangement is very fast. Intergranular forces holding the pellet assembly are reduced and the material is prone to macroscopic collapse. Upon vapour saturation, inter-pellet voids remain dry and pellets are slowly hydrated. Intergranular forces are progressively reduced, while grains progressively swell.

Liquid water hydration from a low suction after progressive suction decrease through the vapour equilibrium technique leads to a similar final state as initial liquid wetting (Alonso et al., 2011; Delage et al., 1998). In repository conditions, owing to the large size of the buffer, vapour transfer is likely to be dominant in the saturation process of the material. In this respect, laboratory tests performed using slow hydration seems to be more adapted to study the transient behaviour of the material. Conversely, vapour transfer requires a very long testing time and provides similar final results as fast wetting using

liquid water. In this respect, it seems convenient to perform fast hydration to study the material final state.

2.4.3.4 Difficulties related to the characterisation in laboratory tests

Pellet based bentonite materials have been shown to be characterised by low permeability, influence of the initial granular structure on the macroscopic response, heterogeneities of density, and eventually heterogeneous distribution of powder, if powder fills inter-pellet voids.

Characterisation in the laboratory to get an insight into the material behaviour or obtain relevant parameters for modelling purpose can be difficult. Some difficulties identified in previous discussions are summarised hereafter.

Fast hydration affects the material granular structure and can induce significant modifications in the macroscopic response. However, equilibrium requires long time to be reached upon vapour hydration. Small-size cells indeed reduce the time required to reach equilibrium. Still, wall effect is increased if a granular material is poured in a small cell, which could affect the behaviour upon hydration.

The material response is affected by its density and it is likely that local heterogeneities of density influence the macroscopic response, at least before eventual homogenisation. Thus, tests performed at the same average dry density may be characterised by different initial states and, consequently, by different macroscopic response in the course of hydration. Another difficulty arising from the material heterogeneity is the suitability of the experimental apparatus. Indeed, if small sensors are used to measure apparent swelling pressure, very different apparent macroscopic response can be obtained if the sensor is located in front of a pellet or an inter-pellet void. Conversely, determining the appropriate sensor size able to properly measure the “local” material response is not straightforward.

2.5 MODELLING THE BEHAVIOUR OF COMPACTED BENTONITE ON HYDRATION

In this section, an overview of the main modelling approaches used in the literature to describe the hydromechanical behaviour of unsaturated compacted expansive clays is presented. A description of the common stress variable approaches is presented in part 2.5.1. Then, an overview of the Barcelona Basic Model (BBM, Alonso et al., 1990) framework, extensively used in the modelling of unsaturated soils, constitutes part 2.5.2. Common methods used to describe the water retention behaviour and water transfer in expansive clays are then presented in part 2.5.3.

2.5.1 Stress variables

In partially-saturated soils, effects of suction on the material behaviour can be described by an extension of Terzaghi’s effective stress or by introducing another stress variable, thus separating effects of mechanical loading and suction on the material strain. Both have advantages and drawbacks. In this part, both approaches are presented.

2.5.1.1 The Terzaghi effective stress in saturated soils

In saturated soils, the stress-strain relationship is described by Terzaghi (1936) effective stress. Relationship between total stress, effective stress and pore pressure in a water-saturated material is given by:

$$\boldsymbol{\sigma}' = \boldsymbol{\sigma} - p_w \mathbf{I} \quad 2-16$$

Where $\boldsymbol{\sigma}'$ is the effective stress tensor, $\boldsymbol{\sigma}$ is the total stress tensor, p_w is the pore pressure and \mathbf{I} is the identity tensor. Following soil mechanics sign convention, compression stresses are positive and tension stresses are negative.

2.5.1.2 Extension of the Terzaghi effective stress to unsaturated soils

Bishop (1959) proposed the following extension to Terzaghi's definition of effective stress for unsaturated materials:

$$\boldsymbol{\sigma}' = \boldsymbol{\sigma} - p_g \mathbf{I} - \chi (p_w - p_g) \mathbf{I} \quad 2-17$$

Where p_g is the gas and vapour phase pressure and χ is a parameter introduced to take into account surface tension effects on the material behaviour. χ is frequently referred to as the "Bishop parameter". Bishop (1959) proposed that χ takes the value 0 in totally dry state and 1 in fully saturated conditions, thus providing a smooth transition between unsaturated and saturated states (equations 2-16 and 2-17 are equivalent for $\chi = 1$). Characterisation of the Bishop parameter is a key issue in the effective stress approach (Alonso et al., 2010b; Vaunat and Casini, 2017). $\boldsymbol{\sigma} - p_g \mathbf{I}$ is referred to as the "net stress". Assuming that suction can be described by the capillary component, $-(p_w - p_g)$ is the suction.

Using this approach, the stress-strain relationship is written in the same way as for saturated materials:

$$d\boldsymbol{\varepsilon} = \mathbf{C} : d\boldsymbol{\sigma}' \quad 2-18$$

Where $d\boldsymbol{\varepsilon}$ is the strain tensor increment, $d\boldsymbol{\sigma}'$ is the effective stress tensor increment and \mathbf{C} is the constitutive fourth order tensor.

Main advantages of using this approach are the direct transition to saturated state as highlighted by equations 2-17 and 2-18, and the theoretically smaller number of model parameters to describe the stress-strain relationship, as both suction and total stress increment are related to the strain increment through the effective stress increment.

However, as highlighted by discussions in previous sections, this approach cannot reproduce some features of compacted bentonite. For instance, depending on the stress, suction decrease can lead to either swelling or shrinkage whereas from equations 2-17 and 2-18, a suction decrease can only induce

swelling. In the void ratio (e)-effective mean stress (p') plane, a suction increase would induce an increase of p' , thus a shift toward the elastic limit in over-consolidated soils.

These drawbacks generally lead to the introduction of additional parameters to reproduce the collapse behaviour and suction-dependency of the apparent preconsolidation pressure (Jommi, 2000; Khalili et al., 2004; Sheng et al., 2004; 2008; Pereira et al., 2005; Laloui and Nuth, 2009; Sun et al., 2017).

2.5.1.3 Two stress variables approach

Fredlund and Morgenstern (1977) highlighted that the volumetric behaviour of unsaturated soils can be described using two independent and non-additive variables, for instance the net stress and suction. While this approach usually leads to the requirement of more material parameters to describe its behaviour, it is convenient as these latter are easier to obtain in the laboratory. Indeed, gas pressure is usually considered constant, and mechanical loadings and control of suction are common stress paths in experimental studies. In addition, experimental observations such as the collapse behaviour or the increase in apparent preconsolidation pressure can be directly introduced in models using this approach.

The main drawback of the two stress variables approach using net stress and suction is that transition to saturated state with positive pore pressures, described by effective stress, is not straightforward. In this case, Sheng et al. (2008) suggest that the two variables “Bishop effective stress” and “suction” can be adopted.

Most of the models used in the literature to describe the mechanical behaviour of unsaturated clayey soils are based on the Barcelona Basic Model (BBM, Alonso et al., 1990) conceptual framework or its extension to double porosity media to enable it to better model expansive clays (BExM, Gens and Alonso, 1992; Alonso et al., 1999). This framework, based on two stress variables, is described in the following parts of the present section.

2.5.2 Barcelona Basic Model

2.5.2.1 General description

The BBM is an extension of the Modified Cam Clay model (Roscoe and Burland, 1968) to unsaturated conditions. The model is meant to describe the mechanical behaviour of low to moderate activity unsaturated soils. It is formulated within the framework of hardening plasticity. The two stress-variable approach is considered. Stress variables in the BBM are the net stress, as defined in 2.5.1.2, and suction. As full saturation is reached, the BBM reduces to a critical state model. A fundamental aspect of the BBM is its ability to reproduce the collapse behaviour of unsaturated soils upon wetting under stress.

The present part provides an overview of the description of the volumetric behaviour in isotropic conditions and the yield surfaces. An overview of the main features of its extension to double porosity media and highly expansive soils is then presented.

A more comprehensive description of the BBM can be found in Alonso et al. (1990). A description of its extension to expansive soils can be found in Alonso et al. (1999) and Sanchez et al. (2005).

2.5.2.2 Volumetric behaviour

The BBM is formulated in the framework of elasto-plasticity. Consequently, the soil volumetric strain is written as:

$$\varepsilon_V = \varepsilon_V^e + \varepsilon_V^p \quad 2-19$$

Where ε_V is the total volumetric strain, corresponding to the trace of the ε tensor (equation 2-18); ε_V^e and ε_V^p are the elastic and plastic part of ε_V , respectively.

Following an increment of mean net stress, \bar{p} , and suction, s , the increment of elastic volumetric strain $d\varepsilon_V^e$ is calculated as:

$$d\varepsilon_V^e = \frac{\kappa_s}{1 + e_0} \frac{ds}{(s + p_{atm})} + \frac{\kappa}{1 + e_0} \frac{d\bar{p}}{\bar{p}} \quad 2-20$$

Where e_0 is the initial void ratio, p_{atm} is the atmospheric pressure, κ and κ_s are elastic stiffness parameters for changes in net stress and suction, respectively. κ and κ_s are considered not to be dependent on suction.

On reaching the preconsolidation pressure, p_0 and the suction yield locus, s_0 , elastoplastic strains may arise following increments of p and s :

$$d\varepsilon_V = \frac{\lambda_s}{1 + e_0} \frac{ds_0}{(s_0 + p_{atm})} + \frac{\lambda(s)}{1 + e_0} \frac{dp_0(s)}{p_0(s)} \quad 2-21$$

Where λ and λ_s are elastoplastic stiffness parameters for changes in net stress and suction, respectively. p_0 and λ are functions of suction. The expression of $p_0(s)$ is given by the Loading-Collapse (LC) curve, described in the following sub-part. $\lambda(s)$ is calculated as:

$$\lambda(s) = \lambda(0) [r + (1 - r) \exp(-\beta s)] \quad 2-22$$

Where r is a constant related to the ratio of $\lambda(s \rightarrow \infty)$ to $\lambda(0)$ and β a model parameter describing the increase of soil stiffness upon suction increase.

From equations 2-19, 2-20 and 2-21, the plastic increment of volumetric strain is obtained:

$$d\varepsilon_V^p = \frac{\lambda_s - \kappa_s}{1 + e_0} \frac{ds_0}{(s_0 + p_{atm})} + \frac{\lambda(s) - \kappa}{1 + e_0} \frac{dp_0(s)}{p_0(s)} \quad 2-23$$

2.5.2.3 Yield surfaces and hardening laws

The BBM considers two yield loci in the plane s - p , for increase in suction and increase in net stress. These latter are denoted SI and LC curves (“*suction increase*” and “*loading collapse*”, respectively). SI does not depend on net stress and is only defined by $s = s_0$. LC is suction-dependent to reproduce the observed increase in apparent preconsolidation pressure with increasing suction in laboratory tests:

$$p_0(s) = p_c \left(\frac{p_0(0)}{p_c} \right)^{\frac{\lambda(s)-\kappa}{\lambda(0)-\kappa}} \quad 2-24$$

Where p_c is a reference stress.

From equations 2-23 and 2-24 the increment of plastic strain following LC yielding, $d\varepsilon_{V LC}^p$, can be written as:

$$d\varepsilon_{V LC}^p = \frac{\lambda(0) - \kappa}{1 + e_0} \frac{dp_0(0)}{p_0(0)} \quad 2-25$$

In the BBM, hardening of SI and LC is controlled by the total increment of plastic strain, thus providing a coupling between the two yield loci. Hardening laws are written:

$$\frac{dp_0(0)}{p_0(0)} = \frac{1 + e_0}{\lambda(0) - \kappa} d\varepsilon_V^p \quad 2-26$$

And

$$\frac{ds_0}{s_0 + p_{atm}} = \frac{1 + e_0}{\lambda_s - \kappa_s} d\varepsilon_V^p \quad 2-27$$

Figure 2-53 presents the two yield loci in the s - \bar{p} plane with an example of hydration path under stress. From state I to state II, an elastic swelling would be computed. From state II to state III an elastic swelling and a plastic collapse, which may overcome the swelling, would be computed. Consequently, LC and SI yield loci undergo hardening.

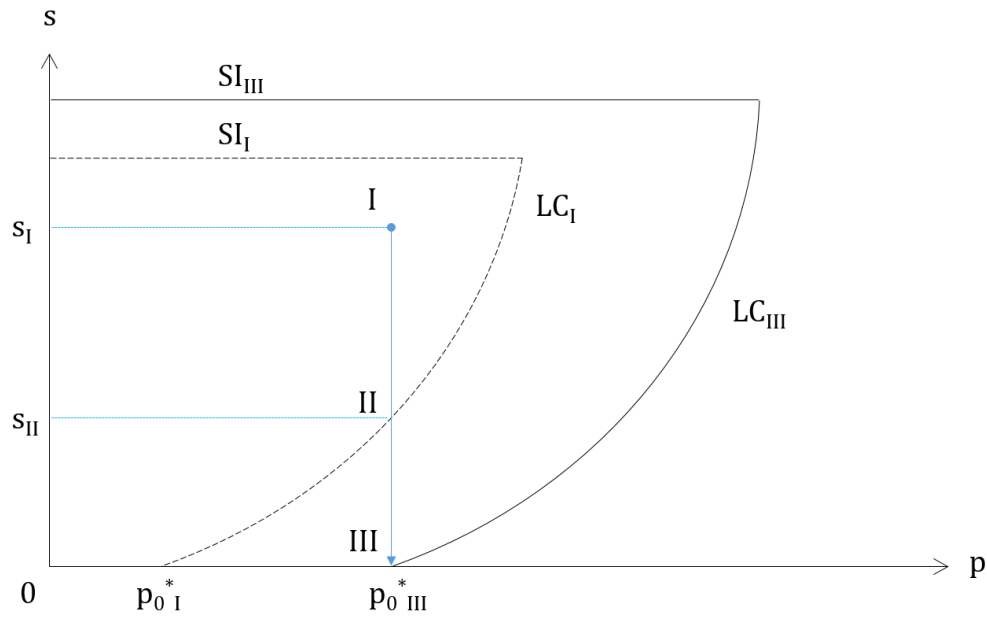


Figure 2-53: Example of stress path in the s - \bar{p} plane and coupling between SI and LC.

2.5.2.4 Modelling the behaviour of compacted expansive materials

The initial formulation of the BBM was not meant to model highly expansive soils. As discussed in previous sections, the double porosity and strong influence of micro-scale phenomena on the macroscopic response of the material are relevant features of these materials.

Gens and Alonso (1992) proposed a conceptual framework to address the modelling of these materials. The mathematical formulation was later provided by Alonso et al. (1999). Comprehensive description can also be found in Sanchez et al. (2005).

The BExM introduces two distinct levels of porosity in the model. The void ratio of the material is written:

$$e = e_m + e_M \quad 2-28$$

Where e_m is the microstructural void ratio, corresponding to intra-aggregate voids, and e_M is the macrostructural void ratio, corresponding to inter-aggregate voids.

In its initial formulation, the BExM proposes to consider the microstructural level to be elastic and described by Bishop's effective stress. Two alternative equations are proposed to describe the volumetric strain of the microstructure:

$$d\varepsilon_{Vm} = d\varepsilon_{Vm}^e = \frac{\kappa_m}{1 + e_{m0}} \frac{dp_m'}{p_m'} \quad 2-29$$

And

$$d\varepsilon_{Vm} = d\varepsilon_{Vm}^e = \beta_m \exp(-\alpha_m p_m') dp_m' \quad 2-30$$

Where κ_m is an elastic stiffness parameter for changes in microstructural effective stress, α_m and β_m are model parameters describing the microstructural stiffness, p_m' is the Bishop effective stress for microstructure.

The macrostructural volumetric behaviour in the BExM is described using BBM equations. LC is defined by equation 2-24. However, the definition of SI is modified and a new yield locus, SD (“*suction decrease*”) is added. In the BExM, macrostructural plastic volumetric strains arise when the microstructural stress state reaches the yield loci SI and SD. The coupling is formulated through interaction functions. Macrostructural plastic volumetric strains induced by microstructural elastic volumetric strains are proportional to these latter. The proportionality coefficient, f , may take either positive or negative values to describe macrostructural swelling or shrinkage as a result of microstructural strains. The total increment of macrostructural plastic volumetric strain is written as follows:

$$d\varepsilon_{VM}^p = f d\varepsilon_{Vm}^e + d\varepsilon_{VLC}^p \quad 2-31$$

Where f is a function of the ratio p/p_0 which depends on the yield locus activated (SI or SD).

This formulation is convenient to reproduce experimental observations such as accumulation of strains upon wetting-drying cycles, stress path dependency, peak phenomenon in swelling pressure tests or macropore intrusion by expanded microstructure. Further information concerning the BExM formulation can be found in Alonso et al. (1999) and Sanchez et al. (2005).

2.5.2.5 Modelling pellet mixtures

Hoffmann et al. (2007), Alonso et al. (2011), Gens et al. (2011), Sanchez et al. (2016) and Mokni et al. (2019) proposed the use of BBM/BExM-based models to describe the behaviour of expansive pellet mixtures.

Main differences between the proposed models were the initial framework (BBM or BExM), thus the consideration of one or two levels of structure. If the BExM is the main framework, models can take into account one suction value (hydraulic equilibrium) or microstructural (s_m) and macrostructural (s_M) suctions (thus inducing water transfer between micro and macrostructure). Plasticity arising on reaching the SD yield locus can be described using interaction functions “ f ” or an elastoplastic stiffness parameter for the microstructure “ λ_m ”, thus inducing plastic strains in the microstructural level (Alonso et al. (2011). Microstructural elastic stiffness can depend on either a constant or suction-dependent parameter κ_m and consider or not a damage parameter to take into account the loss of granular structure (Mokni et al., 2019). An overview of the modelling approaches is presented in Table 2-6.

Table 2-6: Overview of the modelling approach for pellet mixtures in the literature.

Reference	Material	Framework	SD	p_m'	s	Microstructural stiffness
Hoffmann et al. (2007)	Pelletised bentonite	BBM	No micro-macro differences			p : $\frac{1+e}{\kappa(s)}p$ s : $\frac{1+e}{\kappa_s(p,s)}(s+p_{atm})$
Alonso et al. (2011)	Pelletised bentonite	BExM	λ_m	$p + \chi s_m$	$s_m \neq s_M$	$\frac{1+e}{\kappa_m} p'_m$
Gens et al. (2011)	Pellet-powder mixture	BExM	f	$p + s_m$	$s_m \neq s_M$	$\frac{1+e}{\kappa_m} p'_m$
Sanchez et al. (2016)	Pellet-powder mixture	BExM	f	$p + \chi s_m$	$s_m \neq s_M$	$\frac{1+e}{\kappa_m(s_m)} p'_m$
Mokni et al. (2019)	Pellet-powder mixture	BExM	f	$p + s_m$	$s_m = s_M$	$(1-D) \frac{1+e}{\kappa_m} p'_m$ *

* D is a damage coefficient which depends on suction (Mokni et al., 2019).

2.5.3 Description of water retention behaviour and transfer laws

2.5.3.1 Water retention curve

Water retention models in unsaturated soils relate the suction to the water content or to the degree of saturation. The most used in numerical models is based on Van Genuchten (1980) equation:

$$\theta = \theta_r + (\theta_{sat} - \theta_r) [1 + (A h_w)^n]^m \quad 2-32$$

Where θ , θ_r and θ_{sat} are the soil total, residual and saturated volumetric water contents respectively, A , n and m are model parameters, h_w is the water head. Van Genuchten's equation is usually formulated using the degree of saturation instead of volumetric water content and suction instead of water head.

Examples of more advanced models able to describe, for instance, micro/macro degree of saturation or hysteretic water retention behaviour can be found in Della Vecchia et al. (2015), Dieudonné et al. (2017) or Nuth and Laloui (2008).

2.5.3.2 Advective fluxes: Darcy's law

Advective fluxes are usually described using Darcy's law. Darcy's law relates fluid flux to a pressure gradient through a permeability coefficient. Neglecting the contribution of gravity, Darcy's law can be written as:

$$\mathbf{q} = - \frac{k_{int} k_r}{\mu_f} \nabla p_w \quad 2-33$$

Where \mathbf{q} is the flux vector, p_w is the water pressure, k_{int} is the material intrinsic permeability, k_r is the material relative permeability, μ_f is the fluid dynamic viscosity. As previously discussed, k_{int} can be considered a function of porosity. k_r is usually considered a function of the degree of saturation. In unsaturated compacted bentonites, the gradient of suction is commonly used instead of the gradient of water pressure.

2.5.3.3 Diffusive fluxes: Fick's law

Diffusive fluxes are usually described using Fick's law. For vapour diffusion in air, Fick's law can be written as:

$$\mathbf{i}_{vap} = \tau_g \phi S_g D_{vap} \nabla \rho_{vap} \quad 2-34$$

With

$$\rho_{vap} = \frac{M_w}{RT} p_{vap} \quad 2-35$$

Where \mathbf{i}_{vap} is the vapour flux vector, τ_g is the medium tortuosity, ϕ is the porosity, S_g is the degree of saturation of the gas phase, D_{vap} is the coefficient of diffusion of vapour in air, of the order of $\sim 2.7 \cdot 10^{-5} \text{ m}^2/\text{s}$ at 20°C (Philip and de Vries, 1957), ρ_{vap} is the vapour density, M_w is the molar mass of water, R the ideal gas constant, T the thermodynamic temperature and p_{vap} the partial pressure of vapour, deduced from relative humidity.

2.6 PERSPECTIVES REGARDING THE MODELLING OF PELLET-POWDER MIXTURES

2.6.1 Overview of pellet-powder mixtures characteristics

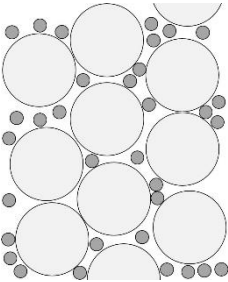
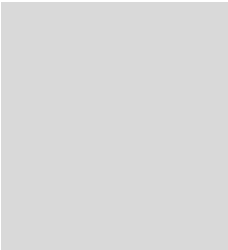
The behaviour of bentonite based materials and particular features related to pellet mixtures have been described in previous sections. In the light of the literature review proposed in the present chapter, pellet materials appear to share features with “non-granular bentonite” materials in addition to particular features related to their granular structure. This final part highlights some key features of pellet-powder mixtures which should be taken into account in the modelling of these materials upon hydration.

As bentonite-based materials, the water retention behaviour of pellet-powder mixtures is characterised by two distinct domains: crystalline and osmotic. Below $\sim 100 \text{ MPa}$ of suction, microporosity is likely to be saturated. Conversely, macroporosity is likely to remain dry until low suction values. The mixture fabric is likely to undergo significant rearrangement at low suction. It is worth mentioning that “low suction” is not straightforwardly defined but, as highlighted in this chapter, the threshold probably is in the range $\sim 3\text{-}7 \text{ MPa}$.

At initial state, the material granular structure controls its mechanical behaviour. Pellet strength and stiffness, intergranular forces, and progressive evolution of these latter in the course of hydration should

be taken into account to properly reproduce the material behaviour. At “low suction”, the granular structure loses its influence on the mechanical behaviour and the mixture is thought to behave as a continuum. An overview of the features influencing the material behaviour is proposed in Table 2-7.

Table 2-7: Overview of the behaviour of pellet-powder mixtures

Material	(Liquid) water retention behaviour	Mixture stiffness	Cause of irreversible strains
 <p>High suction: Granular mixture</p>	<p>Micro: ~saturated Macro: ~dry</p>	<p>Inter-pellet contact interactions</p>	<p><i>i)</i> Grain failure <i>ii)</i> Granular assembly rearrangement <i>iii)</i> Evolution of the bentonite fabric</p>
 <p>Low suction: Continuous material</p>	<p>Micro: ~saturated Macro: ~unsaturated</p>	<p>Double porosity clayey material</p>	<p><i>i)</i> Evolution of the bentonite fabric</p>

2.6.2 Limitations of the existing models

Each of the modelling framework used to describe pellet mixtures upon hydration (see 2.5.2.5) introduced interesting features: Hoffmann et al. (2007) and Sanchez et al. (2016) proposed a suction-dependent stiffness parameter; Alonso et al. (2011) introduced plastic strains for the microstructural (*i.e.* pellets) level; Gens et al. (2011), Alonso et al. (2011), Sanchez et al. (2016) introduced water transfer between macropores and pellets; Mokni et al. (2019) introduced a damage coefficient to model the progressive loss of stiffness of pellets. All these features are consistent with the experimental results on granular bentonites. Still, aforementioned modelling frameworks do not explicitly take into account the granular structure of the material. In the suction range controlled by the granular structure, the material average dry density is heterogeneous: pellets density is much higher than the powder filling inter-pellet voids. Experimental results have highlighted the difficulty to prepare homogeneous samples because of powder migration during preparation. Upon hydration under constant-volume conditions, considering that the loose powder phase is hydrated under the same conditions as the pellet assembly is not straightforward.

The main perspective arising is therefore the characterisation of the influence of pellet and powder on the macroscopic behaviour at different hydration states and the proposition of constitutive laws able to reproduce the material behaviour.

2.6.3 Proposition of an experimental and numerical program

The relative influence of pellet phase and powder phase in the macroscopic response during hydration has to be studied to understand and model the behaviour of pellet-powder mixtures. In this way, the description of the material behaviour and eventual local heterogeneities of powder content could be explicitly addressed. Suction-controlled swelling pressure tests performed on samples with varying powder content can be performed for this purpose.

Modelling pellet mixtures at high suction using Discrete Element Method (DEM) can provide an insight into the influence of intergranular interaction on the macroscopic response of the material. The DEM model can be validated against the aforementioned swelling pressure test. Numerical results could help to identify relevant material parameters to introduce in a constitutive model. Pellet scale experimental characterisation can be performed to obtain grain parameters in the simulations.

Hydration kinetics has been shown to significantly influence the material behaviour. In addition, the transition from “granular” behaviour to “continuous” behaviour is likely to be influenced by hydration kinetics. Hydration mock-up test can be performed, using bottom infiltration only to avoid significant water flow in the macroporosity (unrealistic with respect to the French concept repository conditions).

The final perspective is the proposition, implementation and validation of a HM-coupled constitutive model taking into account the initial granular structure and local heterogeneities of density. It is the main objective of the present work.

3 SUCTION-CONTROLLED SWELLING PRESSURE TESTS

3.1 INTRODUCTION

In repository conditions, the behaviour of pellet-based engineered barrier is thought to be controlled by its granular structure in the first stages of hydration. Hydration in repository concepts involving a clayey host rock is slow and mainly controlled by vapour transfer. Heterogeneities of powder content can be expected following installation of pellet-powder based engineered barriers. The literature review presented in the previous chapter highlighted the lack of data concerning the influence of the granular structure and powder content on the mechanical behaviour of bentonite pellet-powder mixtures upon vapour hydration.

In this work, swelling pressure tests are considered as an appropriate testing procedure to study the behaviour of a representative elementary volume since hydration conditions are close to those experienced by the barrier in repository conditions. Laboratory-scale swelling pressure tests on pellet-based bentonite materials have been carried out by Hoffmann et al. (2007). It was suggested that interactions at contacts have a significant influence on the material behaviour. However, inter-pellet voids in these tests were not filled with powder. Imbert and Villar (2006) performed swelling pressure tests on pellet-powder mixture. No influence of the granular structure was evidenced, but hydration was performed by flooding samples using liquid water in small cells. It is therefore not known if the absence of observed influence of the granular structure is a consequence of the hydration method or if the powder indeed inhibited the influence of the granular structure.

In this chapter, suction-controlled swelling pressure tests performed in the laboratory are presented. Hydration is performed using the vapour equilibrium technique. Slow vapour phase hydration is considered closer to repository conditions. Three different mixtures are tested to assess the influence of the powder content. The main objectives of this experimental work are:

- Study the influence of the granular structure on the macroscopic response upon hydration;
- Study the influence of powder content to assess the influence of powder content heterogeneities in repository conditions;
- Compare obtained results with results on compacted blocks and assess the influence of bentonite microstructure on the macroscopic response;
- Determine the material final swelling pressure to assess the validity of estimations provided in the literature.

Tested material and different mixtures are presented in part 3.2. Description of the experimental methods and sample preparation constitute part 3.3. Experimental results are then presented in part 3.4. These latter are discussed in part 3.5. Finally, conclusions and perspectives arising from this experimental work and interpretations of its results constitute part 3.6.

3.2 MATERIAL

The materials used in the suction-controlled swelling pressure test are MX80 pellet-powder mixtures. Three different mixtures are tested. All mixtures contained the same absolute dry mass of pellets and different powder contents.

3.2.1 Bentonite pellets

Pellets are obtained from MX80 bentonite powder by pressure casting (compaction in a mould). Granules are composed of a central cylinder-shaped part and two spherical caps at both ends (Figure 3-1).

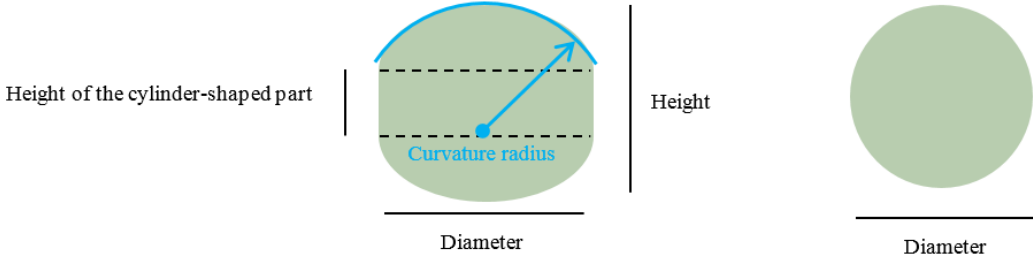


Figure 3-1: Diagram of the pellets used in the present work. Left: radial view, right: axial view

Table 3-1 summarises pellet initial geometrical properties. Pellets initial suction, s_i , is measured using a WP4 dew point potentiometer from Decagon. Initial gravimetric water content, w_i , is obtained by oven drying. For MX80 pellets used in the present study, $s_i = 89$ MPa and $w_i = 0.12$. Initial dry density, ρ_{d0} , is obtained from the paraffin wax method (Molinero-Guerra et al., 2019a) and initial void ratio, e_0 , is deduced by considering a particle density ρ_s of 2.77 (Saba et al., 2014b). These physical properties are summarised in Table 3-2. A picture of a pellet assembly is presented in Figure 3-2.

Table 3-1: Pellet geometrical properties at initial state.

Geometrical property at initial state	Value
Diameter	7 mm
Height of the cylinder-shaped part	5 mm
Height	7 mm
Curvature radius	6.5 mm

Table 3-2: Pellet physical properties at initial state.

Physical property at initial state	Value
Suction	89 MPa
Water content	0.12
Dry density	1.91 Mg/m ³
Void ratio	0.45



Figure 3-2: Assembly of the MX80 pellets used in the present work.

3.2.2 Bentonite powder

The material referred to as “powder” in the present study is obtained by crushing pellets. It is therefore composed of the same material as pellets. Its initial suction and water content are obtained using a WP4 dew point potentiometer from Decagon and oven-drying respectively. Initial suction and water content of the powder are $s_{i\text{pow}} = 185$ MPa and $w_{i\text{pow}} = 0.035$.

3.2.3 Pellet-powder mixtures

The material used in swelling pressure tests is a bentonite pellet-powder mixture. Bentonite pellet-powder mixture is a candidate material for the sealing plugs preventing fluid migrations in the French concept of radioactive waste disposal. The dry density of the candidate material and its dry mass proportion of pellets and powder are 1.50 Mg/m³ and 70/30, respectively.

In the present work, three different pellet-powder mixtures are used in suction-controlled swelling pressure tests to determine the influence of the pellet assembly on the mixture mechanical behaviour. On the other hand, the influence of powder content on the mixture behaviour can be assessed. Heterogeneity of powder content may indeed arise in repository conditions as a consequence of either an imperfect laying or particle segregation.

The three tested materials have the same pellet dry mass and different powder dry masses. These three different mixtures are referred to as “70/30”; “70/15” and “70/0” in the following. Mixtures properties are summarised in the following sub-parts.

3.2.3.1 70/30 pellet-powder mixture

The 70/30 mixture is composed of 70 % pellets in dry mass and 30 % powder in dry mass. It was mentioned in previous part that pellets and powder do not have the same initial water content. Mixture are prepared taking into account the water content. 70/30 is thus related to dry state and not to initial state. The sample average dry density is 1.50 Mg/m^3 .

3.2.3.2 70/15 pellet-powder mixture

The 70/15 mixture is composed of ~82 % pellets in dry mass and 18 % powder in dry mass. The dry mass of pellets in the 70/15 mixture is the same as in the 70/30 mixture. The dry mass of powder in the 70/15 mixture is half the dry mass of powder of the 70/30 mixture. The sample average dry density is 1.275 Mg/m^3 .

3.2.3.3 70/0 pellet-powder mixture

The 70/0 mixture is a pellet assembly. No powder is laid in the sample. The dry mass of pellets in the 70/0 mixture is the same as the 70/30 mixture. The sample average dry density is 1.05 Mg/m^3 .

3.3 SUCTION-CONTROLLED SWELLING PRESSURE TESTS

Suction-controlled swelling pressure tests are performed at room temperature in isochoric cells. In this part, the experimental apparatus and protocol are described.

3.3.1 Isochoric cell

Cylindrical isochoric cells made of stainless steel (X17CrNi16-2 steel) are used to perform swelling pressure tests. Swelling pressure in the present work is determined as the vertical axial pressure developed by the material upon hydration in a constant-volume cylinder cell. A total pressure sensor (BER-A-5MP15S from Kyowa, capacity of 5 MPa) is placed at the centre of the upper wall. Two porous disks are placed at the top and bottom of the cell. A diagram of the cell is presented in Figure 3-3. A picture is presented in Figure 3-4. The cell dimensions are summarised in Table 3-3.

The dimensions of the cell and pressure sensor, normalised using the initial pellet diameter, are the following:

- Cell height to pellet initial diameter = ~4.3;
- Cell diameter to pellet initial diameter = ~8.6;
- Sensor diameter to pellet initial diameter = ~4.3.

Since pellets are not perfectly spherical, these values only provide a general overview of the order of magnitude of the dimension ratio.

Table 3-3: Dimensions of the cell and sensor used in swelling pressure tests.

Dimensions	
<i>Cell</i>	
Height: mm	30
Diameter: mm	60
<i>Sensor</i>	
Diameter: mm	30

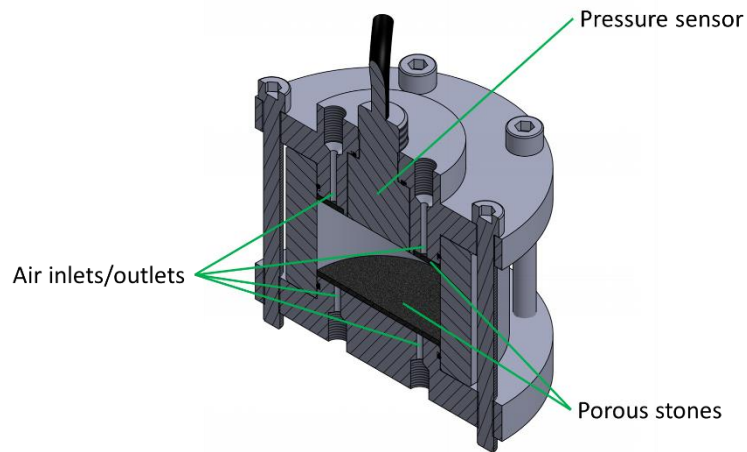


Figure 3-3: Diagram of the isochoric cell designed for swelling pressure tests.

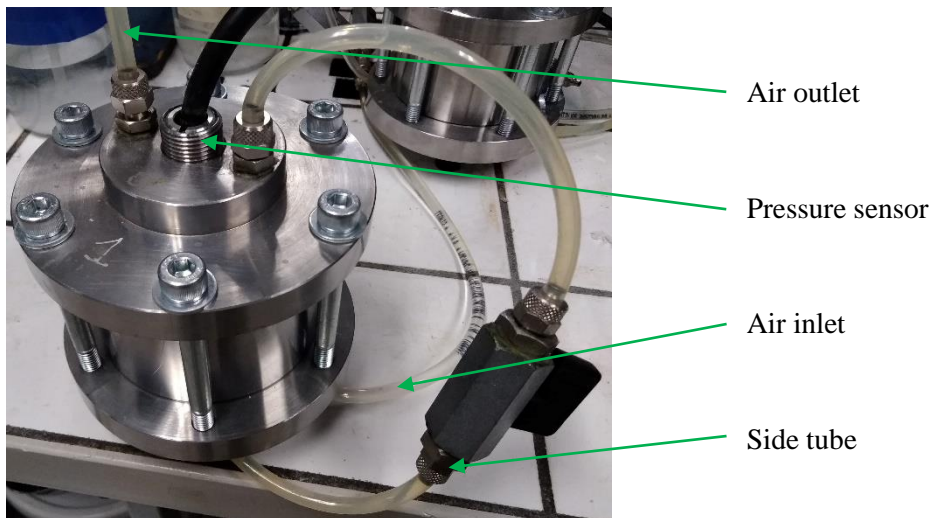


Figure 3-4: Picture of the isochoric cell used for swelling pressure tests.

3.3.2 Preparation of the samples

3.3.2.1 Preparation protocol

Molinero-Guerra et al. (2017) highlighted that the sample heterogeneities are influenced by its preparation. In the present work, Molinero-Guerra et al. (2017) third protocol is adopted to prepare the samples. Pellet are placed one by one in the cell to form a layer, then the proportion of powder associated to the laid proportion of pellet is poured in the inter-pellet voids.

3.3.2.2 Determination of pellet and powder mass

Pellet and powder initial water contents are different. In this respect, initial mass ratio and dry mass ratio are slightly different. For each type of mixture, the pellet and powder mass is determined from their respective water content following this protocol:

- estimation of the inter-pellet-porosity;
- estimation of the pellet initial mass;
- estimation of the powder average dry density;
- estimation of the powder initial mass.

Inter-pellet porosity, ϕ_{int} is determined as follows:

$$\phi_{int} = 1 - \frac{\rho_d^*}{\rho_{d0}} \quad 3-1$$

Where ρ_d^* is the mixture average dry density, given in 3.2.3 for the three mixtures, ρ_{d0} is the pellet initial dry density.

Pellet mass to introduce in the cell, m_{pel} , is then obtained as follows:

$$m_{pel} = (1 - \phi_{int}) (1 + w_i) \rho_{d0} \Omega \quad 3-2$$

Where w_0 is the pellet initial water content, Ω is the sample total volume.

The powder in the inter-pellet porosity can be considered to occupy all the available space to determine an averaged dry density of the powder phase:

$$\rho_{d\ mat} = x_{S0} \frac{\rho_d^*}{\phi_{int}} \quad 3-3$$

Where $\rho_{d\ mat}$ is the “matrix” average dry density (*i.e.* the ratio of dry mass of powder to inter-pellet void volume), $x_{s\ 0}$ is the target mass proportion of powder in the sample.

Powder mass to introduce in the cell, m_{pow} , is then obtained as follows:

$$m_{pow} = \phi_{int} (1 + w_{i\ pow}) \rho_{d\ mat} \Omega \quad 3-4$$

Table 3-4 summarises the mass of pellets and powder required to prepare the three different mixtures.

Table 3-4: Pellet and powder mass laid in the cell to prepare the samples.

Mixture	Pellet mass: g	Powder mass: g
70/30	99.9	39.5
70/15	99.9	19.75
70/0	99.9	0

3.3.2.3 Cell closure

The cell is closed after the mixture preparation. All samples have the same dimensions. In some samples, an initial pressure develops after reaching the target height. The initial pressure is in the range of 0.004-0.145 MPa.

3.3.2.4 Characteristics of the samples prepared

Five samples are prepared using the protocol described in the previous sub-parts. Table 3-5 summarises the initial features of these latter.

Table 3-5: Summary of the characteristics of the suction-controlled swelling pressure tests performed in the laboratory.

Sample	Mixture	Average dry density: Mg/m ³	Pellet volume fraction: dimensionless	Matrix dry density: Mg/m ³	Initial pressure: MPa
SP30a	70/30	1.50		1.00	0.004
SP15a	70/15	1.275		0.50	0.145
SP15b	70/15	1.275	0.55	0.50	0.015
SP0a	70/0	1.05		0	0.055
SP0b	70/0	1.05		0	0.010

3.3.3 Suction-controlled hydration at constant room temperature

Hydration is performed step by step through the vapour equilibrium technique (Lloret et al., 2003; Tang and Cui, 2005; Hoffmann et al., 2007) from initial state to either 4 MPa or 9 MPa of suction. Salt solutions used in the study are listed in Table 3-6 along with their corresponding suction values. Hydration paths followed by all the samples are listed in Table 3-7.

A peristaltic pump makes air circulate through the salt solution to maintain a constant target relative humidity, then through the isochoric cell. Humid air is allowed to circulate directly from the bottom to the top of the cell through a side tube. Thus, no excessive air pressure is developed when using the peristaltic pump and humid air is considered to circulate freely inside the inter-pellet porosity (Figure 3-4, Figure 3-5). Room temperature is controlled and kept constant ($20^{\circ}\text{C} \pm 1^{\circ}\text{C}$).

During hydration, the apparent swelling pressure measured by the axial sensor is constantly recorded. Equilibrium is considered reached when the pressure measured by the sensor remains constant for a minimum of 3 days. The current salt solution is then replaced by the subsequent one (Table 3-6) to impose the next relative humidity step. The final pressure value is used to draw the suction-swelling pressure relationship.

Following the equilibrium at the lowest suction, the sample is wetted using synthetic water of similar chemical composition as Bure Underground Research Laboratory (URL) pore water. Wetting is performed from top and bottom to accelerate the process.

Table 3-6: Salt solutions used for vapour equilibrium technique.

	Solution	Suction at 20°C : MPa
Mg(NO ₃) ₂	Magnesium nitrate	82
NH ₄ NO ₃	Ammonium nitrate	59
NaNO ₃	Sodium nitrate	40
NaCl	Sodium chloride	38
(NH ₄) ₂ SO ₄	Ammonium sulphate	25
Na ₂ CO ₃	Sodium carbonate	13
KNO ₃	Potassium nitrate	9
K ₂ SO ₄	Potassium sulphate	4

Table 3-7: Hydration paths followed by the samples.

Sample	I	II	III	IV	V	VI	VII	VIII
SP30a	82	59	40	25	13	9	4	0*
SP15a	82	59	40	38	25	13	9	-
SP15b	82	59	40	25	9	4	0*	-
SP0a	82	59	40	38	25	13	9	-
SP0b	82	59	40	25	9	4	0*	-

* samples wetted using liquid water

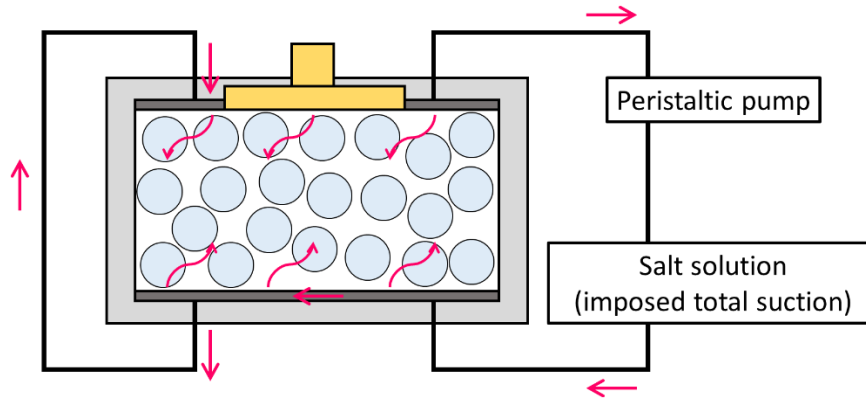


Figure 3-5: Sketch of the suction-controlled system. Red arrows represents humid air circulation.

Samples SP0a and SP15a are opened following the final vapour hydration step to determine their real suction, water content and observe the evolution of the initial granular structure of the pellet assembly. SP0b is opened to observe the granular structure and closed immediately to perform the final liquid wetting. Only the final swelling pressure is of interest for the final hydration path. The opening/closure step is not considered to affect the final swelling pressure as the dry density remains identical.

3.4 EXPERIMENTAL RESULTS

The experimental protocol described in the previous section allows the development of swelling pressure upon decreasing suction to be studied.

The present section presents experimental results obtained using this protocol. Evolution of swelling pressure as a function of elapsed time and identification of the equilibrated swelling pressure at each hydration step constitutes part 3.4.1. Suction-swelling pressure relationships for each of the five tests are then presented in part 3.4.2. State of the samples following dismantling is then presented in part 3.4.3.

3.4.1 Evolution of swelling pressure as a function of elapsed time

The evolution of the swelling pressure is measured as a function of elapsed time. Following a change of imposed suction value (start of new hydration step), the pressure increases (or decreases), then reaches a plateau. A new suction value is then imposed. As highlighted in experimental results presented in the following sub-parts, some pressure fluctuations are measured. It is thought to be related to the experimental conditions. Room temperature and humidity variations, slight voltage variations in the measurement apparatus, or opening of the bottle containing salt solutions for cleaning (thus temporary modifying the imposed suction), are examples of external perturbations thought to influence the measurements. Regular cleaning of the bottle was actually compulsory as salt crystallising on the bottle side would increase the suction, and salt crystallising inside the tube plunged in the solution would prevent the air circulation.

The present part is divided in five sub-parts, each sub-part corresponding to one suction-controlled swelling pressure test (see Table 3-5). The evolution of swelling pressure as a function of elapsed time is presented along with the transition from one hydration step to the following one.

3.4.1.1 SP30a results

SP30a sample is a 70/30 pellet/powder mixture. Hydration for this sample is performed by imposing the following suction steps: Initial state; 82 MPa; 59 MPa; 40 MPa; 25 MPa; 13 MPa; 9 MPa; 4 MPa; 0 MPa (liquid water).

Evolution of swelling pressure as a function of elapsed time for SP30a test is presented in Figure 3-6. Dashed lines separate hydration steps. I, II, III, IV, V, VI, VII, and VIII correspond to the hydration path described in Table 3-7.

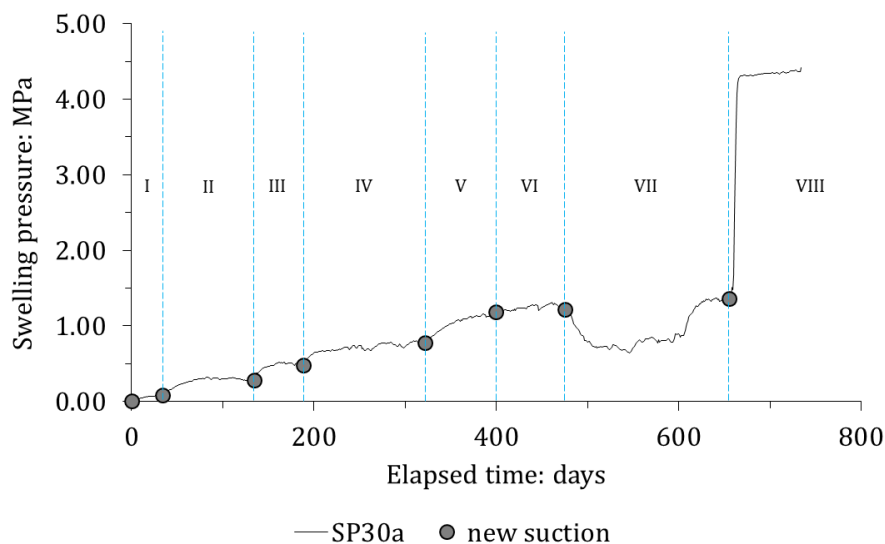


Figure 3-6: Swelling pressure as a function of elapsed time for test SP30a. The dots on the solid line are the values considered at equilibrium.

Following the cell closure, SP30a initial pressure was 0.004 MPa. Equilibrium then required ~35; ~100; ~55; ~135; ~80; ~75 and ~180 days on imposing suction values of 82; 59; 40; 25; 13; 9 and 4 MPa, respectively.

Hydration steps I to VI were all characterised by an increase then stabilisation of the measured swelling pressure. Hydration step VII (imposed suction 4 MPa from equilibrium at 9 MPa) was characterised by a notable decrease of the measured swelling pressure from 1.220 MPa to 0.65 MPa, followed by an increase to 1.362 MPa.

Hydration step VIII (liquid water hydration from equilibrium at 4 MPa) was characterised by a significant and fast increase of the measured swelling pressure from 1.35 MPa to ~4.3 MPa, followed by a much slower increase/plateau. At 735 days, the measured swelling pressure was 4.45 MPa. The trend suggests that equilibrium still is not reached, but increase of swelling pressure is very slow.

3.4.1.2 SP15a results

SP15a sample is a 70/15 pellet/powder mixture. Hydration for this sample is performed by imposing the following suction steps: Initial state; 82 MPa; 59 MPa; 40 MPa; 38 MPa; 25 MPa; 13 MPa and 9 MPa.

Evolution of swelling pressure as a function of elapsed time for SP15a test is presented in Figure 3-7.

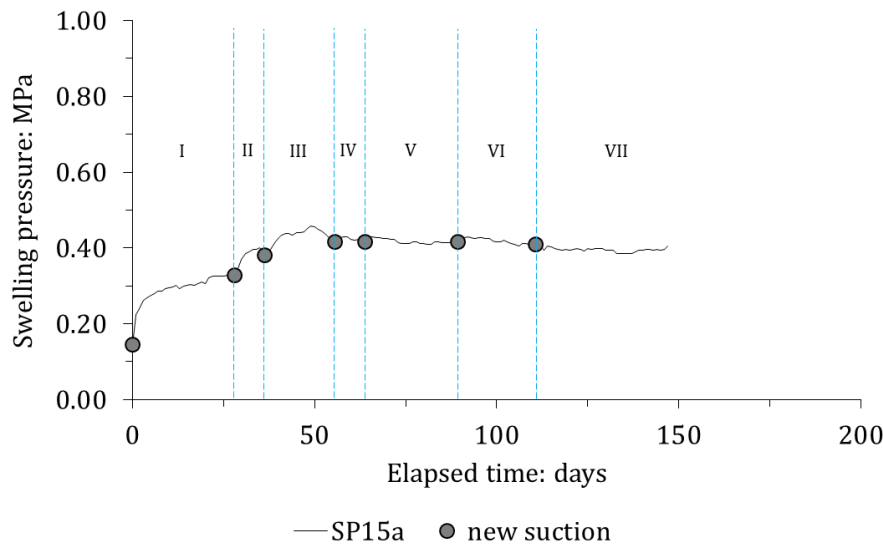


Figure 3-7: Swelling pressure as a function of elapsed time for test SP15a. The dots on the solid line are the values considered at equilibrium. Dashed lines separate hydration steps (Table 3 7).

Following the cell closure, SP15a initial pressure was 0.145 MPa. Equilibrium then required ~30; ~10; ~20; ~10; ~25; and ~20 days on imposing suction values of 82 MPa; 59 MPa; 40 MPa; 38 MPa; 25 MPa; 13 MPa and 9 MPa; respectively.

Hydration steps I to III were characterised by an increase then stabilisation of the measured swelling pressure. Hydration steps IV to VII were characterised constant/slightly decreasing swelling pressure. At 40 MPa of suction, the apparent swelling pressure was 0.417 MPa (*i.e.* net increase of 0.272 MPa compared to initial state). At 9 MPa of suction, the apparent swelling pressure was 0.413 MPa.

3.4.1.3 SP15b results

SP15a sample is a 70/15 pellet/powder mixture. Hydration for this sample is performed by imposing the following suction steps: Initial state; 82 MPa; 59 MPa; 40 MPa; 25 MPa; 9 MPa; 4 MPa and 0 MPa (liquid water).

Evolution of swelling pressure as a function of elapsed time for SP15b test is presented in Figure 3-8.

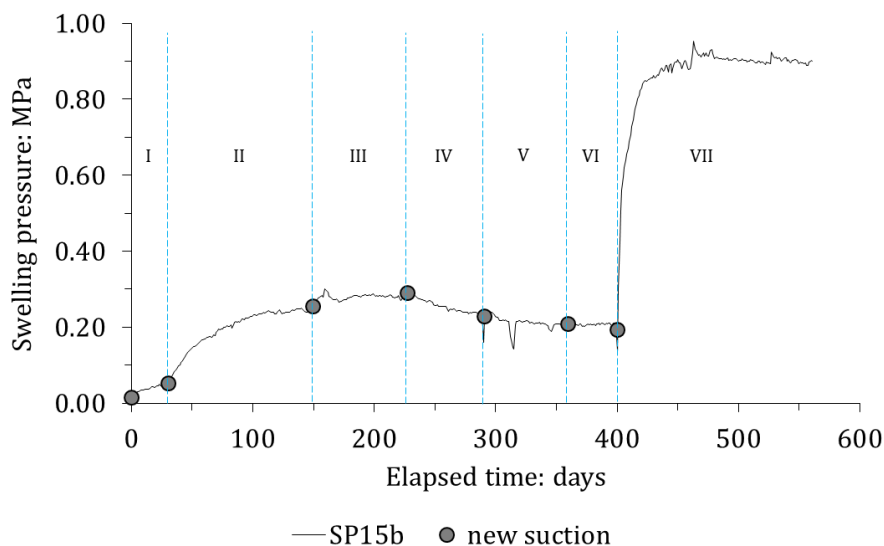


Figure 3-8: Swelling pressure as a function of elapsed time for test SP15b. The dots on the solid line are the values considered at equilibrium. Dashed lines separate hydration steps (Table 3 7).

Following the cell closure, SP15b initial pressure was 0.015 MPa. Equilibrium then required ~30; ~120; ~80; ~60; ~70; and ~40 days on imposing suction values of 82 MPa; 59 MPa; 40 MPa; 25 MPa; 9 MPa and 4 MPa; respectively.

Hydration steps I to III were characterised by an increase then stabilisation of the measured swelling pressure. Hydration steps IV to VI were characterised constant/slightly decreasing swelling pressure. At 40 MPa of suction, the apparent swelling pressure was 0.291 MPa (*i.e.* net increase of 0.276 MPa compared to initial state). At 4 MPa of suction, the apparent swelling pressure was 0.195 MPa.

Hydration step VII (liquid water hydration from equilibrium at 4 MPa) was characterised by a significant and fast increase of the measured swelling pressure from 0.195 MPa to ~0.9 MPa, followed by a plateau. At 560 days, the measured swelling pressure was 0.902 MPa. The trend suggests that equilibrium still is not reached, but the pressure variations are very slow.

3.4.1.4 SP0a results

SP0a sample is a pellet assembly with no powder filling the inter-pellet macroporosity. Hydration for this sample is performed by imposing the following suction steps: Initial state; 82 MPa; 59 MPa; 40 MPa; 38 MPa; 25 MPa; 13 MPa and 9 MPa.

Evolution of swelling pressure as a function of elapsed time for SP0a test is presented in Figure 3-9. Following the cell closure, SP0a initial pressure was 0.055 MPa. Equilibrium then required ~30; ~10; ~20; ~20; ~15; ~25 and ~30 days on imposing suction values of 82; 59; 40; 38; 25; 13 and 9 MPa, respectively.

Hydration steps I to III were characterised by an increase then a stabilisation of the measured swelling pressure. Hydration steps IV to VII were characterised by a constant or decreasing swelling pressure. At 40 MPa of suction, the apparent swelling pressure was 0.173 MPa (*i.e.* net increase of 0.118 MPa compared to initial state). At 9 MPa of suction, the apparent swelling pressure was 0.128 MPa.

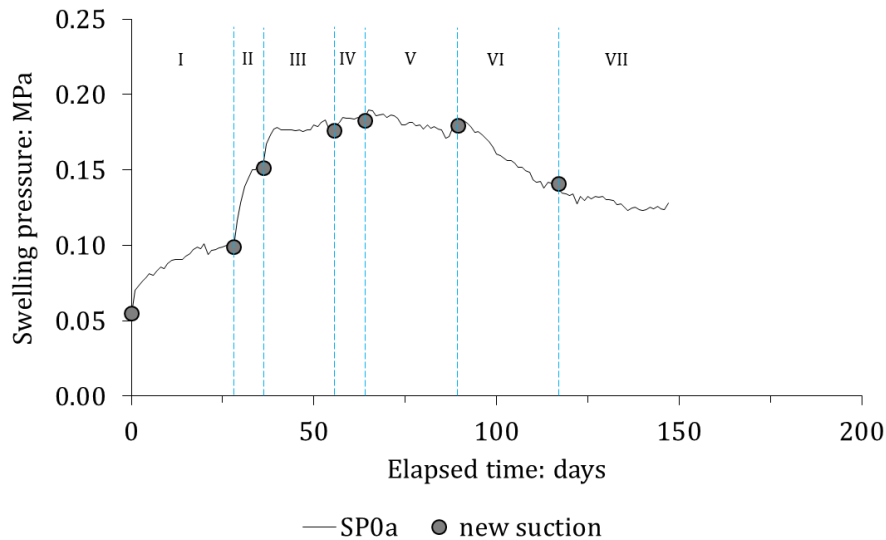


Figure 3-9: Swelling pressure as a function of elapsed time for test SP0a. The dots on the solid line are the values considered at equilibrium. Dashed lines separate hydration steps (Table 3 7).

3.4.1.5 SP0b results

SP0b sample is a pellet assembly with no powder filling the inter-pellet macroporosity. Hydration for this sample is performed by imposing the following suction steps: Initial state; 82 MPa; 59 MPa; 40 MPa; 25 MPa; 9 MPa; 4 MPa and 0 MPa (liquid water).

Evolution of swelling pressure as a function of elapsed time for SP0b test is presented in Figure 3-10. Following the cell closure, SP0b initial pressure was 0.010 MPa. Equilibrium then required ~30; ~120; ~80; ~75; ~30 and ~60 days on imposing suction values of 82; 59; 38; 25; 9 and 4 MPa, respectively.

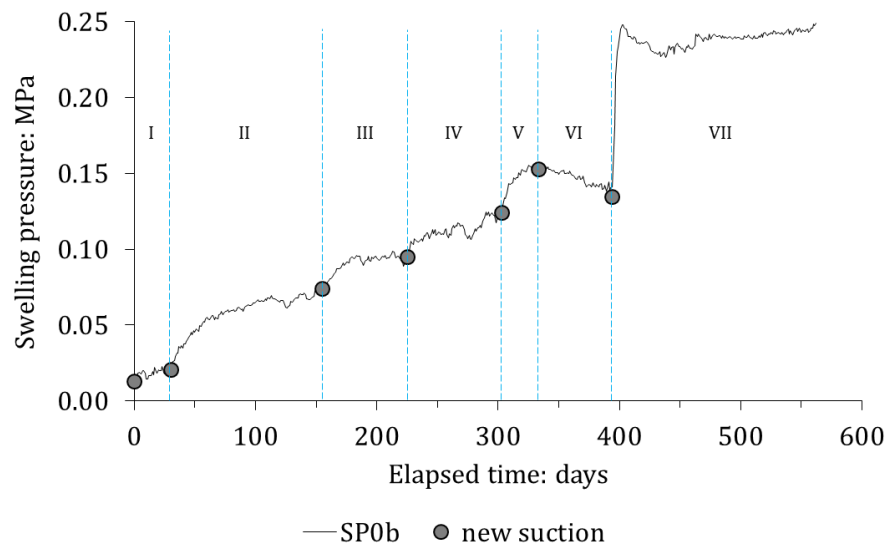


Figure 3-10: Swelling pressure as a function of elapsed time for test SP0b. The dots on the solid line are the values considered at equilibrium. Dashed lines separate hydration steps (Table 3 7).

Hydration steps I to V were characterised by an increase followed by a stabilisation of the measured swelling pressure. Hydration step VI (imposed suction 4 MPa from equilibrium at 9 MPa) was characterised by a decrease then stabilisation of the swelling pressure. At 9 MPa of suction, the apparent swelling pressure was 0.153 MPa. At 4 MPa of suction, the apparent swelling pressure was 0.135 MPa.

Hydration step VII (liquid water hydration from equilibrium at 4 MPa) was characterised by a significant and fast increase of the measured swelling pressure from 0.135 MPa to ~0.25 MPa, followed by a peak then a second increase and a plateau. After 560 days, the measured swelling pressure was 0.249 MPa. The trend suggests that equilibrium still is not reached, but the pressure variations are very slow.

3.4.2 Suction-swelling pressure relationship

For each suction value, the equilibrium (plateau) value is retained as the corresponding swelling pressure. In Figure 3-6 to Figure 3-10, the dots plotted on the solid lines correspond to the value of swelling pressure associated to the suction imposed during the previous step.

The present part is divided in five sub-parts, each sub-part corresponding to one suction-controlled swelling pressure test (see Table 3-5). The evolution of swelling pressure as a function of decreasing suction is presented.

Initial state in the following sub-parts is plotted at 89 MPa of suction. It is indeed right for 70/0 samples. However, samples containing powder may have a slightly higher initial suction as 15 % to 30 % (in dry mass proportion) are MX80 powder, the initial suction of which was found to be ~185 MPa. However, experimental data presented in Chapter 6 suggest that suction at initial state in these cases is not higher than 95 MPa.

Suction-swelling pressure relationships are plotted in a semi-logarithmic plane. Zero-suction in the following is plotted at 0.1 MPa.

3.4.2.1 SP30a results

Evolution of swelling pressure during hydration is presented in Figure 3-11. Swelling pressure and suction used to plot Figure 3-11 are summarised in Table 3-8.

The swelling pressure in SP30a test was found to increase continuously when suction decreased from the initial state to 13 MPa. Between 13 MPa and 9 MPa of suction, the swelling pressure slightly increased from 1.188 MPa to 1.220 MPa. Between 9 MPa and 4 MPa of suction, the swelling pressure decreased then increased again. At equilibrium, in the swelling pressure-suction semi-logarithmic plane, this transient behaviour is not represented. The swelling pressure increase between 13 MPa and 4 MPa is however much slower than at higher suction. The swelling pressure following water flooding is plotted at 4.45 MPa. It is worth mentioning that results from Figure 3-6 suggest that the swelling pressure (following the water flooding step) may not be equilibrated yet.

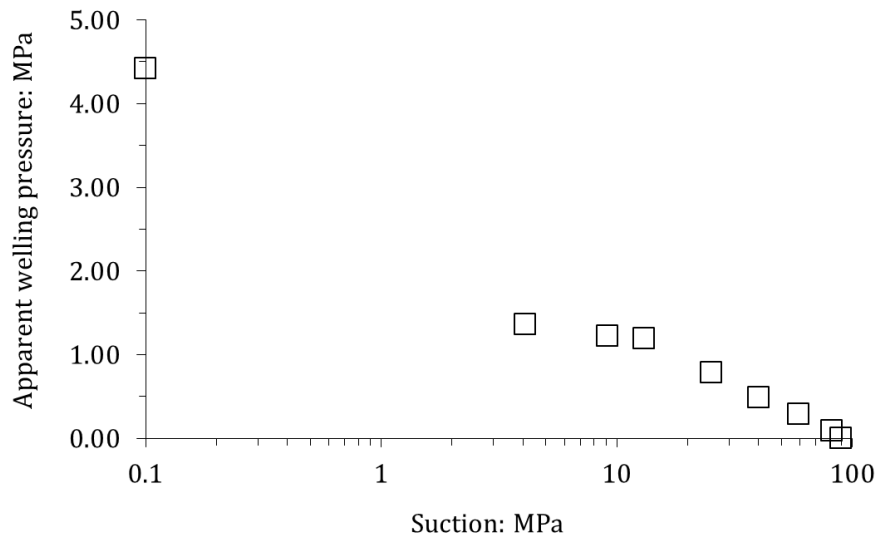


Figure 3-11: Swelling pressure as a function of decreasing suction for test SP30a.

3.4.2.2 SP15a results

Following cell closure, SP15a sample initial pressure was 0.145 MPa. Upon hydration, the swelling pressure was found to increase during the first hydration step (imposed suction 82 MPa). Then, apparent swelling pressure only slightly increased or remained constant when suction decreased to 13 MPa. Slight decrease of swelling pressure is measured on imposing a suction of 9 MPa.

Evolution of swelling pressure during hydration is presented in Figure 3-12. Swelling pressure and suction used to plot Figure 3-12 are summarised in Table 3-8.

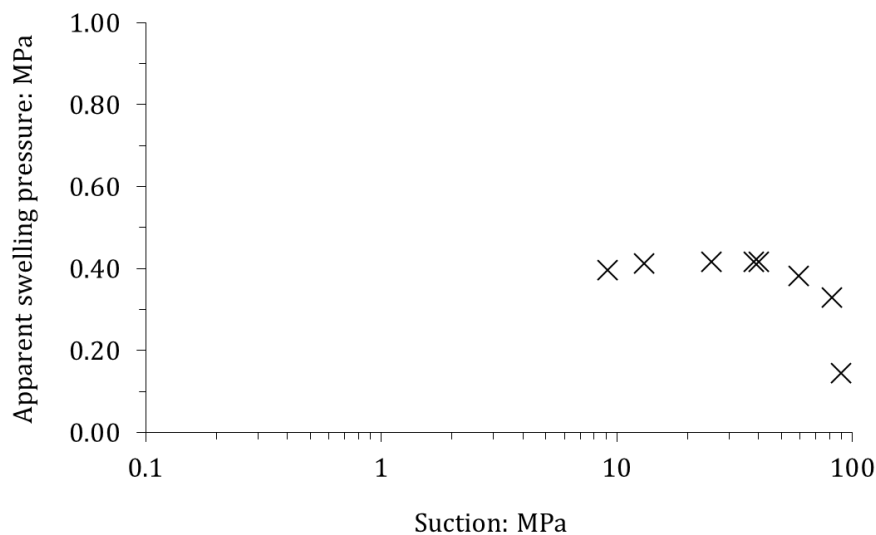


Figure 3-12: Swelling pressure as a function of decreasing suction for test SP15a.

3.4.2.3 SP15b results

Evolution of swelling pressure during hydration is presented in Figure 3-13. Swelling pressure and suction used to plot Figure 3-13 are summarised in Table 3-8.

The initial pressure of SP15b was 0.015 MPa after the cell closure. Upon hydration, swelling pressure was found to increase from 0.015 MPa to 0.291 MPa from initial state to a suction of 40 MPa. Then swelling pressure slightly decreased and reached 0.190 MPa as suction reached 4 MPa. Upon liquid water flooding, the swelling pressure sharply increased to reach 0.902 MPa. Results of Figure 3-8 suggest that the swelling pressure (following the water flooding step) may not be at its final value yet.

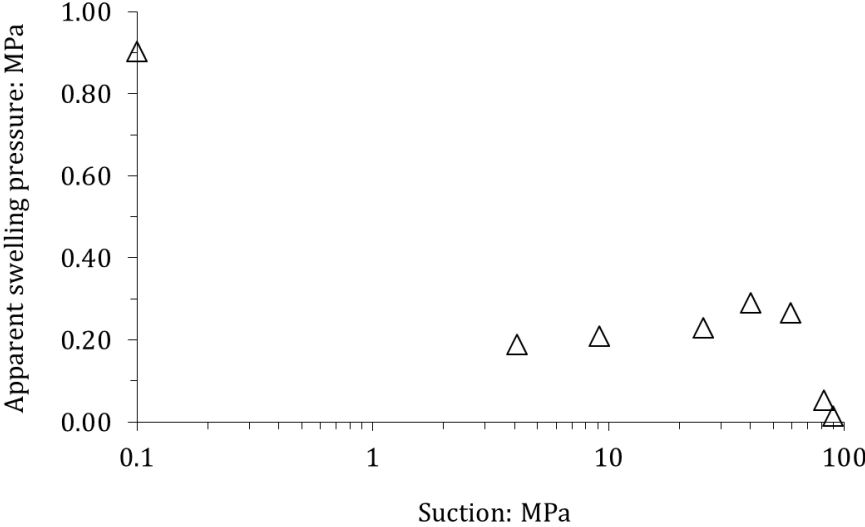


Figure 3-13: Swelling pressure as a function of decreasing suction for test SP15b.

3.4.2.4 SP0a results

Evolution of swelling pressure during hydration is presented in Figure 3-14. Swelling pressure and suction used to plot Figure 3-14 are summarised in Table 3-8.

The initial pressure of sample SP0a was 0.055 MPa following cell closure. Upon hydration, two phases of swelling pressure evolution are observed. From initial state to an imposed suction of 40 MPa, swelling pressure increased from 0.055 MPa to 0.173 MPa. Then, swelling pressure remained nearly constant until 25 MPa of suction and decreased to reach 0.128 MPa as suction reached 9 MPa.

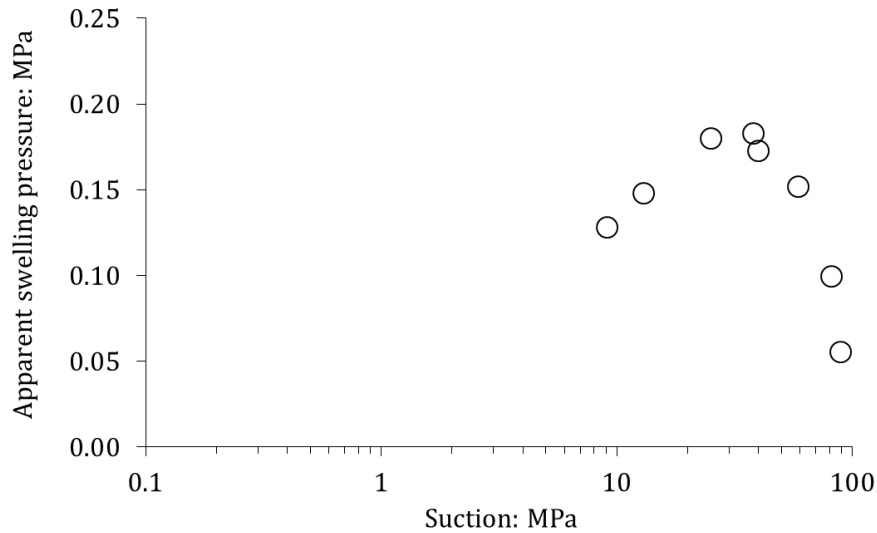


Figure 3-14: Swelling pressure as a function of decreasing suction for test SP0a.

3.4.2.5 SP0b results

Evolution of swelling pressure during hydration is presented in Figure 3-15. Swelling pressure and suction used to plot Figure 3-15 are summarised in Table 3-8.

The initial pressure of sample SP0a was 0.010 MPa following cell closure. Upon hydration at suction higher than 4 MPa, two phases of swelling pressure evolution are also observed. From initial state to an imposed suction of 9 MPa, swelling pressure increased from 0.010 MPa to 0.153 MPa. Then, swelling pressure decreased to reach 0.135 MPa as suction reached 4 MPa. Upon water flooding, the swelling pressure sharply increased to ~0.249 MPa. The collapse observed in Figure 3-10 is a transient phenomenon and therefore is not observable on the suction-swelling pressure relationship.

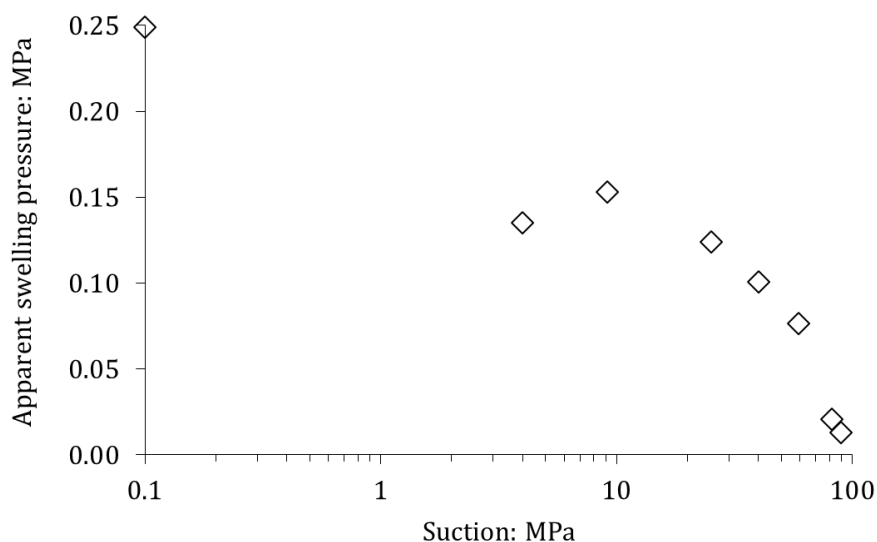


Figure 3-15: Swelling pressure as a function of decreasing suction for test SP0b.

Table 3-8: Summary of the swelling pressure at equilibrium upon suction-controlled hydration for all swelling pressure tests.

Suction: MPa	Swelling pressure: MPa				
	<i>SP30a</i>	<i>SP15a</i>	<i>SP15b</i>	<i>SP0a</i>	<i>SP0b</i>
Initial state	0.004	0.145	0.015	0.055	0.010
82	0.087	0.330	0.054	0.099	0.021
59	0.287	0.382	0.266	0.151	0.076
40	0.484	0.417	0.291	0.173	0.101
38	-	0.418	-	0.183	-
25	0.784	0.417	0.230	0.180	0.124
13	1.188	0.413	-	0.148	-
9	1.220	0.396	0.210	0.128	0.153
4	1.362	-	0.190	-	0.135
0	4.45	-	0.902	-	0.249

3.4.3 Evolution of the granular structure

Samples SP0a; SP0b and SP15a were dismantled at suction of 9 MPa; 4 MPa; and 9 MPa, respectively, to observe the evolution of their granular structure.

Both SP0a and SP0b samples appeared to be granular. Pellets and inter-pellet pores could easily be identified (Figure 3-16). Some pellets in contact with the upper wall were deformed in both samples. It was not possible to determine whether it occurred during the closure or during swelling.

SP15a sample was found to be granular too. Pellets could be identified. The powder concentration was found to be lower at the top of the sample. Except at the top of the sample, powder was filling the inter-pellet pores. This observation highlights the difficulty to perform tests on low powder content samples, in which the powder is very loose in the macropores and prone to migration. Pictures of SP15a samples after dismantling are presented in Figure 3-17.



Figure 3-16: Picture of samples SP0a and SP0b after dismantling. a: SP0a equilibrated at 9 MPa of suction; b: SP0b equilibrated at 4 MPa of suction; c: SP0a removed from the isochoric cell.



Figure 3-17: Picture of SP15a sample after dismantling. Left: Top of the sample in the cell, right: sample removed from the isochoric cell. The sample lost its integrity. However, single pellets are clearly identified.

Suction was measured using the WP4 potentiometer for samples SP0a and SP15a. In both cases, suction was 10 MPa. It is reminded that the imposed suction using the vapour equilibrium technique and a saturated KNO_3 salt solution was 9 MPa. The gravimetric water content for these two samples was 0.23 (Table 3-9). Sample SP0b was closed immediately after opening to flood the sample and obtain the final swelling pressure.

Table 3-9: Final measured suction and water content of samples SP0a and SP15a.

Sample	Imposed suction: MPa	Measured suction: MPa	Measured water content: dimensionless
SP0a	9	10	0.23
SP15a	9	10	0.23

3.5 DISCUSSION

3.5.1 Final swelling pressure

The final swelling pressure of MX80 bentonite can be estimated using Wang et al. (2012) estimation (equation 2-6). The dry density of the three mixtures used in the present study are 1.50 Mg/m^3 ; 1.275 Mg/m^3 ; 1.05 Mg/m^3 for pellet/powder proportion of “70/30”; “70/15”; “70/0” respectively.

The final swelling pressure using this estimation and the final value measured by sensors are compared in Table 3-10, for each mixture.

Table 3-10: Comparison between estimated final swelling pressure (Wang et al., 2012) and measured swelling pressure.

Mixture	Estimated swelling pressure: MPa	Measured swelling pressure: MPa
70/30	4.44	4.45
70/15	0.970	0.902
70/0	0.210	0.249

The three mixtures have estimated and measured values in the same order of magnitude. Two interpretations can be proposed: *i*) Even if the swelling pressure is measured on samples not fully equilibrated, it can be inferred that the measured swelling pressure will not significantly evolve; *ii*) At REV-scale, the material has homogenised at full saturation. Indeed, if the material had not homogenised, strong initial heterogeneities of density (*i.e.* dense pellets and loose powder-matrix) would not give the same final swelling as estimated from homogeneous compacted block. It is reminded that at initial state, pellet dry density is 1.91 Mg/m^3 and pellets correspond to 55 % of the total volume (Table 3-5). Depending on the mixture, “powder” dry density is 1.00 Mg/m^3 ; 0.50 Mg/m^3 or 0 Mg/m^3 and corresponds to 45 % of the total volume. In the course of hydration, pellet density is progressively reduced from 1.91 Mg/m^3 to the mixture density while loose powder phase, if any, progressively becomes denser to reach the mixture average dry density.

3.5.2 Influence of the powder content

Three different mixtures with different powder content and identical pellet content have been tested in suction-controlled swelling pressure tests. Depending on the powder content, samples can be characterised by a “dense” powder phase (70/30 mixture), “loose” powder phase (70/15 mixture) and no powder phase (70/0) filling the inter-pellet macroporosity.

Comparison of the suction-swelling pressure relationships upon hydration suggests that the powder content has a variable influence on the macroscopic response of the material. In particular, at suction higher than 4 MPa, as highlighted in Figure 3-18, SP0a, SP0b and SP15b samples display identical evolution of swelling pressure: an increase of swelling pressure until low values of $\sim 0.2 \text{ MPa}$, then a plateau/slight decrease as suction decreases. On imposing zero-suction, the evolution was however different between 70/0 and 70/15 samples: both reached their respective final values related to the average dry density, thus to the powder phase.

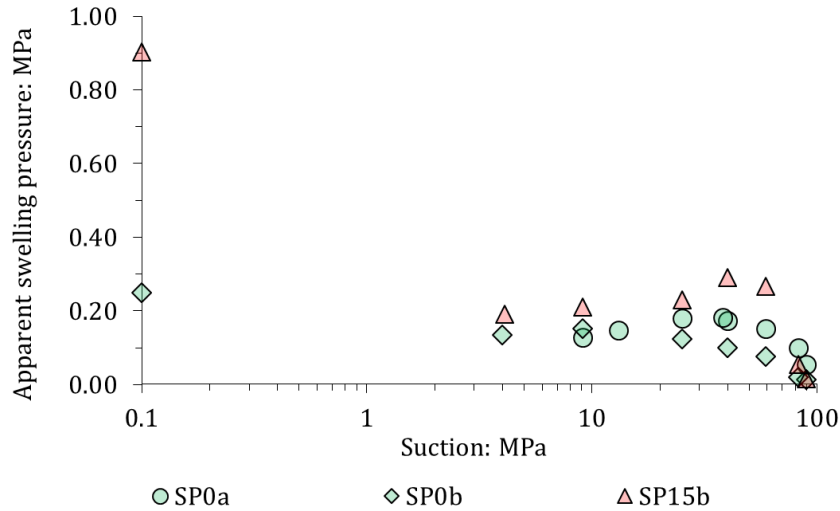


Figure 3-18: Comparison of SP15b; SP0a and SP0b test results.

70/30 sample (SP30a) displayed a different evolution of swelling pressure upon hydration. No transient swelling pressure plateau was observed. Upon suction decrease, the measured swelling pressure is higher than “loose” powder and no powder samples (Figure 3-19).

At suction higher than 60 MPa, all samples seem to follow the same trend of swelling pressure evolution. Then, the “dense” powder sample has a higher swelling pressure. All samples have the same pellet solid fraction. Differences between results is thus attributed to the presence of powder in the inter-pellet porosity. However, until 4 MPa of suction, “loose” and no powder samples follow the same trend which suggests that powder does not have significant influence on the material mechanical behaviour in the 70/15 mixture.

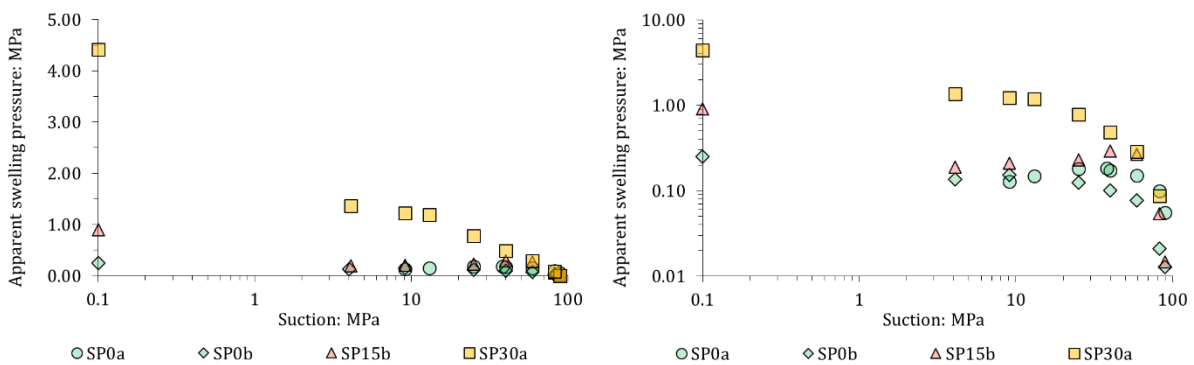


Figure 3-19: Comparison of SP30a; SP15b; SP0a and SP0b test results. Left: semi-logarithmic plot, right: logarithmic-logarithmic plot.

In the light of experimental results discussed in the present part, it can be suggested that the mechanical behaviour of pellet mixtures upon hydration is first controlled by the granular assembly of pellets. Then, as suction decreases and powder density in the inter-pellet porosity progressively increases, the material behaviour is no longer controlled by the pellet assembly. Powder contribution to the mechanical behaviour becomes significant and the material can be considered “continuous”.

In “dense” powder samples, powder influences the macroscopic response of the material almost from the beginning of hydration. In “loose” powder samples, the macroscopic response is close to no powder samples and the powder is thought to be in free-swelling conditions in the large inter-pellet voids. As suction decreases, pellet density decreases, powder density increases, and the mixture progressively homogenises.

3.5.3 Influence of the initial granular structure

The previous part highlighted that the granular structure of the materials controls its behaviour as long as the powder phase is considered “loose” and in free-swelling conditions. Figure 3-20 presents the evolution of both SP0a and SP0b swelling pressure as a function of decreasing suction, along with a vertical line representing the suction at which the material is known to be a granular assembly, as observed on Figure 3-16.

In these two tests, no powder is filling the inter-pellet voids and all the response is indeed controlled by the granular assembly of pellets. In the course of hydration, pellet swelling in constant-volume conditions induces an increase of inter-granular forces and swelling pressure increases. As inter-granular forces reach pellet strength, swelling pressure no longer increases and a plateau/decrease of swelling pressure is measured as suction decreases. The influence of initial granular structure can be divided in two phases: *i*) increase of inter-granular forces, controlled by pellet stiffness; *ii*) plateau/decrease of swelling pressure controlled by pellet strength and stiffness decreasing upon wetting.

These suggestions are consistent with Hoffmann et al. (2007) and Alonso et al. (2011) conclusions. In addition, they are supported by observations on Figure 3-16, in which some pellets in contact with the upper wall clearly have undergone plastic strains in contact areas.

Below 4 MPa of suction, samples were wetted using liquid water. Swelling pressure sharply increased, displayed a peak, and then stabilised. These features are shared by bentonite materials (see Chapter 2), regardless of their initial granular/continuous structure, and cannot be interpreted as an influence of the granular structure.

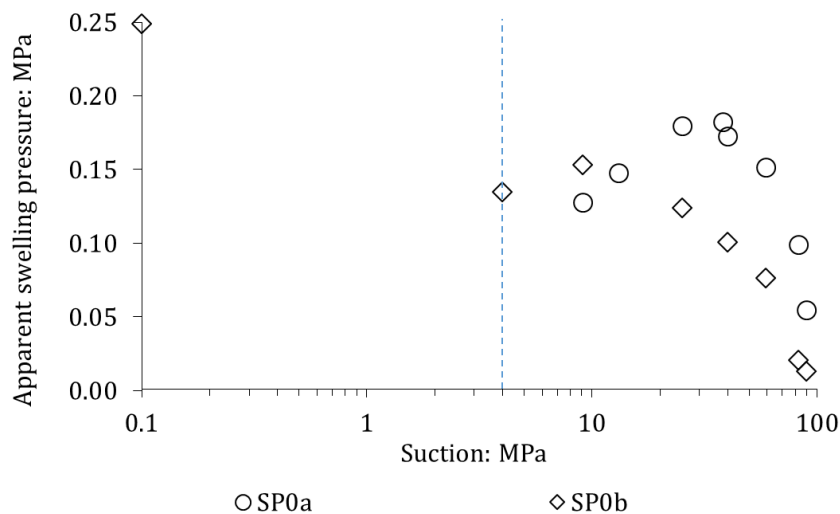


Figure 3-20: Comparison of SP0a and SP0b test results. The vertical dashed line correspond to the suction at which the material has been observed to be granular.

3.5.4 Influence of the sample preparation

The influence of sample preparation can be highlighted for instance by comparing SP15a and SP15b tests. Composition of SP15a sample is identical to SP15b. As already mentioned, the initial pressure of these two tests was 0.145 MPa and 0.015 MPa, respectively. This difference can be explained by a different pellet arrangement following the preparation step.

As discussed in the previous part, “loose” powder sample behaviour is mostly influenced by the pellet assembly at high suction, powder being considered in free-swelling conditions in the inter-pellet voids. In the suction range where the mechanical behaviour is controlled by the granular arrangement, pellet strength is considered to influence the occurrence of a first peak in the swelling pressure-suction relationship. It is thus clear that an initial pressure upon cell closure may influence the material response upon hydration. Should pellet strength be reached upon the closure step, swelling pressure may be entirely controlled by pellet strength and not display the trend described in the previous part.

This interpretation is consistent with the comparison of test results presented in Figure 3-21. SP15a swelling pressure was almost constant during hydration until 9 MPa of suction, while SP15b swelling pressure exhibited an increase, decrease, then a plateau from initial state to a suction of 4 MPa.

In SP15a test, the initial pressure applied during closure to reach the target sample volume may have been high enough to let contact forces reach the pellet strength. Actually, even if the strength is not reached during closure, if granular assembly rearrangement are prevented (due to friction or wall effect), then intergranular forces increase upon pellet swelling and strength may be reached earlier. It is suggested also by comparing SP0a and SP0b: swelling pressure decrease started at higher suction in the sample prepared under higher closure pressure (Figure 3-20). This point will be discussed in further details in Chapter 4.

This non-negligible influence of the eventual closure pressure increases the difficulty to perform constant-volume swelling pressure tests in the laboratory at REV scale. Sample of small sizes allow long testing duration to be avoided. However, the preparation step may be difficult due to the wall effect, described in Chapter 2, between pellets and the cell wall. In the present work, test durations were in some cases longer than two years.

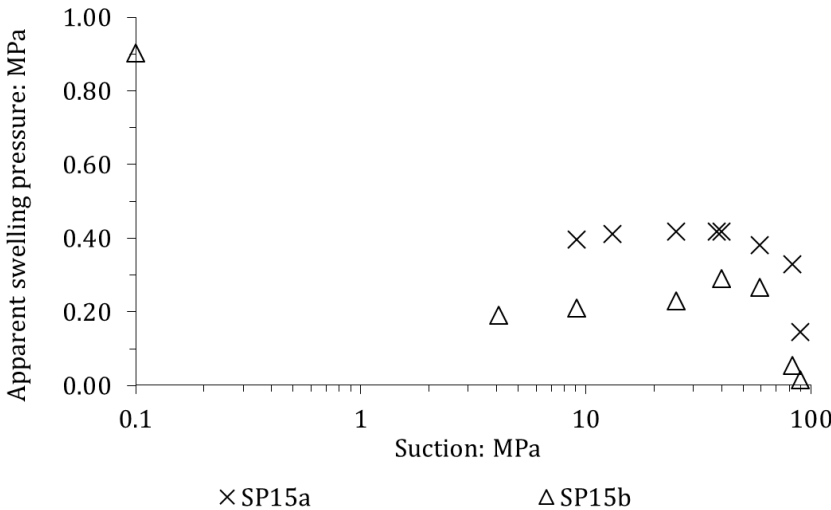


Figure 3-21: Comparison of SP15a and SP15b test results.

3.5.5 Hydration mechanisms

The experimental apparatus presented in Figure 3-5 is composed of a side tube connecting the bottom porous disk to the top porous disk. No gas overpressure can arise within the sample and diffusion of water vapour in the inter-pellet voids is considered the dominant hydration mechanism in this test.

The time required to reach equilibrium is generally slightly longer for samples containing more powder. However, all durations are within the same order of magnitude. It can be inferred that relative humidity in the macroporosity is mainly homogeneous and that powder and macropores are nearly at hydraulic equilibrium. It is suggested that water transfer from vapour in macropores to pellets controls the time required to reach equilibrium.

As mentioned in Chapter 2, previous works on pellet mixture modelling already considered these transfers in the description of the material behaviour (Alonso et al., 2011; Gens et al., 2011; Sanchez et al., 2016), which seems appropriate in the light of experimental results presented in the present Chapter.

3.5.6 Conceptual interpretation of the macroscopic response of tested samples

In “loose” powder phase and no powder phase materials, pellets form a coarse granular assembly and powder grains are in free-swelling conditions. Upon hydration in constant-volume conditions, the macroscopic response is first controlled by contact interactions between pellets. Evolution of pellet stiffness and strength controls the mechanical behaviour. As contact forces reach pellet strength, a plateau/decrease of swelling pressure occurs. Upon further suction decrease, the material progressively homogenises. The same behaviour as compacted blocks of bentonite materials is then observed. At low suction a transition from crystalline swelling to osmotic swelling domains causes the material fabric to rearrange and a decrease of swelling pressure may be observed. Then, swelling pressure increases again to its final value.

In “dense” powder phase materials, the first phase is not clearly observed in experimental results. It can be inferred that in materials with dense powder phases, even if strong density heterogeneities still exist between the two phases of the mixture, the powder phase is not in free-swelling conditions. Its swelling therefore influences the macroscopic response and may balance the influence of contact interactions between pellets.

In any case, it is suggested that mixtures can be considered to behave as continuous bentonite materials at suction lower than 3 MPa, as a result of the significant fabric rearrangement described in Chapter 2. Both the 70/30 and the 70/0 materials seem to have been affected by this phenomenon.

In the light of experimental results presented in this Chapter and literature review concerning binary granular mixtures, the difference between “loose powder” and “dense powder” behaviours can be related to the concept of dominant phase. As the initial powder content decreases, pellets become the dominant phase in the mixture and control its behaviour. As the powder content increases, x_S approaches $x_{S\text{crit}}$, and powder starts influencing the mixture mechanical behaviour. It is worth mentioning that in initially “loose” powder phase materials, constant-volume hydration pellet swelling causes the powder phase to swell in a progressively decreasing available volume. Pellets may stop being the dominant phase during hydration even if $x_S < x_{S\text{crit}}$.

If pellets are not considered the dominant phase, it seems reasonable to consider that, using appropriate set of parameters, existing modelling approaches can satisfactorily reproduce the mixture behaviour. Below the proposed threshold at 3 MPa, these frameworks seem appropriate to describe the macroscopic response.

However, none of the existing conceptual frameworks in the literature can describe the behaviours observed in tests performed on 70/0 and 70/15 mixtures. Both mixtures have significantly different average dry densities, thus different amount of bentonite particles available for swelling or macroporosity affected by compaction. Yet, they displayed the same macroscopic response at suction higher than 4 MPa. Between 4 MPa and 0 MPa of suction, swelling pressure increased to a final value which correlates to the mixture dry density in both samples.

Interpretations regarding the macroscopic behaviour observed during suction-controlled swelling pressure tests of different pellet-powder mixtures can be summarised as follows (Figure 3-22):

- In “loose”/no powder samples, two peaks phenomena may occur, corresponding to distinct phenomena: *i*) a peak corresponding to pellet strength, not related to the macrostructure LC yield locus concept; *ii*) a peak corresponding to fabric rearrangement, satisfactorily described by the LC yield locus concept;
- In “dense” powder samples, only the second phenomenon is observed;
- Two domains are proposed to describe the mechanical behaviour of pellet-powder mixtures upon hydration. The first domain is related to the dominance of the pellet assembly in the binary granular mixture and can be described by the mechanical behaviour of the pellet assembly. The second domain is related to either the influence of powder on the macroscopic response or occurrence of fabric rearrangement, preventing the mixture behaviour to be described as controlled by the initial granular structure. In the second domain, the material is considered “continuous” and can be described by traditional conceptual frameworks;
- Transition between these two domains is considered to be related to either the relative densities of pellet and powder phases or suction at which the microstructural rearrangement occurs.

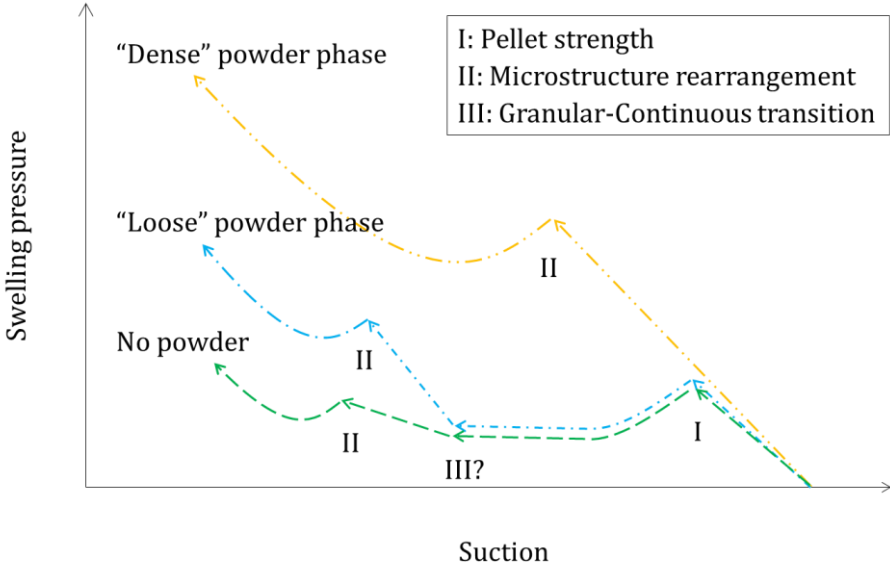


Figure 3-22: Interpretation of the experimental results in terms of involved mechanisms. It is not clear if a “granular-continuous” transition occurred in “dense” powder samples or if only the “continuous” behaviour was observed.

3.6 CONCLUDING REMARKS AND PERSPECTIVES

An experimental study of bentonite pellet-powder mixtures was presented in the present Chapter. Suction-controlled swelling pressure tests on mixtures with different powder content and constant pellet mass have been performed. The main conclusions, interpretations and perspectives arising from experimental results are presented in this final section.

3.6.1 Similitudes and differences between continuous and granular bentonite materials

The behaviour of continuous bentonite materials upon constant-volume hydration is characterised by the occurrence of a peak as a result of fabric rearrangement if macroporosity is developed enough for aggregate to invade this latter. It was suggested in Chapter 2 that this phenomenon is related to the transition between two different hydration mechanisms following the insertion of water layers at the surface of clay particles. In pellet-powder mixtures, the influence of this transition is also observed at low suction, in both “dense” powder and no powder samples.

At suction higher than this threshold, if pellets are the dominant phase in the binary granular mixture, it can be inferred that powder is in free-swelling conditions in the inter-pellet porosity. In this case, the mechanical behaviour of the material can be described by the mechanical behaviour of the pellet assembly. Swelling pressure increases as a consequence of pellet swelling upon hydration and increase of contact forces. Reaching pellet strength induces a peak at high suction, distinct from the second peak aforementioned.

If pellet is the dominant phase, the behaviour of the material cannot be described by an equivalent continuous medium characterised by the average dry density of the mixture. It is likely that the swelling of the mixture is related to the swelling of the pellet assembly upon pellet swelling. It is likely that the mixture compressibility is related to a pellet assembly compressibility, evidenced by Molinero-Guerra et al. (2019b) to be somewhat different to compacted blocks compressibility.

Upon hydration, density of pellet and powder phases progressively decreases and increases, respectively. The material can be described as a continuous medium if the granular structure no longer controls its behaviour, at a threshold that still needs to be determined. In any case, experimental results reported in the literature suggest that a suction of ~3 MPa is likely to be the lowest limit at which the material behaviour can be considered controlled by the granular structure.

The final swelling pressure of pellet-powder mixtures can be estimated from empirical relationships determined on continuous materials.

3.6.2 Limitations of the testing procedure

The realisation, dismantling and interpretation of test results highlighted some difficulties and limitations of the testing procedure for determination of swelling pressure evolution at laboratory-scale. This part summarises the points which require attention in laboratory testing of these materials and some limitations which should be addressed in future experimental works.

3.6.2.1 Difficulties to perform swelling pressure tests

Attention is drawn on some difficulties in the performance of suction-controlled swelling pressure tests.

As discussed in the present Chapter, the preparation step must be carefully performed since it can affect the material response on hydration. Applying pressure during the closure step must be avoided. Hydration performed on samples prepared using initial closure pressure displayed different behaviour. The first peak (related to pellet strength) is reached earlier in these samples. In SP15a sample, for instance, the swelling pressure remained nearly constant during hydration, whereas SP15b sample displayed the same trend as 70/0 mixtures. At laboratory scale, if the ratio of pellet dimensions to cell dimensions is not low enough, preparation may become difficult as a result of wall effect, resulting in turn of closure pressure to reach the target dry density and modifying the material behaviour.

Hydration of the mixture should be performed by allowing free vapour diffusion in the macroporosity. Indeed, in repository conditions, vapour transfer is likely to be the dominant saturation process (Kröhn, 2005). In addition, liquid water inhibits the influence of intergranular interaction in small cells. If cell dimensions represent few pellets in height and diameter, liquid water hydration would induce the very fast destruction of the granular structure of a non-negligible part of the sample. In addition, macroporosity provides preferential path at the initial state which, at laboratory scale, would allow a significant part of the sample to be in contact with liquid water early in the test. This latter point is strongly suggested by results from Hoffmann et al. (2007) and Molinero-Guerra et al. (2018b). It is also highlighted by the short time required to reach a swelling pressure plateau in all three samples following water hydration. The influence of granular structure may be inhibited if liquid water flooding is performed instead of vapour hydration at REV-scale. It might actually explain the perfectly identical behaviour obtained by Imbert and Villar (2006) on compacted powder and pellet-powder mixture on liquid hydration in constant-volume conditions.

Drawbacks of using vapour diffusion are the long testing duration required. In the present study, some tests required more than two years for hydration from ~89 MPa to 0 MPa of suction, including a liquid water hydration step from 4 MPa to 0 MPa. Attention is required to avoid salt crystallisation on bottle sides since it would reduce the air relative humidity.

3.6.2.2 Limitations of the testing procedure

The following points are identified as limitations of the testing procedure which should be addressed in future experimental works.

The dimensions of the cell can influence the sample preparation and the ability to observe representative behaviour. In the present work, cell diameter and height are close to 8 and 4 times the size of the pellet at initial state. However, the ideal cell size for this type of test at REV-scale is not known. Results presented in Figure 3-18 suggest that the observed behaviour is reproducible, but influence of the wall on these latter is not known.

The tested material is intrinsically heterogeneous. The diameter of pressure sensor is thus likely to be a key parameter in the design of this type of test. In this respect, the pressure sensor(s) should be large enough to measure the material response instead of variability associated to heterogeneities, especially since test duration makes repeatability difficult. While it is obvious that sensor must be larger than pellets, it is not clear what an ideal ratio of pellet dimensions to sensor dimensions should be. In the present study, this ratio at initial state was close to 4.

Suction was measured after dismantling of SP0a and SP15a samples. Good agreement between imposed and measured suction was obtained. It can only be supposed for previous hydration steps since only the evolution of pressure could be used to characterise equilibrium.

It is clear from 70/0 and 70/15 mixtures behaviour that in “loose” powder samples the behaviour is controlled by the pellet assembly. It is however less clear in 70/30 mixture. Relative contribution of pellets and powder can be studied by performing a comparison test on MX80 powder compacted to a dry density of 1.50 Mg/m³. Comparison between this test, 70/0 and 70/30 samples would provide valuable information about the material behaviour.

3.6.3 Modelling the particular features of pellet-powder mixtures

In repository conditions, even if the buffer material has relative phase proportions close to the transition in dominant phase, heterogeneities and powder migration following installation may arise. In this respect, it is suggested that a suitable modelling framework should take into account the following material features:

- Transition from *i*) a “pellet assembly controlled behaviour” domain to *ii*) a “continuous” domain;
- Behaviour controlled by parameters related to pellets and the pellet assembly in the first domain;
- Traditional conceptual frameworks describing expansive soils behaviour are appropriate in the second domain.

Study of the behaviour of a single pellet upon partial hydration (*i.e.* higher than the identified suction threshold) and its influence on the pellet assembly mechanical behaviour is an interesting perspective arising from this conclusion.

In this respect, Discrete Element Method (DEM) is a suitable tool to study these features. Using DEM would allow to determine relevant parameters to describe the material in the first identified domain. Chapter 4 presents the development, implementation and validation of a DEM-based model from pellet-scale experimental characterisation.

4 PROPOSITION AND VALIDATION OF A DEM-BASED NUMERICAL APPROACH PROVIDING INSIGHT INTO THE MECHANICAL BEHAVIOUR OF PELLET ASSEMBLIES

4.1 INTRODUCTION

Chapter 3 presented suction-controlled swelling pressure tests performed on pellet-powder mixtures prepared at different powder contents and constant pellet mass. It was suggested from experimental results that the behaviour of the pellet assembly controls the material behaviour if powder is loose in the inter-pellet porosity.

Using DEM allows the mechanical behaviour of a granular assembly to be modelled from the grain behaviour and from intergranular interactions. In the framework of the present study, this numerical method is appropriate to determine relevant properties related to pellet and pellet assembly able to describe the material behaviour at high suction, as suggested in Chapter 3. In addition, DEM ability to access grain-scale phenomena and significantly lower repeatability cost compared to experimental tests makes it an interesting tool to study the behaviour of pellet assemblies under various hydromechanical loadings, provided a relevant and validated model is available. Some limitations of the experimental procedure described in Chapter 3 may also be addressed using DEM, such as the influence of sample preparation or variability associated to the sensor size. In this respect, the objective of the present Chapter is to propose a DEM modelling approach suitable for the simulation of the behaviour of pellet assemblies at high suction, *i.e.* in the range where granular behaviour dominates.

In the present chapter, an experimental study is first presented to determine the hydromechanical behaviour of a single pellet upon partial hydration. A simple method to model the swelling behaviour of a pellet upon suction decrease is presented. The experimental characterisation at pellet scale constitutes section 4.2. Constitutive laws proposed to describe the hydromechanical behaviour of a single pellet are then implemented in a DEM code. Description of the model, validation through swelling pressure test simulations and analysis of some identified limitations of the experimental procedure then constitute section 4.3. A general discussion about pellet characterisation in the laboratory and numerical results is presented in section 4.4. Finally, conclusions and perspectives arising from the present Chapter constitute section 4.5.

4.2 HYDROMECHANICAL BEHAVIOUR OF A PELLET UPON PARTIAL HYDRATION

4.2.1 Introduction

Discrete element method (*e.g.* Cundall and Strack, 1979; Roux and Chevoir, 2005; Agnolin and Roux, 2007a; Radjaï and Dubois, 2011) is envisaged as a convenient tool to study the hydromechanical behaviour of bentonite pellet mixtures accounting for the granular nature of the material and address the influence of pellet behaviour on the pellet assembly behaviour. In DEM simulations, each particle is modelled individually. A model describing the hydro-mechanical behaviour of a single pellet is therefore required. This approach is valid for granular materials, thus the model has to focus on a hydration state at which a pellet has not lost its initial structure.

For this purpose, the present section focuses on the hydromechanical behaviour of a single pellet upon partial hydration. Suction is controlled by the vapour equilibrium technique. Pellet volumetric strain, stiffness and strength are determined as functions of suction. Experimental results are interpreted using the conceptual framework proposed by Alonso et al. (1999) for compacted expansive soils.

4.2.2 Material

Two different pellets have been characterised: a 32-mm diameter pellet and a 7-mm diameter pellet.

The 32-mm diameter pellet is the candidate material considered in the French concept for radioactive waste disposal. This pellet is composed of a central cylinder-shaped part and two spherical caps at both ends. Table 4-1 summarises pellet initial geometrical properties. Pellet initial suction, s_i , is measured using a WP4 dew point potentiometer from Decagon. Initial gravimetric water content, w_i , is obtained by oven drying. In the present study, $s_i = 154$ MPa and $w_i = 0.06$. Initial dry density, ρ_{d0} , is obtained from the paraffin wax method (Molinero-Guerra et al., 2019a) and initial void ratio, e_0 , is deduced by considering a particle density ρ_s of 2.77 (Saba et al., 2014b). These physical properties are summarised in Table 4-2. A picture of a pellet assembly is presented in Figure 4-1.

Table 4-1: 32-mm pellet geometrical properties at initial state.

Geometrical property at initial state	Value
Diameter	32 mm
Height of the cylinder-shaped part	15 mm
Height	32 mm
Curvature radius	18 mm

Table 4-2: 32-mm pellet physical properties at initial state.

Physical property at initial state	Value
Suction	154 MPa
Water content	0.06
Dry density	2.06 Mg/m ³
Void ratio	0.34



Figure 4-1: Picture of an assembly of 32-mm pellet.

The 7-mm diameter pellet characterised in the laboratory is the same as the pellet used in the suction-controlled swelling pressure tests described in Chapter 3.

The 7-mm pellet is a miniature of the 32-mm pellet. It is conveniently used in the laboratory tests for reduction of wall effect at laboratory scale and test duration.

4.2.3 Experimental methods

Experimental methods concerning hydration of pellets, determination of volumetric strain, stiffness and strength, are presented in the present part.

4.2.3.1 Suction-controlled partial hydration

Suction-controlled hydration is performed through the vapour equilibrium technique (Tang and Cui, 2005; Delage et al., 2006). Pellets are placed within a desiccator containing a saturated salt solution. When equilibrium is reached (verified by pellet mass), pellets are removed from the desiccator to determine the volumetric strain, water content, and perform compression tests.

A picture of pellets inside a desiccator is presented in Figure 4-2. Table 4-3 presents the salt used to prepare the saturated salt solution to control the suction. Room temperature is maintained at $20\text{ }^{\circ}\text{C} \pm 1\text{ }^{\circ}\text{C}$.

In the present work, beside the initial suction, eight values of suction (ranging from 9 MPa to 82 MPa) are considered. For each one, several pellets are analysed to assess the repeatability of the experimental results.

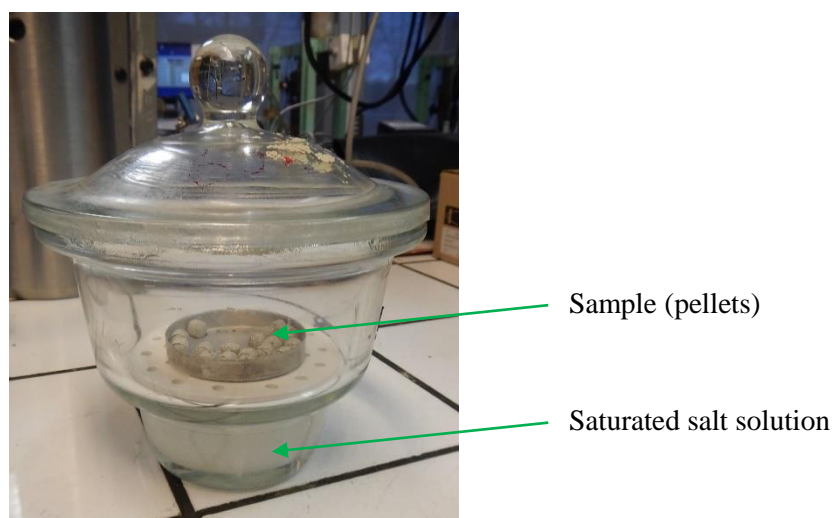


Figure 4-2: Desiccator used for the vapour equilibrium technique.

Table 4-3: Salt solutions used for vapour equilibrium technique.

	Solution	Suction at 20°C: MPa
Mg(NO ₃) ₂	Magnesium nitrate	82
NH ₄ NO ₃	Ammonium nitrate	59
NaNO ₂	Sodium nitrite	57
NaNO ₃	Sodium nitrate	40
NaCl	Sodium chloride	38
(NH ₄) ₂ SO ₄	Ammonium sulphate	25
Na ₂ CO ₃	Sodium carbonate	13
KNO ₃	Potassium nitrate	9

4.2.3.2 Determination of volumetric strain

Pellet volumetric strain is determined by measuring the variations in pellet height and pellet diameter. Pellet dimensions are measured using a camera (Figure 4-3). Axial strain, ε_a , and radial strain, ε_r , are determined by comparison of pellet height and diameter with their initial values.

Volumetric strain, ε_V is then determined using equation 4-1:

$$\varepsilon_V = (1 + \varepsilon_a) (1 + \varepsilon_r)^2 - 1 \quad 4-1$$



Figure 4-3: Picture of a 32-mm pellet following equilibrium at a controlled suction of 9 MPa. Left: Pellet height; Right: Pellet diameter.

4.2.3.3 Compression tests

Compression tests are carried out by using a load frame. The displacement rate is imposed at 0.1 mm/min. Displacements are recorded by a linear variable differential transformer (LVDT) and the contact force between the pellet and the frame is recorded by a force transducer. Compression tests are performed in both axial and radial directions.

A picture and diagram of the load frame are presented in Figure 4-4. Figure 4-5 presents a diagram showing the compression directions corresponding to axial and radial tests.

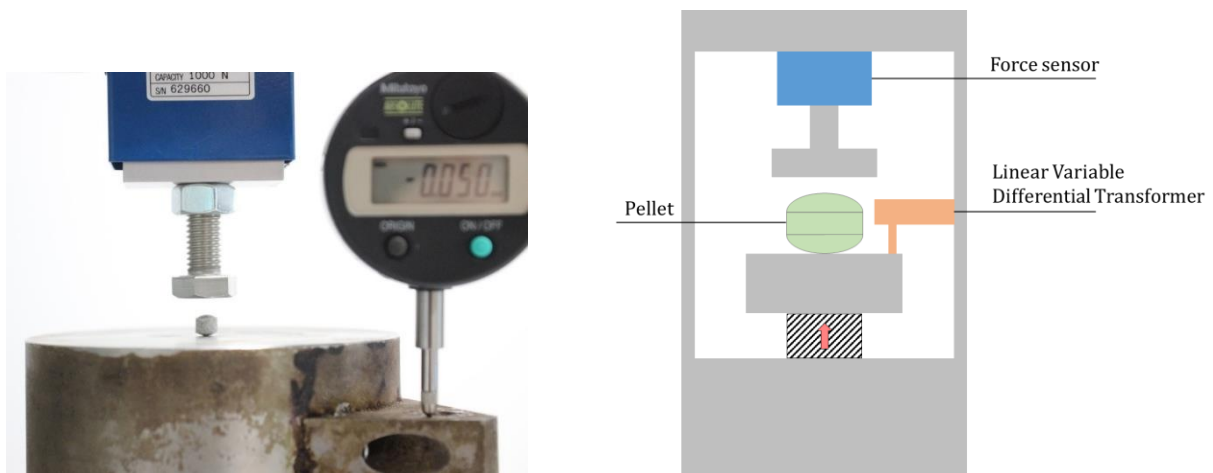


Figure 4-4: Load frame used for the compression test. Left: Picture; Right: Diagram.

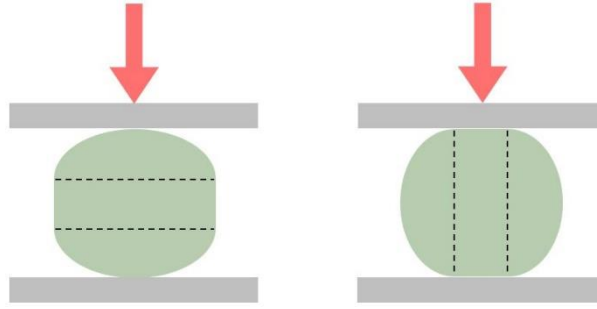


Figure 4-5: Compression directions. Left: Axial tests; Right: Radial tests.

Pellet stiffness is determined in both axial and radial directions.

In axial compression tests, contact between the load frame and the pellet is sub-punctual. Assuming isotropic linear elastic behaviour, the Hertz law is adapted to obtain Young modulus (Johnson, 1985).

The Hertz law is given by equation 4-2. It relates the elastic normal force at contact between two spherical bodies “1” and “2”, N_{12} , to their Young modulus, E_1 and E_2 , curvature radii, r_{c1} and r_{c2} , and elastic normal deflection at contact, δ_{N12} :

$$N_{12} = \frac{4}{3} E^* R^{*1/2} \delta_{N12}^{3/2} \quad 4-2$$

With E^* an equivalent Young modulus:

$$E^* = \frac{1}{\frac{1 - \nu_1^2}{E_1} + \frac{1 - \nu_2^2}{E_2}} \quad 4-3$$

And R^* an equivalent radius:

$$R^* = \frac{1}{\frac{1}{r_{c1}} + \frac{1}{r_{c2}}} \quad 4-4$$

Denoting the measured displacement in experiments by u_N , and assuming that the inverse of steel Young modulus is negligible compared to the inverse of pellet Young modulus, the relationship between the measured contact force, N , and pellet Young modulus, E , Poisson ratio, ν , and curvature radius, r_c , may be expressed as:

$$N = \frac{1}{3} \frac{E}{(1 - \nu^2)} (2 r_c)^{1/2} u_N^{3/2} \quad 4-5$$

In radial compression test, the contact is assumed to be linear. Johnson (1985)'s elasticity law, relating normal deflection to normal force for a contact between an infinite plate and a cylinder, is applied to determine E . Note that Johnson (1985)'s equation was proposed for long cylinders. In the present work, the height of the cylinder shaped part of the pellet, h , is slightly higher than the radius of the pellet (*i.e.* $D/2$, where D denotes the diameter of the pellet).

In experiment, the relationship between u_N and pellet properties is expressed as:

$$u_N = 2 \frac{N}{h} \frac{1 - \nu^2}{\pi E} \left[2 \ln \left(2 \sqrt{\frac{\frac{\pi D}{2} \frac{E}{1 - \nu^2}}{\frac{N}{h}}} \right) - 1 \right] \quad 4-6$$

In both axial and radial tests, pellet strength is determined as the final value before pellet failure.

4.2.4 Experimental results

4.2.4.1 Water retention and saturation of the pellets

Figure 4-6 presents the evolution of water content, w , as a function of elapsed time during the suction equilibrium phase for the 7-mm pellet. From its initial value (0.12), w increases quickly during the first days and equilibrium is reached after ~10 to ~30 days, depending on the imposed suction. The values obtained at equilibrium are plotted as functions of decreasing suction in Figure 4-7.

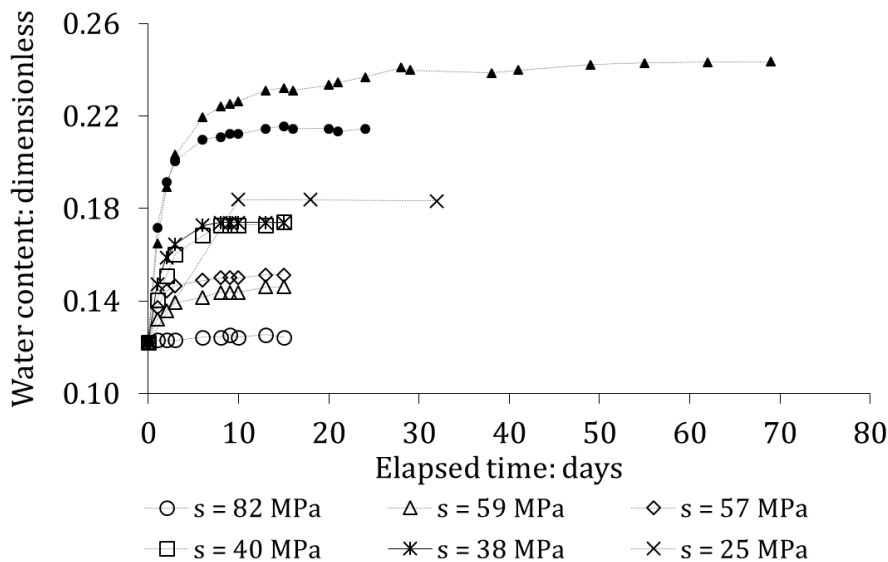


Figure 4-6: Evolution of 7-mm pellet water content upon hydration at controlled relative humidity in the desiccators.

Only a wetting path is performed and corresponds to a decrease of suction from initial suction to 9 MPa. Along this wetting path, w increases from 0.12 to 0.24 for the 7-mm pellet and from 0.06 to 0.23

for the 32-mm pellet. Results obtained on a comparable material (MX80 7-mm pellet) by Molinero-Guerra et al. (2019a) are also plotted. Within the investigated suction range, the water retention behaviours of the three pellets are similar.

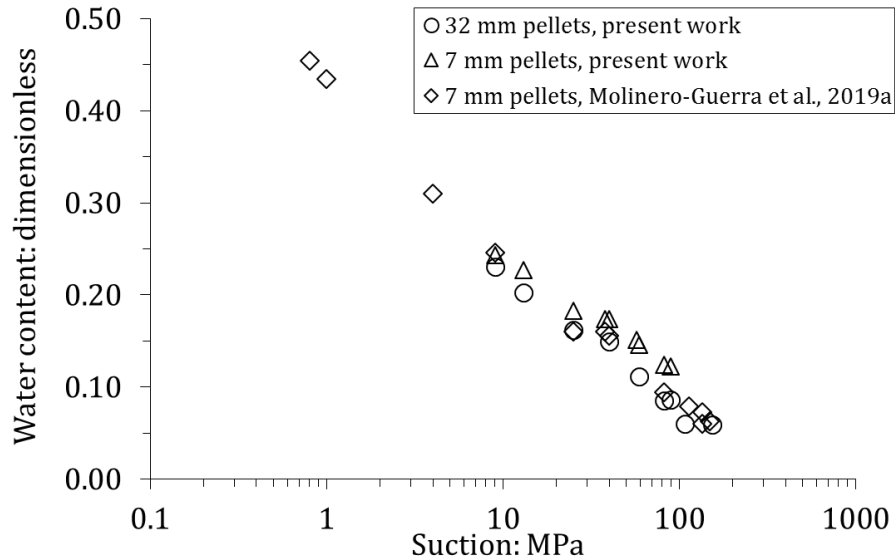


Figure 4-7: Evolution of water content upon suction decrease for three MX80 pellets in free-swelling conditions.

From the water content-suction relationship, the evolution of the degree of saturation can be determined using the following equation:

$$S_r = \frac{w}{\left((1 + \varepsilon_v) \frac{\rho_s}{\rho_{d0}} - 1 \right) \rho_w} \quad 4-7$$

The values of ε_v are presented in the following sub-part. Evolution of the degree of saturation upon suction decrease for the same three materials is presented in Figure 4-8. The degree of saturation remains nearly constant in the investigated suction range. Results from the present study and from Molinero-Guerra et al. (2019a) on the 7-mm pellet present good repeatability, with two different methods to determine the pellet volumetric strain/void ratio.

The degree of saturation for the 32-mm pellet is significantly lower than for the 7-mm pellet. It can be explained as a consequence of the higher swelling strains and large cracks opening for these samples in the course of hydration.

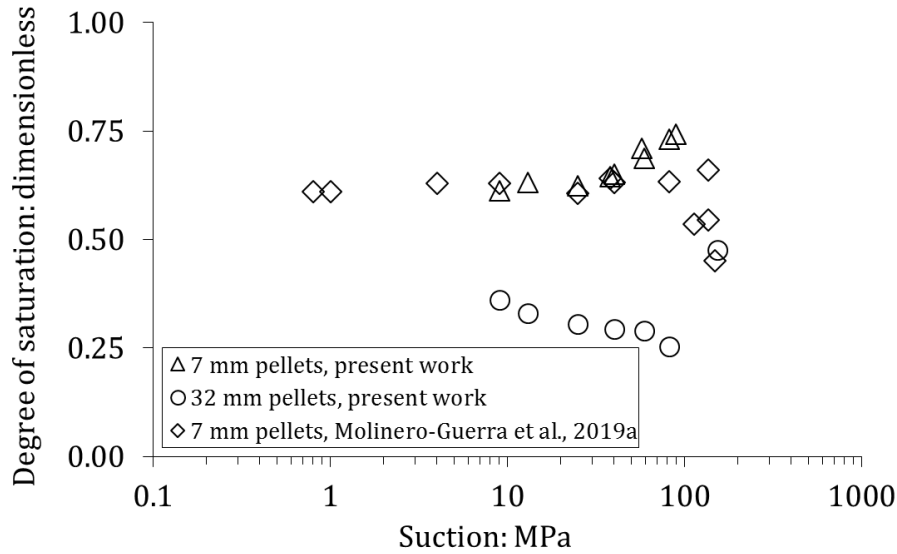


Figure 4-8: Evolution of the degree of saturation upon suction decrease for three MX80 pellets.

4.2.4.2 Volumetric strain evolution upon suction decrease

The evolution of ε_a and ε_r is determined upon suction decrease. Upon hydration, ε_a was generally higher than ε_r , especially at low suction, for both 7-mm and 32-mm pellets. From the mean values obtained for ε_a and ε_r , ε_V is obtained by application of equation 4-1.

Radial and axial strains obtained on 7-mm pellets are presented in Figure 4-9. Their mean values and corresponding volumetric strain evolution upon hydration are presented in Figure 4-10. Figure 4-11 presents the same data as Figure 4-10, for 32-mm pellets. Dashed red curves on Figure 4-10 and Figure 4-11 represents the predictions of the model presented in the following part (4.2.5).

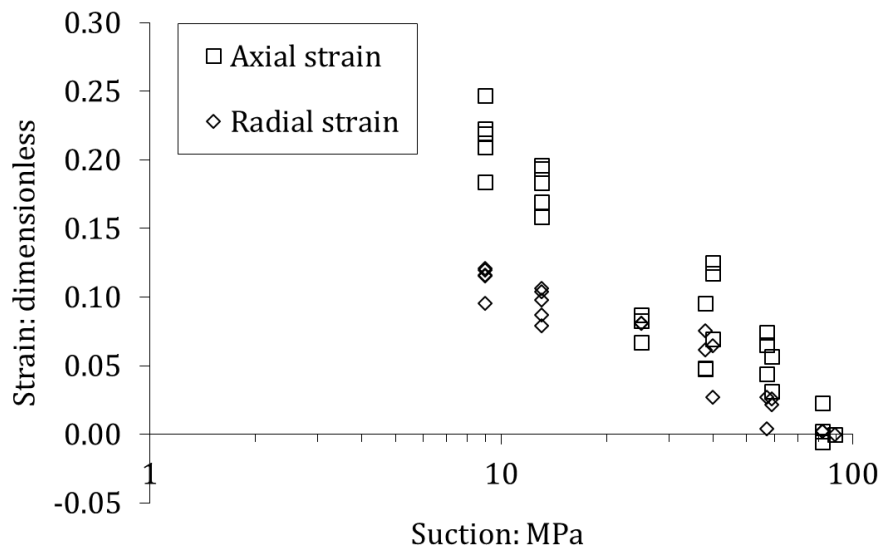


Figure 4-9: Experimental results for axial strain and radial strain of 7-mm pellets.

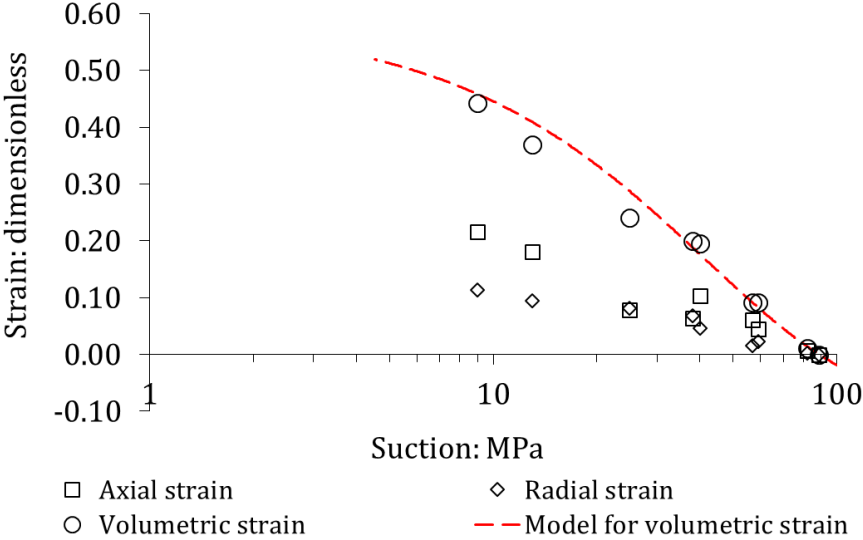


Figure 4-10: Evolution of mean radial strain, mean axial strain, and corresponding volumetric strain of 7-mm pellet upon suction decrease. The red dashed line is the model prediction (see 4.2.5).

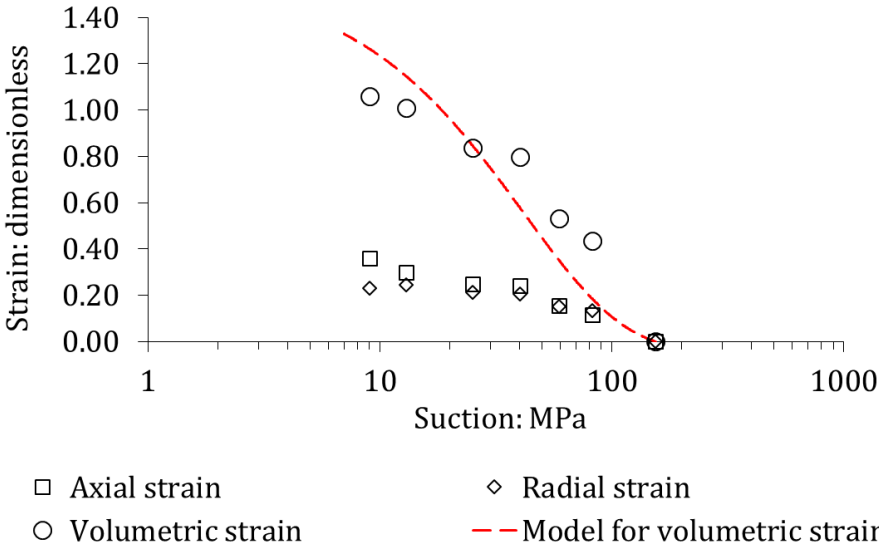


Figure 4-11: Evolution of mean radial strain, mean axial strain, and corresponding volumetric strain of 32-mm pellet upon suction decrease. The red dashed line is the model prediction (see 4.2.5).

In 32-mm pellets, large cracks develop upon swelling, which causes the void ratio to significantly increase upon suction decrease (Figure 4-12). Pictures of pellets at equilibrium at different imposed suction values are presented in Figure 4-3 and Figure 4-13. Cracks are clearly observed on 32-mm samples while no cracks (at this scale) can be observed even at 9 MPa on 7-mm pellets (Figure 4-14). Actually, as evidenced by Molinero-Guerra et al. (2017), cracks indeed develop in 7-mm pellets upon free swelling. Experimental results withal highlight that 32-mm pellets are significantly more affected by this phenomenon.

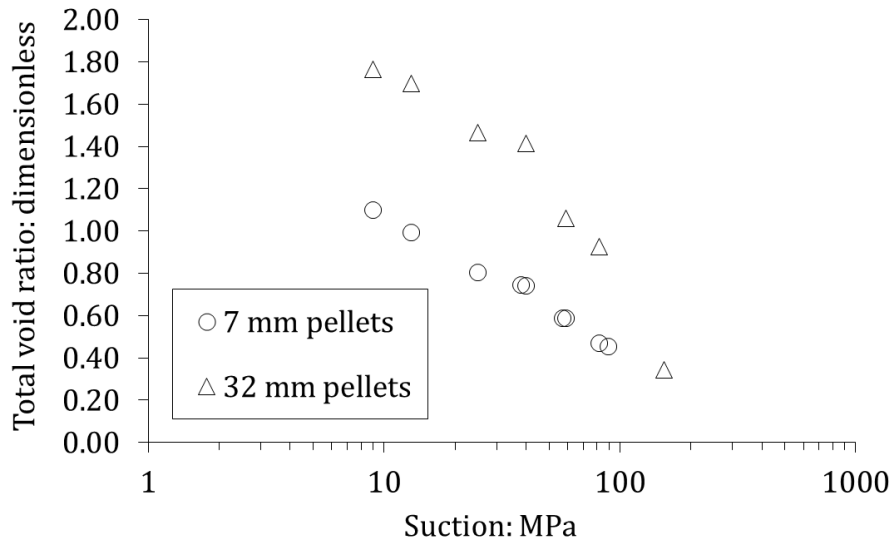


Figure 4-12: Evolution of total void ratio of pellets upon suction decrease.



Figure 4-13: Pictures of 32-mm pellets at equilibrium at different suctions. Left: 59 MPa; Centre: 40 MPa; Right: 13 MPa.

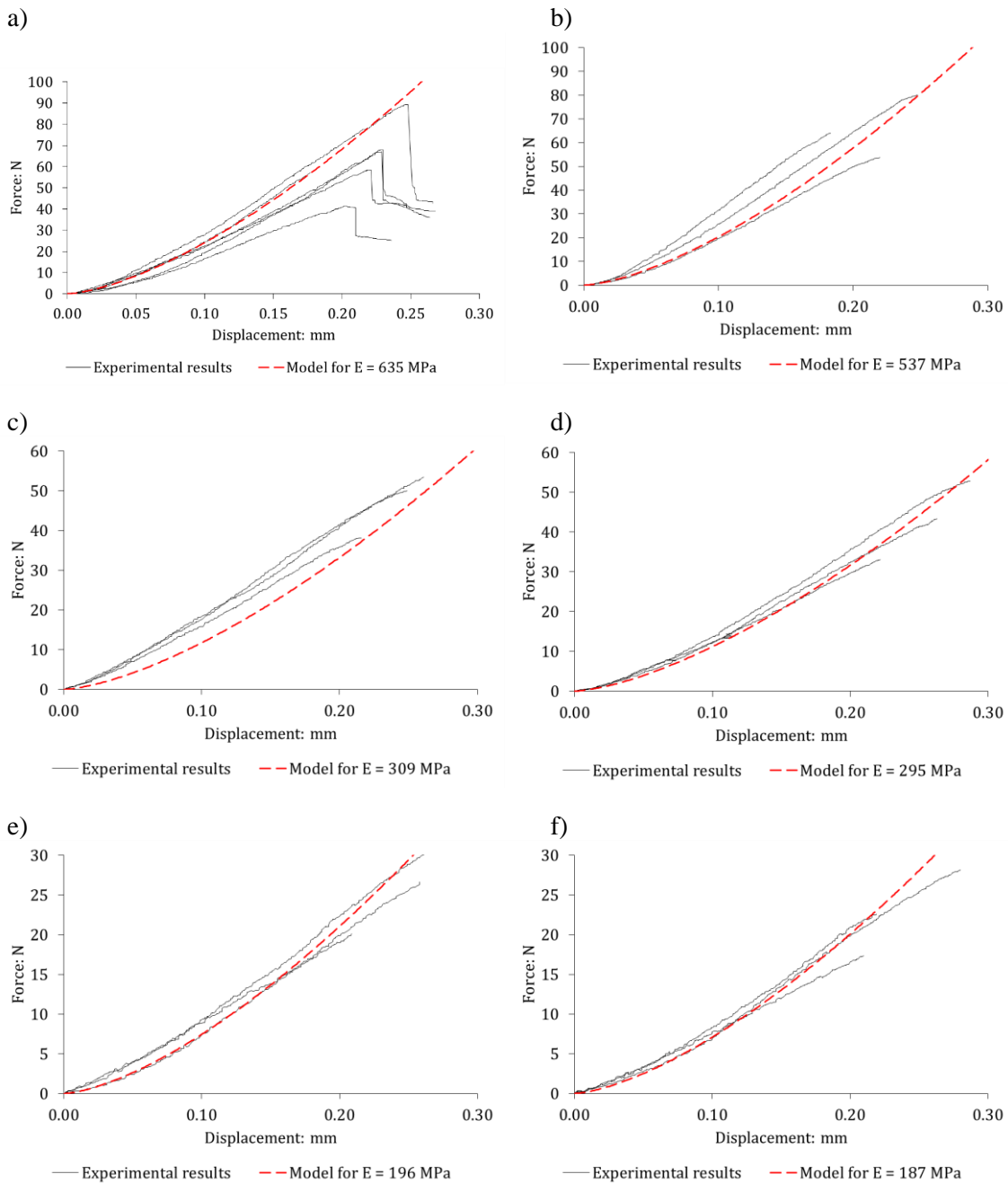


Figure 4-14: Picture of 7-mm pellets at equilibrium at 9 MPa suction.

4.2.4.3 Determination of pellet stiffness and strength

Pellet stiffness is determined using equation 4-5 for axial tests and equation 4-6 for radial tests.

Figure 4-15 presents axial test results for 7-mm pellets. On these figures, the red dashed lines correspond to a value of E retained to fit the experimental results (equation 4-5). Figure 4-16 presents axial test results for 32-mm pellets along with the equation 4-5 fitting.



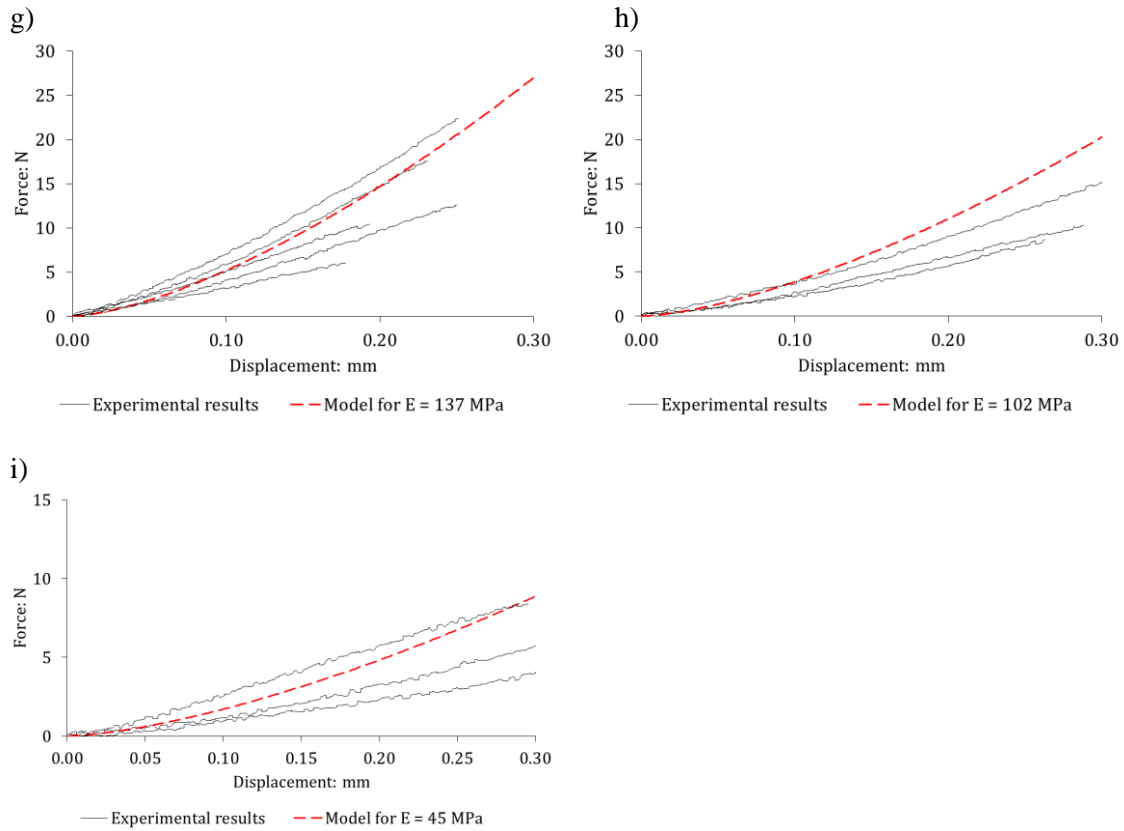


Figure 4-15: Axial test results for 7-mm pellets. Solid black lines are the experimental force-displacement relationships. The dashed red lines are the relationship obtained through equation 4-5 for a given value of E . Tests are performed at different suctions: a) 89 MPa; b) 82 MPa; c) 59 MPa; d) 57 MPa; e) 40 MPa; f) 38 MPa; g) 25 MPa; h) 13 MPa; i) 9 MPa.

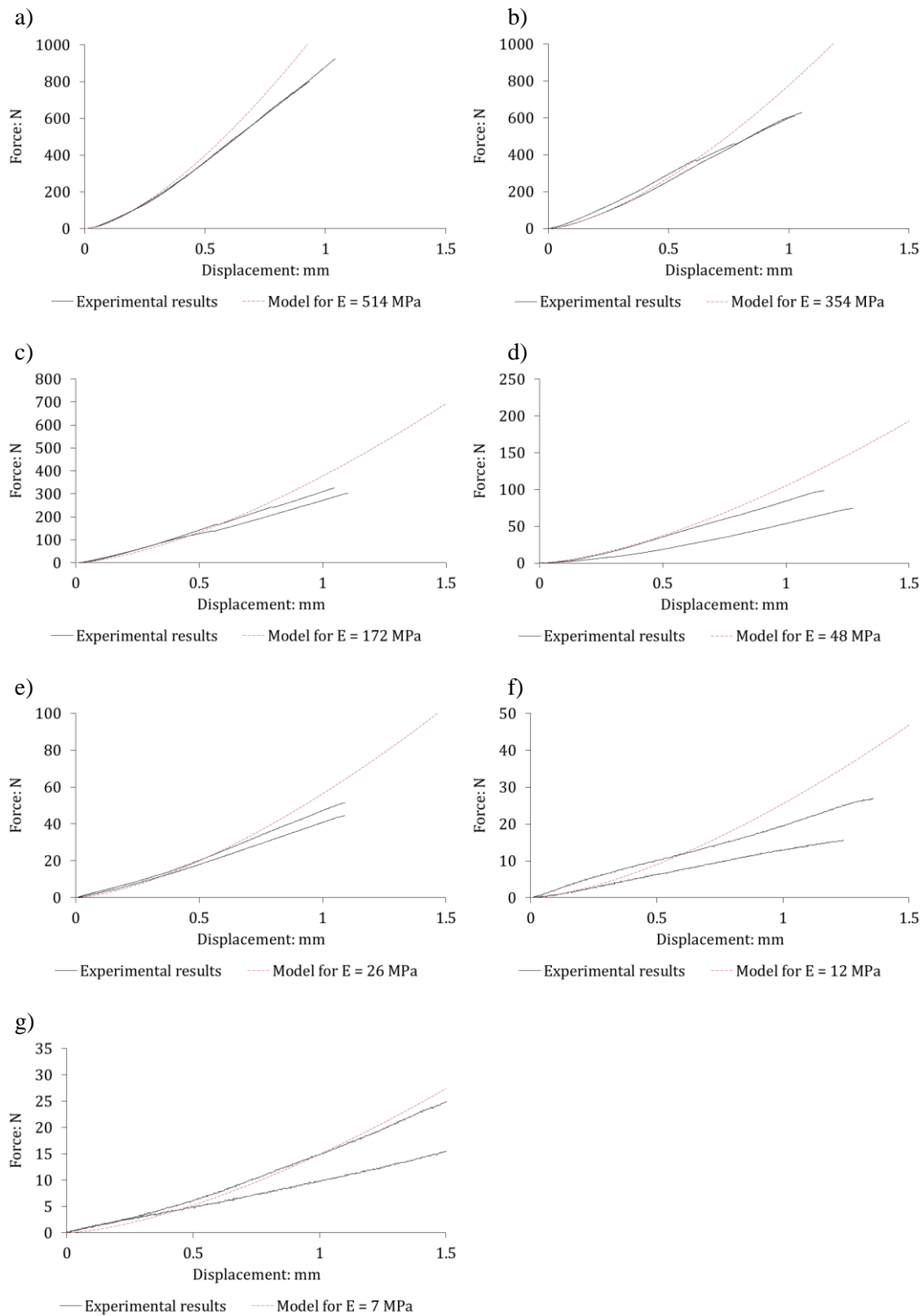


Figure 4-16: Axial test results for 32-mm pellets. Solid black lines are the experimental force-displacement relationships. The dashed red lines are the relationship obtained through equation 4-5 for a given value of E . Tests are performed at different suctions: a) 107 MPa (equilibrium with laboratory conditions); b) 82 MPa; c) 59 MPa; d) 40 MPa; e) 25 MPa; f) 13 MPa; g) 9 MPa.

During axial compression tests, N increases with increasing displacement until failure. At failure, N decreases. Equation 4-5 is used to fit experimental data from the start to the failure and determine E . In this work, ν is not known and assumed to be equal to 0.3 for simplicity.

For 7-mm pellet, Hertz's law satisfactorily reproduces the experimental results in terms of trend of the force-displacement relationship. For 32-mm pellet, the trend of the experimental force-displacement relationship is not perfectly reproduced for some tests at low suction. It may be a consequence of the development of the large cracks. However, the order of magnitude of the predicted normal force remains close to experimental results.

For radial compression tests, N increases with increasing displacement in two distinct phases: first, a slow increase; second, a more significant and sub-linear increase. The first phase is interpreted as the consequence of an imperfect contact between the frame and the pellet at the beginning of the test. As displacement increases, the contact becomes linear and the force-displacement relationship is significantly modified. Considering this hypothesis, equation 4-6 is used to fit experimental data only from the start of the second phase to the failure. Figure 4-17 presents an example of fitting used to determine E from equation 4-6 for 7-mm pellet at 89 MPa of suction.

Figure 4-18 then presents experimental results at all suction values for 7-mm pellets, where the two aforescribed phases are identified. Figure 4-19 presents the results for 32-mm pellets without the first phase. Only one test is performed at each suction on 32-mm pellets.

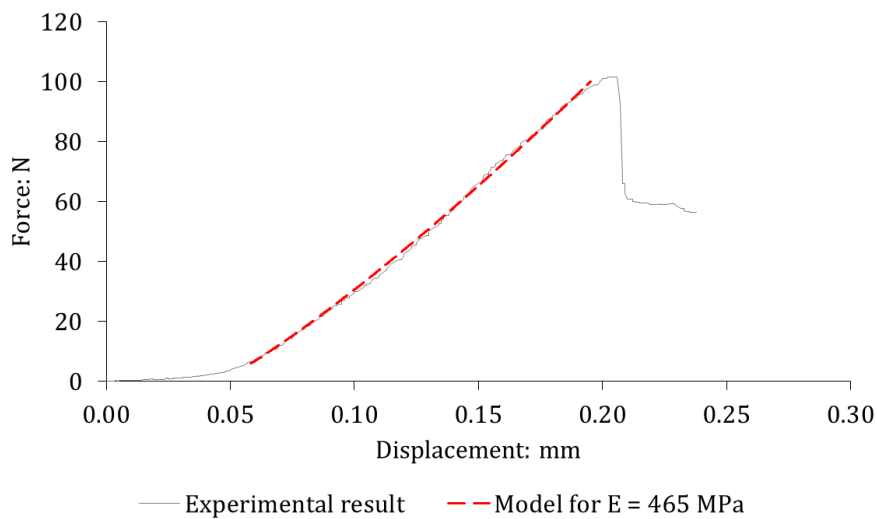
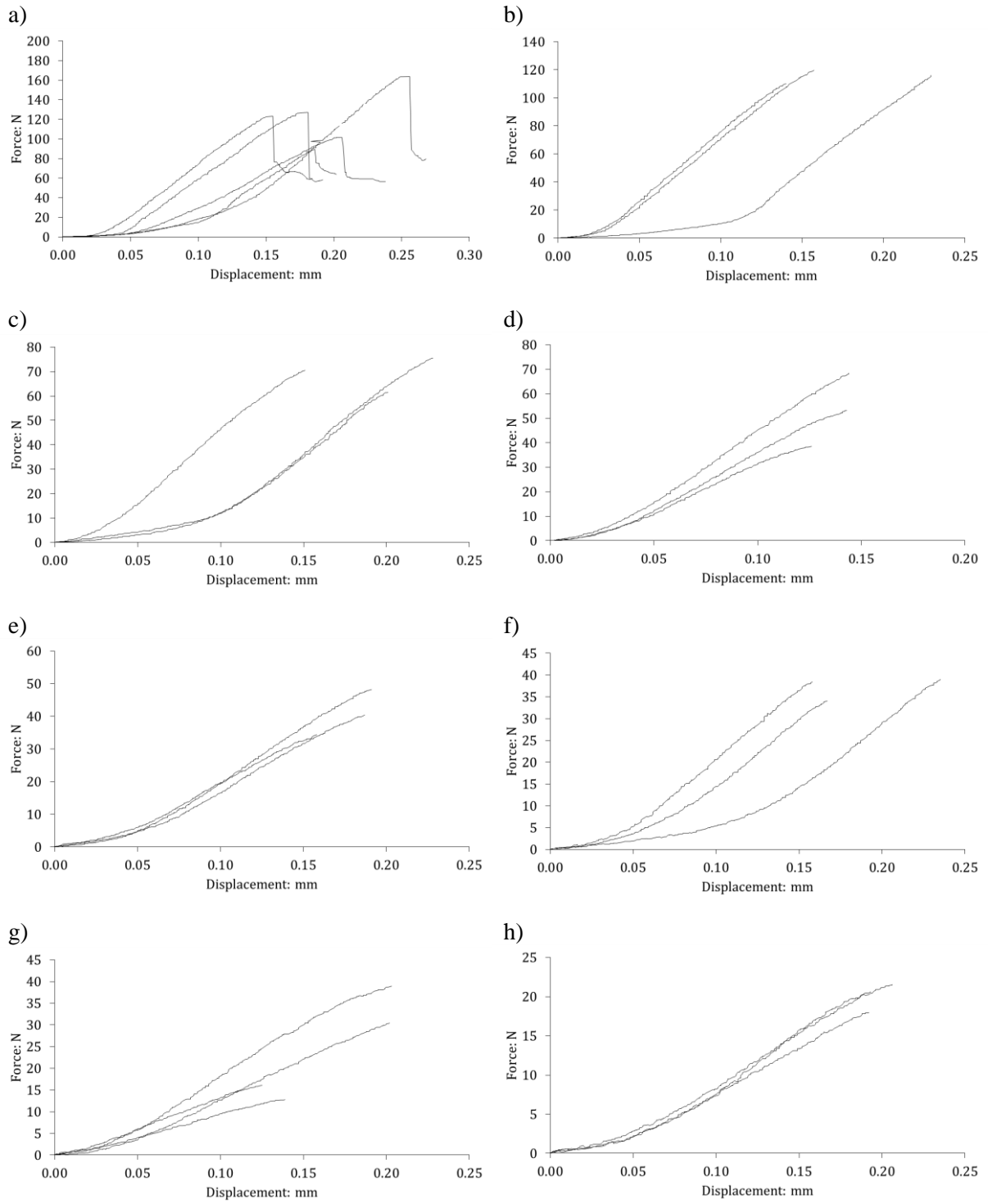


Figure 4-17: Determination of E in radial tests using equation 4-6.



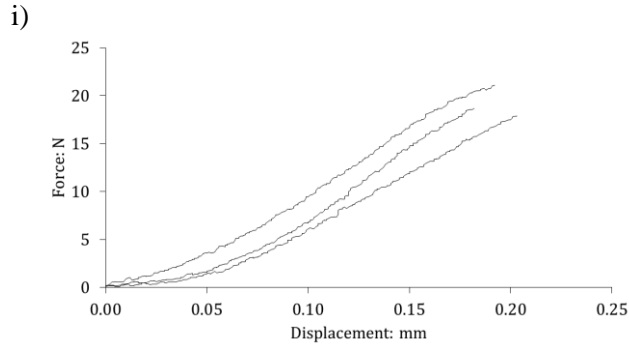


Figure 4-18: Radial test results for 7-mm pellets. Solid black lines are the experimental force-displacement relationships. Tests are performed at different suctions: a) 89 MPa; b) 82 MPa; c) 59 MPa; d) 57 MPa; e) 40 MPa; f) 38 MPa; g) 25 MPa; h) 13 MPa; i) 9 MPa.

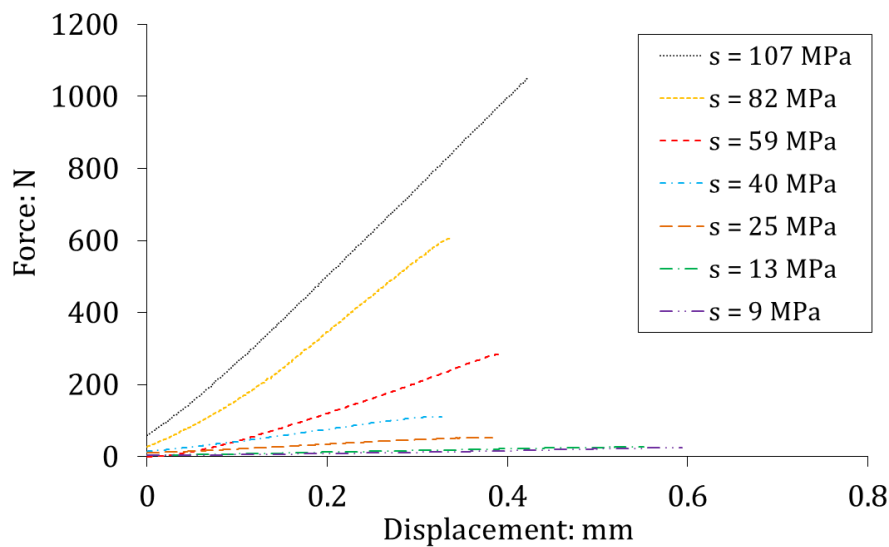


Figure 4-19: Radial test results for 32-mm pellets.

4.2.4.4 Stiffness evolution upon suction decrease

The values obtained for E using equations 4-5 and 4-6 for axial and radial tests, respectively, are plotted as functions of suction in Figure 4-20 (7-mm pellet) and Figure 4-21 (32-mm pellet). In the investigated suction range, moduli obtained in both directions are of the same order of magnitude. In this respect, a single mean value of the modulus can be proposed for each suction. For 7-mm pellets, the modulus decreases from ~ 625 MPa to ~ 55 MPa when suction decreases from 89 MPa to 9 MPa. For 32-mm pellets, the modulus decreases from ~ 515 MPa to ~ 10 MPa when suction decreases from 107 MPa to 9 MPa.

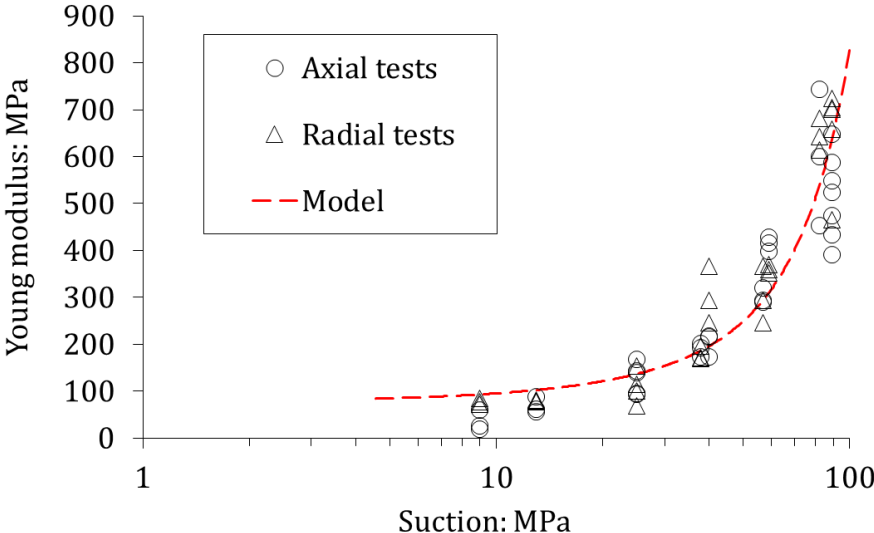


Figure 4-20: Evolution of the experimental results for E in axial and radial tests for the 7-mm pellet.

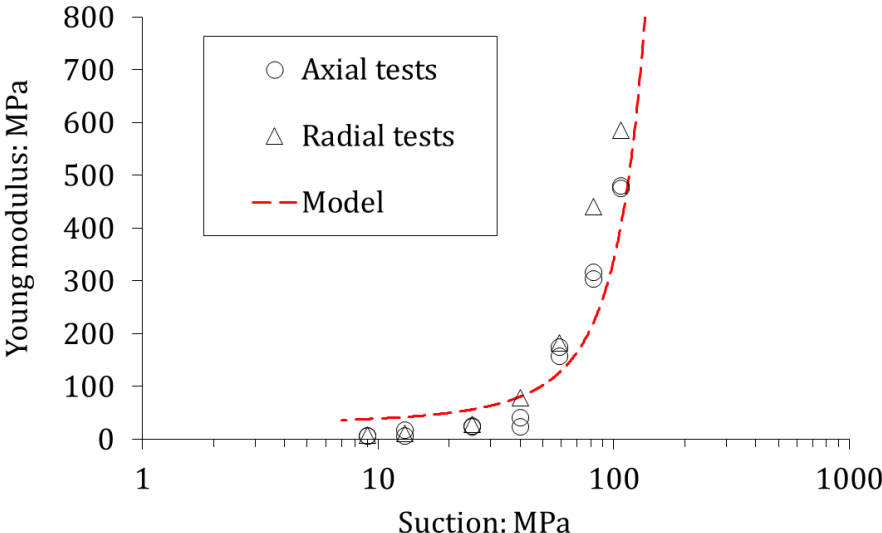


Figure 4-21: Evolution of the experimental results for E in axial and radial tests for the 32-mm pellet.

4.2.4.5 Strength evolution upon suction decrease

Figure 4-22 and Figure 4-23 present experimental results for axial strength and radial strength, for 7-mm pellet and 32-mm pellet, respectively. Upon hydration from 89 MPa to 9 MPa of suction, for 7-mm pellet, the mean value of normal force at failure during radial compression, R_R , decreases from ~120 N to ~20 N while during axial compression the mean value of normal force at failure, R_A , decreases from ~70 N to ~10 N. Upon hydration, R_R decreases from ~1050 N to ~25 N while R_A decreases from ~860 N to ~25 N for 32-mm pellet. It is reminded that R_A is determined from tests in which contact between pellet and the load frame is punctual while R_R is determined from tests in which contact between pellet and the load frame is linear.

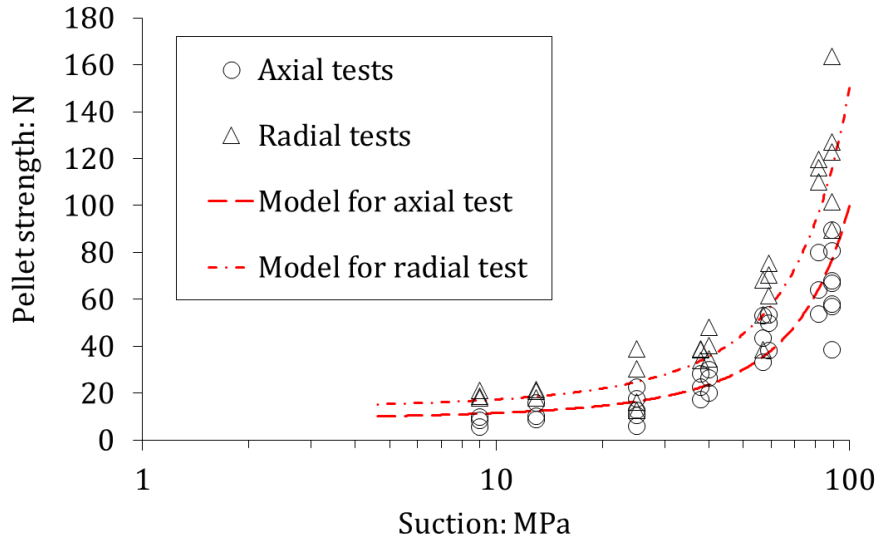


Figure 4-22: Experimental results for pellet (7 mm) strength upon suction decrease in axial and radial directions. Red dashed lines represent the model predictions for $R_A(s)$ and $R_R(s)$.

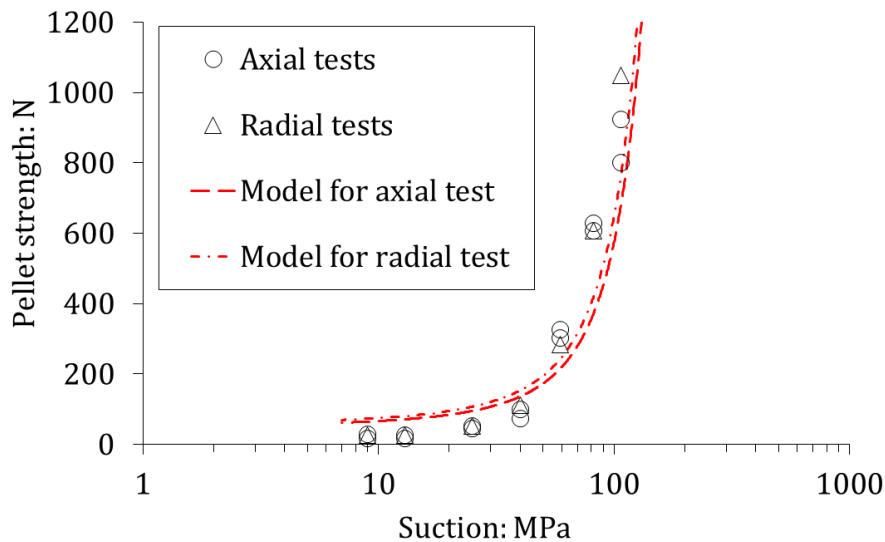


Figure 4-23: Experimental results for pellet (32 mm) strength upon suction decrease in axial and radial directions. Red dashed lines represent the model predictions for $R_A(s)$ and $R_R(s)$.

4.2.5 Model describing the hydromechanical behaviour of a pellet

In the present work, pellet initial dry density is high and it is assumed that its behaviour can be described, in the conceptual framework of double porosity expansive materials, by its microstructure and described by the effective stress (*e.g.* Mašin and Khalili, 2016). As highlighted in 4.2.4.1, pellets are not fully saturated. However, as discussed in Chapter 2, the microstructure of MX80 bentonite is likely to be saturated below ~ 100 MPa of suction. The behaviour being assumed to be described by the microstructure, partial saturation is not taken into account in the model for a pellet. Alonso et al. (1999) expressed the increment of microstructural volumetric strain as:

$$d\varepsilon_{vm} = \frac{dp'_m}{K_m} \quad 4-8$$

Where p'_m and K_m are the microstructural effective stress and microstructural bulk modulus, respectively. Considering that microstructure is saturated, p'_m can be expressed as:

$$p'_m = p_m + s_m \quad 4-9$$

Where p_m is the mean stress applied to the microstructure and s_m is the microstructural suction.

It is proposed to use the exponential relationship initially proposed by Alonso et al. (1999) for expansive clays microstructure for the pellet bulk modulus K_m :

$$K_m = \frac{1}{\beta_m} \exp(\alpha_m p'_m) \quad 4-10$$

In experimental results presented in the present section, pellets experience free-swelling conditions and it is assumed that $p'_m = s_m$. Figure 4-24 and Figure 4-25 present the relationship between pellet strengths in axial and radial directions and pellet Young modulus.

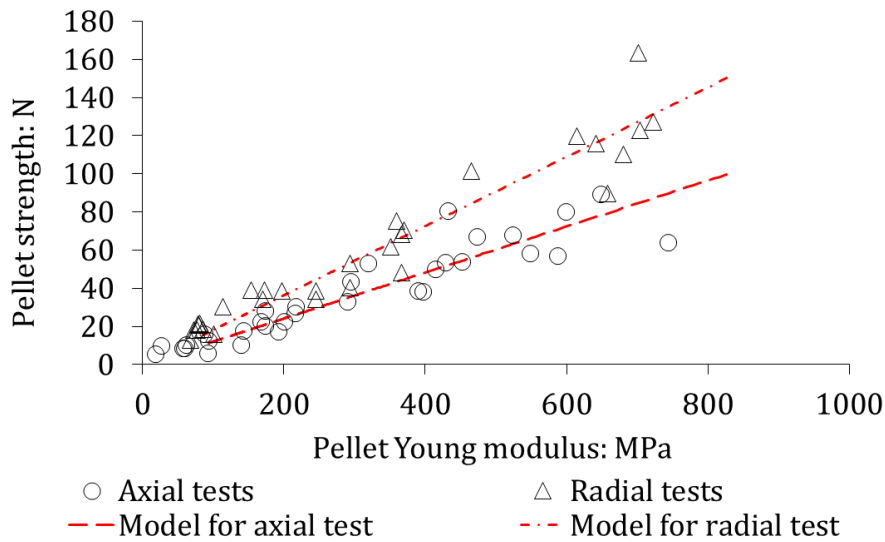


Figure 4-24: Relationship between pellet strength and pellet Young modulus. Experimental results for 7-mm pellet. The red dashed lines represent the model predictions.

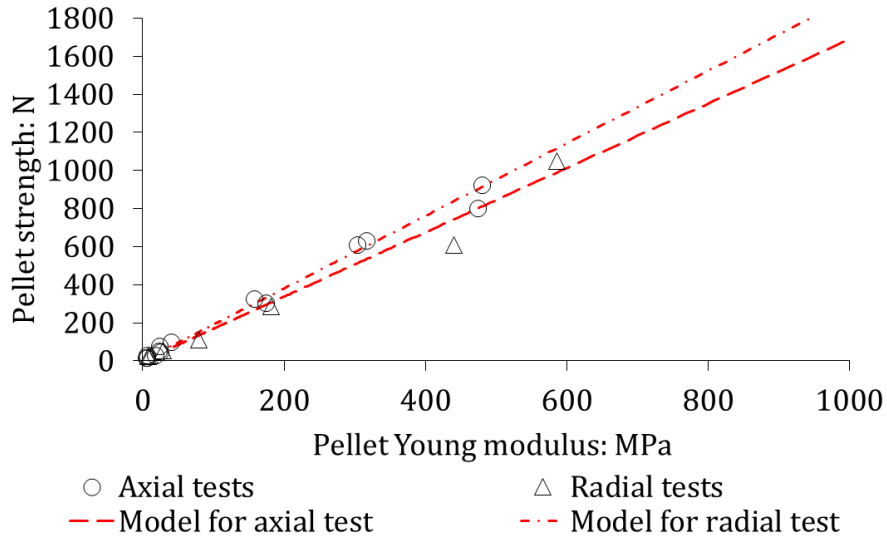


Figure 4-25: Relationship between pellet strength and pellet Young modulus. Experimental results for 32-mm pellet. The red dashed lines represent the model predictions.

From these results, it is conveniently assumed that pellet strength is proportional to pellet Young modulus. R_A and R_R are therefore expressed as:

$$R_A = C_A E \quad 4-11$$

And

$$R_R = C_R E \quad 4-12$$

Where C_A and C_R are model parameters relating the strength to the modulus for axial and radial compression tests, respectively. From equations 4-10, 4-11, and 4-12, the evolution of pellet axial and radial strengths are expressed as follows:

$$R_A = 3 C_A (1 - 2\nu) \frac{1}{\beta_m} \exp(\alpha_m p'_m) \quad 4-13$$

And

$$R_R = 3 C_R (1 - 2\nu) \frac{1}{\beta_m} \exp(\alpha_m p'_m) \quad 4-14$$

From compression test results only, values of α_m , β_m , C_A and C_R are determined for 7-mm and 32-mm pellets. These values are summarised in Table 4-4.

Table 4-4: Parameters proposed to describe the hydromechanical behaviour of single MX80 pellets, determined from compression tests.

Model parameter	7-mm pellet	32-mm pellet
α_m : MPa ⁻¹		0.024
β_m : MPa ⁻¹	0.016	0.039
C_A : m ²	1.21 x10 ⁻⁷	16.9 x10 ⁻⁷
C_R : m ²	1.82 x10 ⁻⁷	19.1 x10 ⁻⁷

From equations 4-8, 4-9 and 4-10, the volumetric strain at a given suction s_m , in free-swelling conditions, is expressed as:

$$\varepsilon_{Vm} = \frac{\beta_m}{\alpha_m} [\exp(-\alpha_m s_m) - \exp(-\alpha_m s_{m0})] \quad 4-15$$

Where s_{m0} is the pellet initial suction. From equations 4-10, 4-13, 4-14, and 4-15, and parameters from Table 4-4, model predictions are plotted and compared to experimental results in Figure 4-10, Figure 4-11, Figure 4-20, Figure 4-21, Figure 4-22, Figure 4-23, Figure 4-24, and Figure 4-25. It is highlighted that, even if the pellet behaviour is simplified, model predictions satisfactorily reproduce the pellet behaviour in the investigated suction range. It is reminded that parameters in Table 4-4 are obtained from compression tests only.

4.3 SIMULATIONS OF SWELLING PRESSURE TESTS USING DEM

4.3.1 Introduction

DEM simulations have been successfully used in engineering problems involving irreversible changes in the volume of grains, such as the effect of particle thermal expansion in granular materials (Vargas and McCarthy, 2007; Zhao et al., 2017); or grain-scale modelling of the swelling behaviour of absorbent polymer particles upon hydration in hygienic products (Sweijen et al., 2017).

The ability of DEM to access microscopic phenomena and vary input parameters can provide valuable information about the behaviour of assemblies of pellets upon hydration-induced pellet swelling, which can be obtained neither through experimental tests, since only macroscopic phenomena are measurable most of the time, nor through FEM simulations, which require a homogeneous continuous medium. In this respect, DEM simulations can be considered as an interesting tool to study the hydromechanical behaviour of pellet materials while providing a better understanding of laboratory tests results.

The present section applies DEM to the simulation of the partial hydration of expansive clay pellet assemblies, based on the hydromechanical model for a single pellet proposed in the previous section. The model is validated by simulating suction-controlled swelling pressure tests carried out at laboratory scale (see Chapter 3). In the present sections, DEM simulations features are first presented. Numerical

results are then compared to experimental results. Finally, results concerning grain-scale phenomena, which can only be obtained through DEM simulations, are presented.

4.3.2 Description of the proposed simulation method

4.3.2.1 Overview of the DEM approach

In the DEM simulations carried out, each particle is modelled as a sphere. The hydromechanical behaviour of each sphere is described by the model proposed in the previous section. The sphere diameter, a_{eq} , is chosen such that its volume coincides with the pellet volume Ω_p :

$$a_{eq} = \left(\frac{6 \Omega_p}{\pi} \right)^{\frac{1}{3}} \quad 4-16$$

The initial value of a_{eq} is obtained from initial values of pellet mass and density: $a_{eq0} = 7.53$ mm.

In order to assess the capability of the model to reproduce the hydromechanical behaviour of the granular assembly, swelling pressure tests are simulated. In the simulations, the isochoric cell is modelled as a rigid cylinder (infinite Young's modulus), the height and diameter of which are the same as the cell used for the swelling pressure tests. 209 particles are simulated in each simulations, corresponding to the number of pellets in the swelling pressure tests performed in the laboratory (thus the same mass).

Simulations are carried out in two main steps:

- the preparation step, corresponding to the installation of model beads inside the cylinder and the cell closure;
- the hydration step.

Three different types of simulations are carried out and referred to as DEM01; DEM02; DEM03. For each type, 100 calculations are performed to quantify the variability of the results. The difference between the simulations is the initial position of the beads following the sample preparation. This point is described in 4.3.2.5. DEM01 simulations aim at reproducing the swelling pressure tests with optimised preparation to avoid initial pressure (no friction during preparation). DEM02 simulations aim at assessing the influence of a less optimised initial state following the preparation step on the material behaviour upon hydration (friction during preparation). In both DEM01 and DEM02, contact friction is taken into account during hydration. In DEM03 simulations, no contact friction is taken into account during both preparation and hydration steps (Table 4-5).

Table 4-5: Friction values used during preparation and hydration steps in DEM01, DEM02 and DEM03 simulations. 100 simulations are performed for each type of simulation.

Simulation	Friction coefficient, μ : dimensionless	
	<i>Preparation step</i>	<i>Swelling step</i>
DEM01	0	0.3
DEM02	0.3	0.3
DEM03	0	0

Details concerning the model for a pellet, hydration, contact laws, and preparation simulation steps are provided in the following sub-parts.

4.3.2.2 Modelled pellet behaviour

In DEM simulations, the pellet behaviour is described by the model described in 4.2.5. Young modulus is given by equation 4-10, pellet volumetric strain is given by equation 4-15. In DEM simulations, the pellet behaviour is assumed to be isotropic and pellets are modelled as spheres. As a consequence, contacts between pellets in DEM simulations are sub-punctual and pellet strength is given by equation 4-13.

4.3.2.3 Hydration behaviour

Pellet hydration and subsequent swelling are simulated by a simultaneous increase of all the bead diameters. It is therefore assumed that all pellets get hydrated at the same rate. The diameter increase at each hydration step varies from 0.1 % to 0.9 % from initial state (89 MPa of suction) to final state (9 MPa of suction). 60 diameter increments are imposed, for an overall diameter increase of ~15 %:

$$a_{eq\ i+1} = \epsilon_i a_{eq\ i} \quad 4-17$$

Where:

$$\epsilon_i = \exp \left[\ln \left(\frac{\epsilon_f}{\epsilon_0} \right) \left(\frac{a_{eq\ i} - a_{eq\ 0}}{a_{eq\ f} - a_{eq\ 0}} \right) + \ln(\epsilon_0) \right] \quad 4-18$$

Where ϵ_i characterises the diameter increment; ϵ_f and ϵ_0 are parameters taken equal to 10^{-2} and 10^{-3} , respectively; $a_{eq\ i}$ and $a_{eq\ f}$ are the equivalent diameters at step i and at the final suction value, respectively.

From imposed radius increments, the volumetric strain is deduced. The suction value corresponding to each hydration stage is obtained from equation 4-15. Stiffness and strength are obtained from equations 4-10 and 4-13, respectively.

Contact laws then allow the granular assembly evolution to be computed, taking into account the suction-dependency of the aforementioned material parameters.

4.3.2.4 Contact laws

In contacts between two bodies described by their respective curvature radius and Young modulus, the Hertz law (equation 4-2) relates the normal contact elastic force N to the normal elastic deflection at contact δ_N . In contacts between two spheres i and j , $\delta_{N\ ij}$ is computed as the difference between the distance between the two sphere centres, r_{ij} , and the sum of their equivalent diameters (Figure 4-26). Contact laws in the simulations are obtained from Hertz's law and the properties of the pellets and the wall.

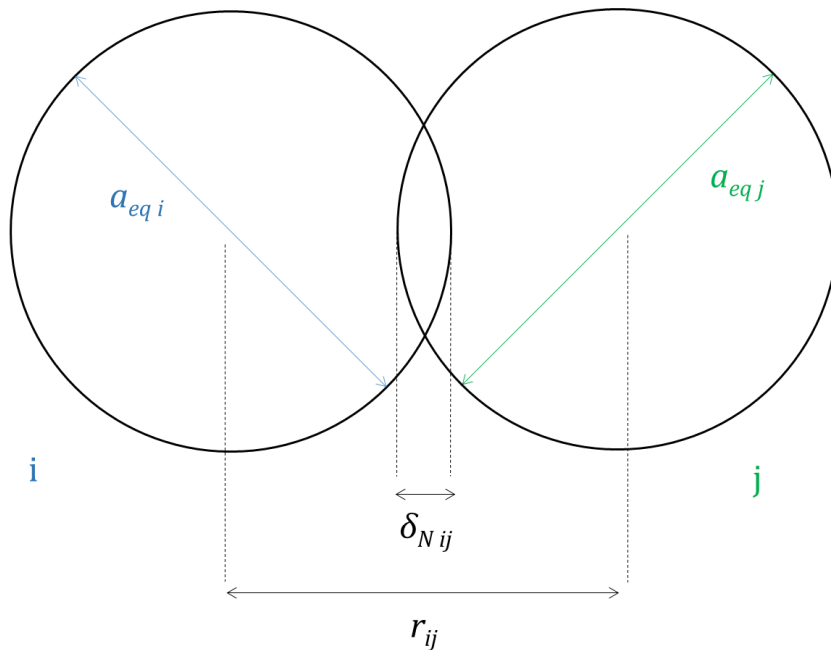


Figure 4-26: Sketch of two spheres in contact in DEM simulations

Contacts between two pellets satisfy:

$$N = \frac{1}{3} \frac{E}{(1 - \nu^2)} a_{eq}^{1/2} \delta_N^{3/2} \quad 4-19$$

Contacts between a pellet and the infinitely stiff flat walls satisfy:

$$N = \frac{2^{3/2}}{3} \frac{E}{(1 - \nu^2)} a_{eq}^{1/2} \delta_N^{3/2} \quad 4-20$$

Pellet strength is taken into account by considering perfect plasticity at contacts. The elastic part is described by the Hertz law (equations 4-19 and 4-20) and the elastic limit is given by equation 4-13 (assuming perfect plasticity). Thus,

$$N \leq R_A \quad 4-21$$

And plastic deflection can arise for $N = R_A$ (Figure 4-27).

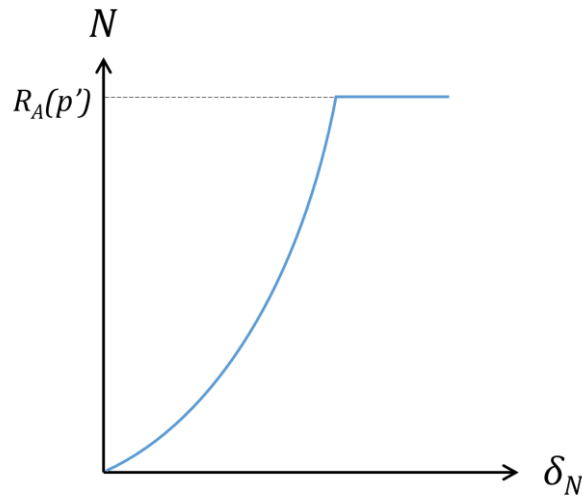


Figure 4-27: Normal force-normal deflection relationship in DEM simulations.

Tangential elasticity at contacts is described by a simplified form of the Cattaneo-Mindlin-Deresiewicz laws (Johnson, 1985), with due care for energetic consistency and objectivity, as proposed by Agnolin and Roux (2007a; 2007b). $d\mathbf{F}_T$, the increment of tangential reaction vector \mathbf{F}_T , is related to $d\delta_T$, the increment of relative tangential displacement vector δ_T , using the following equation:

$$d\mathbf{F}_T = \frac{2 - 2\nu}{2 - \nu} \frac{dN}{d\delta_N} d\delta_T \quad 4-22$$

The Coulomb condition is checked so that:

$$F_T \leq \mu N \quad 4-23$$

Where F_T is the norm of the \mathbf{F}_T vector and μ is a friction coefficient.

Sliding can arise for $F_T = \mu N$ (Figure 4-28). The same μ is taken for both pellet-pellet and pellet-wall contacts.

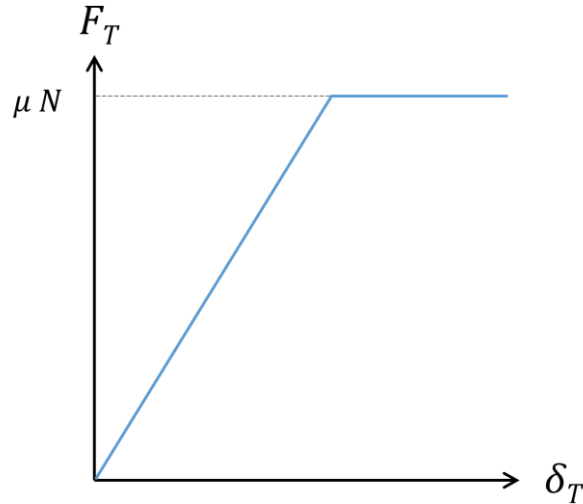


Figure 4-28: Diagram representing the tangential reaction-tangential displacement relationship in DEM simulations.

Damping is taken into account by adding a viscous component to the hertzian elastic force. The viscous component of the total contact force, N^v , in a contact between two pellets is written as:

$$N^v = \alpha_v \left(2 m_p \frac{dN}{d\delta_N} \right)^{1/2} \dot{\delta}_N \quad 4-24$$

Where α_v is a fraction of the critical damping coefficient, m_p is the mass of the particle, $\dot{\delta}_N$ is the time derivative of the normal deflection. Further discussion concerning the damping in contacts can be found in Agnolin and Roux (2007a).

4.3.2.5 Numerical sample preparation

Numerical samples are prepared by placing 209 pellets one by one in a rigid cylinder. The initial height of the cylinder, $H_{cell 0}$, is set at a value of $H_{cell} + a_{eq 0}$ to ensure that all the pellets can be placed in the cylinder (where H_{cell} is the cylinder height during the swelling step). A pellet is placed in the cell each second. The first 20 pellets are randomly placed at the bottom of the cell. Then, each pellet is placed at a calculated position corresponding to the lowest available point in the cell (Figure 4-29). During this process, the granular assembly is constantly being equilibrated under gravity. When all the pellets are placed in the cell, calculation continues until equilibrium is reached (details concerning equilibrium are provided in the following sub-part). The cell closure is then simulated by incrementally decreasing the cylinder height from $H_{cell 0}$ to H_{cell} . Each height decrease is followed by a calculation of a new equilibrium under gravity before a new decrease. Initial solid fraction of all the samples is the same as in experiment (0.553, corresponding to an inter-pellet porosity of 0.447).

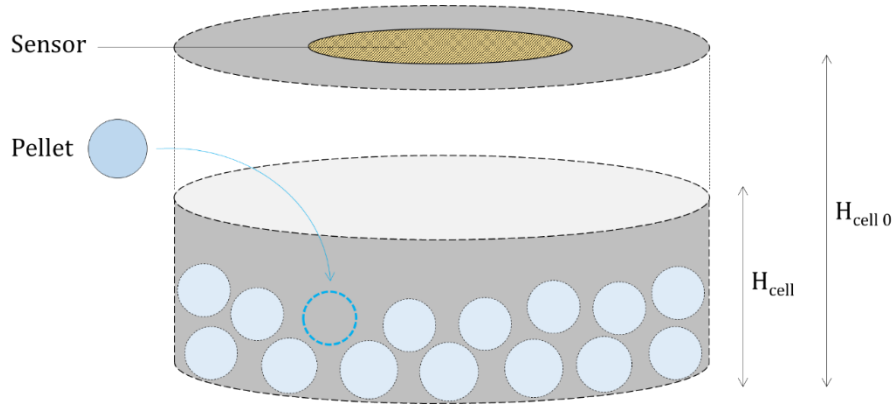


Figure 4-29: Preparation step in DEM simulations.

4.3.2.6 Equilibrium of forces and moments

At each calculation step (*i.e.* height decrease during preparation or new suction value during swelling), the granular assembly is considered at equilibrium if both the ratio of the net force F_{net} to the maximum normal force F_{max} and the ratio of the net moment Γ_{net} to the maximum moment Γ_{max} ratio are, on each pellet, smaller than a tolerance value ϵ :

$$|F_{net}| < \epsilon |F_{max}| \quad 4-25$$

$$|\Gamma_{net}| < \epsilon |F_{max}| \frac{a_{eq}}{2} \quad 4-26$$

ϵ is taken equal to 10^{-4} in all the simulations.

4.3.2.7 Swelling pressure calculation

At equilibrium, the swelling pressure P_S^* is computed as the total normal force exerted by the material onto the sensor, divided by the sensor area (Figure 4-30). The sensor area is at the centre of the upper wall and defined by the sensor diameter D_{sensor} . Thus, different values of swelling pressure can be obtained from one simulation results, depending on the value of D_{sensor} .

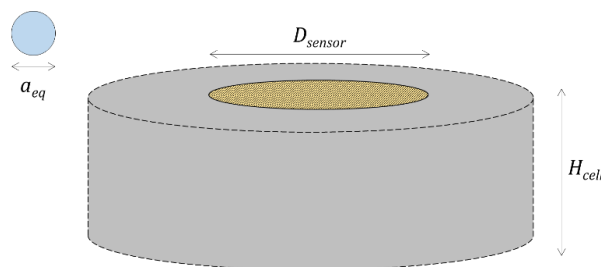


Figure 4-30: Dimensions of the simulated cell.

4.3.3 Numerical simulation results

4.3.3.1 Suction-swelling pressure relationship

Figure 4-31 presents the results of swelling pressure as functions of suction obtained in simulations DEM01; DEM02 and DEM03. As a reminder, 100 calculations were carried out for each type of simulations. Only the mean values of swelling pressure are plotted, for a ratio of sensor diameter to initial pellet diameter of 4 (close to the value of the ratio in experimental tests).

In DEM01 simulations, swelling pressure increases from 0 to 0.33 MPa as suction decreases from 89 MPa to 60 MPa, then slowly decreases to reach 0.11 MPa at 4 MPa of suction. In DEM02 simulations, swelling pressure reaches 0.50 MPa during the closure step, then slowly decreases to reach 0.11 MPa at 4 MPa of suction. In DEM03 simulations, the pressure slowly increases to 0.01 MPa from 89 MPa to 80 MPa of suction, then increases to 0.25 MPa at 60 MPa of suction, then slowly decreases to 0.11 MPa as suction decreases to 4 MPa.

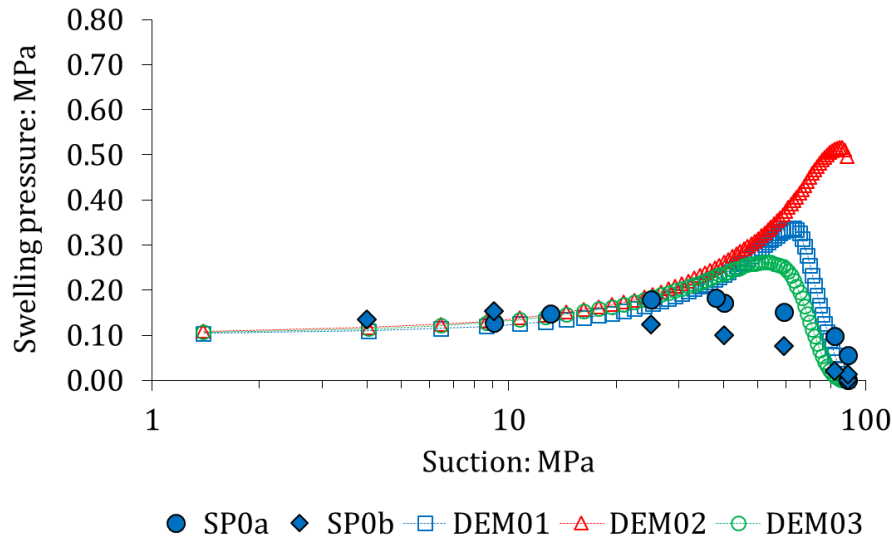


Figure 4-31: Evolution of the apparent swelling pressure in DEM01, DEM02 and DEM03 numerical samples and SP0a and SP0b experimental samples upon suction decrease. The mean values determined over 100 simulations are plotted for numerical results.

4.3.3.2 Contact plasticity in numerical samples

The evolution of the number of plastic contacts upon hydration is measured in numerical samples. Figure 4-32, Figure 4-33, and Figure 4-34 present the evolution of the mean plastic contacts proportion for the whole sample, $x_{c\ tot}^P$, and for contacts between pellets and the upper wall, where pressure is measured, $x_{c\ sup}^P$, for simulations DEM01, DEM02 and DEM03. Results are presented along with the swelling pressure development on suction decrease. In all samples, the increase in $x_{c\ sup}^P$ is more significant than the increase in $x_{c\ tot}^P$.

In DEM01, from initial state to 70 MPa of suction, the swelling pressure increases while no contact has reached the elastic limit. The number of plastic contacts increases sharply between 70 MPa and

60 MPa of suction. This suction range corresponds to the peak swelling pressure. The swelling pressure then slowly decreases, as $x_{c\ sup}^p$ keeps slowly increasing in the whole sample.

The evolution of plastic contacts in DEM03 simulations exhibited a similar overall trend as in DEM01, but the increase of $x_{c\ tot}^p$ and $x_{c\ sup}^p$ was not as sharp as in DEM01. In DEM02 simulations, the pressure increase due to the cell closure induced contact plasticity. The influence of the closure step in this case is significant. 25 “pellet-upper wall” contacts were created during this step. 15 of these contacts reached the elastic limit during the process, which represents 2.5 % of the overall 600 contacts in the samples (mean values determined for the 100 simulations). Yet, no significant increase of swelling pressure is recorded upon hydration. The measured pressure keeps decreasing as $x_{c\ tot}^p$ and $x_{c\ sup}^p$ increase.

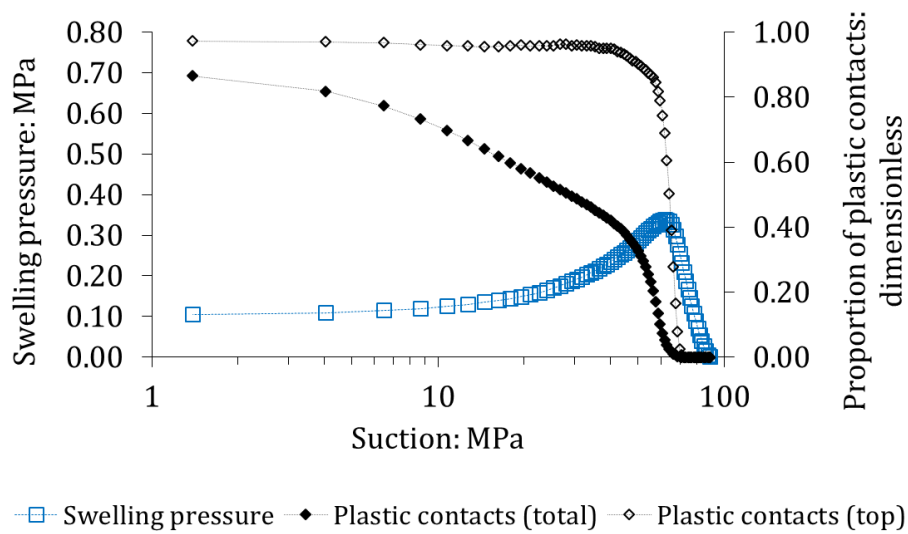


Figure 4-32: Evolution of the apparent swelling pressure and contact plasticity in DEM01 numerical samples upon suction decrease. The mean values determined over 100 simulations are plotted.

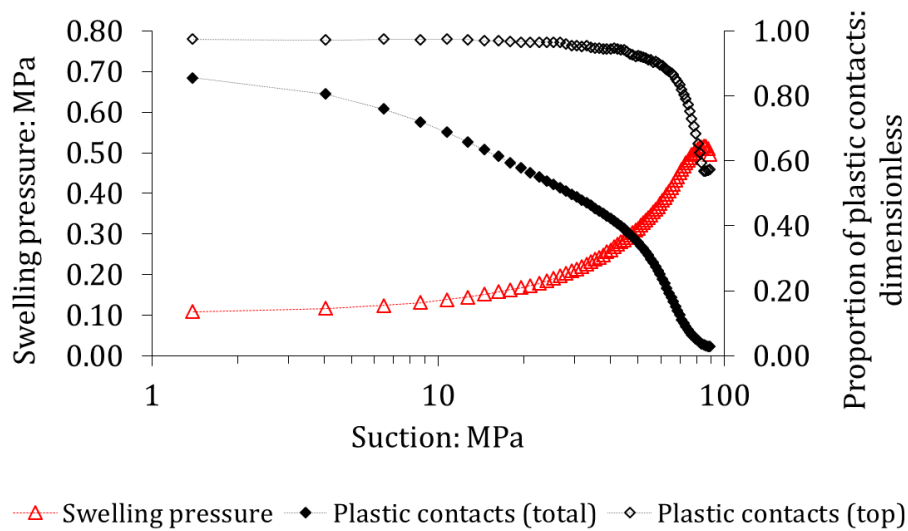


Figure 4-33: Evolution of the apparent swelling pressure and contact plasticity in DEM02 numerical samples upon suction decrease. The mean values determined over 100 simulations are plotted.

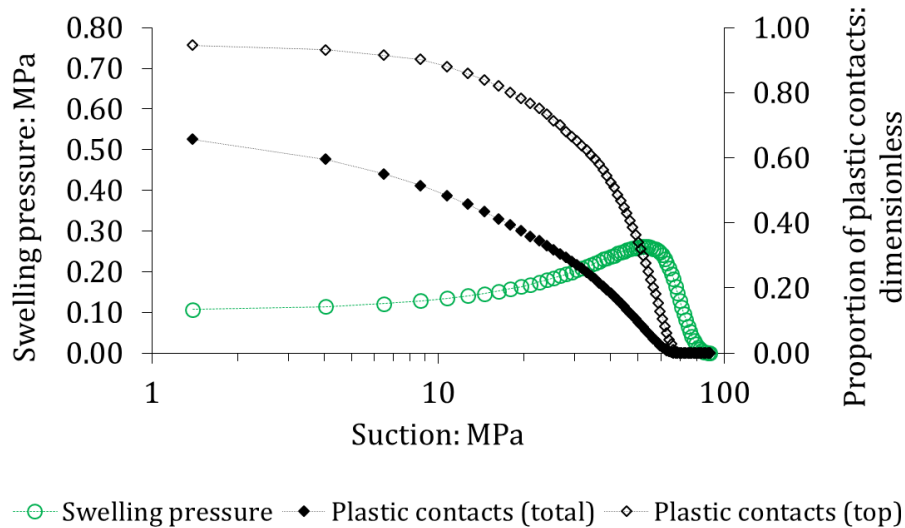


Figure 4-34: Evolution of the apparent swelling pressure and contact plasticity in DEM03 numerical samples upon suction decrease. The mean values determined over 100 simulations are plotted.

4.3.3.3 Coordination number in numerical samples

The coordination number Z , as defined by the average number of force-carrying contact per grain, relates to the number of particles N_p , the number of particle-particle contacts N_{c1} and the number of particle-wall contacts N_{c2} as:

$$Z = \frac{2 N_{c1} + N_{c2}}{N_p} \quad 4-27$$

Z is calculated following preparation and upon hydration. Results are presented in Figure 4-35 for simulations DEM01, DEM02 and DEM03.

After closure, the mean coordination number in samples prepared under zero-friction conditions (DEM01 and DEM03) is 5.4. The mean number of contacts in this case is 635, slightly higher than $3 N_p$, as it should be for frictionless beads approaching the limit of small deflections (Roux, 2000).

The presence of friction in the assembling stage reduces the number of contacts (Agnolin and Roux, 2007a). Thus samples DEM02 contain 600 contacts on average, with a coordination number of 5.1.

Upon hydration, the coordination number of frictionless samples (DEM03) increases to a final value of 8.2 (net increase: + 2.8). The coordination number of both DEM01 and DEM02 samples increased at the same rate, reaching final values of 7.5 and 7.2 respectively (net increase: + 2.1).

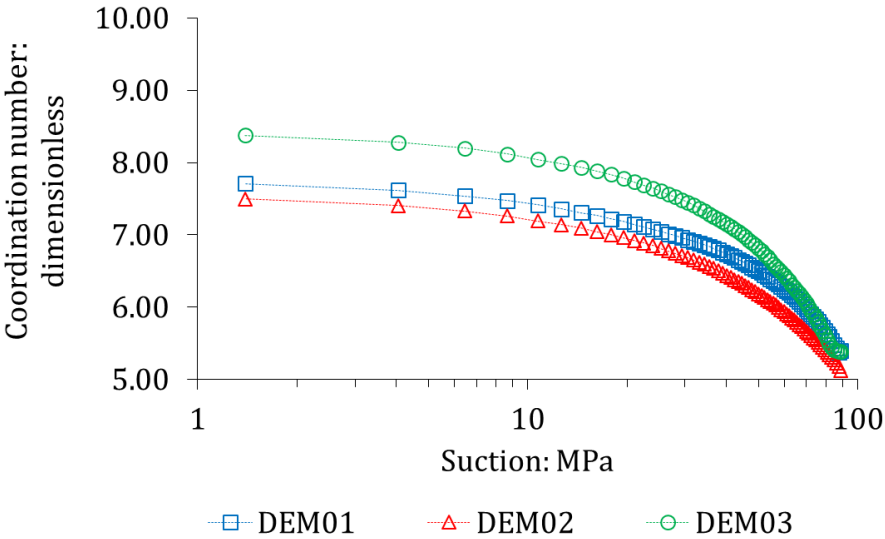


Figure 4-35: Evolution of the coordination number in numerical samples upon suction decrease. The mean values determined over 100 simulations are plotted.

4.3.3.4 Variability of DEM simulation results

The coefficient of variation, *CV*, (standard deviation to mean value ratio) of swelling pressure, proportion of plastic contacts and coordination number for the three simulation types is calculated from the 100 simulations performed and presented in Figure 4-36.

The result variability for swelling pressure and proportion of plastic contacts decreased upon hydration for the three types of simulation. At 9 MPa of suction, its value for swelling pressure reached ~0.10-0.15 (for $D_{sensor} / a_{eq} = 4$). Its value for proportion of plastic contacts reached ~0.03-0.04. The coefficient of variation of coordination number remained low (< 0.02) for the three types of simulation upon hydration.

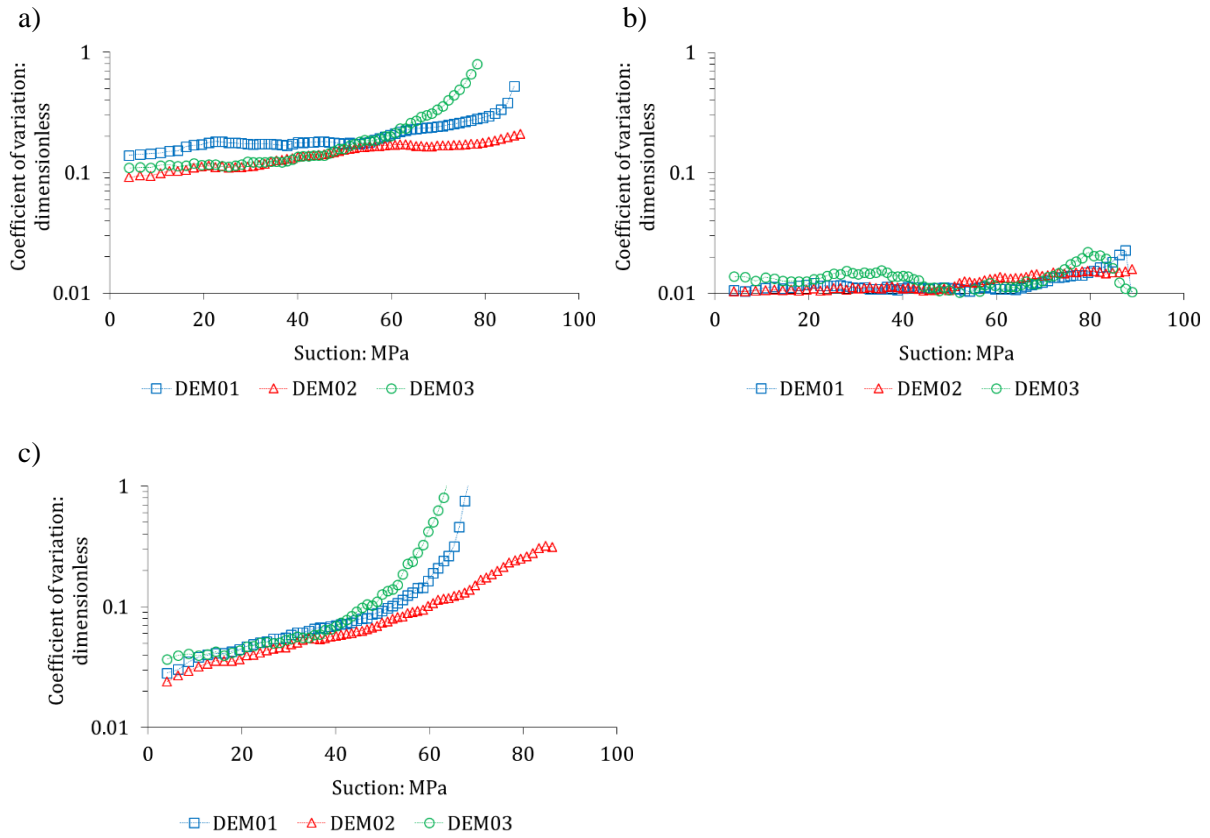


Figure 4-36: Evolution of the coefficient of variation of some features of numerical samples during hydration: a) swelling pressure; b) coordination number; c) proportion of plastic contacts.

4.3.3.5 Influence of the sensor diameter to pellet diameter ratio

In DEM01 simulations, the calculation of swelling pressure from contact forces between pellets and the upper wall is carried out for different values of D_{sensor} . For the same calculation, different suction-swelling pressure relationships are thus obtained. For instance, Figure 4-37 presents the swelling pressure calculated for two values of the diameter ratio $D_{sensor} / a_{eq 0}$. In both cases, an interval of two standard deviations from the mean value is determined over the 100 simulations.

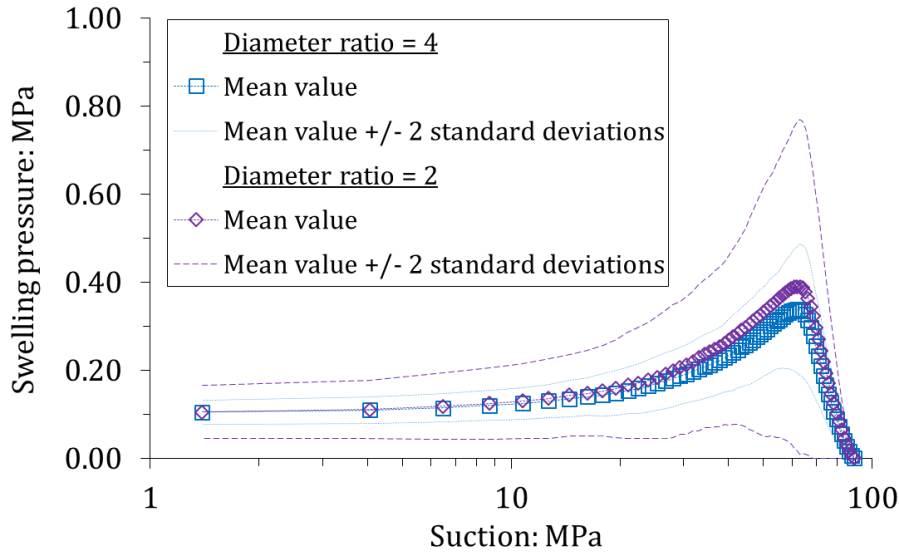


Figure 4-37: Evolution of apparent swelling pressure in DEM01 numerical samples upon suction decrease for two diameter ratios.

The coefficient of variation is determined for six sensor diameter to pellet diameter ratios, at peak and at 9 MPa of suction. Results are plotted in Figure 4-38. The coefficient of variation for the apparent swelling pressure reaches 0.8 to 1.3 in the case where both the sensor diameter and the initial pellet diameter are identical.

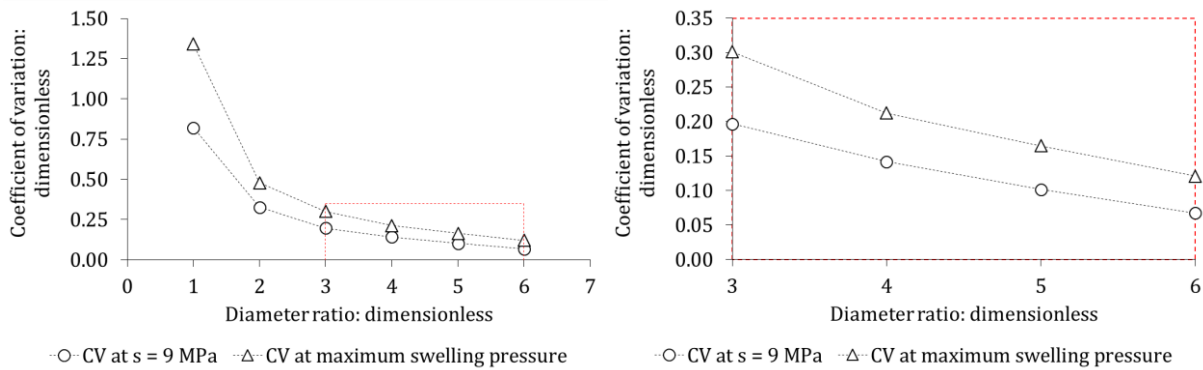


Figure 4-38: Variability of the calculated swelling pressure as a function of the diameter ratio ($D_{sensor} / a_{eq 0}$). Left: overview, right: zoom on diameter ratio between 3 and 6.

4.4 DISCUSSION

A numerical approach based on DEM has been proposed from pellet-scale experimental characterisation in the laboratory. This latter allows the hydromechanical behaviour of expansive clay pellet materials to be studied through DEM simulations of swelling pressure tests, providing interesting access to microscopic phenomena. In the following parts, the behaviour of a single pellet and the model validity are first discussed. Then, the material behaviour upon hydration under constant-volume conditions as well as interesting contributions of DEM to interpretation of laboratory tests results and constitutive modelling using double structure models are discussed.

4.4.1 Hydromechanical behaviour of a single pellet

The numerical results presented in the previous section have been obtained by describing the pellet behaviour using the model presented in 4.2.5. This latter is based on a pellet-scale experimental characterisation and hypotheses to simplify the pellet behaviour.

Experimental results show that partial hydration induces an increase in water content and pellet volume and a decrease in Young's modulus and strength. These trends agree with existing results on bentonite-based materials (Wiebe et al., 1998; Blatz et al., 2002; Lloret et al., 2003; Tang and Cui, 2009; Carrier et al., 2016).

The volumetric strain obtained in this study for 32-mm pellet is found to be higher than the volumetric strain obtained for 7-mm pellet. Besides, the volumetric strain obtained for 7-mm pellet is higher than that observed on a single MX80 bentonite aggregate (Tang and Cui, 2009). From the values of α_m and β_m proposed by Tang and Cui (2009) and those obtained in the present study, the evolution of the bulk modulus and volumetric strain of a MX80 aggregate, 7-mm pellet, and 32-mm pellet are plotted as a function of suction in Figure 4-39.

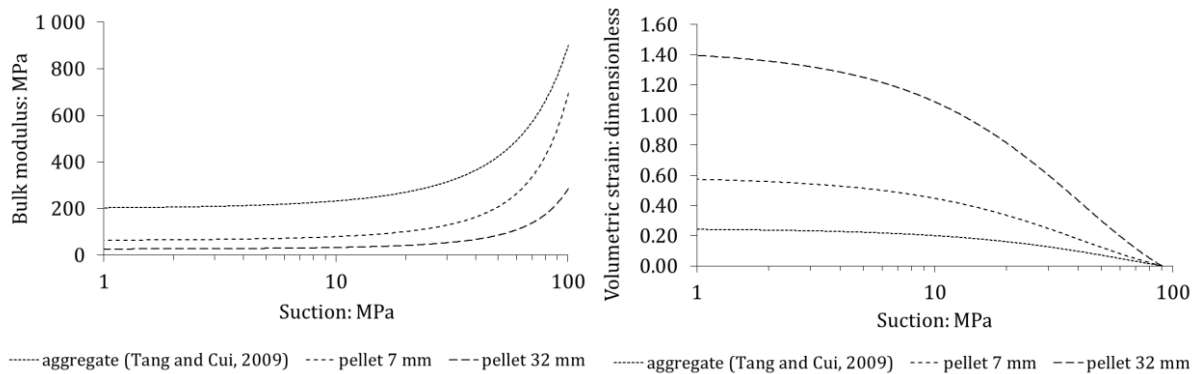


Figure 4-39: Evolution of the bulk modulus and volumetric strain of a MX80 aggregate, 7-mm pellet, and 32-mm pellet from values of α_m and β_m determined by Tang and Cui (2009) and in the present study.

In addition, Young's modulus measured in this study is generally smaller for 32-mm pellet than for 7-mm pellet. 7-mm pellet Young's modulus also is found to be nearly one order of magnitude smaller than that measured by Carrier et al. (2016) on MX80 bentonite clay film over the same suction range (obtained in the direction parallel to the film through tensile experiments). The Young modulus for the clay film was ~ 3000 MPa at $s \approx 100$ MPa; ~ 2000 MPa at $s \approx 60$ MPa; and ~ 1000 MPa at $s \approx 30$ MPa, whereas it is, as predicted by the model (equation 4-10), 826 MPa at $s = 100$ MPa; 316 MPa at $s = 60$ MPa; and 154 MPa at $s = 30$ MPa for the 7-mm pellet. It highlights that the mechanical behaviour of the material is affected by the dimensions of the sample.

It is also interesting to note that the results obtained by compression tests can be used to predict the results obtained by wetting (*i.e.* considering that hydration is an elastic unloading). As discussed in Chapter 2, suction in bentonite materials cannot be straightforwardly compared to a negative pore pressure. It is therefore interesting to note that, according to the results presented in the present work, the contribution of suction and total stress to the volumetric behaviour are comparable in the investigated suction range. This observation may help justifying the use of a model formulation implicitly considering that suction is a negative pore pressure, since it does not prevent the material behaviour to be satisfactorily reproduced.

However, it is reminded that the behaviour of the pellet observed in this study does not correspond to all the assumptions proposed for an aggregate in the model of Alonso et al. (1999): *i*) the pellet is not fully saturated; *ii*) its behaviour is not reversible upon unloading and *iii*) the volumetric behaviour of the pellet is not isotropic. In spite of these disagreements, the model correctly predicts the hydromechanical behaviour of a pellet during this partial hydration path (up to 9 MPa of suction). Because of the assumptions previously described, it is suggested that extrapolation at suction not inside the investigated suction range should be made carefully. In addition, at suction slightly lower than the lower limit of the investigated range, the pellet is likely to undergo fabric rearrangement as discussed in Chapter 2. This feature cannot be described by this simple model.

4.4.2 Validity of the DEM model

The proposed DEM model validity mainly depends on the following assumptions:

- the material remains granular;
- the shape retained for the simulated pellets does not induce significant behaviour differences;
- the contact laws are valid;
- pellet hydration can be simulated by a radius increase.

Sample dismantling allowed the material granular nature to be observed upon hydration to suction value as low as 4 MPa (Figure 3-16). Furthermore, the shape of the pellets was not notably modified. Only local deformation is observable at contact area. These deformations are irreversible.

In the simulations, pellets are modelled as isotropic spheres. Their real shape is shown to remain nearly identical upon hydration (Figure 3-16), but is characterised by a cylinder-shaped part between two spherical ends. Pellets are nonetheless sub-spherical and characterised by an aspect ratio (total height to diameter ratio) equal to 1. Wiacek et al. (2012) showed that uniaxial compression of sub-spherical pea seeds could effectively be modelled by spheres in DEM simulations. Furthermore, experimental results show small differences between axial and radial values of elastic modulus for pellets within the investigated suction range. It is thus thought that isotropic beads are a suitable choice to model these bentonite pellets.

Assuming linear elasticity, the normal force-deflection relationship at contact is described by the Hertz law (equations 4-2, 4-19, and 4-20) which has been shown to satisfactorily reproduce the experimental pellet force-deflection relationship in part 4.2.4. It is proposed to include the influence of pellet failure in the model to avoid reaching unrealistic high normal force values. It is assumed that failure initiates at contact and does not depend on the pellet stress state. The pellet strength in the granular assembly is thus assumed to be described by the empirical equation proposed for free-swelling conditions (equation 4-11). As suggested by Figure 3-16, pellet failure is more characterised by an irreversible deformation at contact or apparition of cracks than by a general crushing. In this respect, contact plasticity is thought to be an interesting way of modelling this phenomenon as it allows irreversible deflection to arise in simulations. Elastic-plastic contact modelling approach (Thornton and Ning, 1998; Thornton et al., 2017) are thus preferred to grain crushing modelling approach (Bolton et al., 2008; Cheng et al., 2004) to take into account grain failure. Compared to the framework introduced by Thornton and Ning (1998), the pellet elastic limit in the present study is given in term of a “limiting contact force”, given by R_A , directly obtained from experimental results, instead of a “limiting contact pressure”. Pellet failure in the simulation is thus taken into account by introducing perfect plasticity in

the contact law, with the pellet strength decreasing upon hydration (equation 4-13). The ratio of the mean total deflection to particle diameter using this approach remains lower than 0.07.

However, it is worth mentioning that experimental results evidenced a decrease of normal force at failure (constant suction), which is not taken into account by the perfect plasticity of the contact behaviour adopted in the present study. The calculated swelling pressure for suctions at which most of the contacts had reached the elastic limit appeared to be in the right order of magnitude nevertheless.

Modelling the swelling of spherical particles within a granular assembly by a radius increase has already been performed using DEM, for super absorbent polymer hydration (Sweijen et al., 2017) or thermal expansion effect in granular materials (Vargas and McCarthy, 2007; Zhao et al., 2017). In these works, a water/heat transfer was introduced and the particles would swell accordingly. In the present work, the approach is slightly different because no transfer law is introduced. All particles swell simultaneously, suction is calculated from equation 4-15 and all mechanical parameters vary accordingly. It is based on the assumption that vapour diffusion in inter-pellet porosity occurs significantly faster than absorption of water by pellets. The macropores are thought to be full of air at the same relative humidity (see Chapter 3). From Figure 3-16, it can be observed that the macroporosity is still clearly observable even at 4 MPa of suction. In addition, humid air is free to enter the sample macroporosity from either the bottom or the top of the cell. It is thus thought that the suction value imposed to all pellets is identical within the isochoric cell.

The model is able to reproduce the general “two phases” trend of the swelling pressure development observed in the laboratory (Figure 4-31). The second phase is close to experimental results. The first phase, characterised by a sharp increase of swelling pressure until a peak value is reached, is however overestimated by the model. These results can be interpreted as a consequence of several features: the modelled pellets are all identically shaped (perfect spheres of same diameter), have the same mechanical characteristics, cannot rearrange as a consequence of the small cell size ($H_{cell} / a_{eq 0} = 4$). During the second phase, the initial features of the granular assembly have less influence on the macroscopic response because contact forces reach the elastic limit. The evolution of swelling pressure mainly depends on the decrease of pellet strength and stiffness upon suction decrease, consistently with Hoffmann et al. (2007) and Alonso et al. (2010) conclusions concerning the behaviour of granular Febex bentonite upon hydration in constant volume conditions.

4.4.3 Modelling at low suction

The final swelling pressure of the studied material is estimated to be close to ~0.25 MPa (Chapter 3). This final value is higher than the final “plateau” value obtained in simulations. The swelling pressure should therefore increase again upon further suction decrease. The DEM model would be unable to reproduce this behaviour. As discussed in Chapter 2, compacted bentonite materials display a change in the hydration and subsequent swelling mechanism at low suction, at a threshold suction likely to be in the range ~3 MPa to ~7 MPa for MX80 in free-swelling conditions. Pellet fabric is significantly affected by this transition (Molinero-Guerra et al., 2019a).

Since the model is not able to reproduce the influence of fabric rearrangement on the pellet behaviour and the second increase of swelling pressure, it is considered not to be appropriate to describe the material behaviour upon further suction decrease. It is suggested that the proposed framework is suitable for suction higher than this threshold suction, even if the material has been observed to still be granular (Figure 3-16).

4.4.4 Influence of the walls on the measured response

Vargas and McCarthy (2007) performed simulations of particles swelling in both a fixed-walls and a free moving-walls cell. In the first case, particle swelling induced an increase of contact force instead of particle rearrangement. In the second case, the mean contact force was not significantly increasing upon particle radius increase. These two extreme cases highlight that the more particles rearrange, the more the coordination number will increase and the less contact forces will increase.

The evolution of the mean elastic normal deflection upon radius increase, at contact between pellets and the upper wall, is presented in Figure 4-40. DEM01 results are characterised by a nearly perfect linear deflection-radius variation relationship until reaching the peak swelling pressure. The linear relationship between these two parameters is close to the “1:1” line (*i.e.* $\Delta\delta_N = \Delta a_{eq}/2$) which implies negligible rearrangement of the granular assembly upon swelling. The swelling pressure increase is thus significant and elastic limit is reached almost simultaneously for many particles, resulting in an overestimated peak value and an accentuated transition between phases 1 and 2.

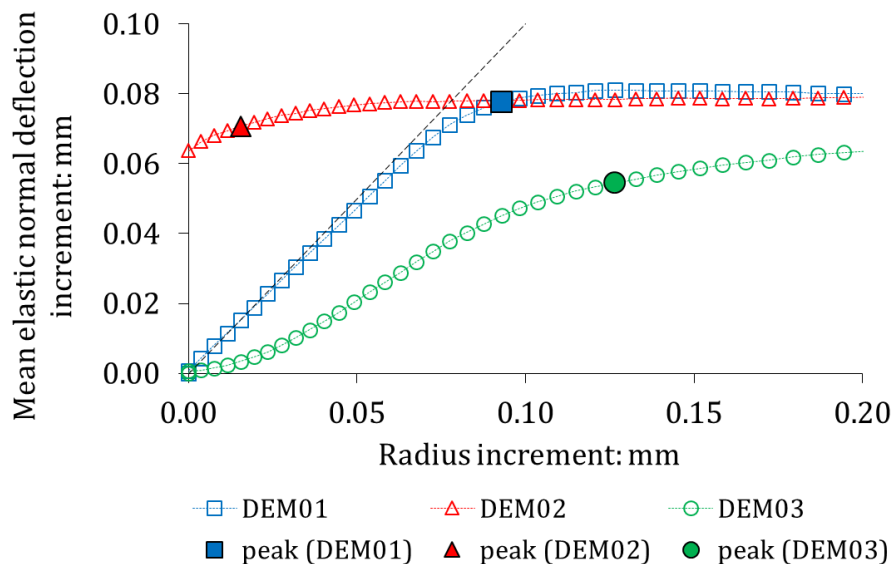


Figure 4-40: Mean elastic normal deflection increment as a function of radius increment for particles-upper wall contacts in simulations DEM01, DEM02, DEM03. The mean values, determined over 100 simulations, are plotted. The coloured dots correspond to the occurrence of the peak of swelling pressure. The black dashed line correspond to a “1:1” line, *i.e.* each radius increment induces a similar increment in mean elastic normal deflection, thus no rearrangement of the granular structure, provided that contacts are elastic.

This tendency towards deflection increase instead of particle rearrangement in the simulations is also underlined in Figure 4-40 by the significant increase of the mean elastic normal deflection after the cell closure in DEM02 simulations. The considered solid fraction (~ 0.553) is low and these features are likely not be observed in larger granular assemblies, less influenced by walls. Negligible rearrangements can also explain the more significant increase in contact plasticity at contacts with walls compared to the mean increase in the samples. As a consequence, the post-peak decrease of swelling pressure can be overestimated if measured at contact with the wall instead of calculating the mean stress in the sample, as highlighted by the comparison between apparent swelling pressure and sample mean stress (Figure 4-41).

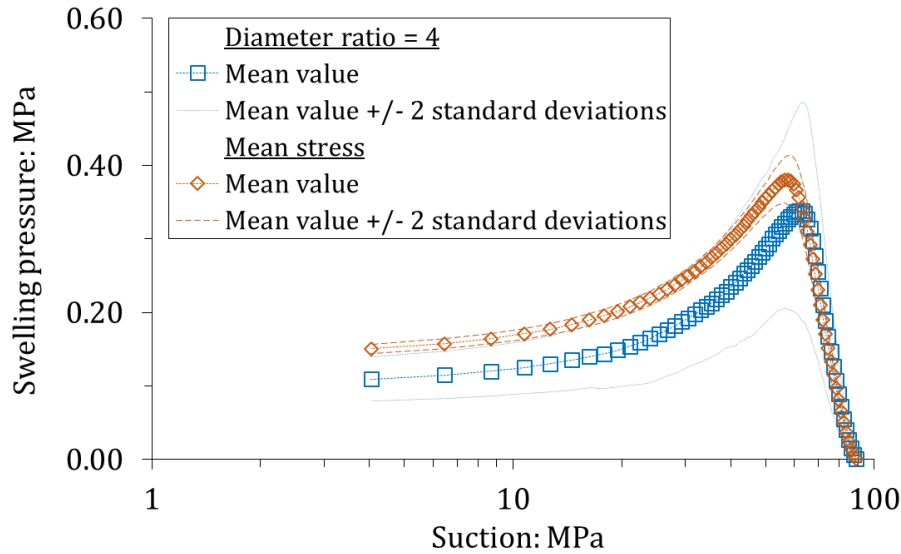


Figure 4-41: Evolution and variability of apparent swelling pressure ($D_{sensor} / a_{eq0} = 4$) and mean stress upon suction decrease in DEM01 simulations.

The influence of the walls is furthermore underlined by the coordination number following preparation (Figure 4-35): the coordination number of frictionless bead assemblies was 5.4 instead of the bulk value ~ 6 (Roux, 2000).

The numerical results suggest that the variability associated to sample preparation stems from wall influence. The ratio $H_{cell} / a_{eq0} = 4$ is thus too low to avoid wall influence. Since experimental tests share the same solid fraction and H_{cell} / a_{eq0} ratio, experimental results are influenced by the walls as well.

4.4.5 Contribution of DEM to laboratory testing

Thanks to the DEM ability to model the wall-particle interaction and access grain-scale phenomena, simulation results provide an insight into swelling pressure tests carried out at laboratory scale.

For instance, the influence of interaction at contacts on the macroscopic response was evidenced by DEM simulation results. The non-negligible influence of the cell wall on the measured response was also highlighted.

The influence of sample preparation on test results was also suggested by DEM simulation results (Figure 4-31). The general trend of DEM02 results suggests that initial pressure required to close the cell before hydration can cause a significant increase of plastic contact proportion (Figure 4-33). As a consequence, hydration phase 1 appeared very limited in DEM02 simulations. The numerical sample behaviour was mainly controlled by equations 4-10 and 4-11 and the number of contacts between pellets and the upper wall, rather than the pellet swelling. Even if plasticity does not arise during the closure step, closure can have an influence on the behaviour upon hydration. At granular state, the mean stress in the sample is proportional to the product of coordination number and mean contact force. It was suggested by results presented in Figure 4-35 that the coordination number evolution upon swelling is related to friction instead of sample preparation. Thus, samples prepared under initial closure pressure are likely to reach the elastic limit more rapidly. It is actually suggested by SP0a and SP0b test results. It is recommended that the control of the initial state is not less important as the target dry density to study the swelling pressure development of pellet materials.

In addition to variability arising from wall influence, small pressure sensors in the laboratory have been shown to increase the apparent swelling pressure variability. DEM allowed the influence of the pressure sensor diameter on the variability of the measured swelling pressure to be quantified. This latter, added to the variability of behaviour associated to the cell small size, increases the difficulty to study pellet mixture intrinsic behaviour at laboratory scale. For pellets with the same mechanical behaviour, the coefficient of variation of swelling pressure obtained from simulations thus depends on both preparation in a small cell and the sensor diameter to pellet diameter ratio.

It was discussed that an overestimation of the calculated swelling pressure can arise in the elastic phase of the pellet swelling from some of the model simplifications, especially at the highest suction values. However, concerning the variability of this measure, these simplifications may induce a decrease of the coefficient of variation. It can be supposed that, owing to the dispersion of the pellet real mechanical properties at high suctions, the calculated coefficient of variation of apparent swelling pressure is likely to be underestimated by the model in the elastic part of the hydration path. As contact forces reach the elastic limit, normal forces reach less dispersed values and the calculated coefficient of variation decreases. Experimental results (Figure 4-20, Figure 4-22) suggest that the dispersion of pellet mechanical properties is less significant at low suctions. The calculated coefficient of variation in the hydration second phase is therefore likely not to be underestimated. These results are of importance, since most of the time the material behaviour is studied at laboratory scale, with inevitable constraints concerning the number and sizes of sensors, related to the cell size. It is suggested that experiments performed to determine material parameters for modelling purpose should be interpreted with the orders of magnitude of variability corresponding to the sensor diameter in mind.

4.4.6 Contribution of DEM to constitutive modelling of pellet materials

The proposed DEM model has been shown to reproduce the main features of the material behaviour upon partial hydration in constant-volume conditions. The relationships between the behaviour of the pellets and the macrostructural behaviour can be identified. It can provide valuable information for the modelling of a full hydration path using double structure models. This modelling framework has been used in previous studies to model pellet materials upon hydration, considering the pellet phase as the microstructure (Alonso et al., 2011; Gens et al., 2011; Sanchez et al., 2016; Mokni et al., 2019).

For this purpose, DEM can be a complementary tool to experimental studies. It was highlighted that results of experimental tests performed at the laboratory scale on pellet mixtures can be characterised by a significant variability. This latter can make the determination of the material intrinsic behaviour difficult. DEM allows uncertainty and variability to be taken into account, at low simulation cost. DEM simulations may be performed in conditions where the intrinsic behaviour of the material can be addressed. For instance, DEM could help determining constitutive laws for the mechanical behaviour at the pellet assembly scale and its relationship with pellet properties.

In this respect, a perspective arising from the present study is to perform DEM simulations of large pellet assemblies of different solid fractions upon hydration, avoiding the influence of wall associated to small cell sizes. In this way, constitutive laws describing the material behaviour before the “granular”-“continuous” transition could be proposed and integrated in a double structure model to simulate the entire saturation path.

4.5 CONCLUSIONS AND PERSPECTIVES

The present Chapter presented the proposition and validation of a DEM modelling framework suitable to address the hydromechanical behaviour of expansive clay pellet assemblies upon partial hydration, before the “granular”-“continuous” transition. The main conclusions are summarised in the present section.

4.5.1 Behaviour of a single pellet upon partial hydration in free-swelling conditions

In this Chapter, the behaviour of a single high-density bentonite pellet upon partial hydration in free-swelling conditions and the associated variation of its mechanical properties are investigated in the laboratory. Pellet Young modulus and strength are shown to decrease upon hydration. A simple model, based on the framework proposed by Alonso et al. (1999) is used to describe the evolution of the pellet mechanical properties upon suction decrease. A single set of parameters can describe the evolution of the pellet volumetric strain, stiffness and strength upon suction decrease. These latter can be determined from compression tests in the laboratory, the realisation of which is simple.

As discussed in the present Chapter, the model satisfactorily describes the pellet behaviour in the investigated suction range. The model is valid for wetting path and is limited to suction higher than the threshold corresponding to the microstructure rearrangement, occurring at ~ 3 MPa to ~ 7 MPa in MX80 in free-swelling conditions. A more advanced model would be required to simulate, for instance, the behaviour of pellet following the microstructural rearrangement threshold, liquid water wetting destroying the granular structure, loading-unloading path or wetting-drying paths.

At high suction, the model is considered relevant to describe the behaviour of a particle in DEM simulations of swelling pressure tests of pellet assemblies.

4.5.2 Behaviour of pellet assemblies upon partial hydration in constant-volume conditions

A DEM-based model was described, implemented and validated against experimental results of suction-controlled swelling pressure tests. Using DEM provided an insight into the behaviour of pellet assemblies upon partial hydration in constant-volume conditions. In particular, the ability of DEM to access grain scale phenomena allowed some macroscopic features of the pellet assembly behaviour to be related to grain feature. The possibility to repeat a significant number of simulations at low time cost allowed the variability of the macroscopic response to be highlighted.

Pellet materials are characterised by an initial granular nature, which was shown in the present study to control the material behaviour upon hydration to suction as low as ~ 3 MPa to ~ 7 MPa. In particular, it was shown that, in constant-volume conditions, the pellet strength and stiffness control the macroscopic response. Upon hydration, the swelling pressure develops in two phases. The first is characterised by an elastic increase of the normal contact forces and is affected by the initial state of the material in small cells (*i.e.* by the sample preparation in laboratory tests). The second is characterised by the occurrence of contact plasticity and is less affected by the initial state.

4.5.3 Differences between measured response in the laboratory and intrinsic behaviour

Numerical results evidenced that the measured response in the laboratory is influenced by the sample preparation, the cell size and the sensor diameter. DEM results suggest that the 30 mm x 60 mm isochoric cell used to perform swelling pressure tests in the laboratory ($H_{cell} / a_{eq0} = 4$) is not a true representative elementary volume, due to its small size and the non-negligible influence of the wall. DEM results highlight that contact plasticity arises faster at contact with cell walls compared to the total sample. Wall effect in small cells can therefore induce differences between measured response and intrinsic behaviour and increase the difficulty of the preparation step. Besides, it was shown that a low value of the ratio of sensor diameter to pellet diameter induces significant measurement variability in the investigated suction range.

4.5.4 Determination of constitutive laws describing the mechanical behaviour of pellet assemblies

As discussed in the present Chapter, the proposed model is considered suitable to simulate the pellet behaviour using DEM upon partial hydration. Besides, DEM provided an insight into the mechanical behaviour of pellet assemblies. It was suggested that the scale of the study in the laboratory, and in associated simulations, is too small to assess the material (pellet assembly) intrinsic behaviour because of wall influence.

In this respect, an interesting perspective arising from the present study is the DEM modelling of large pellet assemblies upon hydration, with no influence of cell walls. The method presented in this Chapter can be applied in a similar way, but to significantly larger samples. Constitutive laws for the material before the “granular”-“continuous” transition could be proposed and would provide an interesting framework for FEM simulations of the entire hydration path, using double structure models.

5 MODELLING THE HYDROMECHANICAL BEHAVIOUR OF PELLET-BASED BENTONITE MATERIALS

5.1 INTRODUCTION

The present Chapter aims at proposing a modelling framework suitable for compacted expansive clay pellet-powder mixtures. The main objective of the proposed framework is to model mixtures as a continuum using FEM, while taking into account the initial granular structure and eventual heterogeneities of powder content.

Discussions in previous Chapters highlighted some relevant features of mixture behaviour which are addressed in the present Chapter. At high suction, a loose powder phase can induce a mechanical behaviour mostly controlled by the pellet assembly behaviour. At low suction, the material can be considered to behave as a continuum. Material parameters of interest are the pellet strength, stiffness and swelling potential in the first case. Following the “granular”-“continuous” transition, these are traditional elastic and elastoplastic stiffnesses.

The development, description and validation of the model against experimental results is presented in the present Chapter. The conceptual approach is first described in section 5.2. DEM simulations of large pellet assemblies, performed to determine constitutive laws for the material at granular state, are presented in section 5.3. Granular-continuous transition is addressed in section 5.4. Modifications of the conceptual framework of the BBM performed to model the material following transition are described in section 5.5. Implementation of the constitutive laws is presented in section 5.6. Model validation against experimental results is presented in section 5.7. Finally, main conclusions, advantages, identified limitations of the proposed approach, and perspectives arising from the present Chapter are summarised in section 5.8.

5.2 CONCEPTUAL APPROACH

An overview of the modelling approach is provided in the present section. Description of the different phases, introduction of some notations and main hypotheses are described in the following parts.

5.2.1 Description of the material phases

In the model, the pellet-powder mixture is described by two different levels of structure, and two different phases. Microstructure and macrostructure are the two structural levels and are associated to micropores and macropores, respectively, as in the conceptual framework introduced by Gens and Alonso (1992) and Alonso et al. (1999). The two phases composing the mixture are the pellet phase and the matrix phase. The pellet phase is composed of pellets only, described by their microstructure. The matrix is composed of the powder grains, described by their microstructure, and the remaining inter-granular voids, referred to as “macropores” in the following. Table 5-1 summarises the description of the phases.

Table 5-1: Overview of the phases and levels of structure describing the material in the model.

Material	Phases		
Mixture	Pellets		Solid phase
			Pores
	Matrix	Powder	Solid phase
			Pores
		Macropores	Pores

5.2.2 Main notations

In the present Chapter, the following notations are adopted:

- Total volume is written Ω , and volume of any phase i is written Ω_i ;
- Volume of solid and voids of any phase i are written Ω_{si} and Ω_{vi} , respectively;
- Volume fraction of any phase i is written Φ_i ;
- Total void ratio is written e , and void ratio of any phase i is written e_i ;
- Degree of saturation of any phase i is written S_{ri} .

The following subscripts are adopted:

- 1 is associated to the pellet phase;
- 2 is associated to the powder within the matrix phase;
- M is associated to the macropores within the matrix phase;
- m is associated to the micropores in pellets and powder.

All these notations are summarised in Table 5-2.

Table 5-2: Overview of the different notations used to describe the different phases in the model

Phase		Volume	Volume fraction	Void ratio	Saturation				
Pellet	Solid	Ω	Ω_1	1	Φ_1	e_1	e_m	S_{r1}	
	Pore								Ω_{v1}
Powder	Solid		Ω_2		Ω_{s2}	Φ_M		e_M	S_{rM}
	Pore								
Macropore	Pore	Ω_M							

Volumes, volume fractions and void ratios are defined by the following equations:

$$\Omega = \Omega_1 + \Omega_2 + \Omega_M \quad 5-1$$

$$\Omega_1 = \Omega_{v1} + \Omega_{s1} \quad 5-2$$

$$\Omega_2 = \Omega_{v2} + \Omega_{s2} \quad 5-3$$

$$\Phi_1 = \frac{\Omega_1}{\Omega} \quad 5-4$$

$$\Phi_2 = \frac{\Omega_2}{\Omega} \quad 5-5$$

$$\Phi_M = \frac{\Omega_M}{\Omega} \quad 5-6$$

$$e_1 = \frac{\Omega_{v1}}{\Omega_{s1}} \quad 5-7$$

$$e_2 = \frac{\Omega_{v2}}{\Omega_{s2}} \quad 5-8$$

$$e = \frac{\Omega_{v1} + \Omega_{v2} + \Omega_M}{\Omega_{s1} + \Omega_{s2}} \quad 5-9$$

$$e_m = \frac{\Omega_{v1} + \Omega_{v2}}{\Omega_{s1} + \Omega_{s2}} \quad 5-10$$

$$e_M = \frac{\Omega_M}{\Omega_{s1} + \Omega_{s2}} \quad 5-11$$

From 5-1, 5-4, 5-5, and 5-6, it is verified that:

$$\Phi_1 + \Phi_2 + \Phi_M = 1 \quad 5-12$$

From 5-9, 5-10, and 5-11 it is verified that:

$$e = e_m + e_M \quad 5-13$$

And

$$e = \frac{\Omega_{s1}}{\Omega_{s1} + \Omega_{s2}} e_1 + \frac{\Omega_{s2}}{\Omega_{s1} + \Omega_{s2}} e_2 + e_M \quad 5-14$$

An additional volume fraction is considered in the present Chapter and corresponds to the matrix volume fraction. This latter is written Φ_{mat} and defined as:

$$\Phi_{mat} = \frac{\Omega_2}{\Omega - \Omega_1} = \frac{\Omega_2}{\Omega (1 - \Phi_1)} = \frac{\Phi_2}{(1 - \Phi_1)} \quad 5-15$$

Total volumetric strain is written ε_V , and volumetric strain of any component i is written ε_{Vi} . Mean stress is written p and mean stress applied to any component i is written p_i . Effective mean stress is written p' and effective mean stress applied to any component i is written p'_i . Suction associated to any component i is denoted s_i .

Volumetric strain can be associated to superscripts e or p , corresponding to elastic or plastic strains, respectively. If no superscript is written, thus the total strain is being used.

The definition of volumetric strains are given by the following equations:

$$\varepsilon_V = \frac{\Omega - \Omega_0}{\Omega_0} \quad 5-16$$

$$\varepsilon_{V1} = \frac{\Omega_1 - \Omega_{10}}{\Omega_{10}} \quad 5-17$$

$$\varepsilon_{V2} = \frac{\Omega_2 - \Omega_{20}}{\Omega_{20}} \quad 5-18$$

$$\varepsilon_{VM} = \frac{\Omega_M - \Omega_{M0}}{\Omega_{M0}} \quad 5-19$$

From 5-4, 5-5, 5-6, 5-16, 5-17, 5-18, 5-19, the total volumetric strain may also be expressed as:

$$\varepsilon_V = \Phi_{10} \varepsilon_{V1} + \Phi_{20} \varepsilon_{V2} + \Phi_{M0} \varepsilon_{VM} \quad 5-20$$

5.2.3 Main hypotheses

In the model, the material mechanical behaviour is described accounting for some hypotheses, described in the present part.

5.2.3.1 Pellet and powder saturation

As already considered in Chapter 3, the pellet is described by its microstructure and this latter is assumed to be fully-saturated. Powder grains in this work are made from pellet crushing and therefore composed of the same material. It is thus assumed that powder grains are also described by their microstructure, fully-saturated:

$$S_{r1} = 1 \quad 5-21$$

And

$$S_{r2} = 1 \quad 5-22$$

In Chapter 5, only the mechanical behaviour is addressed. Features related to water transfer are addressed in further details in Chapter 6. Hypotheses concerning the degrees of saturation however are of importance, since they avoid determining a Bishop-like coefficient when using the effective stress principle.

5.2.3.2 Hydraulic equilibrium

It was suggested in Chapter 3, from experimental observations, that pellets and macropores are not necessarily at hydraulic equilibrium. At the REV scale, it follows that along a wetting path, suction in pellets remains higher than or equal to the suction corresponding to the relative humidity in the macroporosity. Conversely, accounting for the small size of powder grains, it can be assumed that powder and macroporosity are at hydraulic equilibrium.

In the present Chapter, the main objective is the development and validation of a modelling framework describing the mechanical behaviour of pellet-powder mixture at REV scale. It will be assumed for simplicity that the same suction value affects both pellets and powder phases.

The consideration of a different suction for pellets and powder along with the associated water transfer law is addressed in Chapter 6.

5.2.3.3 Elastic behaviour of the microstructure

It was highlighted in Chapter 2 that in most of the modelling frameworks for pellet mixtures available in the literature, microstructure is considered elastic.

In the present work, the behaviour of a pellet is described by the behaviour of its microstructure. In the pellet-scale experimental characterisation presented in Chapter 4, it was stated that pellet behaviour is not fully reversible, thus not truly elastic. However, the pellet behaviour is considered elastic in the present work for simplicity. A method allowing to account for pellet strength in the model is described in section 5.3.

5.2.3.4 Granular and Continuous states

The material progressively homogenises upon hydration. In the present work, two distinct domains are defined for simplicity. Transition from granular to continuous states is related to criteria discussed in section 5.4.

5.2.3.5 Pellet, powder and total volumetric strains in the granular domain

In the granular domain, powder is considered in free-swelling conditions. The mechanical behaviour of the material is controlled by the pellet assembly. In this domain, it is proposed that the powder phase is not affected by mechanical loading. Conversely, pellets are affected by mechanical loadings.

The total volumetric strain of the pellet assembly is affected by hydraulic and mechanical loadings. Mechanical loadings are associated to a variation of the volume of the granular assembly following rearrangement of the pellet assembly and increase of contact forces, as well as a variation of the pellet stiffness (equation 4-10) and volume (equation 4-15). Hydraulic loadings (*i.e.* suction variation) are associated to a variation of the pellet stiffness and volume.

The total volume of the granular assembly can be affected by rearrangement of the granular structure, variation of contact deflection, variation of pellet volume. Mean stress can affect these three phenomena. Suction can affect the last two of these three phenomena. Directly characterising the influence of mean stress and suction on the volumetric strain of the pellet assembly using DEM can thus be tricky.

It is proposed in the present Chapter to indirectly account for suction and mean stress variations by relating the volume variation of the pellet assembly to *i*) variation of mean stress and pellet stiffness at constant pellet volume (distinct from a variation of mean stress at constant suction); and *ii*) variation of pellet volume at constant mean stress and pellet stiffness (distinct from a variation of suction at constant mean stress).

It is proposed to introduce a dimensionless pressure parameter, m_g , accounting for both mean stress and pellet stiffness, to allow the characterisation of the volumetric strain of the pellet assembly under *i*) a variation of m_g at constant pellet volume; and *ii*) a variation of pellet volume at constant m_g . Details concerning the parameter m_g are provided in 5.3.2.

In this respect it is proposed that:

- *i*) can be addressed by DEM simulation of a pellet assembly under isotropic compression at constant pellet volume. Under these conditions, the total volumetric strain results from rearrangement of the pellet assembly and creation of new contacts between pellets, and of

increase of contact deflections. Deflection is directly affected by the contact stiffness, thus the pellet stiffness;

- *ii*) can be addressed by a theoretical approach and verified by DEM simulation of swelling grains in a granular assembly, under constant mean stress and constant pellet stiffness.

5.3 DEM SIMULATION OF LARGE PELLETT ASSEMBLIES

5.3.1 Objectives

This section follows the suggested perspectives mentioned in the conclusion of Chapter 4. It is proposed to use DEM and the model described in Chapter 4 to perform simulations of larger granular assemblies. All particles in the present study have the same mechanical behaviour as a pellet. The main objective of the present section is to determine constitutive laws for the granular domain. These latter should take into account the particular feature of a granular material while allowing an implementation in a FEM code, thus be based on a continuum approach.

The main advantage of the proposed procedure is that the modelled granular assemblies can be large enough to obtain representative results, avoiding influence of a cell wall. This approach is only numerical.

The behaviour of the granular assembly is addressed in terms of response under mechanical and hydraulic loadings. As discussed in 5.2.3.5, these latter are indirectly addressed by determining *i*) the pellet assembly response under isotropic compression at constant pellet volume using DEM; and *ii*) the pellet assembly response under pellet swelling at constant mean stress and pellet stiffness using a theoretical approach, verified using DEM.

Details regarding the method adopted to characterise the behaviour of pellet assemblies using DEM are presented in part 5.3.2. Then, part 5.3.3 presents the numerical results and their discussion. Part 5.3.4 finally presents the proposed equations describing the material behaviour in the granular domain.

5.3.2 Method

The present part is divided in four sub-parts which aim to *i*) introduce dimensionless parameters used in the simulations; *ii*) describe the preparation and features of numerical samples used in DEM simulations; *iii*) present details concerning the DEM simulations of isotropic compression at constant pellet volume; *iv*) present details concerning the theoretical characterisation and numerical verification of the influence of pellet swelling on the volumetric strain of the pellet assembly, at constant mean stress and pellet stiffness.

5.3.2.1 Definition of mean stress and dimensionless parameters

Two dimensionless control parameters are used in DEM simulations. A dimensionless pressure parameter, m_g , is used to describe the compression state of the granular assembly. A dimensionless inertia parameter, I , is used to control the strain rate of the cell.

Definition of the dimensionless pressure parameter:

In a granular assembly, the diagonal components of the Cauchy stress tensor can be written as follows:

$$\sigma_{\alpha\alpha} = \frac{1}{\Omega} \left[\sum_{i=2}^{N_p} \left(\sum_{j=1}^{i-1} r_{ij}^{(\alpha)} F_{ij}^{(\alpha)} \right) \right] \quad 5-23$$

Where α is the reference coordinate axis ($1 \leq \alpha \leq 3$), Ω is the total volume of the granular assembly, N_p is the number of particles, $r_{ij}^{(\alpha)}$ are the α -coordinates of vector \mathbf{r}_{ij} joining the centre of particles i and j in contact, $F_{ij}^{(\alpha)}$ are the α -coordinates of the corresponding contact force F_{ij} (Christoffersen et al., 1981; Agnolin and Roux, 2007a). From 5-23, the mean stress p is written as:

$$p = \frac{1}{3} \sum_{\alpha=1}^3 \sigma_{\alpha\alpha} = \frac{1}{3\Omega} \sum_{\alpha=1}^3 \left[\sum_{i=2}^{N_p} \left(\sum_{j=1}^{i-1} r_{ij}^{(\alpha)} F_{ij}^{(\alpha)} \right) \right] \quad 5-24$$

Equations 5-23 and 5-24 are sums on all the contacts in the granular assembly. Introducing N_c , the total number of contacts, and $\overline{(r F)}$, the mean value of the product of the distance between two particles in contact and the contact force, equation 5-24 can be written as:

$$p = \frac{1}{3\Omega} N_c \overline{(r F)} \quad 5-25$$

In a monodisperse granular assembly with no wall, N_c is the number of contacts. From equations 5-4 and 4-27, and in conditions where normal deflection at contact is negligible compared to the bead diameter (*i.e.* $r_{ij} \approx a_{eq}$, in the case of a contact between pellets), equation 5-25 can be written as:

$$p = \frac{Z \Phi_1}{\pi a_{eq}^2} \bar{F} \quad 5-26$$

Where Z is the coordination number (equation 4-27) and \bar{F} is the mean value of contact force in the granular assembly.

From equation 5-26 and the Hertz law introduced in Chapter 4 (equation 4-2), the ratio of average normal deflection, $\overline{\delta_N}$, to bead diameter in a granular assembly can be written as:

$$\frac{\overline{\delta_N}}{a_{eq}} = \left(\frac{3\pi}{Z\Phi_1} \right)^{2/3} \left(\frac{p}{E} \right)^{2/3} \quad 5-27$$

Which introduces a dimensionless stiffness parameter, κ_g (Agnolin and Roux, 2007a):

$$\kappa_g = \left(\frac{E}{1 - \nu^2} \right)^{2/3} \quad 5-28$$

In the present work, a dimensionless pressure parameter, m_g , is introduced for convenience:

$$m_g = \frac{1}{\kappa_g} \quad 5-29$$

Which makes m_g directly proportional to the $\overline{\delta_N}/a_{eq}$ ratio. The limit of rigid grains is thus defined as $\kappa_g \rightarrow \infty$ or $m_g \rightarrow 0$.

m_g and κ_g are convenient to describe the state of a granular assembly. In the present work, it is particularly adapted since m_g takes into account both the mean stress and the stiffness variation of pellets. The volumetric strain of the granular assembly under variation of m_g can be characterised using DEM. It allows to determine influences of mean stress variation as well as variation of pellet stiffness on the total volumetric strain.

Definition of the dimensionless inertia parameter:

In the DEM simulations, the strain rate of the periodic cell, $\dot{\epsilon}$, is controlled by a dimensionless inertia parameter, I , defined as (Agnolin and Roux, 2007a):

$$I = \dot{\epsilon} \left(\frac{m_p}{a_{eq} p} \right)^{1/2} \quad 5-30$$

Where m_p is the mass of a particle and a_{eq} the diameter of a particle.

A constant value of I can be imposed to apply a constant strain rate of the cell, or a maximum value of I can be imposed to limit the strain rate of the granular assembly. Further discussion concerning I can be found in Agnolin and Roux (2007a).

5.3.2.2 Sample preparation

In DEM, the simulations are performed on different samples, prepared at different initial pellet volume fractions. All numerical samples are composed of 4000 beads, in a cubic cell with periodic boundary conditions, thus no pellet-wall interaction exists (Agnolin and Roux, 2007a).

Five different types of granular assemblies are prepared. Each type of sample corresponds to an initial pellet volume fraction, Φ_{I0} . For each type of granular assembly, three samples are prepared to assess the calculation repeatability.

Samples are prepared by compression of a granular gas with varying friction coefficient (all samples except C-samples) or by shaking (C-samples). This procedure allows samples of various initial pellet volume fraction and coordination number to be obtained. The procedure is discussed in details in

Agnolin and Roux (2007a). Table 5-3 and Figure 5-1 summarise the main initial properties of the periodic samples.

Table 5-3: Initial state properties of the numerical samples. All samples are cubic and contain 4000 beads.

Sample	N_c	Z	Φ_{10}
A	1	12093	6.0
	2	12115	6.1
	3	12059	6.0
B	1	8736	4.4
	2	8465	4.2
	3	8635	4.3
C	1	8811	4.4
	2	8689	4.3
	3	8742	4.4
D	1	8971	4.5
	2	8755	4.4
	3	8749	4.4
J	1	11546	5.8
	2	11537	5.8
	3	11573	5.8

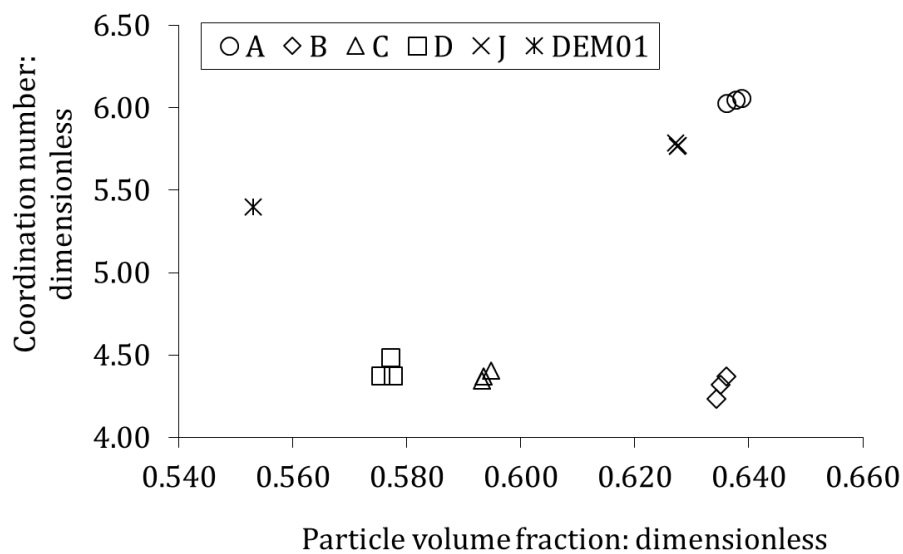


Figure 5-1: Representation of the initial states of all numerical samples, along with DEM01 initial state for comparison.

5.3.2.3 Isotropic compression of pellet assemblies at constant pellet volume

Isotropic compressions of pellet assemblies are performed at constant pellet volume and constant particle Young modulus (thus constant elastic limit following equation 4-11). Since pellets are modelled by perfect spheres which remain spherical, the condition of constant pellet volume corresponds to a constant sphere diameter in the simulations.

I is set to 10^{-5} to model an isotropic compression at a constant slow rate. Results are presented in terms of volumetric strain as a function of m_g . Calculation are stopped when the particle volume fraction reaches 0.8.

Characterising the volumetric strain as a function of m_g allows the influence of both mean stress and variation of pellet stiffness to be characterised from a simple simulation.

5.3.2.4 Influence of pellet swelling at constant mean stress and pellet stiffness

The volumetric strain of the granular assembly resulting from variation of pellet volume is addressed from a theoretical perspective. The objective is to determine the ratio of total volumetric strain to pellet volumetric strain under conditions where the pellet volume varies at constant m_g .

Then, DEM simulations of pellet swelling in a granular assembly, at constant mean stress and constant pellet stiffness (thus constant m_g), are performed to verify the proposed method. Simulations consist in applying “swelling-shrinkage” paths to the pellets.

Theoretical study of the relationship between pellet swelling and pellet assembly swelling:

The proposed approach is based on the definition of stress in granular assemblies (equation 5-25). From equation 5-25, the problem concerning pellet swelling at constant Young modulus and constant mean stress can be described addressed by writing the mean stress following pellet swelling and resulting pellet assembly expansion:

$$p = \frac{1}{3 \Omega_0 (1 + \varepsilon_V)} N_c \overline{\left(r_0 (1 + \varepsilon_V)^{\frac{1}{3}} F \right)} \quad 5-31$$

Where subscript 0 denotes initial state, ε_V is the volumetric strain of the pellet assembly, $\overline{(\)}$ denotes the average value over all contacts, $r_0 (1 + \varepsilon_V)^{1/3}$ is the distance between two pellets in contact following the granular assembly expansion, and F is the contact force, given by Hertz's law (equation 4-2). Considering the evolution of the pellet diameter and the deflection at contact between pellets (equal to $r - a_{eq}$), F is written

$$F = \frac{1}{3} E (a_{eq0})^{\frac{1}{2}} (1 + \varepsilon_{V1})^{\frac{1}{6}} \left(r_0 (1 + \varepsilon_V)^{\frac{1}{3}} - a_{eq0} (1 + \varepsilon_{V1})^{\frac{1}{3}} \right)^{\frac{3}{2}} \quad 5-32$$

Where $r_0 (1 + \varepsilon_V)^{1/3} - a_{eq0} (1 + \varepsilon_{V1})^{1/3}$ is the deflection at contact between two pellets following the granular assembly expansion and the pellet swelling and ε_{V1} is the pellet volumetric strain.

From equations 5-25, 5-31 and 5-32, it follows that, at constant m_g , thus constant p/E , under the assumption that N_c remains constant upon particle swelling, then $\varepsilon_V = \varepsilon_{V1}$. Therefore, introducing f_{Mm} the ratio between the two volumetric strains:

$$f_{Mm} = \frac{\varepsilon_V}{\varepsilon_{V1}} = 1 \quad 5-33$$

Which reminds the equality between the linear thermic dilation coefficients of a material and that of its matrix (*i.e.* $\varepsilon_V = \varepsilon_{Vm}$) upon heating at constant mean stress and fluid pressure, as demonstrated by Coussy (1995) for thermo-poro-elastic materials.

Since equation 5-33 is obtained for F given by Hertz's law, it is valid for elastic contacts. In the limit case where all contact forces have reached plasticity, swelling at constant stiffness also occurs at constant contact force (equal to the elastic limit). In this case, from equation 5-31, it is shown that $p/p_0 = (1 + \varepsilon_V)^{-2/3}$. The pressure therefore cannot be kept constant if the granular assembly swells.

In a granular assembly where grains swell at constant mean stress and constant grain stiffness, for elastic contact forces, the total volumetric strain is thus equal to the grain volumetric strain, and $f_{Mm} = 1$.

Verification of theoretical results using DEM:

In DEM, the value of f_{Mm} upon pellet swelling at constant mean stress and constant pellet Young modulus (thus constant elastic limit, following equation (4-11) is studied in elasticity for the numerical samples described in Table 5-3.

Particle diameter is progressively and simultaneously increased or decreased by small successive increments of $\Delta a_{eq}/a_{eq} \approx 10^{-4}$. Equilibrium as defined in Chapter 4 ($\epsilon = 10^{-4}$) is reached before each new increment to avoid instability occurrence in the calculation. The maximum value of I is set to 10^{-6} . 15 swelling steps are performed (final $\varepsilon_{V1} \approx 5 \times 10^{-3}$) followed by 15 shrinkage steps (return to $\varepsilon_{V1} = 0$), at constant $m_g \approx 10^{-3}$. The resulting f_{Mm} are calculated after each calculation steps.

5.3.3 Numerical simulation results and discussion

Results of the DEM simulations performed on periodic granular assemblies are described in the present part. The first three sub-parts address the results of isotropic compression and their interpretations. The fourth sub-part presents results of the simulations performed to verify the theoretical value proposed for the f_{Mm} parameter.

5.3.3.1 Influence of the dimensionless pressure parameter on the volumetric strain of the granular assembly

For all samples, the relationship between ε_V and m_g is obtained in isotropic compression simulations. All plotted points correspond to equilibrated configurations, with a tolerance $\epsilon = 10^{-4}$.

Results for A, B, C, D and J samples (Table 5-3) are presented in Figure 5-2, Figure 5-3, Figure 5-4, Figure 5-5, and Figure 5-6, respectively. All three samples of each configuration are plotted.

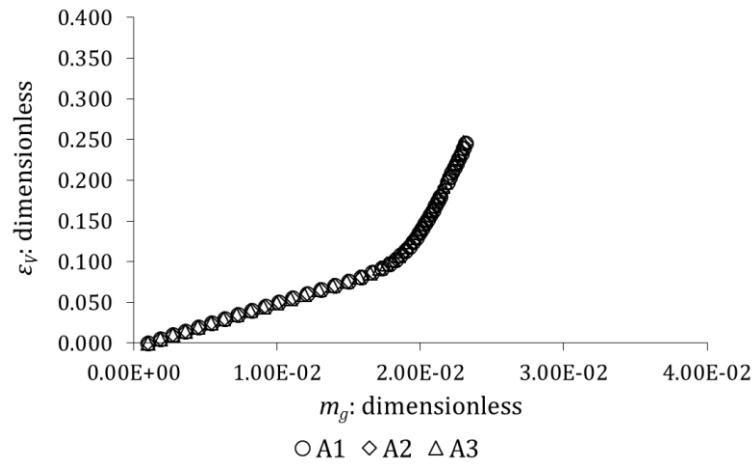


Figure 5-2: Evolution of the granular assembly volumetric strain as a function of the dimensionless pressure parameter during isotropic compression in A-samples.

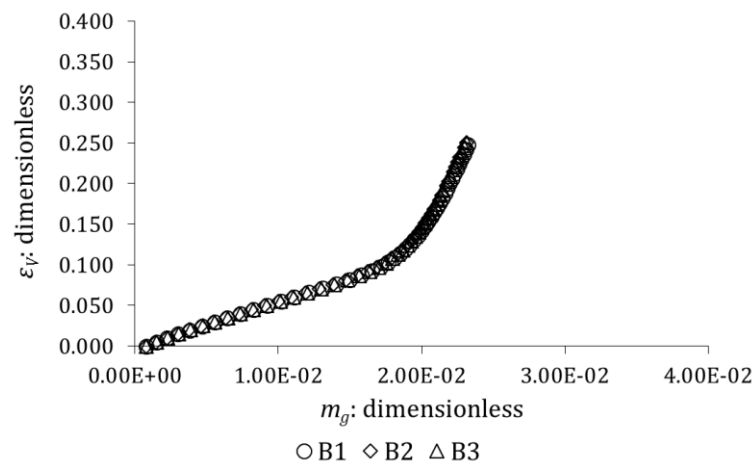


Figure 5-3: Evolution of the granular assembly volumetric strain as a function of the dimensionless pressure parameter during isotropic compression in B-samples.

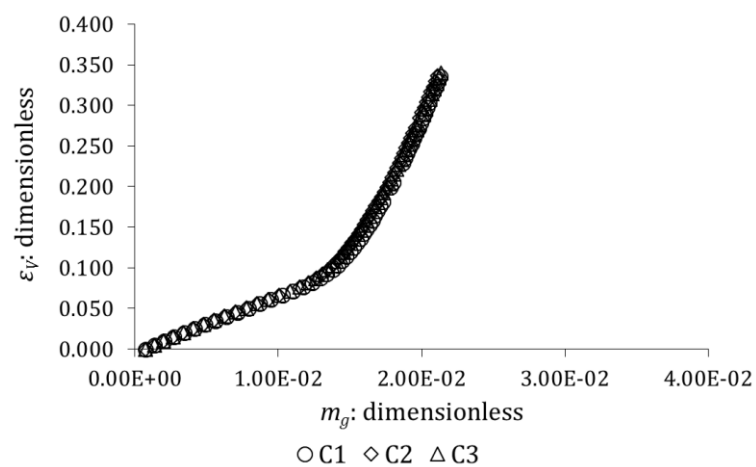


Figure 5-4: Evolution of the granular assembly volumetric strain as a function of the dimensionless pressure parameter during isotropic compression in C-samples.

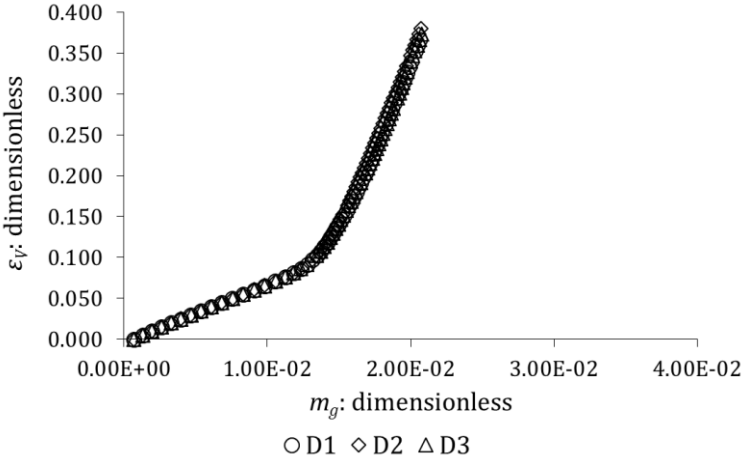


Figure 5-5: Evolution of the granular assembly volumetric strain as a function of the dimensionless pressure parameter during isotropic compression in D-samples.

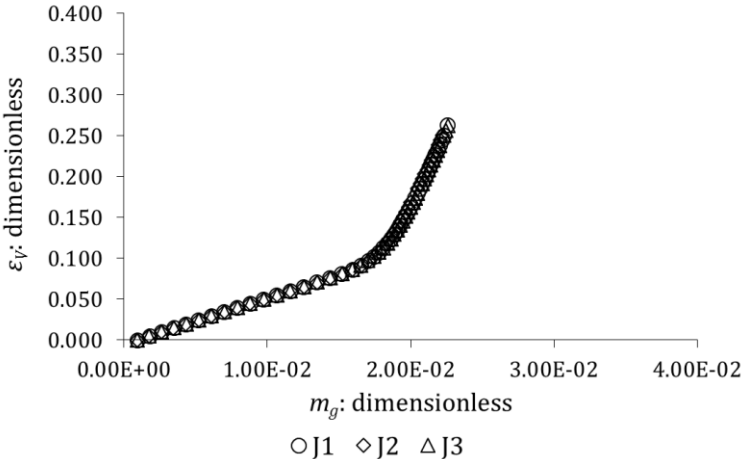


Figure 5-6: Evolution of the granular assembly volumetric strain as a function of the dimensionless pressure parameter during isotropic compression in J-samples.

All samples are characterised by a good repeatability of the results, highlighting that the 4000 particles periodic boundary conditions samples are reasonably representative of the granular assembly behaviour. Variability associated to small size of the sample discussed in Chapter 4 is avoided in the present study. Numerical results can thus be interpreted to deduce the material intrinsic behaviour.

All samples display a comparable trend upon variation of m_g . The macroscopic response of the granular assembly is considered bilinear upon m_g increase. It is associated to contact forces reaching the elastic limit. The relevant parameters describing the material behaviour upon variations of m_g are discussed in sub-part 5.3.3.3

5.3.3.2 Influence of the grain strength on the mechanical behaviour of the granular assembly

In DEM simulations, the strength of the pellets is taken into account by considering perfect plasticity in the contact law. Elastic limit is described by the pellet strength as given by equation 4-11. Influence of the pellet strength is thus highlighted by the evolution of the proportion of plastic contacts as a function of m_g during isotropic compression.

Figure 5-7, Figure 5-8, Figure 5-9, Figure 5-10, and Figure 5-11 present the evolution of this parameter as a function of m_g . As for the volumetric strain results, a satisfactory repeatability is obtained for all samples.

In all samples, all contacts remain elastic until a limit value of m_g is reached. Contact plasticity then increases continuously. This limit value of m_g is denoted by m_g^* . Values taken by m_g^* in all samples roughly correspond to the m_g values at which the slope change is obtained in the ε_V - m_g plane.

The bilinear response of the samples in the ε_V - m_g plane is thus interpreted as a consequence of the plasticity occurrence in contacts. At m_g values below m_g^* , contacts remain elastic and the granular assembly volumetric strain is proportional to m_g . As m_g reaches m_g^* , normal forces in contacts start reaching pellet strength and a different response is obtained. Upon increase of m_g , the total number of contacts increases in the sample. Even if contacts are characterised by a perfect plasticity, the macroscopic response is not characterised by perfect plasticity because *i*) all existing contacts do not reach the elastic limit simultaneously; *ii*) new contacts are created.

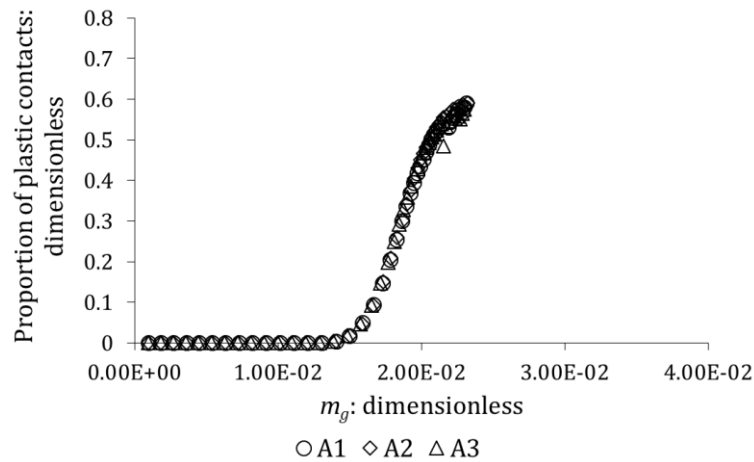


Figure 5-7: Evolution of the proportion of plastic contacts in the granular assembly as a function of the dimensionless pressure parameter during isotropic compression in A-samples.

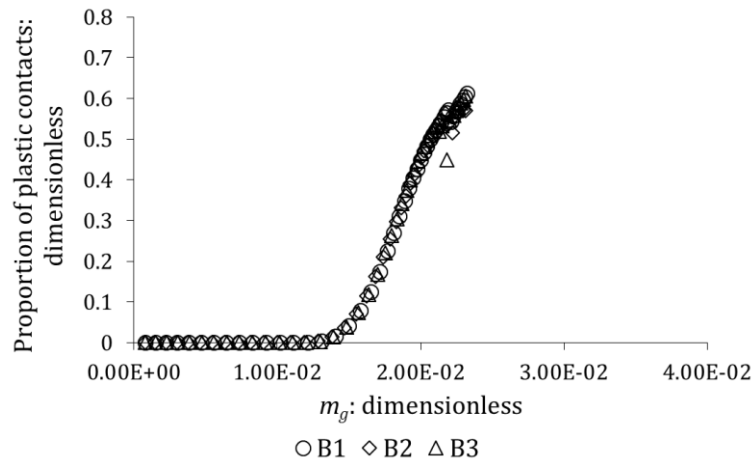


Figure 5-8: Evolution of the proportion of plastic contacts in the granular assembly as a function of the dimensionless pressure parameter during isotropic compression in B-samples.

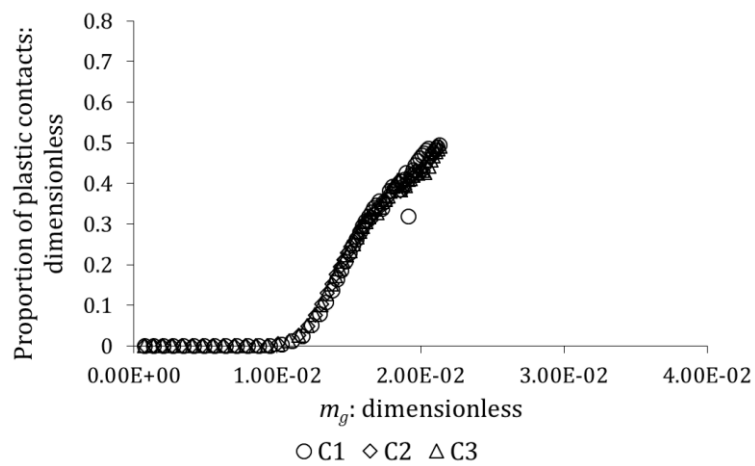


Figure 5-9: Evolution of the proportion of plastic contacts in the granular assembly as a function of the dimensionless pressure parameter during isotropic compression in C-samples.

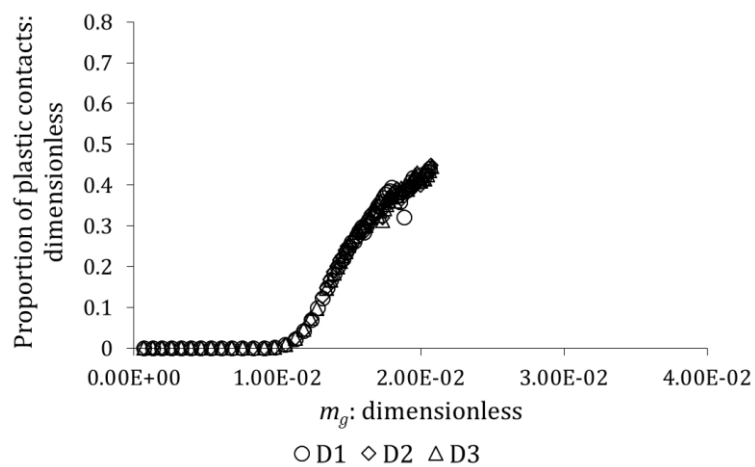


Figure 5-10: Evolution of the proportion of plastic contacts in the granular assembly as a function of the dimensionless pressure parameter during isotropic compression in D-samples.

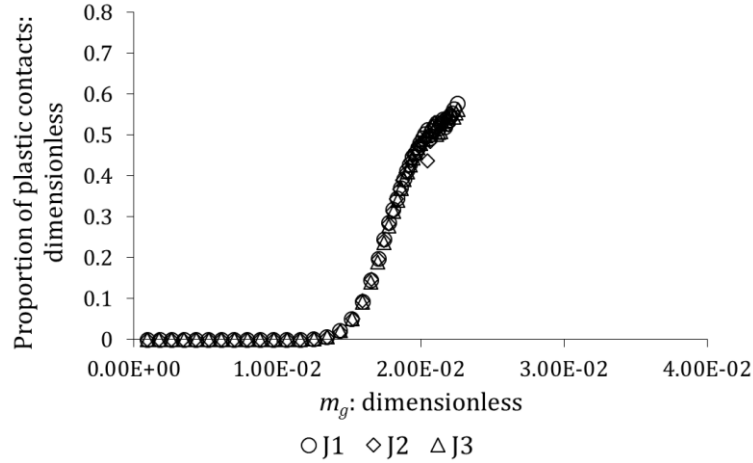


Figure 5-11: Evolution of the proportion of plastic contacts in the granular assembly as a function of the dimensionless pressure parameter during isotropic compression in J-samples.

5.3.3.3 Influence of the initial particle volume fraction on the mechanical behaviour

It was highlighted in the previous sub-parts that the volumetric strain evolution during isotropic compression evolves in two phases, characterised by elastic and plastic reactions in contacts, respectively. Equation 5-27 allows the following relationship to be written for elastic contacts in a granular assembly:

$$\Phi_1 = \frac{3\pi}{Z} \left(\frac{m_g}{\overline{\delta_N}/a_{eq}} \right)^{3/2} \quad 5-34$$

And, from equations 5-4 and 5-16 (definitions of Φ_1 and ε_V), it follows that, at constant particle volume:

$$\varepsilon_V = \frac{\Phi_{10}}{\Phi_1} - 1 \quad 5-35$$

It appears that ε_V is related to m_g through Z and $\overline{\delta_N}/a_{eq}$. These are particular features of the granular assembly which depend on initial state and the arrangement of particles. Such relationships may be difficult to characterise and extrapolate for a modelling purpose using a continuum approach. Simplifications are proposed, from the interpretation of numerical results.

At high values of m_g , comparison of A-samples and B-samples suggests that the initial arrangement of particles may rapidly be lost (Figure 5-12). New contacts are created upon compression and the initially low Z in B-samples is found to be comparable to that of A-samples long before reaching pellet strength. Comparison of the ε_V - m_g relationship of these two types of sample (Figure 5-13) actually suggests that the initial arrangement of particles is not relevant to characterise the material response under isotropic compression at these values of m_g .

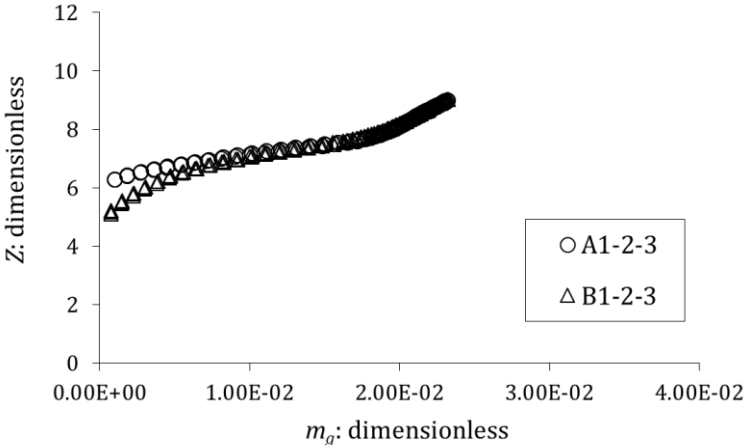


Figure 5-12: Evolution of the coordination number as a function of the dimensionless pressure parameter in A- and B-samples.

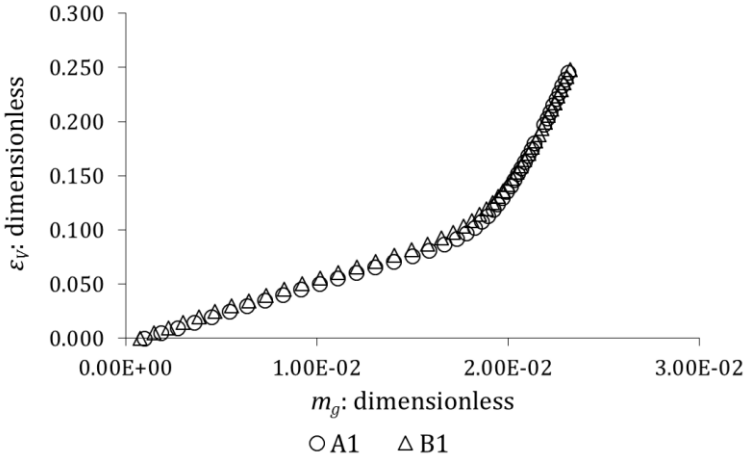


Figure 5-13: Evolution of the granular assembly volumetric strain as a function of the dimensionless pressure parameter during isotropic compression in A1- and B1-samples.

In Figure 5-14, the results of one sample of each type of simulation are compared. The main observations from these results are:

- The higher the initial particle volume fraction, the lower the slope in the “elastic contacts” domain, in the $\epsilon_v - m_g$ plane;
- The higher the initial particle volume fraction, the higher m_g^* ;
- The higher the initial particle volume fraction, the lower the slope in the “plastic contacts” domain, in the $\epsilon_v - m_g$ plane.

The influence of Φ_{10} on the two slopes is however not significant. The volumetric strain of the granular assembly upon variation of mean stress and pellet stiffness, at constant pellet volume, may thus be described by characterising m_g^* and the two slopes of the bilinear response. It is suggested to retain the following expressions:

$$f_{\varepsilon} = \frac{d\varepsilon_V}{dm_g} = f_{\varepsilon A} = 6; \quad m_g \leq m_g^* \quad 5-36$$

And

$$f_{\varepsilon} = \frac{d\varepsilon_V}{dm_g} = f_{\varepsilon B} = 40; \quad m_g > m_g^* \quad 5-37$$

Where f_{ε} describes the evolution of ε_V upon m_g variations, and $f_{\varepsilon A}$ and $f_{\varepsilon B}$ are parameters. Model prediction for elastic contacts is plotted using red dashed line in Figure 5-14.

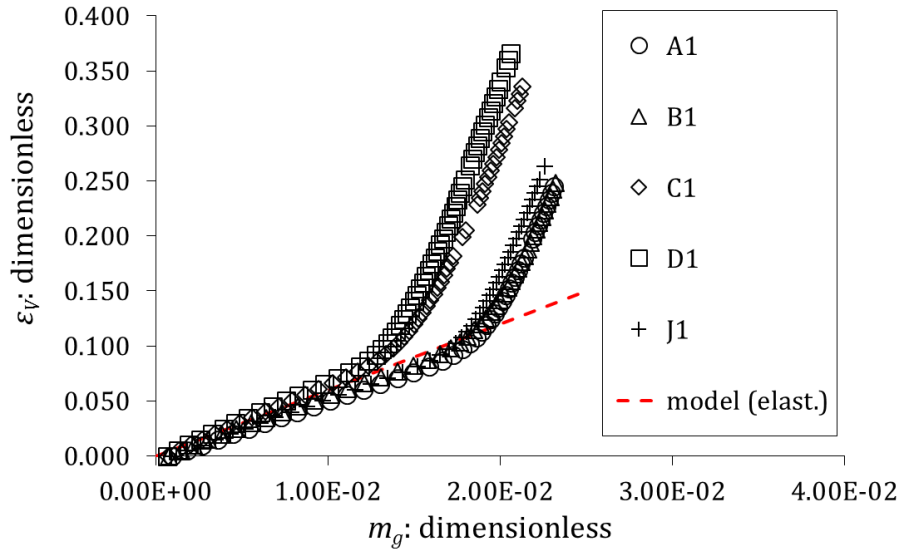


Figure 5-14: Comparison of the volumetric strains calculated upon isotropic compression for A1, B1, C1, D1, and J1 samples. The red dashed line corresponds to the model predictions for elastic contacts.

Conversely, the influence of Φ_{10} on m_g^* is clear. The relationship between these two parameters is plotted in Figure 5-15. A linear expression is proposed to fit numerical results:

$$m_g^* = f_{mA} \Phi_{10} + f_{mB} \quad 5-38$$

Where f_{mA} and f_{mB} are model parameters. $f_{mA} = 0.067$ and $f_{mB} = -0.031$ are proposed to describe the numerical results.

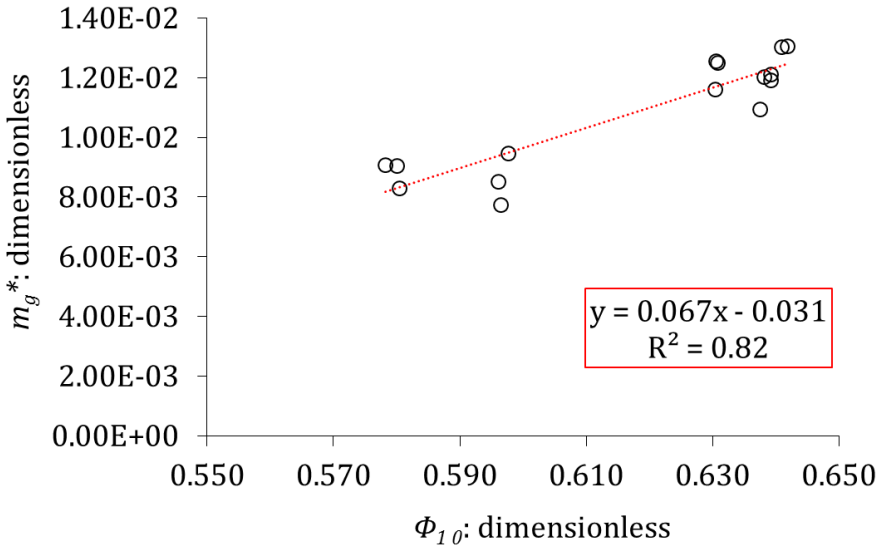


Figure 5-15: Relationship between m_g^* and Φ_{10} for all simulation results.

Finally, the four parameters proposed to describe the material behaviour upon isotropic compression are summarised in Table 5-4.

Table 5-4: Proposed values for the dimensionless parameters describing the behaviour of pellet assemblies.

Dimensionless parameter	Proposed value
$f_{\varepsilon A}$	6
$f_{\varepsilon B}$	40
$f_{m A}$	0.067
$f_{m B}$	- 0.031

Initial particle volume fraction is thus considered to provide a satisfactory approximation of the material response upon variations of m_g . It is worth mentioning that in the results presented in this work, volumetric strains are significant and the domain defined by $m_g < m_g^*$ corresponds to elastic *contacts* and not to strict elastic behaviour of the granular assembly.

For $m_g > m_g^*$, the proportion of plastic contacts increases. The observed behaviour in this domain is related to the simplified perfect plasticity law implemented in the DEM code, and interpretation regarding the intrinsic behaviour of pellet assemblies in this case should be prudent, as a consequence.

5.3.3.4 Influence of grain swelling on the volumetric strain of the granular assembly

Numerical results for swelling-shrinkage simulations at constant m_g are presented in Figure 5-16. As suggested in 5.3.2.4, at low m_g value and for all contact forces in the elastic domain ($m_g < m_g^*$), f_{Mm} is verified to be equal to 1 regardless of the initial particle volume fraction.

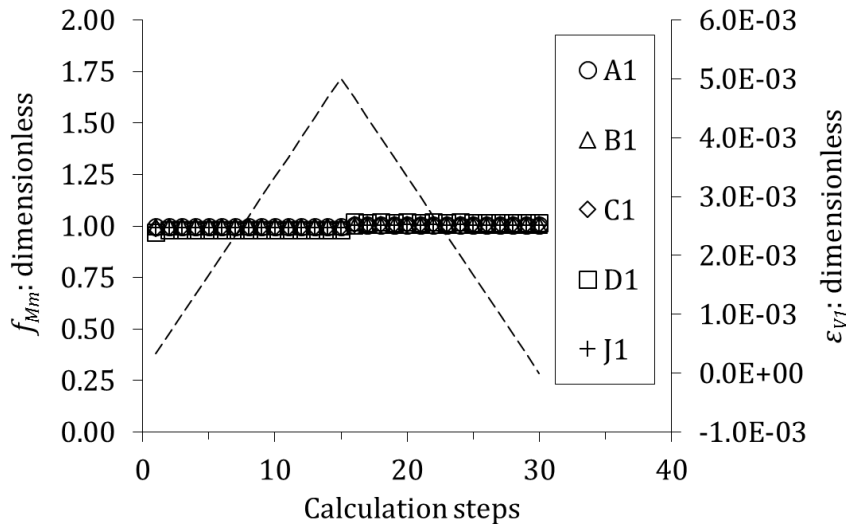


Figure 5-16: Relationship between f_{Mm} obtained for all types of samples (dots) and ε_{VI} (dashed line) determined by swelling-shrinkage simulations using DEM. m_g is taken equal to $\sim 10^{-3}$.

It is reminded that the results for f_{Mm} only address the influence of particle swelling at constant particle stiffness. In the modelling of bentonite pellet mixtures using BExM (Alonso et al., 1999), interaction functions used to relate pellet swelling to mixture swelling (*e.g.* Gens et al., 2011; Mokni et al., 2019) should not straightforwardly be compared to f_{Mm} since, under constant mean stress, a suction variation would in addition make the pellet stiffness vary and in turn induce a volume change of the granular assembly. In the present work, this feature is taken into account by the m_g - ε_V relationship.

5.3.4 Proposition of a model for the “granular” state

5.3.4.1 Overview of the approach

In the light of the results presented in the previous part, a model describing the behaviour of pellet-powder mixture is proposed. In the present part, constitutive equations describing the material behaviour in the granular domain are presented.

The model is based on hardening elastoplasticity. Equations relate increments of volumetric strain of each levels of structure to increments of mean stress and suction, which are the two stress variables considered. The concept is to some extent comparable to the traditional BBM framework, using three distinct porosities as mentioned in section 5.2.

Parameters described in the previous part are used to describe the volumetric strain of the whole granular assembly, ε_V , of pellets, ε_{VI} , and of powder grains, ε_{V2} . ε_{VI} and ε_{V2} are related to their respective effective stresses through the relationship determined from the pellet-scale experimental characterisation (see Chapter 4). ε_V is described as a function of m_g and ε_{VI} as discussed in 5.2.3.5.

Plasticity is taken into account by using the LC concept. From a conceptual perspective, it means that plasticity is considered to affect the bentonite fabric while the pellet strength, thought to be responsible for the first identified peak/plateau of swelling pressure in Chapter 3, is taken into account by using $f_{\varepsilon A}$ and $f_{\varepsilon B}$ parameters in the elastic domain.

Details concerning each point are provided in the following sub-parts.

5.3.4.2 Microstructural effective stresses

In the granular domain, it is considered that powder is not affected by the mechanical pressure. Pellets are considered the only component to undergo mechanical loading. In addition, the total mean stress is considered an average value for all the mixture. Mean stress applied to the pellet phase is thus higher than the total mean stress. These hypotheses are expressed as:

$$p'_1 = \frac{p}{\phi_1} + s_1 \quad 5-39$$

And

$$p'_2 = s_2 \quad 5-40$$

A transfer law is proposed in Chapter 6 to relate s_1 to s_2 and pellet properties. In the present Chapter, hydraulic equilibrium is assumed and:

$$s_1 = s_2 = s \quad 5-41$$

5.3.4.3 Microstructural elastic volumetric strains

Microstructural volumetric strains are considered elastic. Increments of these latter are expressed as follows:

$$d\varepsilon_{V1} = d\varepsilon_{V1}^{(e)} = \frac{dp'_1}{\frac{1}{\beta_m} \exp(\alpha_m p'_1)} \quad 5-42$$

And

$$d\varepsilon_{V2} = d\varepsilon_{V2}^{(e)} = \frac{dp'_2}{\frac{1}{\beta_m} \exp(\alpha_m p'_2)} \quad 5-43$$

5.3.4.4 Total elastic volumetric strain

Variations of p and s_1 both affect the pellet volumetric strain ε_{V1} , and the pellet stiffness, thus m_g . As previously discussed, in the model, the total elastic volumetric strain is expressed as a function of m_g and ε_{V1} :

$$d\varepsilon_V^{(e)} = \frac{\partial \varepsilon_V^{(e)}}{\partial m_g} dm_g + \frac{\partial \varepsilon_V^{(e)}}{\partial \varepsilon_{V1}} d\varepsilon_{V1} \quad 5-44$$

Where:

$$\frac{\partial \varepsilon_V^{(e)}}{\partial \varepsilon_{V1}} = f_{Mm} = 1 \quad 5-45$$

And

$$\frac{\partial \varepsilon_V^{(e)}}{\partial m_g} = f_\varepsilon \quad 5-46$$

The aforescribed equations (5-44; 5-45; 5-46) are used in the implementation of the model. Using these expressions, the pellet strength can be taken into account in the elastic domain by using equations 5-36 and 5-37 to set the value of f_ε in equation 5-46. For convenience, $f_{Mm} = 1$, valid for elastic contacts, is always used.

In the literature, constitutive equations of models are commonly formulated as functions of mean stress and suction. In this respect, from equation 5-44, an alternative expression of the elastic volumetric strain is:

$$d\varepsilon_V^{(e)} = \left(\frac{\partial \varepsilon_V^{(e)}}{\partial m_g} \frac{\partial m_g}{\partial s_1} + \frac{\partial \varepsilon_V^{(e)}}{\partial \varepsilon_{V1}} \frac{\partial \varepsilon_{V1}}{\partial s_1} \right) ds_1 + \left(\frac{\partial \varepsilon_V^{(e)}}{\partial m_g} \frac{\partial m_g}{\partial p} + \frac{\partial \varepsilon_V^{(e)}}{\partial \varepsilon_{V1}} \frac{\partial \varepsilon_{V1}}{\partial p} \right) dp \quad 5-47$$

With:

$$\frac{\partial \varepsilon_{V1}}{\partial s_1} = \beta_m \exp(-\alpha_m p'_1) \quad 5-48$$

And

$$\frac{\partial \varepsilon_{V1}}{\partial p} = \frac{\beta_m}{\Phi_1} \exp(-\alpha_m p'_1) \quad 5-49$$

And

$$\frac{\partial m_g}{\partial s_1} = -\frac{2}{3} \alpha_m \left(\frac{\beta_m}{3} \frac{1 - \nu^2}{1 - 2\nu} \right)^{2/3} p^{2/3} \exp\left(-\frac{2}{3} \alpha_m p'_1\right) \quad 5-50$$

And

$$\frac{\partial m_g}{\partial p} = \frac{2}{3} \left[\left(\frac{1}{p} \right) + \left(-\frac{\alpha_m}{\Phi_1} \right) \right] \left(\frac{\beta_m}{3} \frac{1 - v^2}{1 - 2v} \right)^{2/3} p^{2/3} \exp \left(-\frac{2}{3} \alpha_m p'_1 \right) \quad 5-51$$

5.3.4.5 Total plastic strains and hardening

Plasticity and hardening in the proposed model are addressed using the concept of the LC curve as introduced by Alonso et al. (1990) for the BBM. Hardening law is related to plastic strains as:

$$\frac{dp_0(0)}{p_0(0)} = \frac{1 + e_0}{\lambda(0) - \kappa} d\varepsilon_V^{(p)} \quad 5-52$$

Where $p_0(0)$ is the preconsolidation pressure at zero suction, $\lambda(0)$ is the elastoplastic stiffness parameter at zero suction and κ is the elastic stiffness parameter, considered constant in the model.

It is considered that the bentonite material is affected by the LC mechanism regardless of its eventual granular structure. Plasticity is described using parameters from the continuous domain (see section 5.5). The same set of equations is used for both granular and continuous domains to describe plasticity.

Further details concerning plasticity are provided in section 5.5.

5.4 TRANSITION FROM “GRANULAR” TO “CONTINUOUS” STATE

In the present section, criteria are proposed to characterise the transition from the granular domain to the continuous domain in the model.

5.4.1 Identified parameters

From Chapter 2 and Chapter 3 discussions, the following aspects are proposed to determine if the initial granular material can be considered continuous in the model: *i*) suction has reached the threshold corresponding to microstructural rearrangement; *ii*) pellet assembly is not the dominant phase in the mixture; *iii*) powder volume fraction is high enough for the powder grains to hold a significant proportion of the mechanical loads.

5.4.1.1 Dominant phase in binary granular mixtures

The concept of dominant phase was introduced in Chapter 2. It defines a critical fine grain proportion, $x_{S\text{ crit}}$, corresponding to the optimal proportion of fine particles associated to the theoretical minimum void ratio of the mixture. In the present work, x_S is the powder volumetric proportion and $x_L = 1 - x_S$ is

the pellet volumetric proportion in the mixture. It is proposed to determine the value of $x_{S\text{ crit}}$ for pellet mixtures and use it as a criterion: for $x_{S\text{ crit}} < x_S$, the mixture is considered as a continuous material.

Since the values of x_S and x_L do not significantly vary upon hydration (as suction is much higher than mean stress in the granular domain), it is suggested to regard this criterion as an initial condition: if the modelled mixture does verify the condition, the pellet assembly does not have a significant influence on the macroscopic response and the proposed framework is likely not to be suitable to describe the material behaviour. If the mixture does not verify this condition, then the proposed framework is considered suitable and the transition from granular to continuous states is described by the criteria presented in the following sub-parts.

The optimal volume fraction of sub-spherical pellets is assumed to be ~ 0.640 in the mixture, corresponding to the value for a random close packing of spherical particles (Agnolin and Roux, 2007a). Following the procedure described in the French standard NF P 94-059 (AFNOR, 2000) (but using manual vibration), the minimum void ratio of the MX80 powder used in experiments (see Chapter 4) is estimated: $e_{\text{min}} = 0.300$. From this value, $x_{S\text{ crit}}$ for the pellets is 0.302. The reference mixture is very close to this value. Experimental observations indeed suggested that the 70/30 mixture did not really behave as a granular assembly while both 70/15 and 70/0 samples did. The 70/30 relative proportions have already been identified in binary mixtures of glass beads to be a boundary between a large particle controlled structure and a fine particle partially controlled structure (Vallejo, 2001).

5.4.1.2 Influence of suction

It was shown in the literature review in Chapter 2 that the bentonite fabric is affected by the progressive insertion of discrete water layers upon hydration. In free-swelling conditions, a significant rearrangement of the microstructure occurs for MX80 at a threshold suction in the range ~ 3 MPa to ~ 7 MPa.

In swelling pressure tests performed in the laboratory and discussed in Chapter 3, the occurrence of this microstructure rearrangement is suggested when imposing a suction of 4 MPa from equilibrium at 9 MPa for a 70/30 pellet mixture of average dry density $\rho_d = 1.50 \text{ Mg/m}^3$. For the pellet assembly (70/0 sample, $\rho_d = 1.05 \text{ Mg/m}^3$), this phenomenon is observed on imposing zero suction (wetting using liquid water) from equilibrium at 4 MPa.

It is proposed to set the threshold at $s_l = 3$ MPa. It would allow the behaviour observed in the 70/0 sample to be reproduced since the sample was observed to be granular at suction as low as 4 MPa. The evolution of swelling pressure in the 70/30 sample suggests that its behaviour is not controlled by the granular structure at suction higher than this threshold. Actually, as discussed in Chapter 4 and suggested in the previous sub-part, this latter is likely to behave as a continuous material because of the density of powder in inter-pellet porosity. The transition from granular to continuous states in this case is thought to be described by a criterion related to the density of the matrix phase.

5.4.1.3 Influence of matrix volume fraction

In the course of hydration, pellets and powder grains swell. Under constant-volume conditions, the pellet swelling induces a decrease of the volume available for powder grains to swell. As a consequence, volume fraction of the pellet assembly and the matrix can significantly vary upon hydration.

Upon powder swelling in a decreasing available volume, a transition from initial free-swelling conditions to constrained volume conditions is thought to occur. Powder grains progressively contribute to the mechanical equilibrium of the granular structure.

It is proposed to determine the relationship between Φ_{mat} and Φ_I and the increase of the powder contribution to the mechanical equilibrium.

DEM simulations of binary granular mixtures are performed in this purpose. An overview of the method is presented in part 5.4.2. Results are presented in part 5.4.3.

5.4.2 Description of DEM simulations of binary granular mixtures

5.4.2.1 Sample preparation

Samples are prepared at relative proportions corresponding to a “70/15” sample. In this case, $x_{S0} = 0.18$ and $x_{L0} = 0.82$. The exact same amount of pellets as in DEM01, DEM02 and DEM03 (209 pellets) is introduced in the cell.

Powder grains are modelled by spherical particles. A diameter ratio of 1/6 is chosen between small and large particles. Using this ratio, the powder grains all have an equivalent diameter as high as ~1.17 mm. 9762 small particles have to be placed in the cell. 209 pellets are modelled, the total number of particles in simulations is 9882.

The preparation step is performed as in DEM01 (see Chapter 4) with the following adaptations:

- Each time a large particle is placed in the cell, x_{S0}/x_{L0} small particles are placed in the cell following the same procedure;
- Each large particle is placed each 1 sec;
- Each small particle is placed each 10^{-4} sec to model a pouring.

As in DEM01, the granular assembly is constantly being equilibrated under gravity. The powder grain density is taken equal to the pellet density. Five samples are prepared following the same procedure.

5.4.2.2 Cell closure

The closure step is performed differently compared to the Chapter 4 procedure. In order to avoid initial closure pressure, the cell is not closed to a target volume. This step is simply performed by setting the top wall at the same elevation as the highest particle in the sample.

As a result, no initial pressure arises during the process. In addition, the dry density of the mixtures will be different to the dry density of 70/15 samples described in Chapter 4.

5.4.2.3 Hydration step

The hydration step is modelled as in Chapter 4. The same law is considered for the volumetric strain-suction relationship of pellet and powder grain. At each calculation step pellet and powder grain both increase following the procedure described in Chapter 4.

It is considered that contacts between two powder grains and between a powder grain and the cell wall remain elastic. All other features are similar to the procedure described for DEM01 simulations in Chapter 4.

5.4.3 Results of DEM simulations

5.4.3.1 Dry density

Following the preparation and closure steps, the five “70/15” samples all have average dry density of 1.160 Mg/m^3 . This value is lower than 1.275 Mg/m^3 because the sample height in this case is $\sim 4.4 a_{eq0}$ while it was $4 a_{eq0}$ in the simulations of Chapter 4. A lower value can be expected if the ratio of large particle diameter (pellets) to small particle diameter (powder grains) is taken higher. A significantly higher number of particles in the simulations would be required for higher ratio.

5.4.3.2 Ratio of mean stresses and ratio of volume fractions

Figure 5-17 presents the evolution of mean stress as a function of decreasing suction. The cell volume in these simulations is not the same as in Chapter 4 for the same pellet mass. It is therefore not relevant to compare the value of mean stress of these simulations. The trend however displays some features already observed for pellet assemblies. The pressure increases, reaches a peak and then a plateau/decrease upon suction decrease.

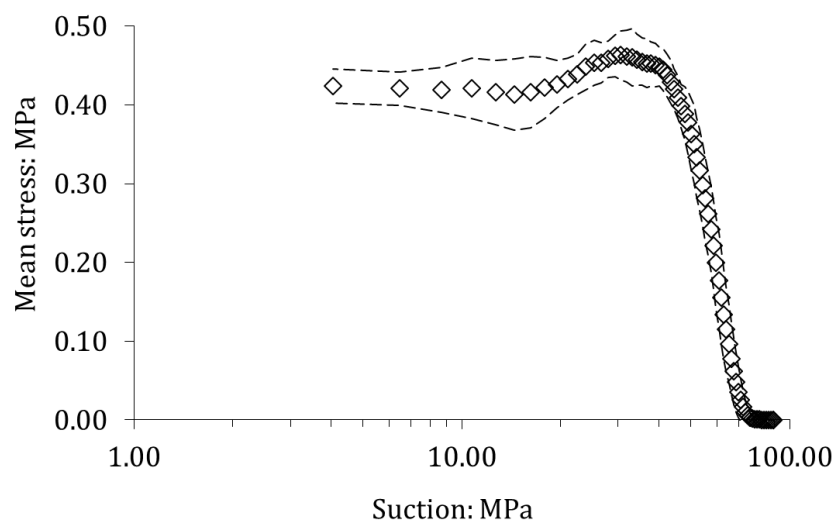


Figure 5-17: Evolution of mean stress as a function of decreasing suction in the simulation of binary granular mixtures using DEM. Dots represent the mean value for five samples while dashed lines represent the interval defined by two standard deviations.

Considering that these features are associated to contact plasticity, it is highlighted that in simulations, interactions at contacts between pellets still influences the macroscopic response.

In order to obtain an insight into the material behaviour, the following notations are introduced:

- The ratio of mean stresses, r_{ms} , is defined as the ratio of the mean stress induced by pellet-pellet contacts and pellet-wall contacts to the total mean stress in the sample. r_{ms} is deduced from equation 5-24 by calculating a p value corresponding to pellet-pellet and pellet-wall contacts only;
- The ratio of volume fractions, r_{vf} , is defined as the ratio of Φ_{mal}/Φ_l .

Following the calculation of the mean stress related to contact forces without powder grains, the same procedure is used to determine the mean stress related to contact forces associated to small particles and wall only. Figure 5-18 is then plotted. In Figure 5-18, it is highlighted that, in the simulations, before pellet strength is reached, all the mean stress is associated to the large particle assembly. Upon further suction decrease, the mean stress in the simulations is progressively dependent on the presence of small particles.

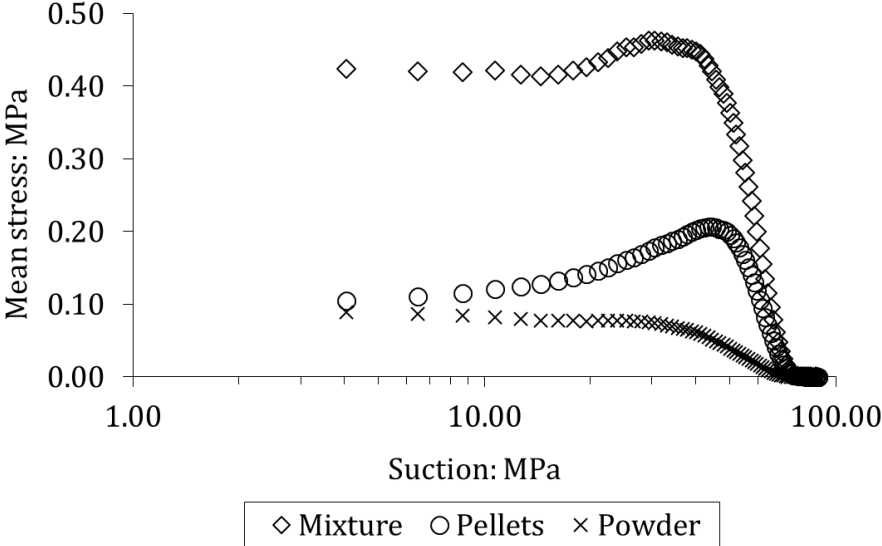


Figure 5-18: Contribution of the pellet assembly without powder grains and of the powder grain assembly without pellets to the total mean stress developed in the samples upon suction decrease. Mean values for the five samples are plotted.

The evolution of both r_{ms} and r_{vf} as functions of decreasing suction are presented in Figure 5-19. The decrease of the influence of the large particle assembly as r_{vf} increases is highlighted. As r_{vf} reaches 1, r_{ms} is slightly below 0.3. The large particle assembly therefore cannot be considered to control the macroscopic behaviour. Comparison between Figure 5-18 and Figure 5-19 also evidences that the mean stress associated to the small particles only increases as r_{vf} increases.

However, as highlighted by the trend of the mean stress-suction relationship, the remaining influence of the granular structure is obvious, since the plasticity at contacts keeps influencing the evolution of mean stress.

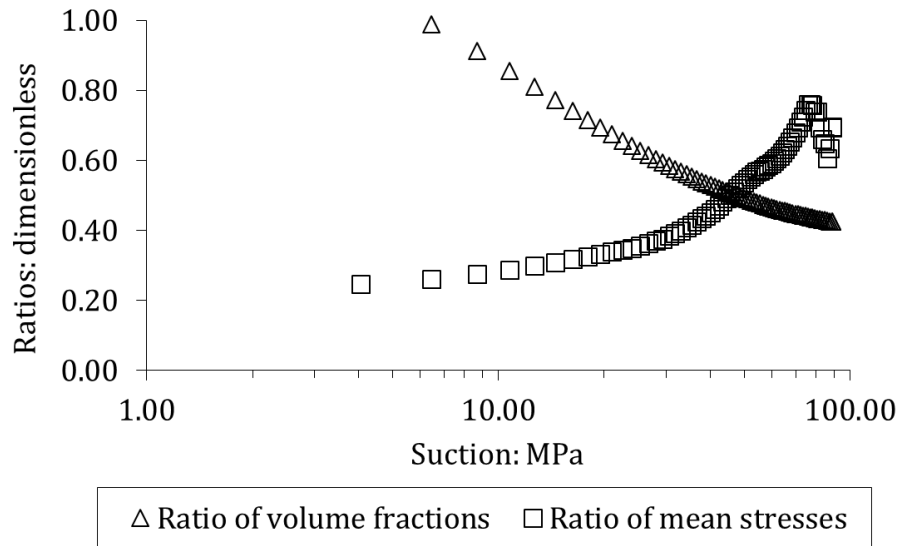


Figure 5-19: Evolution of r_{vf} and r_{ms} as functions of decreasing suction in the five samples. Mean values are plotted.

5.4.3.3 Proposition of a criterion

DEM simulations performed on a binary granular mixture highlighted that the small particles progressively contribute to the total mean stress in the sample. From these results, the proposition of a criterion is not straightforward but it is considered that r_{vf} is a relevant parameter in this purpose. DEM simulations also highlight that the influence of the granular structure, notably plasticity in contacts, remains even if r_{ms} becomes low.

Owing to the cost required to perform simulations of high number of particles at satisfactory equilibrium tolerance, these latter were performed at a diameter ratio of 1/6 and in a small cell.

It was suggested that powder in the inter-pellet porosity is at initial state in free-swelling conditions. From a simple geometrical perspective, it is considered that the 1/6 ratio cannot be related to a powder phase in free-swelling conditions, since a small particle cannot fit in the void defined by three adjacent large particles.

The realisation of simulations using more adapted ratios would significantly increase the number of particles. For instance, ratios 1/7; 1/10; 1/15 would induce (considering 209 pellets) 15362, 44786, and 151152 small particles in the cell, respectively, to obtain the same values of x_S and x_L .

Still, a perspective for the determination of an accurate criterion is the realisation of DEM simulations of binary mixtures at a more adapted diameter ratio, determined from the real size of powder grains. Different initial Φ_I/Φ_{mat} could be considered. Periodic boundary conditions presented in the present section could be considered to avoid influence of the simulated cell. In this respect, less than 4000 pellets should be placed in samples to avoid significant simulation duration. Larger samples would indeed induce significant simulation duration, but variability is reduced in periodic simulations. Few simulations would be required to obtain representative results.

In the present work, owing to the lack of data, an accurate criterion in terms of relative volume fractions is not presented. It is considered that the granular structure defined by the pellet assembly controls the behaviour for $\Phi_{mat} \ll \Phi_I$. It was not really the case in the simulations. However, the

simulated mixture was not really a pellet-powder mixture because of the 1/6 ratio. It was highlighted that influence of the pellet assembly decreases as r_{vf} increases.

The value of $r_{vf} = 1$ is suggested as a criterion. In other terms, it is considered that powder is in free-swelling conditions until the volume fraction of powder grains in inter-pellet porosity is the same as the pellet assembly volume fraction in the total volume.

5.4.4 Conclusions

The influence of the pellet assembly progressively decreases upon suction decrease. The definition of a criterion to describe the transition from granular state to continuous state is therefore a simplification of the material behaviour.

In the present section, it was proposed that the conceptual framework proposed in this Chapter is valid for materials characterised by $x_S < x_{S\text{crit}}$, the value of which has been determined equal to 0.302. If this condition is verified, the material is considered either granular, with increment of elastic volumetric strain described by equations presented in section 5.3, or continuous, with increment of elastic volumetric strain described by equations presented in section 5.5.

Two criteria are proposed, in terms of a threshold suction and a threshold r_{vf} , r_{vf}^* . Transition occurs if one criterion is verified. For MX80 pellet-powder mixtures, the following values are proposed:

- $s^* = 3$ MPa;
- $r_{vf}^* = 1$.

5.5 MODELLING THE “CONTINUOUS” MATERIAL MECHANICAL BEHAVIOUR

5.5.1 Objectives

The present section focuses on the behaviour of the material following the “granular”-“continuous” transition. In this section, the material is considered to behave as a continuum. No influence of the initial granular structure is taken into account. The conceptual framework of the BBM is modified to reproduce the relevant features of the material.

Compared to the BExM, generally preferred over the BBM to model the mechanical behaviour of compacted expansive clays, the BBM lacks relevant features such as the consideration of two levels of structure or the ability for the microstructure to induce large macrostructural swelling strains.

An overview of proposed modifications of the BBM is presented in part 5.5.2. Then, constitutive equations describing the behaviour of the material are presented in part 5.5.3.

5.5.2 Modification of the Barcelona Basic Model

The model considers three different families of porosity: macroporosity in the matrix, microporosity in pellets, microporosity in powder grains in the matrix. Each of these separated component is associated to a dimensionless stiffness parameter instead of using a single “ κ ” as in the BBM.

In the BExM, interaction functions describing the volumetric strain of macropores associated to the volumetric strain of micropores are added to the BBM framework to reproduce the behaviour of double structure materials. These latter are not considered in the present work. A stiffness parameter for suction change is provided for the macrostructure instead. This parameter is considered related to the mixture density.

Compared to the traditional BBM, the LC curve is not modified as already discussed in part 5.3.4.

5.5.3 Constitutive equations

5.5.3.1 Microstructural effective stresses

In the continuous domain, it is considered that both powder and pellets are equally affected by the mechanical pressure. Following the stress partition hypothesis presented in 5.3.4.2, the effective mean stresses in the pellet and powder phases are written as:

$$p'_1 = \frac{p}{\phi_1 + \phi_2} + s_1 \quad 5-53$$

And

$$p'_2 = \frac{p}{\phi_1 + \phi_2} + s_2 \quad 5-54$$

5.5.3.2 Microstructural elastic volumetric strains

Microstructural volumetric strains are considered elastic. These latter are expressed as follows:

$$d\varepsilon_{V1} = d\varepsilon_{V1}^{(e)} = \frac{\kappa_m}{1 + e_{10}} \frac{dp'_1}{p'_1} \quad 5-55$$

And

$$d\varepsilon_{V2} = d\varepsilon_{V2}^{(e)} = \frac{\kappa_m}{1 + e_{20}} \frac{dp'_2}{p'_2} \quad 5-56$$

5.5.3.3 Total elastic volumetric strain

The total elastic volumetric strain is expressed as a function of ε_{V1} ; ε_{V2} and ε_{VM} . From equation 5-14 relating e to e_1 , e_2 and e_M , $d\varepsilon_V$ is written as:

$$d\varepsilon_V^{(e)} = \frac{1}{1 + e_0} \left[(1 + e_{M0}) d\varepsilon_{VM}^{(e)} + (1 - x_{S0})(1 + e_{10}) d\varepsilon_{V1} + x_{S0} (1 + e_{20}) d\varepsilon_{V2} \right] \quad 5-57$$

Where x_{S0} is the initial volumetric proportion of powder in the mixture (thus equal to the ratio of the volume of solid in the powder to the total volume of solid, as pellets and powder are considered to have the same initial dry density), expressions of $d\varepsilon_{V1}$ and $d\varepsilon_{V2}$ are given by equations 5-55 and 5-56, and $d\varepsilon_{VM}^{(e)}$ is written as:

$$d\varepsilon_{VM}^{(e)} = \frac{\kappa}{1 + e_{M0}} \frac{dp}{p} + \frac{\kappa_s}{1 + e_{M0}} \frac{ds_2}{s_2 + p_{atm}} \quad 5-58$$

It is proposed to infer κ , κ_s and κ_m from literature or available experiments. κ_s characterises the macroscopic swelling induced as a result of suction variations. In the case of compacted expansive clays, this phenomenon occurs as a result of microstructural swelling and is considered dependent on dry density. κ_m characterises the microstructural strain and is considered, based on experimental results discussed in Chapter 2, not to be related to the material dry density. Variation of swelling potential related to the material dry density is thus, in the framework of the proposed model, though to be related only to the κ_s parameter. In these conditions, it is suggested from experimental results on compacted expansive materials (see Chapter 2) that, assuming constant κ_m , κ_s is higher at higher ρ_d .

5.5.3.4 Total plastic strains and hardening

Plasticity and hardening in the proposed model are addressed using the concept of the LC curve as introduced by Alonso et al. (1990) for the BBM. Plastic strains are governed by the plastic flow rule, identical for both granular and continuous domains.

Evolution of the preconsolidation pressure as a function of suction is described by the same equation as in the BBM:

$$p_0(s_2) = p_c \left(\frac{p_0(0)}{p_c} \right)^{\frac{\lambda(0) - \kappa}{\lambda(s) - \kappa}} \quad 5-59$$

Where p_c is the BBM reference stress (Alonso et al., 1990). It follows from the use of this expression for the evolution of the LC curve that equation 5-52 (hardening law) is equivalent to:

$$\frac{dp_0(s_2)}{p_0(s_2)} = \frac{1 + e_0}{\lambda(s) - \kappa} d\varepsilon_V^{(p)} \quad 5-60$$

The evolution of the dimensionless elastoplastic stiffness parameter λ as a function of suction is described by the same equation as in the BBM:

$$\lambda(s) = \lambda(0) [r + (1 - r) \exp(-\beta s)] \quad 5-61$$

Where values of β and r can be determined from experimental results from the literature. Based on oedometer test results from Marcial (2003), Villar (2005), Molinero-Guerra et al. (2019b), it is suggested that $p_0(0)$ is an exponential decreasing function of e . In the light of their results, presented in Chapter 2 (see Figure 2-26), it is proposed in the model to use equation 2-5 to determine the initial value of $p_0(0)$, and values of p^*_o in the range 75-150 MPa, values of n_p in the range 3.5-4, found to give values close to experimental results for MX80 bentonite.

Evolution of the material cohesion as a function of suction is addressed using the same equation as in the BBM:

$$p_s(s) = k_s s \quad 5-62$$

Where $p_s(s)$ is the intersection between the yield surface (modified Cam Clay ellipse) and the p-axis at $p < 0$ values and k_s is a parameter describing the evolution of material cohesion with suction.

In triaxial stress state, the yield surface is the same as in the modified Cam Clay model:

$$F = q^2 - M^2(p + p_s(s))(p_0(s) - p) = 0 \quad 5-63$$

Where q is the deviatoric stress and M is the slope of the critical state line. An associated flow rule is considered for simplicity, whereas the flow rule is non-associated in the original BBM formulation.

5.6 IMPLEMENTATION OF THE MODEL

5.6.1 Introduction

The model described in sections 5.3, 5.4, and 5.5, is implemented in the open source FEM code Bil. The model is written in the framework of hardening elastoplasticity and is an extension of the modified Cam-Clay. In the present section, the main features of the model as well as hypotheses considered for its implementation are presented in part 5.6.2. Then, details regarding the determination of elastic stresses from volumetric strain at each time step are provided in part 5.6.3. Calculation of microstructural strains is addressed in part 5.6.4.

5.6.2 Summary of the model features

Previous sections have addressed the development of a model describing the mechanical behaviour of pellet-powder mixtures where pellets are the dominant phase at initial state. The transition from granular to continuous states is described by two criteria. Table 5-5 summarises the criteria considered to define the transition from granular to continuous states.

Table 5-5: Criteria describing the transition from granular to continuous states.

Criterion	Parameter	Value
Suction	s_l	3 MPa
Powder density	r_{vf}	1

Different equations are used to describe the material behaviour in granular and continuous states. Table 5-6 summarises the equations used to determine the value of the main parameters of the model. All the laws given by equations summarised in Table 5-6 are integrable.

At each time step, Δp is determined from $\Delta \varepsilon_V$ and Δs . The following procedure is applied:

- *i)* Verification of the two conditions mentioned in Table 5-5;
- *ii)* Newton-Raphson iterative procedure to determine Δp from integration of elastic equations mentioned in Table 5-6;
- *iii)* Verification of the admissibility of the trial stress state;
- *iv)* Eventual plastic correction of the stress state and calculation of plastic strains;
- *v)* Calculation of ε_{V1} and ε_{V2} .

In the present Chapter, it is reminded that hydraulic transfers are not addressed and “time” does not have an actual physical meaning.

Table 5-6: List of the main equations of the model.

Notation	Equation in granular state	Equation in continuous state
<i>Mixture properties</i>		
Φ_1		$\Phi_1 = \frac{\Omega_1}{\Omega}$
Φ_2		$\Phi_2 = \frac{\Omega_2}{\Omega}$
Φ_{mat}		$\Phi_{mat} = \frac{\Omega_2}{\Omega (1 - \Phi_1)}$
p'_1	$p'_1 = \frac{p}{\Phi_1} + s_1$	$p'_1 = \frac{p}{\Phi_1 + \Phi_2} + s_1$
p'_2	$p'_2 = s_2$	$p'_2 = \frac{p}{\Phi_1 + \Phi_2} + s_2$
<i>Elastic volumetric strain</i>		
$\varepsilon_V^{(e)}$	$d\varepsilon_V^{(e)} = \frac{\partial \varepsilon_V^{(e)}}{\partial m_g} dm_g + \frac{\partial \varepsilon_V^{(e)}}{\partial \varepsilon_{V1}} d\varepsilon_{V1}$	$d\varepsilon_V^{(e)} = \frac{1}{1 + e_0} \left[\begin{array}{l} (1 + e_{M0}) d\varepsilon_{VM}^{(e)} \\ + (1 - x_{S0})(1 + e_{10}) d\varepsilon_{V1} \\ + x_{S0} (1 + e_{20}) d\varepsilon_{V2} \end{array} \right]$
ε_{V1}	$d\varepsilon_{V1} = \frac{dp'_1}{\frac{1}{\beta_m} \exp(\alpha_m p'_1)}$	$d\varepsilon_{V1} = \frac{\kappa_m}{1 + e_{10}} \frac{dp'_1}{p'_1}$
ε_{V2}	$d\varepsilon_{V2} = \frac{dp'_2}{\frac{1}{\beta_m} \exp(\alpha_m p'_2)}$	$d\varepsilon_{V2} = d\varepsilon_{V2}^{(e)} = \frac{\kappa_m}{1 + e_{20}} \frac{dp'_2}{p'_2}$
<i>Plasticity</i>		
Yield surface		$F = q^2 - M^2(p + p_s(s))(p_0(s) - p) = 0$
Associated flow rule		$d\varepsilon^{(p)} = \lambda_p \frac{\partial F}{\partial \sigma}$
Initial $p_0(0)$		$p_0(0) = p_0^* \exp(-n_p e_0)$
$p_0(s)$		$p_0(s) = p_c \left(\frac{p_0(0)}{p_c} \right)^{\frac{\lambda(0) - \kappa}{\lambda(s) - \kappa}}$
$\lambda(s)$		$\lambda(s) = \lambda(0) [r + (1 - r) \exp(-\beta s)]$
$p_s(s)$		$p_s(s) = k_s s$
Hardening law		$\frac{dp_0(0)}{p_0(0)} = \frac{1 + e_0}{\lambda(0) - \kappa} d\varepsilon_V^{(p)}$

5.6.3 Calculation of stress state from total volumetric strain

In the present part, notations are associated to subscript t or $t + \Delta t$ to distinguish values of these latter at time step t or $t + \Delta t$. Δs and $\Delta \varepsilon$ are given:

Criteria associated to the material state are first verified. Elastic trial stress state is then determined for either granular or continuous state. Finally, plasticity and hardening eventually arise if the trial stress state is located outside the elastic domain.

5.6.3.1 Granular-continuous transition

If the material was granular at time step t , then the material state is verified before calculation of material properties at time step $t + \Delta t$. Transition is considered irreversible. The material remains “continuous” once a criterion has been reached.

Verification of the material state requires some properties to be determined. The following calculation steps are realised:

$$p_t = \frac{1}{3}(\sigma_{11_t} + \sigma_{22_t} + \sigma_{33_t}) \quad 5-64$$

$$\varepsilon_{V_t} = \varepsilon_{11_t} + \varepsilon_{22_t} + \varepsilon_{33_t} \quad 5-65$$

$$\Phi_{1_t} = (1 - x_{S_0}) \frac{\rho_{d1_0}}{\rho_{d_0}} \frac{1 + \varepsilon_{V1_t}}{1 + \varepsilon_{V_t}} \quad 5-66$$

$$\Phi_{2_t} = x_{S_0} \frac{\rho_{d1_0}}{\rho_{d_0}} \frac{1 + \varepsilon_{V2_t}}{1 + \varepsilon_{V_t}} \quad 5-67$$

$$r_{vf\ t+\Delta t} = \frac{\Phi_{2_t}}{\Phi_{1_t}(1 - \Phi_{1_t})} \quad 5-68$$

Where ρ_{d1_0} is the initial pellet dry density.

The material state is then determined from comparison of $s_{t+\Delta t}$ (given) and $r_{vf\ t+\Delta t}$ (equation 5-68) with values of Table 5-5.

5.6.3.2 Elastic trial stress in granular state

In the granular state, mean stress, $p_{t+\Delta t}$, is determined from the increment of volumetric strain and suction:

$$\Delta\varepsilon_{V_{t+\Delta t}} = \varepsilon_{V_{t+\Delta t}} - \varepsilon_{V_t} \quad 5-69$$

Where:

$$\varepsilon_{V_{t+\Delta t}} = \varepsilon_{11_{t+\Delta t}} + \varepsilon_{22_{t+\Delta t}} + \varepsilon_{33_{t+\Delta t}} \quad 5-70$$

And

$$\Delta s_{t+\Delta t} = s_{t+\Delta t} - s_t \quad 5-71$$

The dimensionless pressure parameter at previous time step is:

$$m_{g_t} = \left(\frac{p_t}{\frac{3(1-2\nu)}{\beta_m(1-\nu^2)} \exp\left(\alpha_m \left(\frac{p_t}{\Phi_{1_t}} + s_{1_t}\right)\right)} \right)^{2/3} \quad 5-72$$

Then, $p_{t+\Delta t}$ is set to the initial value p_t before starting the iterative procedure. In the following, superscript (i) refers to the i^{th} iteration:

$$i = 0$$

$$p_{t+\Delta t}^{(i=0)} = p_t \quad 5-73$$

A Newton-Raphson iterative procedure is then performed until convergence or max number of iterations is reached to determine a value of $\Delta p_{t+\Delta t}$ inducing an increment of elastic volumetric strain of $\Delta\varepsilon_{V_{t+\Delta t}}$:

Step 1

The dimensionless pressure parameter is determined for iteration i :

$$m_g^{(i)} = \left(\frac{p_{t+\Delta t}^{(i)}}{\frac{3(1-2\nu)}{\beta_m(1-\nu^2)} \exp\left(\alpha_m \left(\frac{p_{t+\Delta t}^{(i)}}{\Phi_{1t}} + s_{1t+\Delta t}\right)\right)} \right)^{2/3} \quad 5-74$$

Step 2

m_g^* is determined using equation 5-38. Then, depending on its value, the elastic increment of volumetric strain associated to variation of m_g , $\Delta\varepsilon_{VA}^{(e)}$, is determined for iteration i :

if $(m_g^{(i)} \leq m_g^*)$ and $(m_g_t \leq m_g^*)$

$$\Delta\varepsilon_{VA}^{(e)(i)} = f_{\varepsilon A} (m_g^{(i)} - m_g_t) \quad 5-75$$

else if $(m_g^{(i)} > m_g^*)$ and $(m_g_t \leq m_g^*)$

$$\Delta\varepsilon_{VA}^{(e)(i)} = f_{\varepsilon B} (m_g^{(i)} - m_g^*) + f_{\varepsilon A} (m_g^* - m_g_t) \quad 5-76$$

else if $(m_g^{(i)} \leq m_g^*)$ and $(m_g_t > m_g^*)$

$$\Delta\varepsilon_{VA}^{(e)(i)} = f_{\varepsilon A} (m_g^{(i)} - m_g^*) + f_{\varepsilon B} (m_g^* - m_g_t) \quad 5-77$$

else if $(m_g^{(i)} > m_g^*)$ and $(m_g_t > m_g^*)$

$$\Delta\varepsilon_{VA}^{(e)(i)} = f_{\varepsilon B} (m_g^{(i)} - m_g_t) \quad 5-78$$

Step 3

The elastic increment of volumetric strain associated to variation of ε_{VI} , $\Delta\varepsilon_{VB}^{(e)}$, is determined for iteration i :

$$\Delta \varepsilon_{V_{B_{t+\Delta t}}^{(e)}}^{(i)} = f_{Mm} \frac{\beta_m}{\alpha_m} \left[\exp \left(-\alpha_m \left(\frac{p_{t+\Delta t}^{(i)}}{\Phi_{1t}} + s_{1t+\Delta t} \right) \right) - \exp \left(-\alpha_m \left(\frac{p_t}{\Phi_{1t}} + s_{1t} \right) \right) \right] \quad 5-79$$

Step 4

The test function, $f_{NR}^{(i)}$ and its derivative with respect to p are then computed at iteration i :

$$\left(\frac{\partial \varepsilon_{V_A}^{(e)}}{\partial m_g} \right)_{t+\Delta t}^{(i)} = f_\varepsilon \quad 5-80$$

Where f_ε is given by equation 5-36 ($m_{g_{t+\Delta t}}^{(i)} \leq m_g^*$) or 5-37 ($m_{g_{t+\Delta t}}^{(i)} > m_g^*$).

$$\left(\frac{\partial m_g}{\partial p} \right)_{t+\Delta t}^{(i)} = \frac{2}{3} \left[\left(\frac{1}{p_{t+\Delta t}^{(i)}} \right) + \left(-\frac{\alpha_m}{\Phi_{1t}} \right) \right] \left(\frac{\beta_m}{3} \frac{1-v^2}{1-2v} \right)^{2/3} (p_{t+\Delta t}^{(i)})^{2/3} \exp \left(-\frac{2}{3} \alpha_m \left(\frac{p_{t+\Delta t}^{(i)}}{\Phi_{1t}} + s_{1t+\Delta t} \right) \right) \quad 5-81$$

$$\left(\frac{\partial \varepsilon_{V_B}^{(e)}}{\partial \varepsilon_{V1}} \right)_{t+\Delta t}^{(i)} = f_{Mm} \quad 5-82$$

$$\left(\frac{\partial \varepsilon_{V1}}{\partial p} \right)_{t+\Delta t}^{(i)} = \frac{\beta_m}{\Phi_{1t}} \exp \left(-\alpha_m \left(\frac{p_{t+\Delta t}^{(i)}}{\Phi_{1t}} + s_{1t+\Delta t} \right) \right) \quad 5-83$$

$$\left(\frac{\partial f_{NR}}{\partial p} \right)_{t+\Delta t}^{(i)} = - \left[\left(\frac{\partial \varepsilon_{V_A}^{(e)}}{\partial m_g} \right)_{t+\Delta t}^{(i)} \left(\frac{\partial m_g}{\partial p} \right)_{t+\Delta t}^{(i)} + \left(\frac{\partial \varepsilon_{V_B}^{(e)}}{\partial \varepsilon_{V1}} \right)_{t+\Delta t}^{(i)} \left(\frac{\partial \varepsilon_{V1}}{\partial p} \right)_{t+\Delta t}^{(i)} \right] \quad 5-84$$

$$f_{NR}^{(i)} = \Delta \varepsilon_{V_{t+\Delta t}} - \left(\Delta \varepsilon_{V_{A_{t+\Delta t}}^{(e)}}^{(i)} + \Delta \varepsilon_{V_{B_{t+\Delta t}}^{(e)}}^{(i)} \right) \quad 5-85$$

If $\left(\frac{\partial f_{NR}}{\partial p} \right)_{t+\Delta t}^{(i)}$ equals zero, then the iterative procedure is stopped and no convergence is reached.

Step 5

Convergence is considered if $f_{NR}^{(i)}$ is lower than a tolerance value. The tolerance value is chosen equal to 10^{-8} . If $f_{NR}^{(i)}$ is higher than this value, the iterative procedure is repeated from step 1. If i reaches 50, then the iterative procedure is stopped and no convergence is reached. If the procedure converges, then $p_{t+\Delta t}$, is equal to $p_{t+\Delta t}^{(i)}$ and the increment of mean stress is obtained:

$$\Delta p_{t+\Delta t} = p_{t+\Delta t}^{(i)} - p_t \quad 5-86$$

Before repeating step 1, i is incremented and $p_{t+\Delta t}^{(i)}$ is actualised.

$$p_{t+\Delta t}^{(i+1)} = p_{t+\Delta t}^{(i)} - \frac{f_{NR}^{(i)}}{\left(\frac{\partial f_{NR}}{\partial p}\right)^{(i)}} \quad 5-87$$

$$i = i + 1$$

5.6.3.3 Elastic trial stress in continuous state

In the continuous state, $p_{t+\Delta t}$, is determined from the increment of volumetric strain and suction, determined using equations 5-69 and 5-71.

The part of the increment of total volumetric strain induced by suction variations, in the pellet phase, $\Delta \varepsilon_{VC}^{(e)}$, and in the matrix phase, $\Delta \varepsilon_{VD}^{(e)}$, are first computed, assuming elasticity:

$$\Delta \varepsilon_{VC}^{(e)} = (1 - x_{S0}) \frac{\kappa_m}{1 + e_0} \ln \left(\frac{s_{1\ t+\Delta t} + \frac{p_t}{\Phi_{1\ t} + \Phi_{2\ t}}}{s_{1\ t} + \frac{p_t}{\Phi_{1\ t} + \Phi_{2\ t}}} \right) \quad 5-88$$

$$\Delta \varepsilon_{VD}^{(e)} = x_{S0} \frac{\kappa_m}{1 + e_0} \ln \left(\frac{s_{2\ t+\Delta t} + \frac{p_t}{\Phi_{1\ t} + \Phi_{2\ t}}}{s_{2\ t} + \frac{p_t}{\Phi_{1\ t} + \Phi_{2\ t}}} \right) + \frac{\kappa_s}{1 + e_0} \ln \left(\frac{s_{2\ t+\Delta t} + p_{atm}}{s_{2\ t} + p_{atm}} \right) \quad 5-89$$

Then, $p_{t+\Delta t}$ is set to the initial value p_t before starting the iterative procedure.

$$i = 0$$

$$p_{t+\Delta t}^{(i=0)} = p_t \quad 5-90$$

A Newton-Raphson iterative procedure is then performed until convergence or max number of iterations is reached to determine a value of $\Delta p_{t+\Delta t}$ inducing an increment of elastic volumetric strain of $\Delta \varepsilon_{V\ t+\Delta t}$:

Step 1

The increment of volumetric strain associated to variation of p , $\Delta\varepsilon_{VE}^{(e)}$, at iteration i , is written:

$$\Delta\varepsilon_{VE}^{(e)(i)} = x_1 \frac{\kappa_m}{1+e_0} \ln \left(\frac{p_{t+\Delta t}^{(i)} + (\Phi_{1t} + \Phi_{2t})s_{1t}}{p_t + (\Phi_{1t} + \Phi_{2t})s_{1t}} \right) + x_2 \frac{\kappa_m}{1+e_0} \ln \left(\frac{p_{t+\Delta t}^{(i)} + (\Phi_{1t} + \Phi_{2t})s_{2t}}{p_t + (\Phi_{1t} + \Phi_{2t})s_{2t}} \right) + \frac{\kappa}{1+e_0} \ln \left(\frac{p_{t+\Delta t}^{(i)}}{p_t} \right) \quad 5-91$$

Step 2

The test function, $f_{NR}^{(i)}$ and its derivative with respect to p are then computed at iteration i :

$$\left(\frac{\partial \varepsilon_{VE}^{(e)}}{\partial p} \right)_{t+\Delta t}^{(i)} = (1-x_{s0}) \frac{\kappa_m}{1+e_0} \frac{1}{p_{t+\Delta t}^{(i)} + (\Phi_{1t} + \Phi_{2t})s_{1t+\Delta t}} + x_{s0} \frac{\kappa_m}{1+e_0} \frac{1}{p_{t+\Delta t}^{(i)} + (\Phi_{1t} + \Phi_{2t})s_{2t+\Delta t}} + \frac{\kappa}{1+e_0} \frac{1}{p_{t+\Delta t}^{(i)}} \quad 5-92$$

$$\left(\frac{\partial f_{NR}}{\partial p} \right)^{(i)} = - \left(\frac{\partial \varepsilon_{VE}^{(e)}}{\partial p} \right)_{t+\Delta t}^{(i)} \quad 5-93$$

$$f_{NR}^{(i)} = \Delta\varepsilon_{V_{t+\Delta t}} - \left(\Delta\varepsilon_{V_C}^{(e)} + \Delta\varepsilon_{V_D}^{(e)} + \Delta\varepsilon_{V_E}^{(e)(i)} \right) \quad 5-94$$

If $\left(\frac{\partial f_{NR}}{\partial p} \right)^{(i)}$ equals zero, then the iterative procedure is stopped and no convergence is reached.

Step 3

Convergence is considered if $f_{NR}^{(i)}$ is lower than a tolerance value. The tolerance value is chosen equal to 10^{-8} . If $f_{NR}^{(i)}$ is higher than this value, the iterative procedure is repeated from step 1. If i reaches 50, then the iterative procedure is stopped and no convergence is reached. If the procedure converges, then $p_{t+\Delta t}$, is equal to $p_{t+\Delta t}^{(i)}$ and the increment of mean stress is obtained:

$$\Delta p_{t+\Delta t} = p_{t+\Delta t}^{(i)} - p_t \quad 5-95$$

Before repeating step 1, i is incremented and $p_{t+\Delta t}^{(i)}$ is actualised.

$$p_{t+\Delta t}^{(i+1)} = p_{t+\Delta t}^{(i)} - \frac{f_{NR}^{(i)}}{\left(\frac{\partial f_{NR}}{\partial p} \right)^{(i)}} \quad 5-96$$

$$i = i + 1$$

5.6.3.4 Bulk modulus of the material

The elastic trial stress state is computed from the increment of mean stress determined using the Newton-Raphson iterative procedure. The material bulk modulus, $K^{(e)}_{t+\Delta t}$ is first computed. Two cases can be distinguished depending on the material state.

Case 1: the material is granular

If the material is granular, $K^{(e)}_{t+\Delta t}$ is computed as:

$$K^{(e)}_{t+\Delta t} = \frac{1}{f_\varepsilon \frac{\partial m_g}{\partial p} + f_{Mm} \frac{\partial \varepsilon_{V1}}{\partial p}} \quad 5-97$$

Where f_ε is given by equation 5-36 and 5-37; f_{Mm} is taken equal to 1; $\frac{\partial m_g}{\partial p}$ is computed using equation 5-51; $\frac{\partial \varepsilon_{V1}}{\partial p}$ is computed using equation 5-49; with $p = p_{t+\Delta t}$; $s_1 = s_{1t+\Delta t}$; and $\Phi_1 = \Phi_{1t}$.

Case 2: the material is continuous

If the material is continuous, $K^{(e)}_{t+\Delta t}$ is computed as:

$$K^{(e)}_{t+\Delta t} = \frac{1 + e_0}{\kappa_{eq\ t+\Delta t}} \quad 5-98$$

Where κ_{eq} is an apparent stiffness parameter computed as:

$$\kappa_{eq\ t+\Delta t} = \left(\frac{(1 - x_{S0})}{p_{t+\Delta t} + (\Phi_{1t} + \Phi_{2t})s_{1\ t+\Delta t}} + \frac{x_{S0}}{p_{t+\Delta t} + (\Phi_{1t} + \Phi_{2t})s_{2\ t+\Delta t}} \right) \kappa_m + \frac{\kappa}{p_{t+\Delta t}} \quad 5-99$$

5.6.3.5 Elastic trial stress state

From values of p_t ; $\Delta p_{t+\Delta t}$; $K^{(e)}_{t+\Delta t}$; $\Delta \varepsilon_{V\ t+\Delta t}$; and the stress tensor at time step t , σ_t , the trial total stress tensor at time step $t + \Delta t$, $\sigma^{(e)}_{t+\Delta t}$, is obtained:

$$\Delta \sigma^{(e)}_{t+\Delta t} = \frac{3(1 - 2\nu)}{(1 + \nu)} K^{(e)}_{t+\Delta t} \Delta \varepsilon_{t+\Delta t} + \left(\Delta p_{t+\Delta t} - \frac{(1 - 2\nu)}{(1 + \nu)} K^{(e)}_{t+\Delta t} \Delta \varepsilon_{V\ t+\Delta t} \right) \mathbf{I} \quad 5-100$$

And

$$\sigma^{(e)}_{t+\Delta t} = \sigma_t + \Delta \sigma^{(e)}_{t+\Delta t} \quad 5-101$$

5.6.3.6 Verification of the trial stress state

If the stress state is located inside the elastic domain, then the stress state remains the one determined from elastic trial stresses.

However, the stress state determined from the calculation of elastic trial stresses may be located outside the elastic domain defined by the modified Cam Clay ellipse in the q-p plane. In this case, a return-mapping procedure restores the stress state to the yield surface and plastic strains are generated according to the consistency condition.

It is reminded that an associated flow rule is used in the present work:

$$d\boldsymbol{\varepsilon}_{t+\Delta t}^{(p)} = \lambda_p \frac{\partial G}{\partial \boldsymbol{\sigma}} = \lambda_p \frac{\partial F}{\partial \boldsymbol{\sigma}} \quad 5-102$$

Where λ_p is the plastic multiplier and G the plastic potential.

The final stress state at time step $t + \Delta t$ is thus obtained and written $\boldsymbol{\sigma}_{t+\Delta t}$.

5.6.4 Microstructural strains

5.6.4.1 Granular material

Following the calculation of the stress tensor, volumetric strains of the pellet and powder phases are computed in granular state as follows:

$$\varepsilon_{V1_{t+\Delta t}}^{(e)} = \varepsilon_{V1_t}^{(e)} + \frac{\beta_m}{\alpha_m} \left[\exp\left(-\alpha_m \left(\frac{p_{t+\Delta t}}{\Phi_{1_t}} + s_{1_{t+\Delta t}}\right)\right) - \exp\left(-\alpha_m \left(\frac{p_t}{\Phi_{1_t}} + s_{1_t}\right)\right) \right] \quad 5-103$$

And

$$\varepsilon_{V2_{t+\Delta t}}^{(e)} = \varepsilon_{V2_t}^{(e)} + \frac{\beta_m}{\alpha_m} \left[\exp(-\alpha_m s_{2_{t+\Delta t}}) - \exp(-\alpha_m s_{2_t}) \right] \quad 5-104$$

5.6.4.2 Continuous material

In continuous state, volumetric strains of the pellet and powder phases are computed as follows:

$$\varepsilon_{V1_{t+\Delta t}}^{(e)} = \varepsilon_{V1_t}^{(e)} + \frac{\kappa_m}{1 + e_{10}} \left[\ln\left(\frac{p_{t+\Delta t} + (\Phi_{1_t} + \Phi_{2_t})s_{1_t}}{p_t + (\Phi_{1_t} + \Phi_{2_t})s_{1_t}}\right) + \ln\left(\frac{\frac{p_t}{\Phi_{1_t} + \Phi_{2_t}} + s_{1_{t+\Delta t}}}{\frac{p_t}{\Phi_{1_t} + \Phi_{2_t}} + s_{1_t}}\right) \right] \quad 5-105$$

And

$$\varepsilon_{V2_{t+\Delta t}}^{(e)} = \varepsilon_{V2_t}^{(e)} + \frac{\kappa_m}{1 + e_{10}} \left[\ln \left(\frac{p_{t+\Delta t} + (\Phi_{1_t} + \Phi_{2_t})s_{2_t}}{p_t + (\Phi_{1_t} + \Phi_{2_t})s_{2_t}} \right) + \ln \left(\frac{\frac{p_t}{\Phi_{1_t} + \Phi_{2_t}} + s_{2_{t+\Delta t}}}{\frac{p_t}{\Phi_{1_t} + \Phi_{2_t}} + s_{2_t}} \right) \right] \quad 5-106$$

Where e_{10} is the initial void ratio of the pellet. It is assumed that the initial void ratio of the powder grain is the same as the one of the pellet.

5.6.4.3 Evolution of volume fractions

The volume fraction of the pellet phase and the powder phase are finally computed as follows:

$$\Phi_{1_{t+\Delta t}} = \Phi_{1_t} \left(\frac{1 + \varepsilon_{V1_{t+\Delta t}}}{1 + \varepsilon_{V_{t+\Delta t}}} \right) \quad 5-107$$

And

$$\Phi_{2_{t+\Delta t}} = \Phi_{1_t} \left(\frac{1 + \varepsilon_{V2_{t+\Delta t}}}{1 + \varepsilon_{V_{t+\Delta t}}} \right) \quad 5-108$$

It follows that

$$\Phi_{mat_{t+\Delta t}} = \frac{\Phi_{2_{t+\Delta t}}}{1 - \Phi_{1_{t+\Delta t}}} \quad 5-109$$

Which allows the calculation of an actualised criterion for the “granular”-“continuous” transition.

5.7 VALIDATION AGAINST EXPERIMENTAL RESULTS

A summary of all the values used in the modelling of MX80 pellet-powder mixtures is presented in part 5.7.1. Finally, simulations of a pellet-powder mixture under mechanical loading at constant suction (from Molinero-Guerra et al., 2019b) and hydration in constant-volume conditions (from Chapter 3) are respectively presented in part 5.7.2 and 5.7.3

5.7.1 Determination of the model parameters

In order for the model to be validated against experimental results, the present part proposes a list of all parameters required to perform simulations along with values of these latter.

5.7.1.1 Mixture properties

Four different pellet-powder mixtures are studied in the present Chapter. Their geotechnical properties are summarised in Table 5-7.

Table 5-7: Main properties of the different MX80 pellet-powder mixtures simulated in the present Chapter.

Property	70/0	70/15	70/30	80/20
ρ_d : Mg/m ³	1.05	1.275	1.50	1.49*
x_{s0}	0	0.18	0.30	0.20*
s : MPa	89	89	89	138*
Φ_{l0}	0.553	0.553	0.553	0.562
r_{vf0}	0	0.48	0.96	0.57

*: Molinero-Guerra et al. (2019b)

5.7.1.2 Parameters describing the “granular” state

The model parameters have been determined either from pellet characterisation in the laboratory (Chapter 4) or DEM simulations of large granular assemblies in section 5.3. The same values are used in the simulations for the model validation. These latter are summarised in Table 5-8.

Table 5-8: Model parameters for the granular state used in the simulations.

Parameter	70/0	70/15	70/30	80/20
α_m : MPa ⁻¹			0.024	
β_m : MPa ⁻¹			0.016	
f_{Mm}			1	
f_{eA}			6	
f_{eB}			40	
f_{mA}			0.067	
f_{mB}			- 0.031	

5.7.1.3 Parameters describing the “granular” state - “continuous” state transition

The transition in the simulations is described by $s^* = 3$ MPa and $r_{vf}^* = 1$.

5.7.1.4 Parameters describing the “continuous” state in the elastic domain

Model parameters to characterise in order to perform simulation in the continuous state are the dimensionless stiffness parameters κ , κ_s , κ_m , and the initial void ratios e_{10} , e_{M0} and e_0 .

The void ratios are obtained by considering that, for MX80, $\rho_s = 2.77$ Mg/m³ (Saba et al., 2014b). In pellets presented in Chapter 3, the initial dry density is 1.91 Mg/m³ and the initial void ratio can thus be estimated: $e_{10} = 0.450$. In Molinero-Guerra et al. (2019b), the void ratio is given: $e_{10} = 0.300$. In all mixtures, the total void ratio is estimated from the average dry density and ρ_s (Table 5-9). Values of e_{m0} and e_{M0} are deduced from these latter.

It is suggested to choose a similar κ and κ_m for all simulations and a κ_s increasing with increasing dry density. Mokni et al. (2019) modelled the behaviour of the 80/20 mixture using $\kappa = 0.028$. A close value of κ (0.025) is considered in the present work. Comparison with literature results for parameters related to suction or microstructure (κ_s and κ_m for instance) has to be careful since these latter can have different definitions depending on the model formulation and thus significantly different influence on the macroscopic response.

It is suggested from the literature review presented in Chapter 2 that κ_s is higher for dense materials. The ratio e_{m0}/e_0 is proposed as a way of describing the closure of macrostructure. To reduce the number of fitted parameters in the present approach while accounting for the material density, it is proposed to determine κ_s from κ_m :

$$\kappa_s = \frac{e_{m0}}{e_0} \kappa_m \quad 5-110$$

Thus, only the value of κ_m needs to be conveniently estimated to reproduce all the test results. Equation 5-110 allows the increase of swelling potential with increasing density to be reproduced. It is purely conceptual and other approach able to reproduce the increase of κ_s with increasing density may provide interesting results. The tendency for κ_s to increase with increasing dry density using this approach is highlighted in Figure 5-20. In Figure 5-20, κ_s values obtained for the three mixtures studied in the present work are presented, along with the values predicted using equation 5-110 for $e_{m0} = 0.450$ (dashed line).

Dimensionless stiffness parameters are presented in Table 5-9. The proposed values are found to satisfactorily reproduce the material behaviour in swelling pressure test or mechanical loading at constant suction, as highlighted in the following parts.

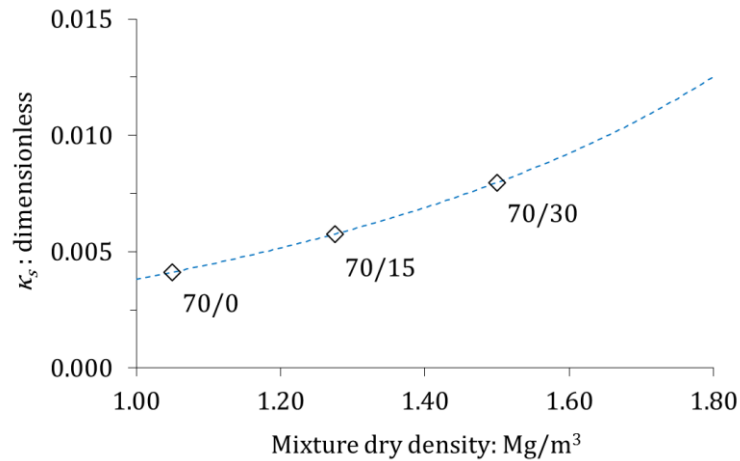


Figure 5-20: Values of κ_s used in the simulations as functions of the material initial dry density.

The κ_m value suggested to reproduce the material behaviour using the present model is 0.015 (Table 5-9). It is lower than the value proposed by Mokni et al. (2019). However, the present study does not consider interaction functions and the resulting κ_s is higher than the value proposed in Mokni et al. (2019).

Table 5-9: Model parameters for the continuous state used in the simulations

Parameter	70/0	70/15	70/30	80/20
e_{m0}		0.450		0.300*
e_{M0}	1.19	0.722	0.396	0.559
e_0	1.64	1.17	0.847	0.859*
κ		0.025		
κ_m		0.015		
κ_s (eq. 5-110)	0.0041	0.0058	0.0080	0.0052

*: Molinero-Guerra et al. (2019b)

5.7.1.5 Parameters describing plasticity and hardening

Parameters describing the material plastic and hardening behaviours are presented in Table 5-10. The saturated value of λ as well as r and β values (describing its evolution as a function of suction) are chosen in the same range as in Mokni et al. (2019) for the MX80 80/20 mixture.

Parameters related to the evolution of $p_0(s)$ should not be directly taken from literature since, depending on the model formulation, yielding may arise either as a result of micro-macro interactions in addition to LC yielding (*e.g.* in BExM), or from LC yielding only (*e.g.* in BBM). The p_c parameter is found to take a wide range of values in the literature. For instance, Wang et al. (2013d) and Dieudonné (2016) proposed values of 0.005 MPa and 0.01 MPa, respectively, in the modelling of the same MX80-sand mixture, but using the BExM and a model based on the BBM framework, respectively. Sanchez et al. (2016) and Mokni et al. (2019) both used BExM based modelling frameworks to model

the behaviour of MX80 pellet-powder mixtures and used values of 0.2 MPa and 0.6 MPa, respectively. In the present work, no information related to this parameter is available and p_c is conveniently taken equal to 0.05 MPa.

Finally, the proposed relationship relating experimental values of $p_o(0)$ to e (equation 2-5) is used, accounting for values of $p_o^* = 80$ MPa and $n_p = 3.7$.

Table 5-10: Model parameters for plasticity and hardening

Mixture	70/0	70/15	70/30	80/20
$\lambda(0)$			0.20	
p_c : MPa			0.050	
r			0.8	
β : MPa ⁻¹			0.1	
p_o^* : MPa			80	
n_p			3.7	

5.7.2 Mechanical loading at constant suction in oedometer conditions

5.7.2.1 Introduction

The first simulation is a constant 138 MPa-suction mechanical loading in an oedometer cell. The test was performed by Molinero-Guerra et al. (2019b) and results were presented in Chapter 2 (SCO1, Figure 2-51).

On imposing loads, volumetric strains occurred almost instantaneously, which authors interpreted as a consequence of the granular assembly rearrangement and/or pellet crushing. This test is simulated using the proposed model.

5.7.2.2 Material

The material is an 80/20 MX80 pellet-powder mixture. Its main properties are summarised in Table 5-7. Parameters of the model are presented in Table 5-7, Table 5-8, Table 5-9, Table 5-10.

5.7.2.3 Geometry of the problem

Molinero-Guerra et al. (2019b) oedometer test is modelled using two-dimensional axisymmetric conditions. The cylindrical oedometer cell is thus represented by a rectangle in the FEM analysis. The y axis is the axis of symmetry. The mesh consists in one Q4 element. This latter is presented in Figure 5-21.

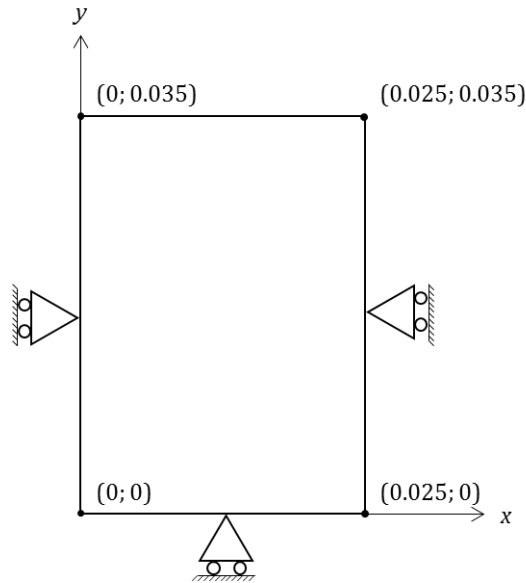


Figure 5-21: Mesh and displacement boundary conditions used in the simulation of the oedometer test.

5.7.2.4 Initial and boundary conditions

The following initial conditions for the displacement field, \mathbf{u} , initial stress state and suction are used in all the model:

- $\mathbf{u} = 0$;
- $s = 138$ MPa;
- $\sigma_{xx 0} = 10^{-5}$ MPa;
- $\sigma_{yy 0} = 10^{-5}$ MPa;
- $\sigma_{zz 0} = 10^{-5}$ MPa.

Compression is positive. The initial stress state is isotropic. Initial mean stress is taken higher than zero to avoid numerical issues associated to zero stress.

The boundary conditions used in the simulations are:

- imposed σ_{yy} on the top boundary ($y = 0.035$);
- $u_y = 0$ on the bottom boundary ($y = 0$);
- $u_x = 0$ on the left boundary ($x = 0$);
- $u_x = 0$ on the right boundary ($x = 0.025$).

The vertical stress is progressively increased from $\sigma_{yy 0}$ to $\sigma_{yy} = 35$ MPa. Gravity is not addressed in the simulation and gas pressure is taken equal to zero.

5.7.2.5 Comparison of numerical and experimental results

Test results and numerical results are presented in Figure 5-22. In Figure 5-22, comparison of void ratios at similar vertical stress highlights the model ability to reproduce the mixture behaviour observed in the laboratory. Figure 5-22 also presents the continuous evolution of the void ratio as a function of vertical stress, along with vertical lines separating the e - $\ln p$ plane in domains. In Figure 5-22, the blue dashed line represents the pressure above which $m_g > m_g^*$ (*i.e.* pellet strength is reached), found to be slightly above 2 MPa. The red dashed line represents the transition from the granular state to the continuous state as a consequence of r_{vf} reaching 1, found to occur at a vertical stress of ~ 5.5 MPa.

It is interesting to note that until a vertical stress of ~ 5.5 MPa, the material behaviour predicted by the model is controlled by interactions between pellets and the pellet strength as suggested by Molinero-Guerra et al. (2019b). Above this value, the “granular”-“continuous” transition predicted by the model is still in the elastic domain and an apparent stiffer behaviour is obtained in the simulation, compared to experiment. However, yielding occurs as vertical stress reaches 22 MPa and apparent stiffness is decreased.

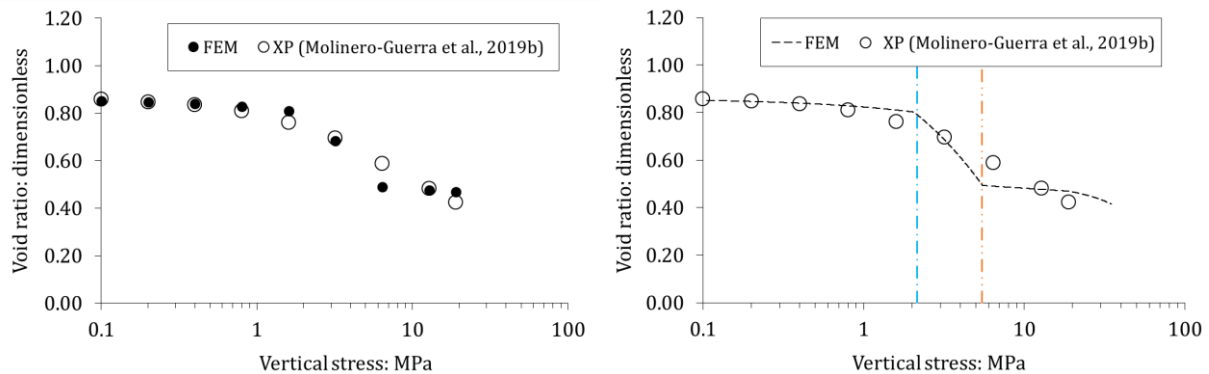


Figure 5-22: Comparison between experimental results of a constant suction mechanical loading in oedometer and numerical modelling of these latter. Left: comparison of results at identical vertical stress; right: evolution of void ratio in the simulation and transition across three domains: granular and “elastic contacts”, granular and “plastic contacts”, continuous.

The apparent stiffness of the granular mixture above 2 MPa seems slightly underestimated. The main model parameter controlling the material response under these conditions is f_{eB} , estimated from DEM simulations. In DEM, the contact law was somewhat simplified for normal forces reaching the pellet strength. The perfect plasticity hypothesis probably causes the apparent stiffness decrease of the material to be overestimated.

5.7.3 Simulation of the swelling pressure tests along the entire hydration path

5.7.3.1 Introduction

The model is used to perform simulation of hydration of pellet-powder mixtures in constant-volume conditions. The swelling pressure tests presented in Chapter 3 are modelled in the present part. As a consequence of the sample small size, it is considered that these tests can be modelled as a REV,

neglecting water transfer in the material. Tests are modelled considering hydraulic equilibrium between powder and pellets. It was suggested in Chapter 3 that these two levels of structure may not be at equilibrium. Water transfer between pellets and powder is addressed in Chapter 6.

5.7.3.2 Material

The materials are MX80 pellet-powder mixture. Their main properties are summarised in Table 5-7. Parameters of the model are presented in Table 5-7, Table 5-8, Table 5-9, Table 5-10. Further details concerning these tests can be found in Chapter 3.

5.7.3.3 Geometry of the problem

Swelling pressure tests are modelled using two-dimensional axisymmetric conditions. The cylindrical cell is represented by a square in the FEM analysis. The y axis is the axis of symmetry. The mesh consists in one Q4 element. This latter is presented in Figure 5-23.

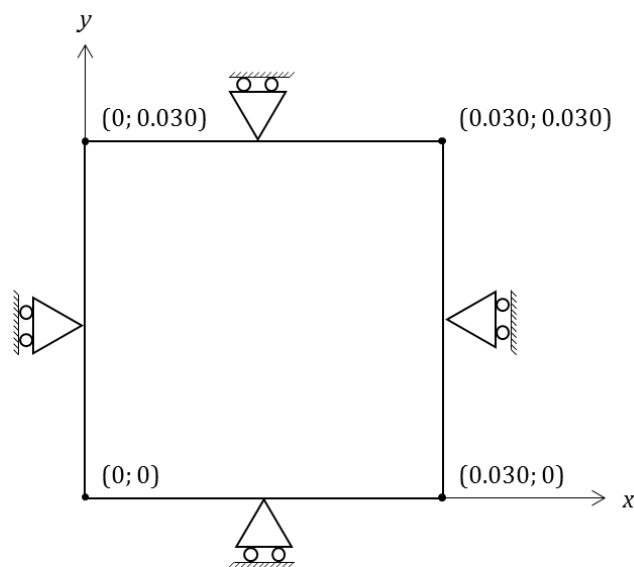


Figure 5-23: Mesh and displacement boundary conditions used in the simulation of the swelling pressure tests.

5.7.3.4 Initial and boundary conditions

The following initial conditions for the displacement field, \mathbf{u} , initial stress state and suction are used in all the model, for the three simulated tests:

- $\mathbf{u} = 0$;
- $s = 89 \text{ MPa}$;
- $\sigma_{xx 0} = 10^{-5} \text{ MPa}$;

- $\sigma_{yy 0} = 10^{-5}$ MPa;
- $\sigma_{zz 0} = 10^{-5}$ MPa.

Compression is positive. The initial stress state is isotropic. Initial mean stress is taken higher than zero to avoid numerical issues associated to zero stress.

The boundary conditions used in the simulations are:

- $u_y = 0$ on the top boundary ($y = 0.030$);
- $u_y = 0$ on the bottom boundary ($y = 0$);
- $u_x = 0$ on the left boundary ($x = 0$);
- $u_x = 0$ on the right boundary ($x = 0.030$).

Suction is progressively decreased from 89 MPa to 0.1 MPa. Gravity is not addressed in the simulation and gas pressure is taken equal to zero.

5.7.3.5 Comparison of numerical and experimental results

Simulation results are presented for the three swelling pressure tests, along with vertical lines separating the p - $\ln s$ plane in domains. The blue dashed line represents, in simulation, the pressure above which pellet strength is considered to influence the material behaviour (*i.e.* pellet strength is reached). The red dashed line represents, in simulation, the transition from the granular state to the continuous state as a consequence of either s reaching 3 MPa or r_{vf} reaching 1. In simulation results, the mean stress is considered as the swelling pressure.

Figure 5-24 presents the comparison between experimental and numerical results for SP0a and SP0b tests (see Chapter 4). In the simulation, the swelling pressure increases then reaches a first peak. Following the peak, swelling pressure decreases and increases again until LC yielding occurs while in the granular domain. Following transition to continuous domain, the swelling pressure increases again to its final value as elastic swelling overcomes the plastic collapse of macropores. The general trend of swelling pressure evolution as well as order of magnitude of this latter are satisfactorily reproduced. The final value in the simulation is close to the final value in experiment.

Some differences between experimental and numerical results still can be observed. Before reaching pellet strength, the apparent stiffness in the simulation and peak swelling pressure are slightly overestimated. Parameters controlling the stiffness of the granular assembly have been determined from periodic DEM simulations. As a reminder, a constant value for $f_{\varepsilon A}$ was chosen to describe the mechanical behaviour of a granular assembly whereas this parameter actually is slightly increasing with decreasing pellet volume fraction, as discussed in section 5.3. In addition, determination of parameters from simulations of ideal spherical particles having the same mechanical properties can induce an overestimation of the peak pressure as suggested in Chapter 4.

As pellet strength is reached, the decrease of swelling pressure following the peak is underestimated in the simulation. It is a direct consequence of the choice to consider a constant value of $f_{Mm} = 1$. This assumption is not exact for $m_g > m_g^*$. After reaching pellet strength, f_{Mm} is likely to be smaller than 1. LC yielding occurs at suction of ~ 7 MPa and corresponds to the plastic collapse of macropores. A second peak is reached as a result. This latter was also observed in experiments but at lower suction.

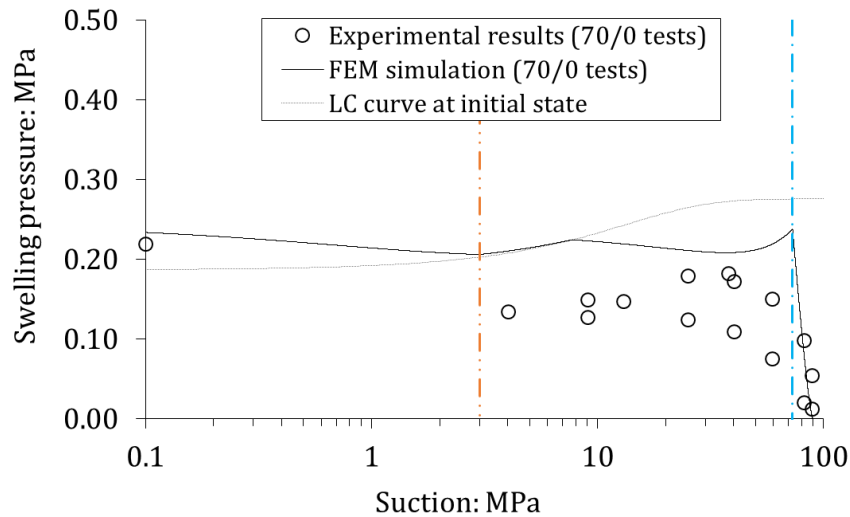


Figure 5-24: Comparison between swelling pressure test results and numerical simulation of these latter for the 70/0 mixture.

The overestimation of f_{Mm} allowed the swelling pressure to reach the LC yield locus in the simulation earlier than expected from experimental results. Yet, the second peak occurs at a swelling pressure comparable to the second peak in the experiment.

Transition occurs at $s = 3$ MPa since there is no powder in the sample. Swelling pressure is then found to increase in the simulation, as in the experiment.

Figure 5-25 presents the comparison between experimental and numerical results for SP15b test (see Chapter 4). In the simulation, the swelling pressure increases and reaches a peak as pellet strength is reached, then remains nearly constant until suction reaches ~ 11 MPa. At this point r_{vf} reaches 1 and the material is considered continuous. Afterward, swelling pressure increases until reaching the LC yield locus. Then, the swelling pressure remains nearly constant. The final swelling pressures in the simulation and the experiment are close but the model slightly overestimates this latter.

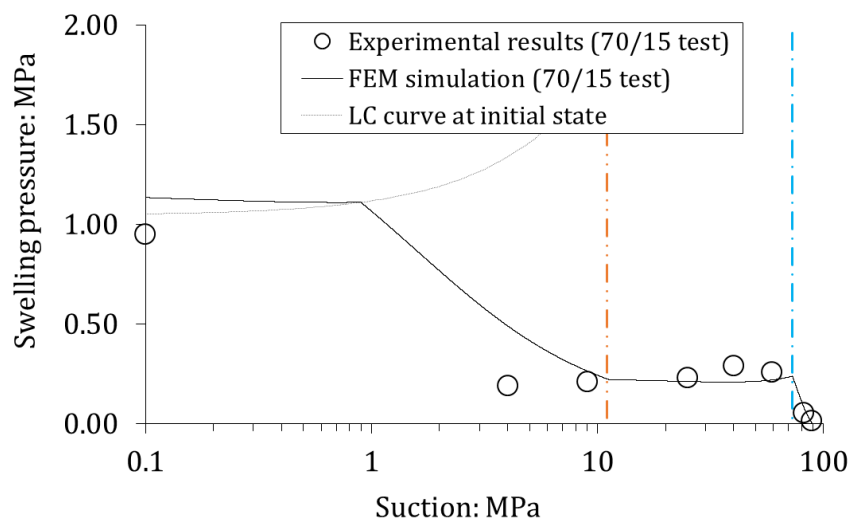


Figure 5-25: Comparison between swelling pressure test results and numerical simulation of these latter for the 70/15 mixture.

In the granular domain, the material response is well reproduced by the model. Transition and subsequent increase of swelling pressure in the simulation are found to occur earlier than in experiment. In experiment, swelling pressure remains nearly constant until a suction of 4 MPa. It can be suggested from section 5.4 that the powder is not in free-swelling condition during all of the hydration path in the granular domain or that pellets swell too rapidly under the hypothesis of hydraulic equilibrium. Thus, Φ_{mat} increases faster in the simulation and the transition is computed at higher suction. Even if the swelling pressure at $s = 4$ MPa is overestimated, it is interesting to note that the overall response provided by the model is quite close to the experimental one, involving a succession of very different phenomena.

Figure 5-26 presents the comparison between experimental and numerical results for the 70/30 mixture (see Chapter 4). As already highlighted in previous discussions, this mixture does not really behave as a granular assembly. This is addressed by the model. Transition occurs as $r_{vf} = 1$ at high suction (~75 MPa in the simulation).

It is interesting to note that, even simplified, the conceptual approach proposed for the continuous domain is able to reproduce the evolution of swelling pressure upon suction decrease. Still, some features cannot be addressed and some differences between numerical and experimental responses can be observed. For instance, in the model, LC yielding is the only way of modelling a peak swelling pressure and hardening only occurs if the stress state reaches the yield surface. As a result, the swelling pressure keeps increasing upon hydration while it is observed in Figure 5-26 that the increase rate decreases at suction in the range 4-10 MPa. The final swelling pressure in the simulation is however close to the experimental one. Except for the swelling pressure at $s = 4$ MPa, the swelling pressure-suction relationship is consistent with experimental observations.

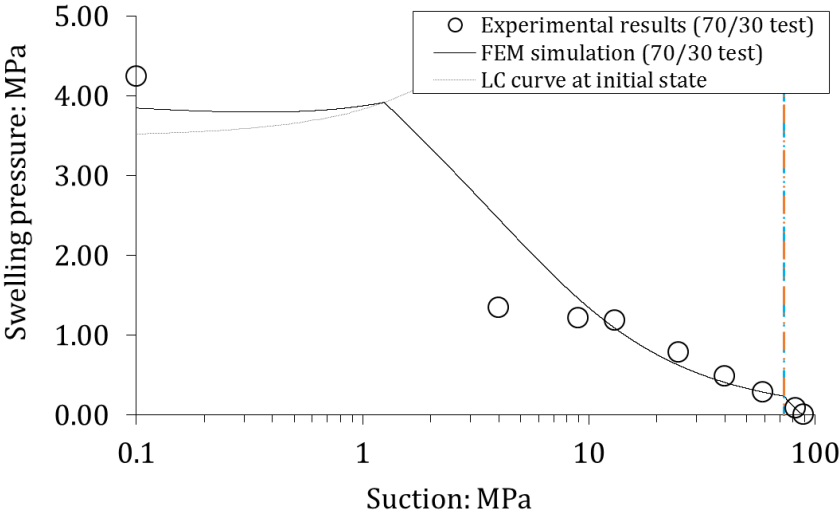


Figure 5-26: Comparison between swelling pressure test results and numerical simulation of these latter for the 70/30 mixture.

A comparison of all numerical and experimental results is presented in Figure 5-27. It is highlighted that the proposed conceptual approach is able to satisfactorily reproduce the mechanical behaviour of pellet-based bentonite materials upon suction decrease, either purely granular (70/0 samples) or with powder of various density in the inter-pellet voids, over a wide range of average dry densities (1.05 Mg/m³ to 1.50 Mg/m³).

It is reminded that a single set of parameter is used for all simulations. κ_s is estimated from the e_{m0}/e_0 ratio. This estimation is not supported by direct experimental evidence, but allows κ_s to increase with increasing e_{m0}/e_0 . Since e_m is not affected by compaction, the higher the dry density the higher the ratio, which is suggested by experimental results.

Some differences were obtained between experimental results and prediction of the model, as previously discussed. However, Figure 5-27 shows that both general trend and amplitude of the swelling pressure evolution upon suction decrease are still comparable to the experimental results.

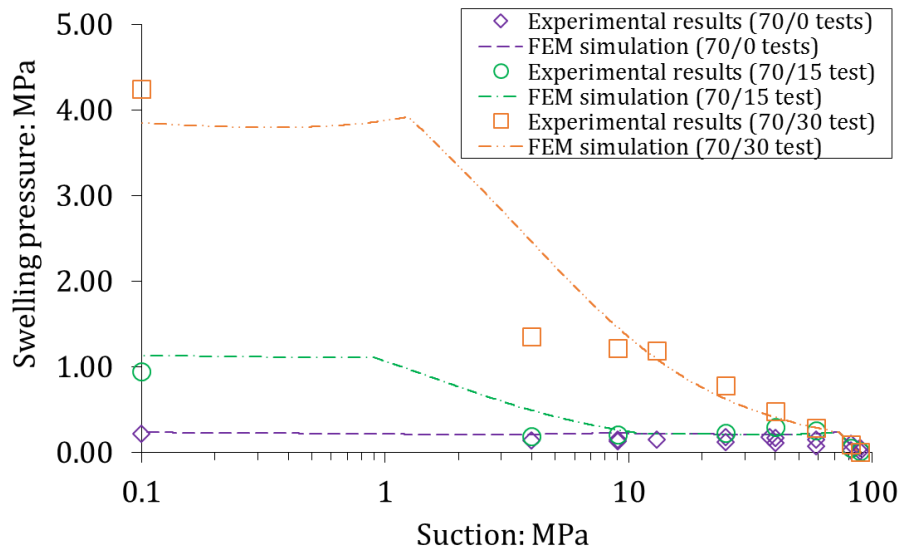


Figure 5-27: Comparison of all experimental and numerical results of swelling pressure tests.

5.8 CONCLUSIONS AND PERSPECTIVES

The present Chapter presented the development, implementation and validation of a model able to reproduce the mechanical behaviour of bentonite pellet-powder mixtures upon suction decrease. The model is able to describe features such as the influence of the granular structure, pellet strength and powder density in the inter-pellet voids. Heterogeneities of density can be addressed using a single set of parameters.

The material is characterised by either a granular state or a continuous state, depending on suction or density of the matrix phase. The description of the material behaviour in granular state has been addressed by DEM simulations of large granular assemblies. DEM simulations of binary mixtures have been performed to characterise the transition from granular to continuous state. It was suggested that the matrix volume fraction was a key parameter in this characterisation but an accurate criterion could not be directly proposed from these results. The description of the material behaviour following the transition is described by a modified BBM model.

The model is implemented in the FEM code Bil and validated against experimental results. A mechanical loading in oedometric conditions at constant suction is simulated. Three swelling pressure tests are then simulated using the model. The model is found to satisfactorily reproduce experimental results.

The following parts summarise the conclusions, limitations and perspectives arising from the present Chapter.

5.8.1 DEM simulations of large granular assemblies

Using DEM to model large pellet assemblies and periodic boundary conditions allowed the behaviour of pellet mixtures to be addressed under various solicitations. In particular, it was highlighted that the parameters with the strongest influence on the macroscopic response are the dimensionless pressure parameter m_g , the initial pellet volume fraction Φ_{I0} which influences the value of m_g at which the pellet strength is reached, and the particle volumetric strain, ε_{VI} .

For simplicity, influence of m_g on the volumetric strain does not depend on Φ_{I0} in the model implementation. This assumption may induce an overestimation of the apparent stiffness of the mixture in the simulation for low Φ_{I0} and an underestimation for high Φ_{I0} (Figure 5-14).

The influence of ε_{VI} on the volumetric strain is also simplified in the model implementation. f_{Mm} is taken constant and equal to 1 which can induce overestimation of the volumetric strain for $m_g \gg m_g^*$

5.8.2 DEM simulations of binary granular mixtures

The procedure described to model swelling pressure tests in Chapter 4 has been adapted to address binary granular mixtures. Hydration of binary mixtures in constant-volume conditions has been simulated. It was highlighted that, as the volume fraction of the powder within the inter-pellet voids increases, its contribution to the mechanical behaviour increases.

It was suggested to consider the ratio Φ_{mat}/Φ_I as a criterion to describe transition from granular to continuous state. However, the possibility to interpret DEM results and propose a criterion was limited. The ratio of small/large particle diameter was not truly representative of pellet-powder mixture. The cell was small compared to pellet diameter, as discussed in Chapter 4, thus wall effect is likely to affect the material response. Realisation of such simulations with a relevant equilibrium tolerance is difficult and time consuming.

Periodic boundary conditions have been found to provide results with low variability. An interesting perspective of this part of the study is the periodic simulation of binary mixtures at acceptable diameter ratio.

$r_{vf} = 1$ was suggested to describe the transition from granular to continuous state, but is an approximation and further information is required to propose an accurate criterion.

5.8.3 Modification of the Barcelona Basic Model

A modification of the BBM has been proposed and implemented. The main modification is the introduction of different levels of structure and associated stiffness parameters.

Interaction functions of the BExM framework are not used and the macrostructural strains induced by suction variations are addressed using the elastic stiffness parameter κ_s . It was suggested to express κ_s as increasing with increasing material density. The ratio e_{m0}/e_0 was proposed to avoid the introduction

of additional parameter but other approach allowing κ_s to increase with increasing density can be considered instead.

Other parameters were determined from the literature except κ_m and p_c which were conveniently taken equal to 0.015 and 0.05 MPa respectively. These latter are nonetheless not significantly different from values commonly found in the literature.

Even if the model simplifies the mechanical behaviour of the material, the overall swelling pressure increase upon suction decrease could be reproduced for the 70/30 mixture, the behaviour of which was mainly described as “continuous”.

5.8.4 Differences between experimental and numerical responses

The material behaviour has been simplified in the model. Still, simulations of the mechanical loading at constant suction or suction decrease in constant-volume conditions highlighted the ability of the proposed conceptual framework to address the main phenomena affecting the mechanical behaviour.

Most of the identified differences between experimental and numerical responses could be attributed to simplification in the characterisation of parameters or model implementation, described in the previous parts.

Even if differences have been identified, encouraging results are obtained. The model was able to satisfactorily reproduce trend and amplitude of the swelling pressure developed upon hydration in constant-volume conditions along an entire hydration path, for:

- A pellet assembly with no powder;
- A pellet-powder mixture with dense powder phase, mostly modelled like a traditional continuous material;
- A pellet-powder mixture with loose powder phase successively behaving as a granular assembly and a continuum,

using a single set of parameters.

5.8.5 Transition from granular to continuous state

In the model, the behaviour of the material is described as either granular or continuous. The mechanical behaviour is considered to be either controlled by the pellet assembly or not to be influenced by this latter.

Even if this part of the study was found to be limited, the DEM simulation of binary granular mixtures suggested that the powder progressively contributes to the total mean stress, while even at high value of r_{vf} the pellet assembly influences the material mechanical behaviour.

The proper characterisation of the transition from granular to continuous state constitutes an important perspective of the present Chapter. The description of a smooth, progressive, transition from a state controlled by the pellet assembly toward the continuous state controlled by BBM features, should be proposed. For this purpose, using DEM to study binary mixtures of pellet and powder could provide interesting insight into their intrinsic behaviour. Experimental tests simultaneously performed on

compacted blocs and mixtures of same average densities could also provide valuable information. To this end, traditional experiments such as vapour hydration under constant stress, loading at constant suction or swelling pressure tests could be performed.

5.8.6 Water transfer

In the present Chapter, simulations were performed at REV scale and by considering similar values for s_1 and s_2 . Hydration at larger scales involves water transfer. Implementation of these latter are required to perform larger scale predictive simulations. In addition, as discussed in Chapter 4, water transfer occurs between the macropores and pellets. A transfer law between this two different porosities should therefore be proposed and implemented.

In the following Chapter, imbibition tests on bigger cells are performed on the same materials as in the swelling pressure tests described in Chapter 4 to characterise their hydromechanical behaviour at larger scale and get an insight into water transfer, influences of the powder content and granular structure, and homogenisation of the mixture.

6 MOCK-UP IMBIBITION TESTS AND WATER TRANSFER LAWS

6.1 INTRODUCTION

The hydromechanical behaviour of pellet-powder mixtures has been addressed in previous Chapters, through experimental and numerical studies, at REV scale. In Chapter 6, the behaviour of these materials upon imbibition at larger scale in constant-volume conditions is studied. Imbibition tests performed on three pellet-powder mixtures in the laboratory are first presented in section 6.2. From experimental results, evolution of the material texture, influence of the granular structure, water transfer in the sample and transfer mechanisms are discussed. Transfer laws are then proposed in section 6.3, accounting for experimental results. Implementation of matrix-pellet transfer law and simulation of swelling pressure tests accounting for two suction values in pellets and in matrix constitute section 6.4. Conclusion and perspectives associated to the present Chapter finally constitute section 6.5.

6.2 MOCK-UP IMBIBITION TESTS IN THE LABORATORY

6.2.1 Objectives

Three mock-up imbibition tests are performed in the laboratory on different mixtures to study the hydromechanical behaviour of pellet materials at larger scales, involving water transfer. Compared to swelling pressure, sample heights are four times as high as isochoric cells tests described in Chapter 3.

Compared to traditional mock-up tests presented in the literature, tests described in the present Chapter are performed on square-cuboid shaped cells, two faces of which are made of glass. This feature allows a camera to be used to take pictures of the material at chosen time intervals.

The main objective of these tests is to study the evolution of the material swelling pressure, relative humidity, water intake, texture, as functions of distance from water inlet and elapsed time, for different mixtures.

6.2.2 Material and methods

6.2.2.1 Material

Three tests are performed on three different MX80 pellet-powder mixtures. The mixture used in imbibition tests are the same as those described in Chapter 3:

- A 70/30 in dry mass pellet/powder mixture;
- A 82/18 in dry mass pellet/powder mixture, referred to as 70/15 to highlight that the pellet mass is the same as in 70/30 mixture;
- A pellet assembly without powder, referred to as 70/0 to highlight that the pellet mass is the same as in 70/30 mixture.

Mock-up tests associated to these mixtures are respectively referred to as MU30; MU15; and MU0 tests in the following.

6.2.2.2 Experimental setup

A sketch and a picture of the cell are presented in Figure 6-1 and Figure 6-2, respectively. Three pressure sensors are placed on a side of the cell. Three relative humidity sensors (HIH-4000 Series from Honeywell) are placed on the other side of the cell, at the same elevation. An additional pressure sensor and relative humidity sensor are placed on the top of the cell, to measure axial swelling pressure and associated relative humidity. The cell is a square cuboid, two faces of which are made of glass. Two porous stones are placed at top and bottom of the cell. A camera is used to take a picture of all three samples each 90 seconds.

The dimensions of the cell and pressure sensors are summarised in Table 6-1. The dimensions of the cell and pressure sensor, normalised with respect to the initial pellet diameter, are the following:

- Cell height to pellet initial diameter = ~4.3;
- Cell side to pellet initial diameter = ~17.1;
- Sensor diameter to pellet initial diameter = ~4.3.

Table 6-1: Dimensions of the cell and sensor used in swelling pressure tests.

Dimensions	
<i>Cell</i>	
Height: mm	120
Side: mm	60
<i>Sensor</i>	
Diameter: mm	30

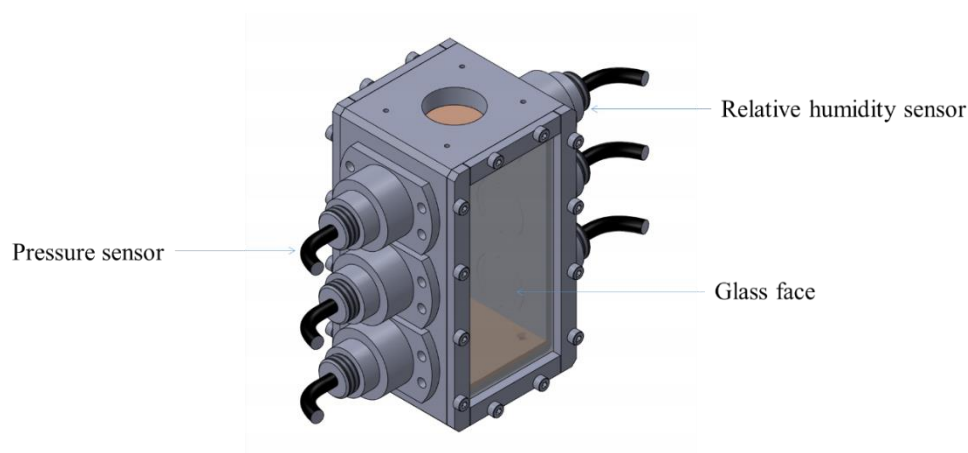


Figure 6-1: Diagram of the imbibition cell.

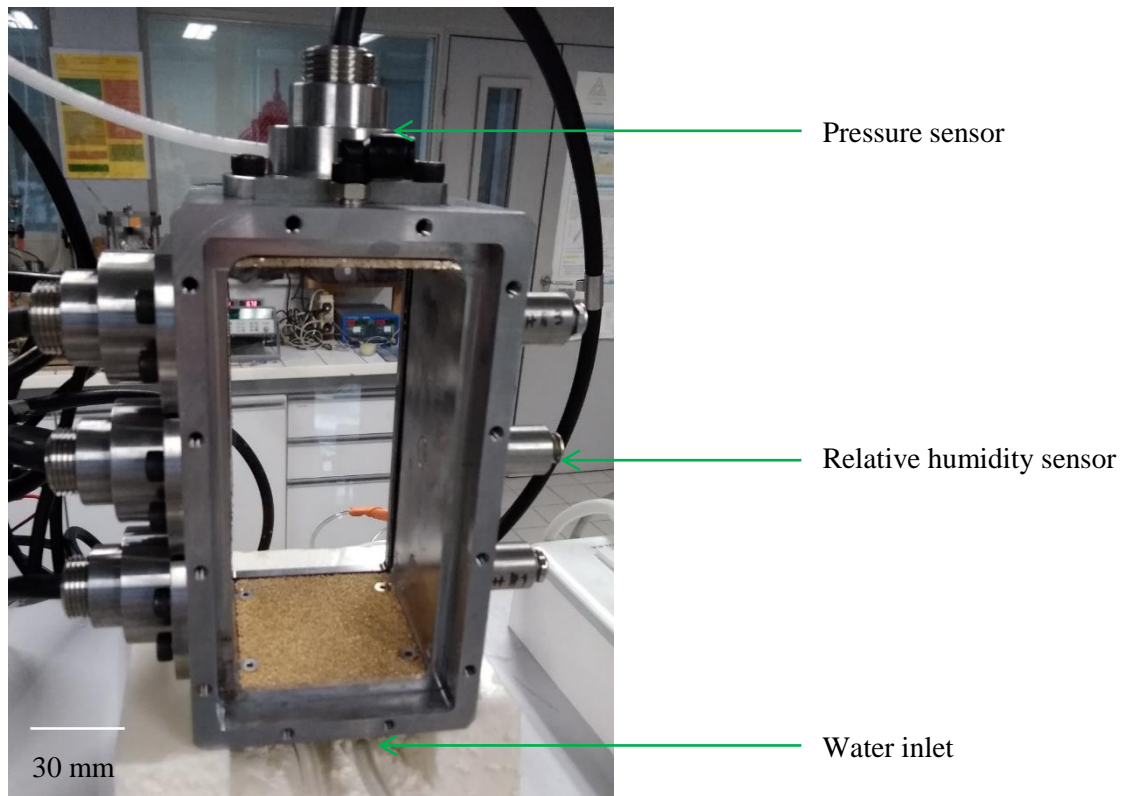


Figure 6-2: Picture of the imbibition cell.

6.2.2.3 Hydration step

Hydration is performed by imbibition from the bottom face of synthetic water having a similar chemical composition as the pore water of the Callovo-Oxfordian claystone from the URL of Andra in Bure, France. The level of infiltrated water is measured using a burette. To avoid fast infiltration in the macropores that would result in unrealistic (compared to site conditions) fast loss of granular structure, the water level in the burette is maintained at the same level as the bottom porous disk for five days. Afterwards, the water level is set at the height of the cell. This protocol allows only the first layer of pellets to lose its structure at the beginning of hydration.

It is considered, regarding the water head ($120 \text{ mm} \approx 1.2 \times 10^{-3} \text{ MPa}$) during the test that the mechanism controlling imbibition is the gradient of suction.

6.2.2.4 Sample preparation

During the preparation step, cells are turned so that a side glass face becomes the bottom face. Samples are prepared by successively pouring one layer on pellets then the proportion of powder associated to the laid proportion of pellets to fill inter-pellet voids. This procedure corresponds to the third protocol proposed by Molinero-Guerra et al. (2017), shown to be suitable to prepare homogeneous samples (Figure 6-3).



Figure 6-3: MU0 sample during the preparation step.

The second glass face is then installed to close the sample and cells are turned back so that square faces are the top and bottom faces. The top face during the preparation of the sample is the face followed by the camera. Compared to swelling pressure tests described in Chapter 3, no closure pressure was necessary in imbibition tests. Figure 6-4 presents the MU0 sample following preparation. Figure 6-5 presents the MU15 sample following preparation. Figure 6-6 presents the MU30 sample following preparation. A black box is then installed around the three cells to allow pictures to be taken in constant-lighting conditions, with no influence of the day/night cycles (Figure 6-7).

The main features of the three samples are summarised in Table 6-2. Finally, a picture of these latter at initial state is presented in Figure 6-8.

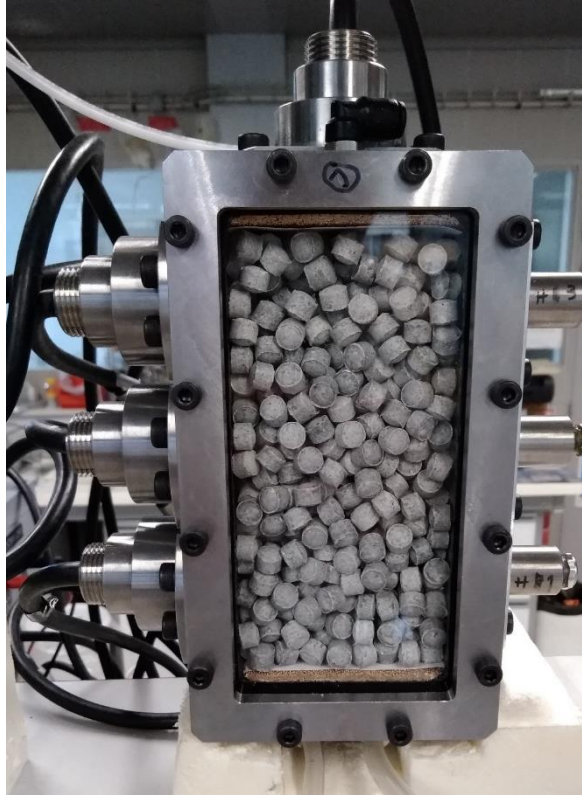


Figure 6-4: Picture of the MU0 sample following the preparation step.



Figure 6-5: Picture of the MU15 sample following the preparation step.



Figure 6-6: Picture of the MU30 sample following the preparation step.

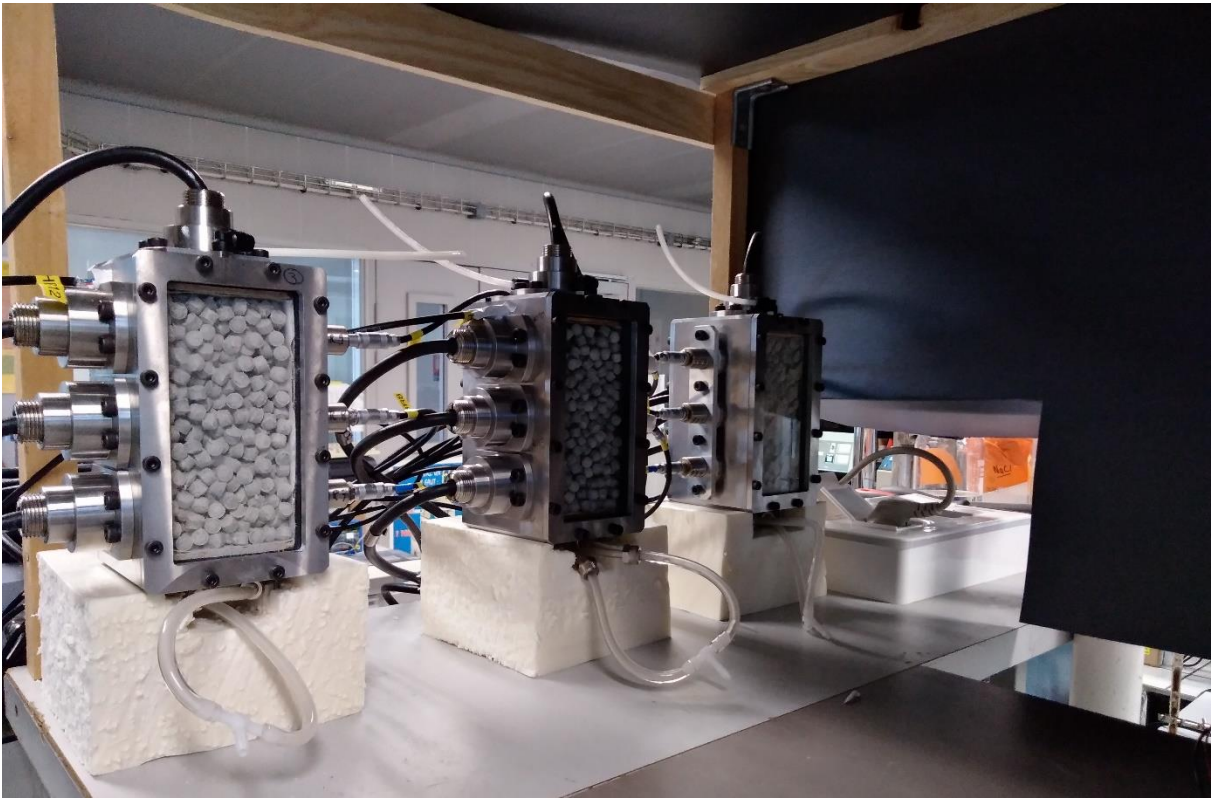


Figure 6-7: Picture of the three cells and the framework of the black box following the preparation step.

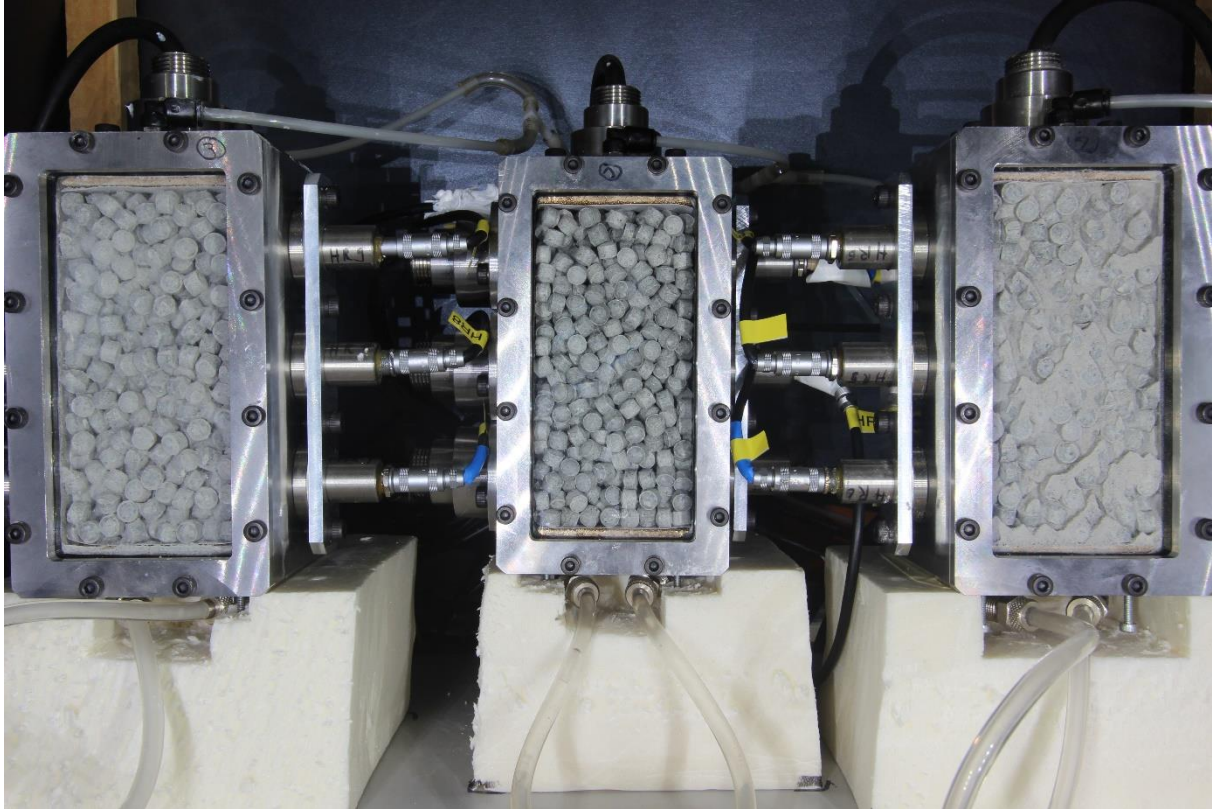


Figure 6-8: Picture of the three samples at initial state.

Table 6-2: Main features of MU30, MU15, and MU0 samples.

Sample	Mixture	Average dry density: Mg/m ³	Pellet volume fraction: dimensionless	Matrix dry density: Mg/m ³
MU30	70/30	1.50		1.00
MU15	70/15	1.275	0.55	0.50
MU0	70/0	1.05		0

6.2.3 Experimental results

The present part presents the results obtained after 1.5 year of imbibition for MU0 and MU15. MU30 glass side broke after 235 days and results are therefore presented for 235 days of imbibition for MU30.

6.2.3.1 Infiltrated volume of water

Figure 6-9 presents the evolution of infiltrated water volume as a function of elapsed time for MU0, MU15, and MU30 samples. Horizontal lines corresponding to the total void ratio in each of these three samples are plotted along experimental results. If water density remains constant upon imbibition, these volumes thus correspond to the maximum water volume infiltrated. These latter are $2.68 \times 10^{-4} \text{ m}^3$; $2.33 \times 10^{-4} \text{ m}^3$; and $1.98 \times 10^{-4} \text{ m}^3$ for the 70/0, 70/15, and 70/30 mixtures, respectively.

Upon imbibition, the increase of infiltrated volume of water was faster during the first 40 days compared to infiltration at longer elapsed time. Interestingly, no differences are obtained in the infiltrated water volume-elapsed time relationship for the three tests. In spite of their significant differences of dry density, 70/0, 70/15, and 70/30 mixtures were all characterised by the same infiltrated volume of water.

After 1 year of imbibition, imbibition became slower for the 70/15 mixture. It is associated to the progressive clogging by rust of the tube providing water to this sample. After cleaning of the tube, imbibition rate increased but remained slower than for the 70/0 sample as the infiltrated volume of water approached the theoretical maximum value.

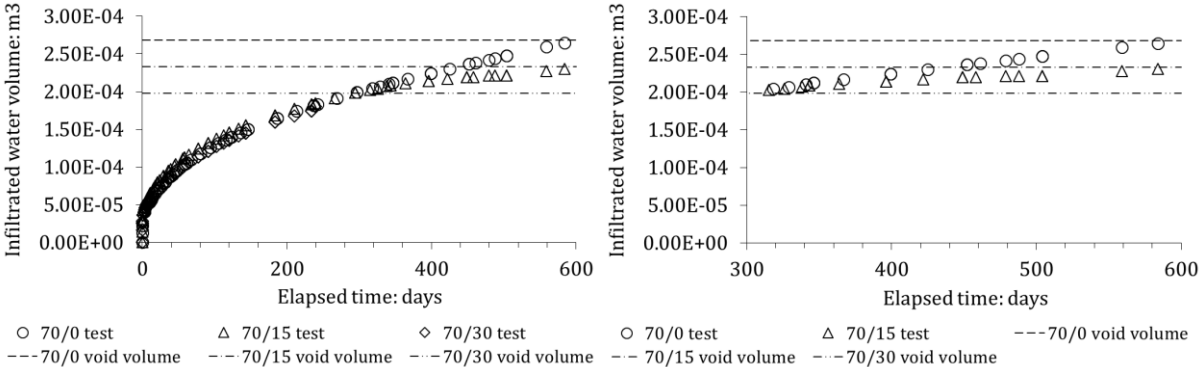


Figure 6-9: Evolution of the infiltrated volume of water as a function of elapsed time for the three imbibition tests (left) and zoom after 300 days of imbibition (right).

6.2.3.2 Evolution of relative humidity during imbibition

Figure 6-10, Figure 6-12, and Figure 6-14 present the evolution of relative humidity as a function of elapsed time measured by the four sensors at different elevations z , for the three mock-up imbibition tests. $z = 0$ corresponds to the bottom of the cell, thus to the water inlet. Figure 6-11, Figure 6-13, and Figure 6-15 present the relative humidity profiles at different elapsed times following imbibition.

The evolution of relative humidity in all three samples is characterised by a similar trend. Relative humidity is found to monotonously increase. In MU0 test, relative humidity was 100 % in all the sample after 105 days. In MU15 test, relative humidity was 100 % in all the sample after 133 days. In MU30 test, relative humidity was 100 % in all the sample after 189 days.

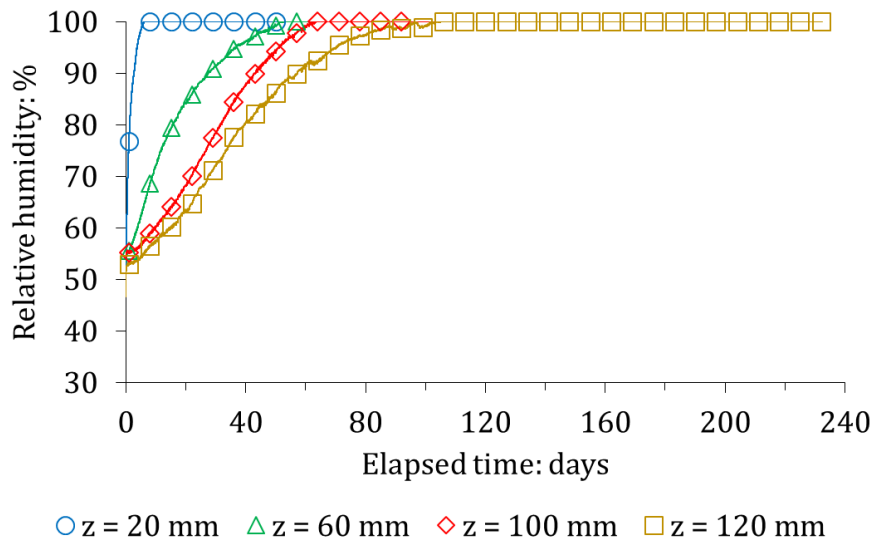


Figure 6-10: Evolution of relative humidity in MU0 imbibition test as a function of elapsed time, at four different elevations.

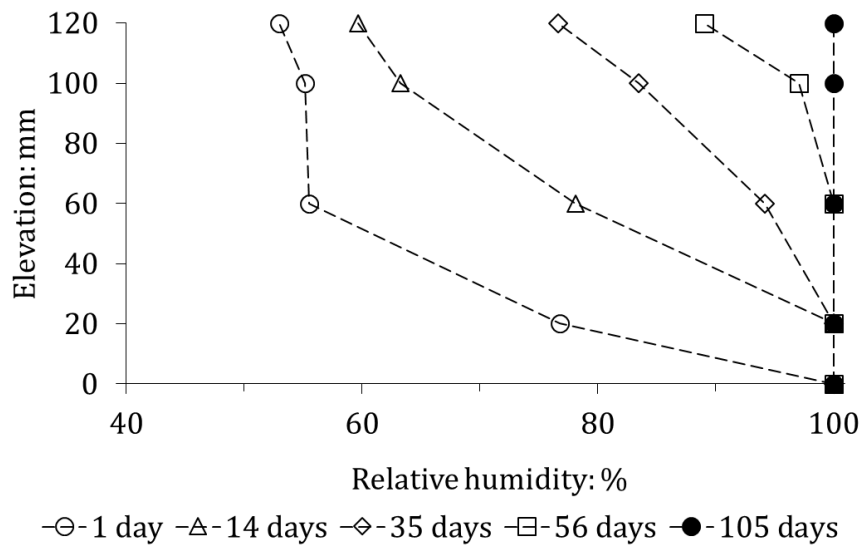


Figure 6-11: Relative humidity in MU0 imbibition test as a function of elevation, at five different elapsed times.

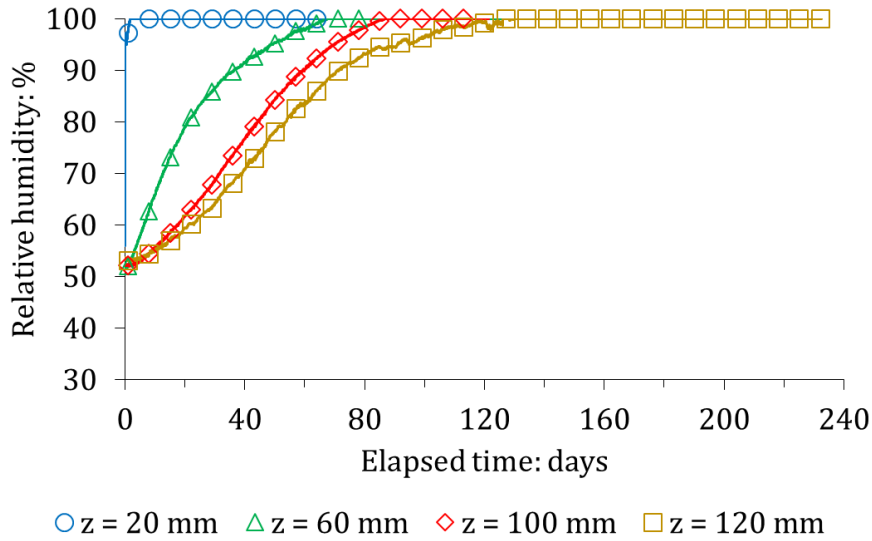


Figure 6-12: Evolution of relative humidity in MU15 imbibition test as a function of elapsed time, at four different elevations.

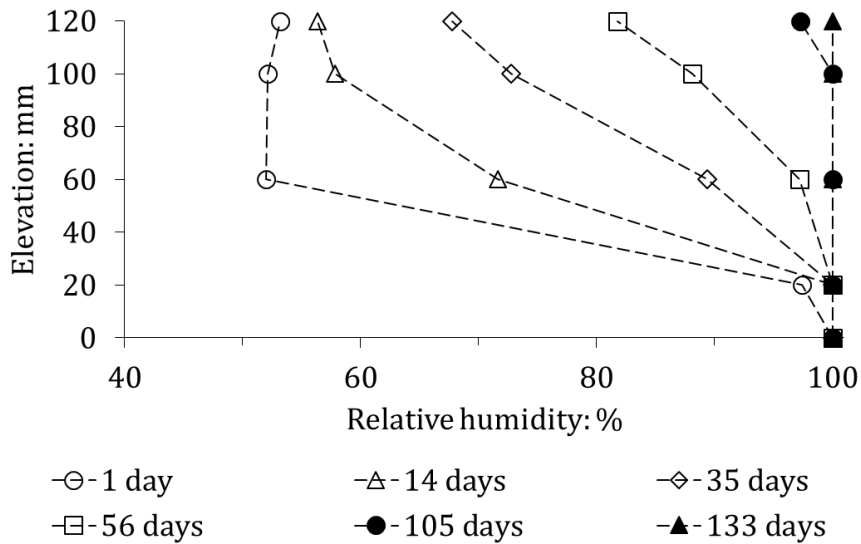


Figure 6-13: Relative humidity in MU15 imbibition test as a function of elevation, at six different elapsed times.

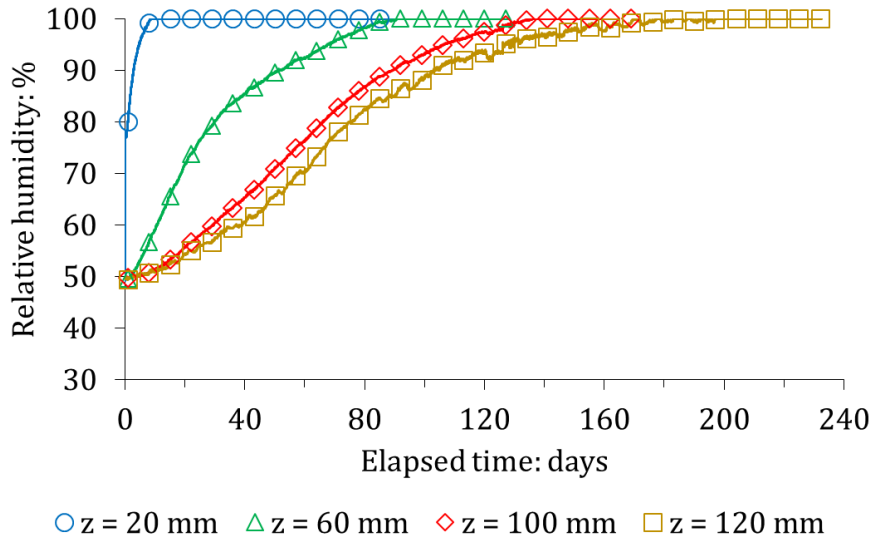


Figure 6-14: Evolution of relative humidity in MU30 imbibition test as a function of elapsed time, at four different elevations.

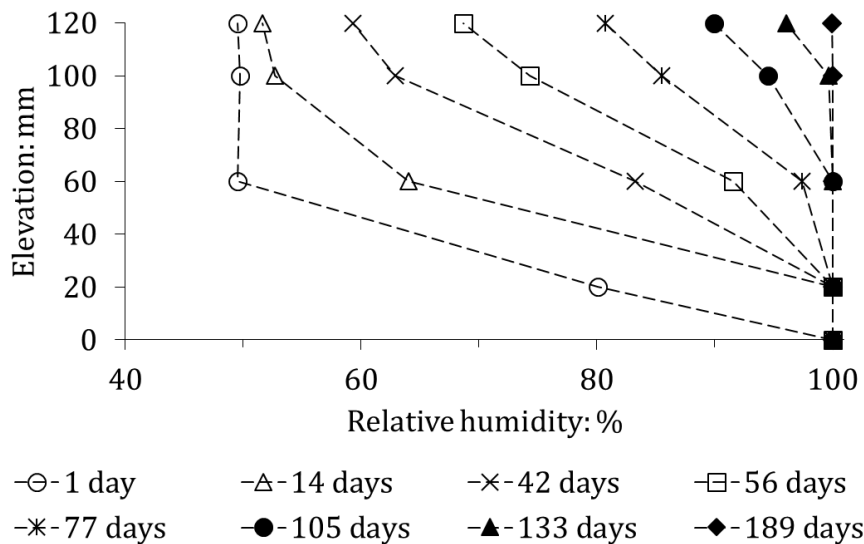


Figure 6-15: Relative humidity in MU30 imbibition test as a function of elevation, at five different elapsed times.

6.2.3.3 Evolution of apparent swelling pressures during imbibition

Figure 6-16 and Figure 6-17 present the evolution of swelling pressure as a function of elapsed time at different z and the profiles of swelling pressure at different elapsed times in MU0 imbibition test, respectively. At $z = 20$ mm, swelling pressure evolution is characterised by an increase, then reaches a peak value at 0.125 MPa after 8 days. Swelling pressure then increases again and reaches a plateau of 0.160 MPa. At $z = 60$ mm, swelling pressure evolution is characterised by an increase, peak, and decrease to a plateau value. Peak swelling pressure, 0.197 MPa, is reached after 22 days. Plateau value is 0.136 MPa. At $z = 100$ mm, swelling pressure evolution is also characterised by an increase, peak, and decrease to a plateau value. Peak swelling pressure, 0.194 MPa, is reached after 38 days. Plateau

value is 0.105 MPa. At $z = 120$ mm, swelling pressure evolution is characterised by an increase, peak, and decrease to a plateau value. Peak swelling pressure, 0.240 MPa, is reached after 32 days. Plateau value is 0.115 MPa.

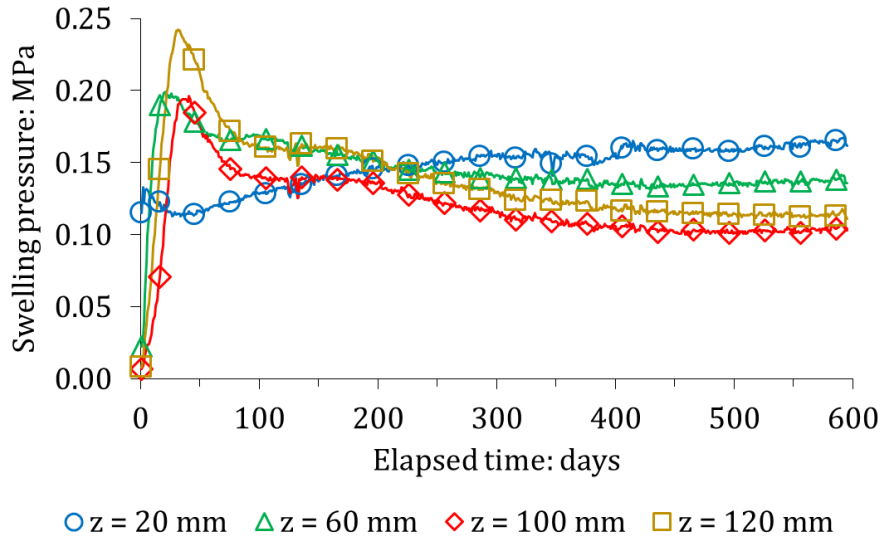


Figure 6-16: Swelling pressure as a function of elapsed time at different elevations in MU0 test.

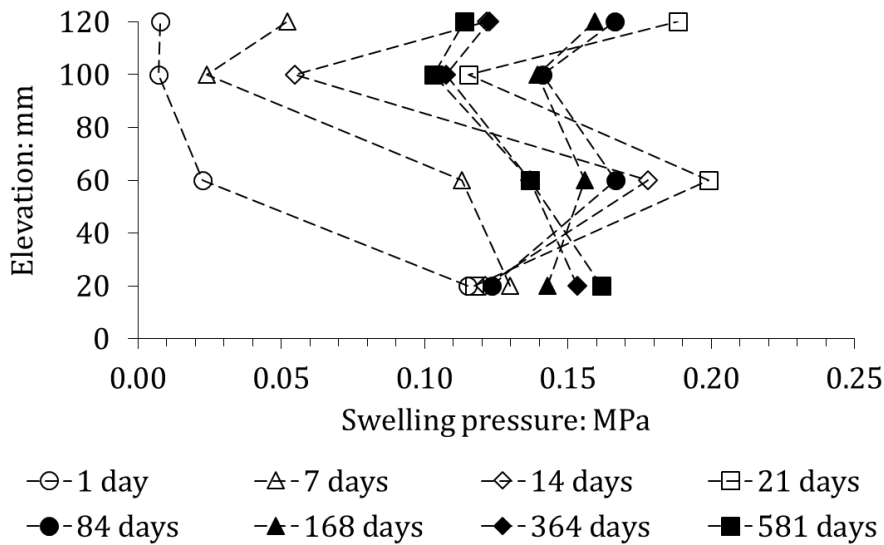


Figure 6-17: Profile of swelling pressure at different elapsed times in MU0 test.

Figure 6-18 and Figure 6-19 present the evolution of swelling pressure as a function of elapsed time at different z and the profiles of swelling pressure at different elapsed times in MU15 imbibition test, respectively. At $z = 20$ mm, swelling pressure evolution is characterised by a fast increase following the start of imbibition, then a slower but continuous increase until a plateau is reached at 0.558 MPa. At $z = 60$ mm, swelling pressure evolution is characterised by an increase, peak, and second increase to a plateau value. Peak swelling pressure, 0.365 MPa, is reached after 35 days. Plateau value is 0.796 MPa. At $z = 100$ mm, swelling pressure evolution is also characterised by an increase, peak, and second

increase to a plateau value. Peak swelling pressure, 0.357 MPa, is reached after 50 days. Plateau value is 0.784 MPa. At $z = 120$ mm, swelling pressure evolution is characterised by an increase, peak, and second increase to a plateau value. Peak swelling pressure, 0.496 MPa, is reached after 36 days. Plateau value is 0.801 MPa. A transient decrease of swelling pressure is measured at ~ 360 days by all sensors. This latter corresponds to rust progressively clogging the tube providing the water to the sample. After cleaning the tube, swelling pressure increased again.

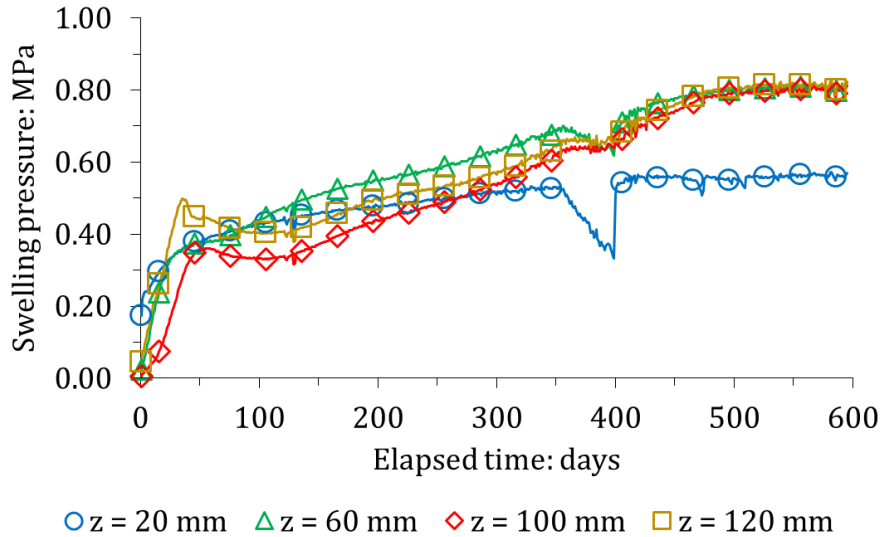


Figure 6-18: Swelling pressure as a function of elapsed time at different elevations in MU15 test.

Figure 6-20 and Figure 6-21 present the evolution of swelling pressure as a function of elapsed time at different z and the profiles of swelling pressure at different elapsed times in MU30 imbibition test, respectively. At $z = 20$ mm, swelling pressure evolution is characterised by a fast increase following the start of imbibition, then a slower but continuous increase until the test was stopped. At $z = 60$ mm, swelling pressure evolution follows a comparable trend. At $z = 100$ mm, swelling pressure evolution is characterised by an increase, peak, and second increase until the end of the test. Peak swelling pressure, 1.80 MPa, is reached after 98 days. At $z = 120$ mm, swelling pressure evolution follows a comparable trend. Peak swelling pressure, 2.31 MPa, is reached after 83 days.

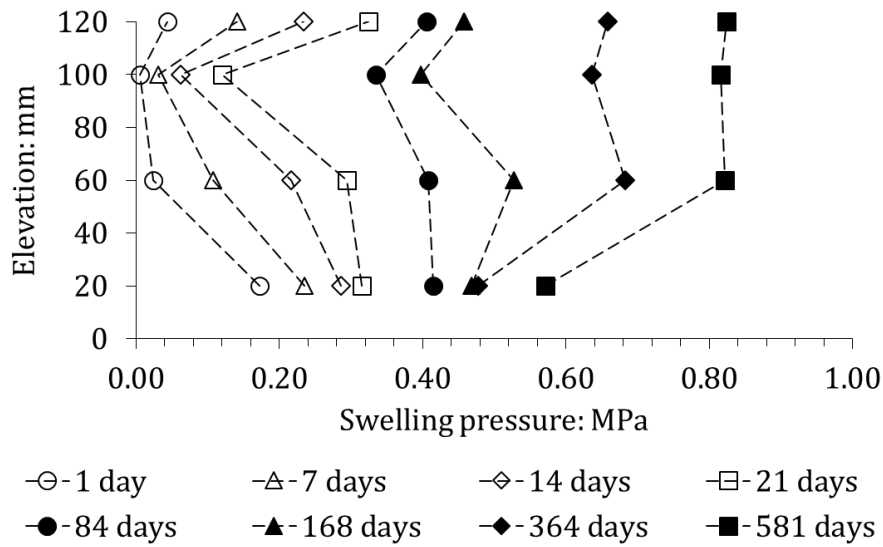


Figure 6-19: Profile of swelling pressure at different elapsed times in MU15 test.

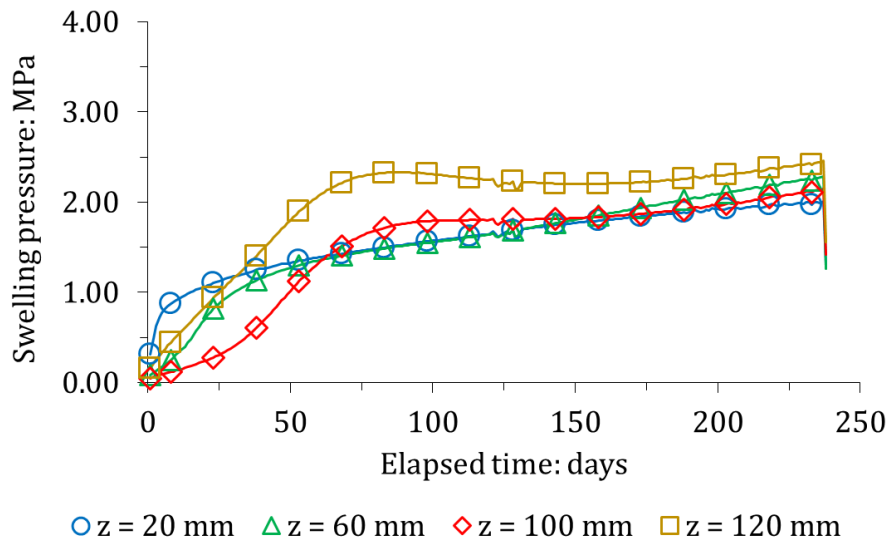


Figure 6-20: Swelling pressure as a function of elapsed time at different elevations in MU30 test.

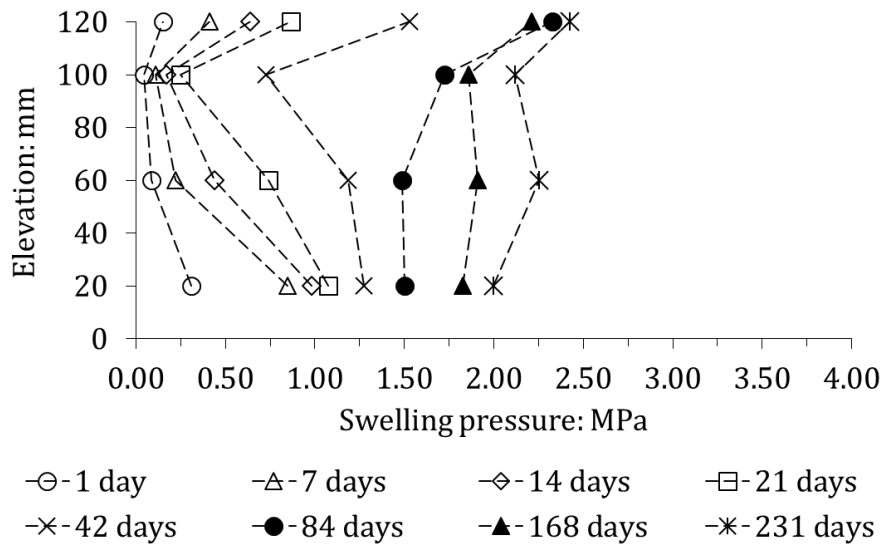


Figure 6-21: Profile of swelling pressure at different elapsed times in MU30 test.

6.2.3.4 Evolution of the sample texture during imbibition

Figure 6-22, Figure 6-23 and Figure 6-24 presents the evolution of the material texture at different times following the start of imbibition, for the 70/0, 70/15, and 70/30 samples, respectively. Initial state, peak pressure measured by the axial pressure sensor and 100 % relative humidity measured by all the sensors in the sample are notably presented. Then, Figure 6-22 and Figure 6-23 present pictures after 1 year and 1.5 year of imbibition while Figure 6-24 only presents a picture after 230 days of imbibition, thus just before the end of the test. Table 6-3 summarises the test duration corresponding to each of the taken pictures.

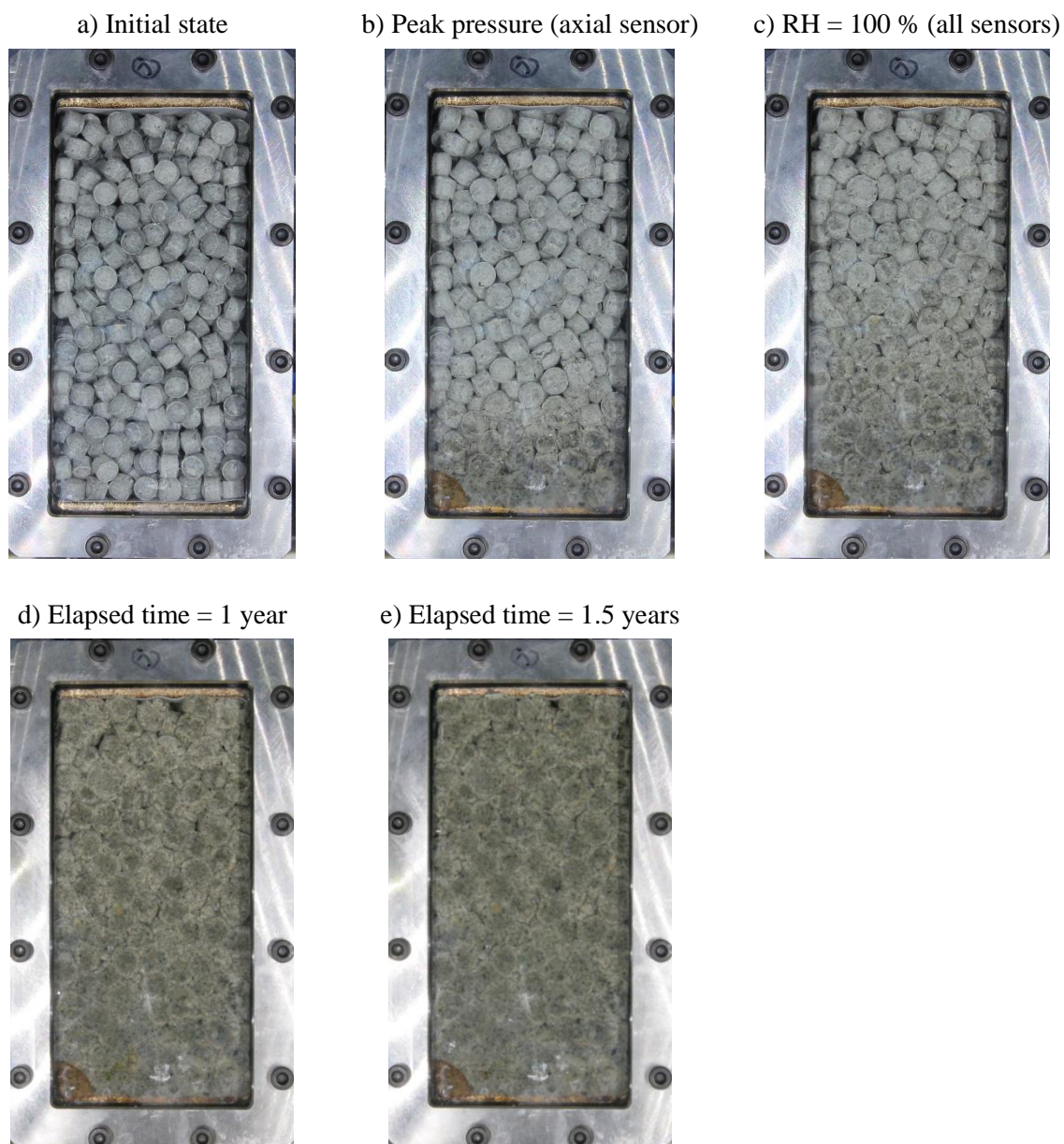


Figure 6-22: Pictures of the 70/0 sample at different elapsed time during imbibition.

In Figure 6-22, the material (70/0 sample) is observed to be a granular assembly at peak pressure and at 100 % relative humidity in the macropores. After 1 year and 1.5 year, pellets can still be identified but the material is no longer a granular assembly characterised by sub-punctual contacts between grains.

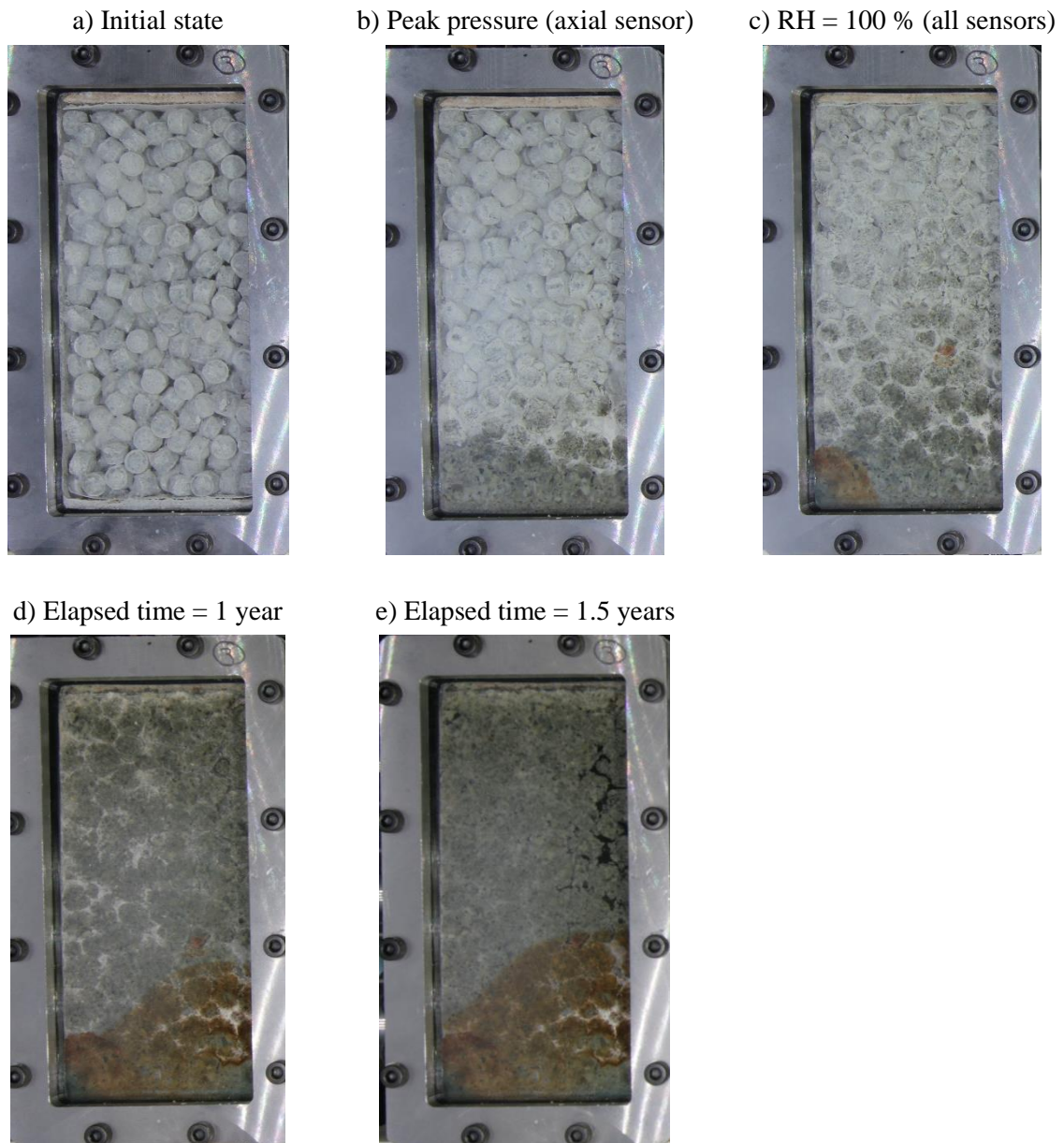


Figure 6-23: Pictures of the 70/15 sample at different elapsed time during imbibition.

In Figure 6-23, the material (70/15 sample) is observed to be a granular assembly with loose powder phase in the inter-pellet voids at axial peak pressure. As all sensors measure 100 % relative humidity in the sample, the material can be described as a granular assembly with a dense powder phase filling the inter-pellet voids. After 1 year and 1.5 year of imbibition, some pellets can be identified but the material is no longer a granular assembly.

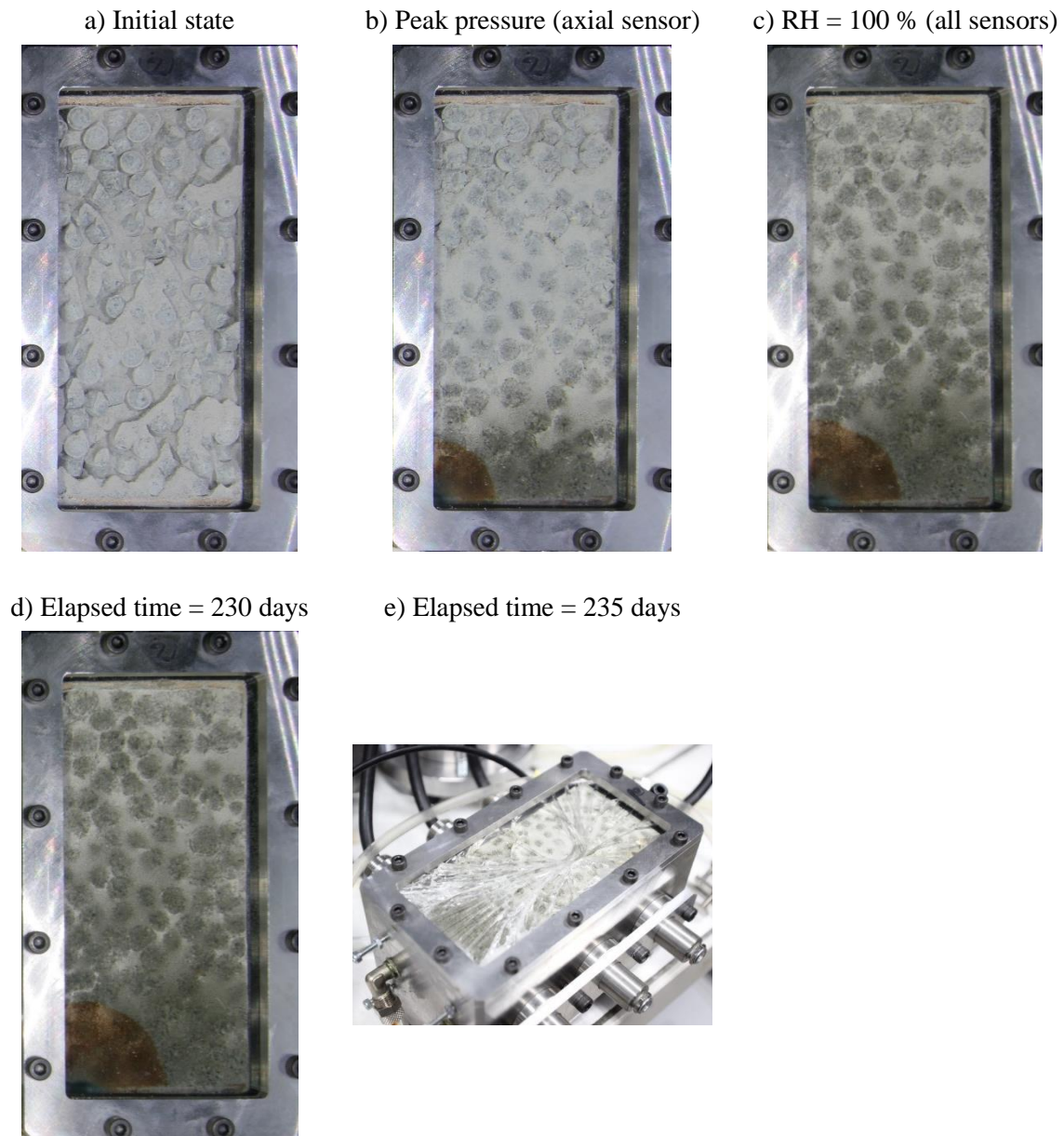


Figure 6-24: Pictures of the 70/30 sample at different elapsed time during imbibition.

In Figure 6-24, at axial peak pressure, pellets can be identified along with a dense powder phase filling the inter-pellet voids. As sensors measure 100 % relative humidity in the inter-pellet voids, some pellets can be identified but the material is no longer a granular assembly. The same observation is made at 230 days after the start of imbibition.

Table 6-3: Elapsed time from the start of imbibition at which pictures are taken in Figure 6-22; Figure 6-23 and Figure 6-24.

Picture (Figure 6-22; Figure 6-23 and Figure 6-24)	Elapsed time: days		
	70/0	70/15	70/30
a		0	
b	32	36	83
c	101	130	197
d	360	360	230
e	540	540	235

6.2.3.5 Pellet vertical displacements

Pictures of the samples allowed the pellet displacement to be estimated in MU0 sample. On the picture of initial state, pellets can easily be identified. The (x,y) coordinates of the centre of the pellet inscribed circle (origin taken at the bottom left of the cell) are determined. The same pellets are identified on pictures obtained at different times and their (x,y) coordinates are determined.

Comparison of these latter allows the vertical displacement to be estimated as a function of elapsed time. Since pellets are 3D elements observed in 2D, this procedure does not provide an exact result. However, pellets rotation is limited, as seen in Figure 6-22 and the estimation is considered to provide results with reasonable accuracy.

Figure 6-25 presents the vertical displacement of pellets at different elevations as a function of elapsed time, for MU0 test. Mean values for three pellets are plotted. Only the beginning of hydration is presented since pellets need to be clearly identified to determine their coordinates.

In MU0 test, pellets at $z = 20$ mm first display an upward displacement at the start of hydration, then a downward displacement. A comparable trend is obtained for pellets at $z = 60$ mm. At $z = 100$ mm, pellet displacement is only upward.

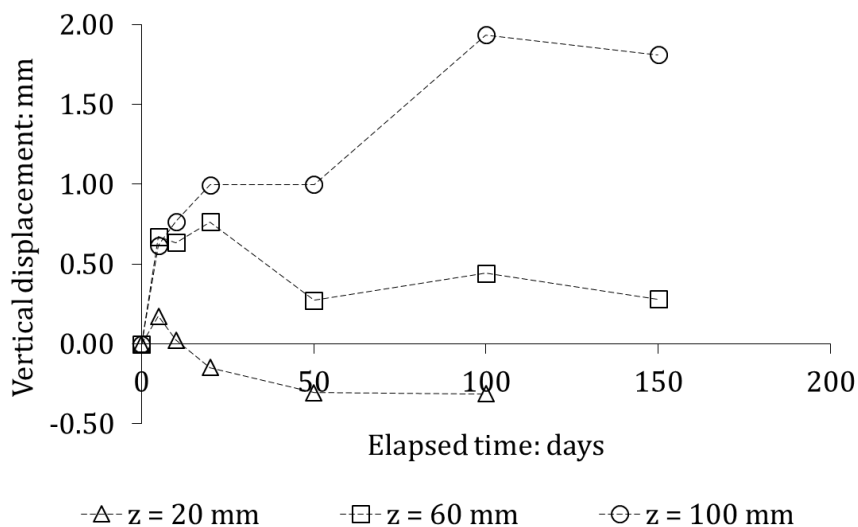


Figure 6-25: Estimation of pellet vertical displacements in MU0 test.

6.2.4 Discussion

6.2.4.1 Influence of the initial granular structure

Pictures of the samples taken at regular time intervals allowed the evolution of the material texture to be observed upon hydration. From these observations, it was observed that the 70/0 material in MU0 test remained a granular assembly until a 100 % relative humidity is measured in all macropores. The evolution of swelling pressure in this sample is thus related to the granular structure. Indeed, the trend and order of magnitude of the swelling pressure is comparable to the results of swelling pressure tests presented in Chapter 3. It is suggested for MU0 test that the increase, peak, decrease and plateau trend observed upon imbibition is associated to the previously discussed hydration phases: first, pellets swell as contacts are elastic, then pellets strength is reached and the decrease and plateau are controlled by pellets strength and stiffness decrease upon further suction decrease. It can be expected that upon further hydration, swelling pressure will increase again. Indeed, as discussed in the next sub-part, dry macropores are still identified on MU0 pictures. Hydration is thus not complete even if relative humidity has been 100 % in all macropores for more than 1 year.

The evolution of pellet vertical displacement in MU0 test can be explained by the influence of the granular structure. Following imbibition, pellets below ~20 mm lose their structure and swell, inducing pellets above to move upward. Pellets at higher elevation undergo more important upward displacement since all lower pellets swell. As upward displacement is prevented by the top wall, pellet swelling induces a downward displacement. Because of water transfer, suction in pellets decreases faster near the bottom of the cell. Stiffness decrease is more significant at lower elevation and maximum near water inlet. Thus, downward displacement tends to be more important at lower elevation because of low contact stiffness. The influence of upward displacement can explain the earlier occurrence of peak swelling pressure in axial sensor than in $z = 100$ mm sensor.

In MU15 test, the evolution of swelling pressure as a function of elapsed time is comparable to MU0 test until the post-peak plateau. Then, a second increase of swelling pressure occurs, which cannot be explained by contact interactions. From pictures of the sample, it was suggested that the 70/15 mixture actually is a granular assembly as the peak swelling pressure is reached, and that pellets can be identified after 130 days, as relative humidity reaches 100 %. After 130 days, powder is observed to completely fill macropores and considering the material as controlled by the pellet assembly behaviour is not straightforward. It is interesting to note that this corresponds to the start of the second increase of swelling pressure in MU15 test. It is suggested that the behaviour from imbibition start to post-peak plateau is mainly controlled by the granular assembly. Swelling pressure at elevation above 20 mm reaches a plateau in the same range as the final swelling pressure in SP15b test described in Chapter 3. However, at 20 mm, the plateau is at lower swelling pressure. It may be a consequence of the imbibition which decreased the material dry density near water inlet. Still, imbibition in this test is not complete yet and no final conclusion can be provided with certainty.

In MU30 test, the evolution of swelling pressure is not the same as in MU0 and MU15 test. Swelling pressure evolution is not characterised by an early peak. Peak occurred at $z = 100$ mm and $z = 120$ mm but is smoother than peak observed in MU0 and MU15 samples. Swelling pressure also is significantly higher at peak value, and associated relative humidity generally lower. This phenomenon can be compared to the transient drop obtained between 9 MPa and 4 MPa of suction in SP30a test (see Chapter 3), associated to a collapse of macrostructure as a result of suction decrease under increasing mean stress in the sample. Pictures of the MU30 test indeed suggest that, as the axial peak swelling pressure is reached, the 70/30 material cannot be considered as controlled by the pellet assembly.

The differences between phenomena controlling the occurrence of peak swelling pressure in the samples is highlighted by plotting the relationship between peak swelling pressure and associated relative humidity in inter-pellet voids (Figure 6-26) or suction, considering that temperature is kept constant ($T = 293$ K, Figure 6-27). Two different domains can be identified: *i*) low pressure and *ii*) high pressure.

It is considered that pellet strength is the main phenomenon involved in the peak observed in the 70/0 and the 70/15 materials, while microstructural phenomena control the occurrence of the peak observed in the 70/30 material. These observations and interpretations are consistent with previous observations at REV scale in Chapter 3 and taken into account in the proposed model in Chapter 5. In swelling pressure tests, no second peak was obtained for the 70/15 mixture, while a second one was obtained upon water hydration for 70/0 sample. Further imbibition could provide information regarding the influence of microstructural phenomena on the behaviour of these two samples.

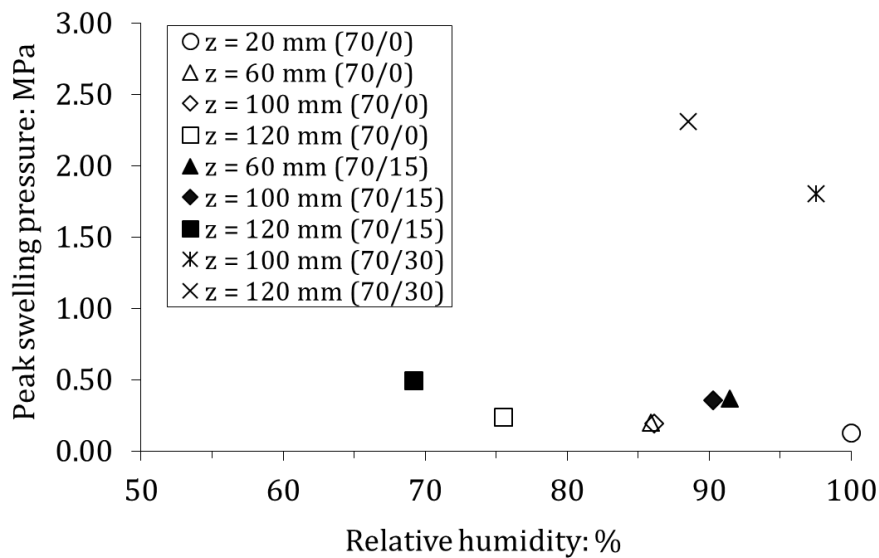


Figure 6-26: Peak swelling pressure as a function of relative humidity in MU0, MU15, and MU30 tests.

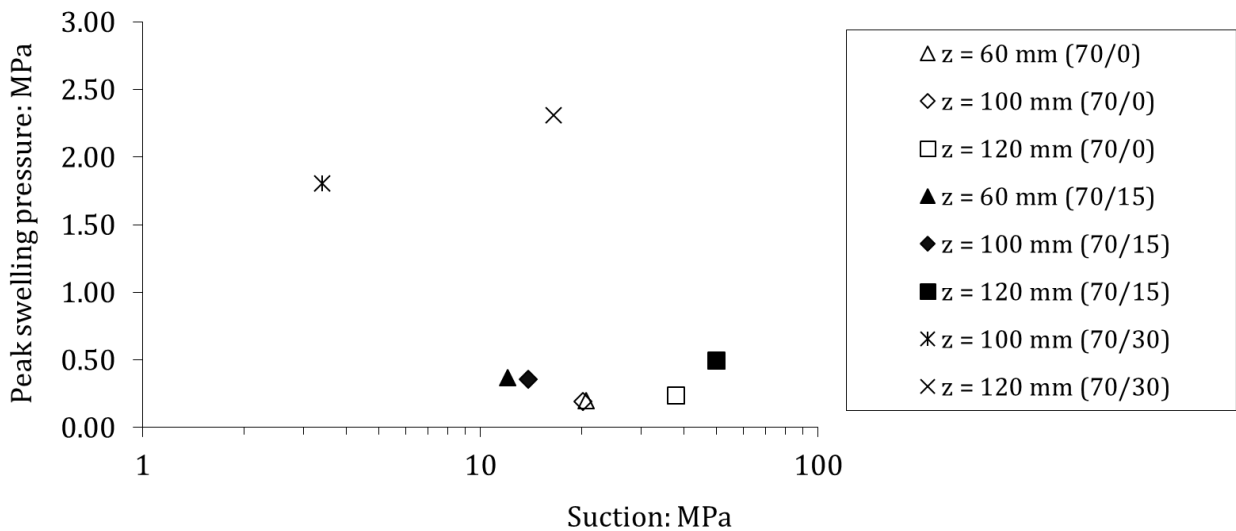


Figure 6-27: Peak swelling pressure as a function of (macrostructural) suction in MU0, MU15, and MU30 tests.

6.2.4.2 Evolution of the liquid water front

Pictures of the samples allow the evolution of the liquid water front to be estimated. Following the test beginning, a ~10-20 mm thick layer of homogenised bentonite material is formed on all the samples. Since pellets immediately above this layer clearly have not lost their initial structure, it can be assumed that the aforementioned layer is associated to the liquid water front. Dry macropores can indeed be observed in MU0 sample above this layer. Interestingly, it can be observed on Figure 6-22, Figure 6-23 and Figure 6-24 that the layer still is identified at comparable distance from water inlet as all sensors measure 100 % relative humidity in the samples. At 1 year and 1.5 year of hydration, the liquid water front is less clearly identified. However, dry macropores can still be identified in the 70/0 sample (Figure 6-28).

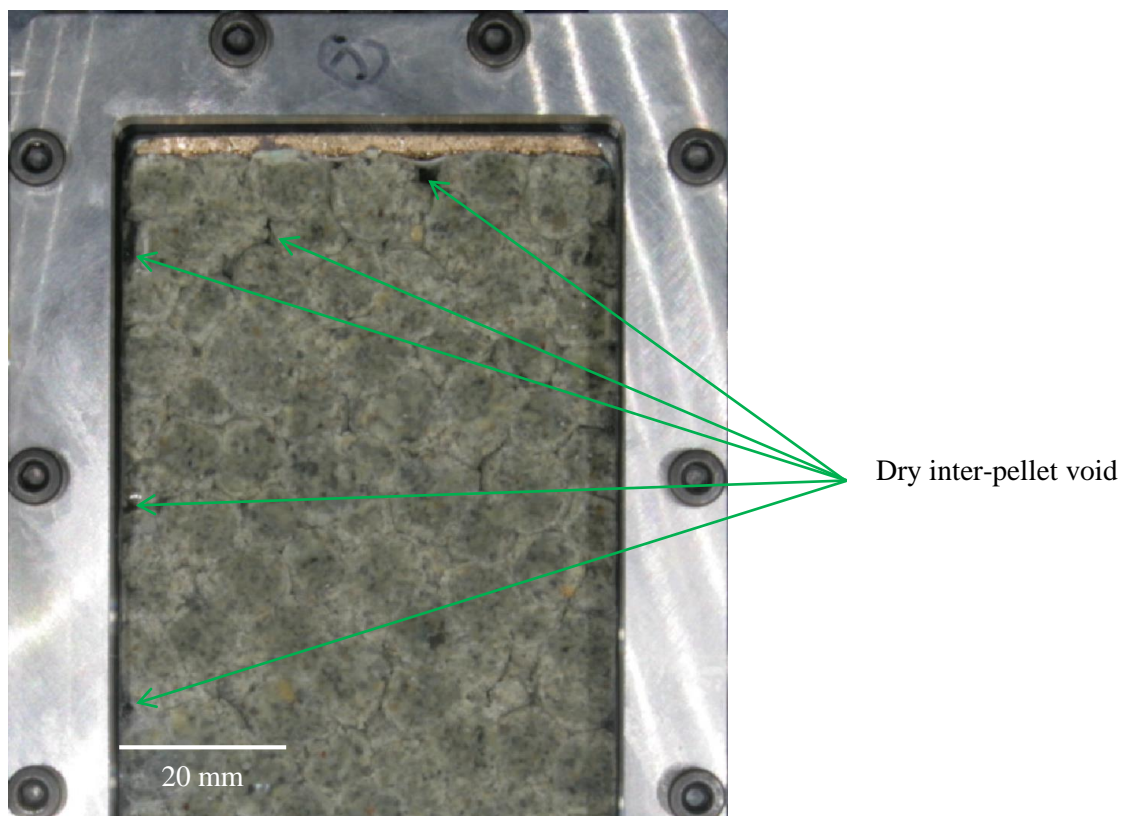


Figure 6-28: Identified dry inter-pellet voids in MU0 test after 1.5 year of imbibition.

In the light of these observations and considering the fact that all sensors have been measuring 100 % relative humidity for more than 1 year, it is highlighted that vapour transfer in the macroporosity is the main process involved in the saturation of the material. It influences the material response since, as already discussed, pellets lose their structure upon fast liquid wetting. This latter has been shown to control the material response in case of no/loose powder phase. Molinero-Guerra et al. (2018a) performed infiltration tests of pellet-powder mixture in cells of comparable dimensions (cylindrical, 120 mm height, 60 mm diameter), using similar 7 mm MX80 pellets. The authors evidenced that upon fast liquid wetting from both top and bottom, the mixture was completely homogenised after less than 100 days through observation by X-ray computed microtomography.

In repository conditions in claystone host rock, water infiltration is likely not to be characterised by fast flooding owing to claystone low permeability ($< 10^{-20} \text{ m}^2$, e.g. Davy et al., 2007). In this respect, vapour diffusion in macroporosity is considered the dominant process in these conditions, as suggested by Kröhn (2005).

6.2.4.3 Liquid water fluxes

Figure 6-9 highlighted that the infiltrated volume of water is not different in the three mixtures of different dry density. From this latter, Figure 6-29 is plotted to present the evolution of liquid water flux in the cell. It is shown that, except at ~ 1 year after the test start, corresponding to the tube clogging problem previously described, fluxes are close for all three mixtures.

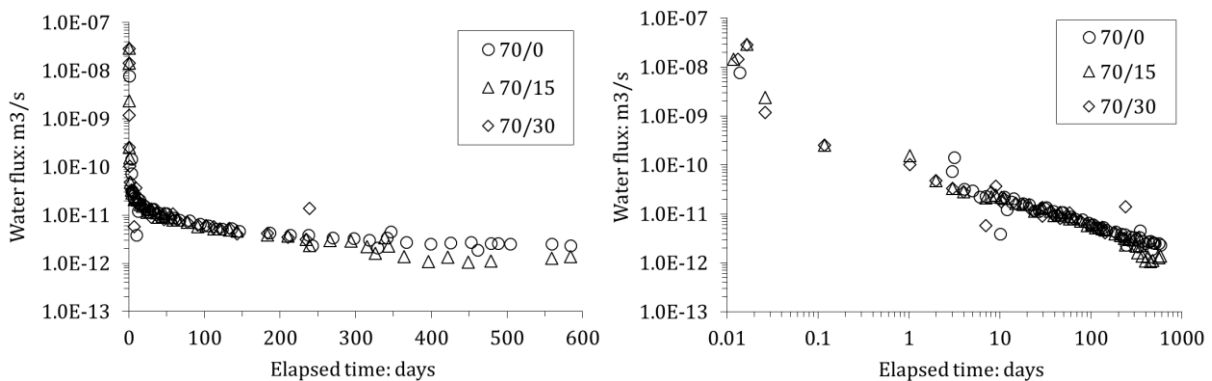


Figure 6-29: Water fluxes at the bottom of the cell in MU0, MU15 and MU30 tests. Left: linear time scale; Right: logarithmic time scale.

It is observed on samples pictures (Figure 6-22, Figure 6-23, and Figure 6-24) that following the test start, water enters samples in liquid phase and flows through the homogenised layer. This latter is obtained from homogenisation of mixtures of different dry densities (1.05 Mg/m^3 , 1.275 Mg/m^3 , and 1.50 Mg/m^3 for 70/0, 70/15, and 70/30 materials, respectively) and is likely not to have the same density in the three samples. Following liquid imbibition in this layer, transfers are likely to continue in vapour phase in macropores.

Assuming that suction gradient is the main phenomenon controlling water flux, the water flux may be expressed by equation 2-33. In this context, it may be assumed that relative permeability is 1 (saturated homogenised layer) and fluid density and viscosity are identical in all samples, which leaves the water fluxes governed by the product of intrinsic permeability and the gradient of suction.

In the case of imbibition conditions where gradient of suction is the mechanism controlling flux, it is suggested that water preferentially flows through micropores, characterised by higher suction values. In these conditions, under no external applied pressure, apparent permeability coefficient is considered to be related to microstructure.

Since water fluxes do not seem to be influenced by dry density, it is proposed that permeability of the microstructure is constant. It is reminded that in these conditions, water is not free and does not behave exactly as a Darcian fluid. Permeability in this case is thus an apparent permeability coefficient, suitable to describe water transfer between macrostructure and pellets.

In Chapter 2, it was highlighted that saturated permeability (with no gradient of suction) in the framework of Darcy's law can be considered an exponentially decreasing function of average dry density, thus related to macroporosity. It is suggested to use two distinct coefficients of permeability to describe water transfer through microporosity on the one hand, and water fluxes in the macroporosity on the other hand.

6.2.4.4 Suction and water content profiles in MU30 test

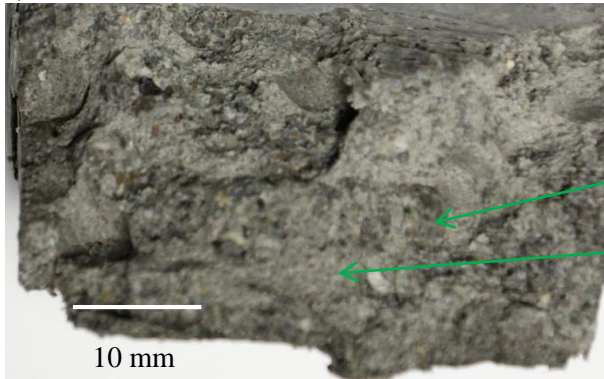
MU30 test was ended after 235 days of imbibition as a result of a glass face failure. MU30 test has been dismantled to determine the profiles of suction and water content after 235 days. The material has homogenised at elevation as high as ~40 mm. Above this elevation, pellets are still clearly identified, but it was not possible to separate matrix from pellets, which is consistent with the assumption that the material behaves as a continuum more than a granular assembly which response is controlled by interactions between pellets. Pictures of 70/30 mixture (at elevations of ~60 mm; ~80 mm; ~110 mm) are presented in Figure 6-30.

Microstructural suction is estimated by isolating pellets from matrix before measuring the suction using WP4. As previously discussed, pellets and matrix were not easily separated and measurement of suction was performed on isolated pellets surrounded by powder. Water content is also measured to compare results with experimental water retention curve of free-swelling pellets. Measured suction and water content profiles are presented in Figure 6-31 along with the theoretical final water content (determined using $\rho_w = 1 \text{ Mg/m}^3$) assuming full homogenisation. Water content was higher near the water inlet and decreased as elevation increased, as observed in other studies (Kröhn, 2004; Villar et al., 2005a; Bian et al., 2018) for compacted bentonite materials. Measured suction were as high as 7 MPa at z higher than 80 mm.

Assuming that the suction measurement is associated to microstructure, it can be suggested that the stress release affected the sample upon dismantling (Molinero-Guerra et al., 2019b). Following the effective stress principle, stress and suction are considered to affect the microstructure in a similar way and it is proposed to correct the measured suction by removing the value of swelling pressure. Results are presented in Figure 6-32. In Figure 6-32, it is highlighted that relative humidity in the sample is 100 %, which is consistent with the assumption that the suction value is associated to microstructure.

The water retention curve accounting for both uncorrected and corrected suction value is presented in Figure 6-33 and compared with results of free-swelling pellets from the present study and from Molinero-Guerra et al. (2019a). Uncorrected suction induces a higher retention behaviour of the constant-volume mixture compared to free-swelling pellets, whereas corrected suction induces a retention behaviour slightly below the free-swelling one at suction lower than 4 MPa, consistently with observations from Molinero-Guerra et al. (2019b). It is proposed that the corrected suction is closer to real test conditions than the uncorrected one.

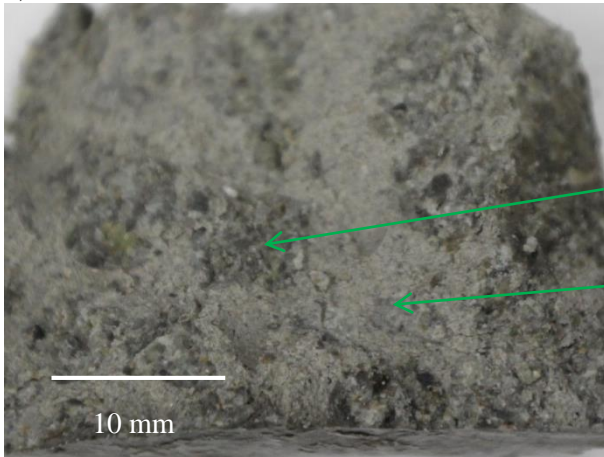
a) 60 mm



Pellet

Matrix

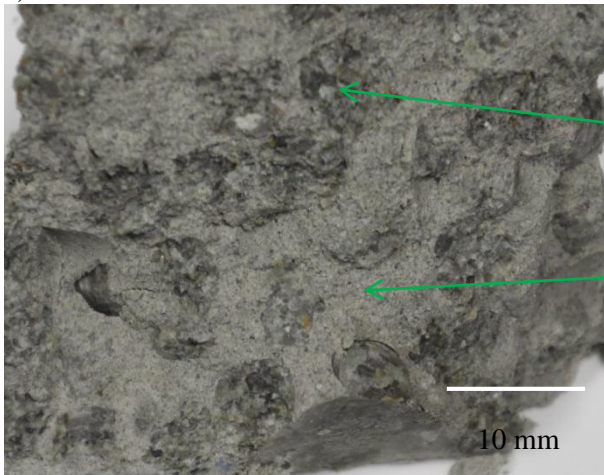
b) 80 mm



Pellet

Matrix

c) 110 mm



Pellet

Matrix

Figure 6-30: Picture of the 70/30 mixtures following MU30 dismantling after 235 days: a) $z \sim 60$ mm; b) $z \sim 80$ mm; c) $z \sim 110$ mm.

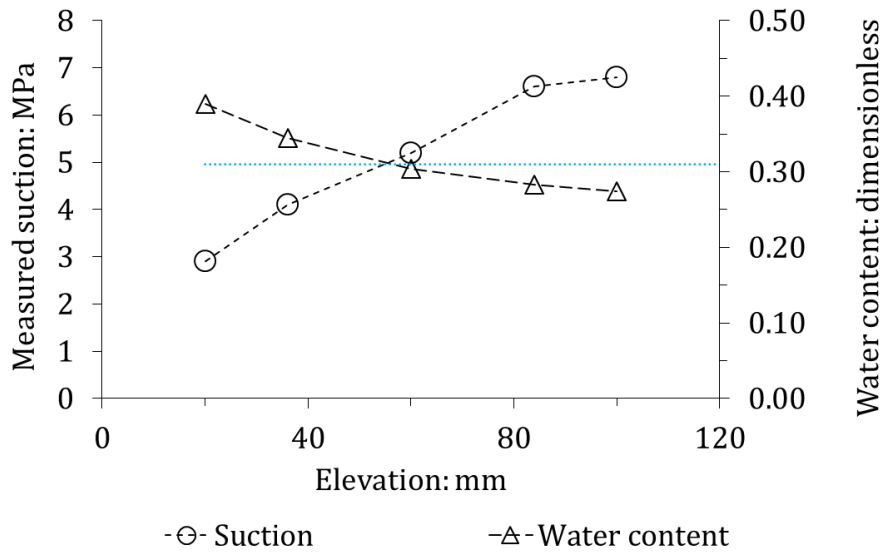


Figure 6-31: Measured suction and water content as functions of elevation in dismantled MU30 test.

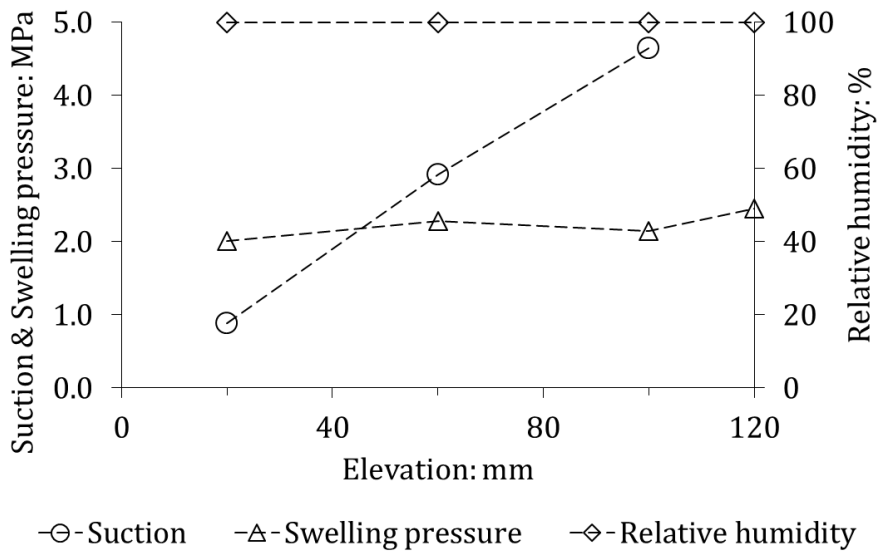


Figure 6-32: Corrected suction, swelling pressure, and measured relative humidity as functions of elevation in dismantled MU30 test.

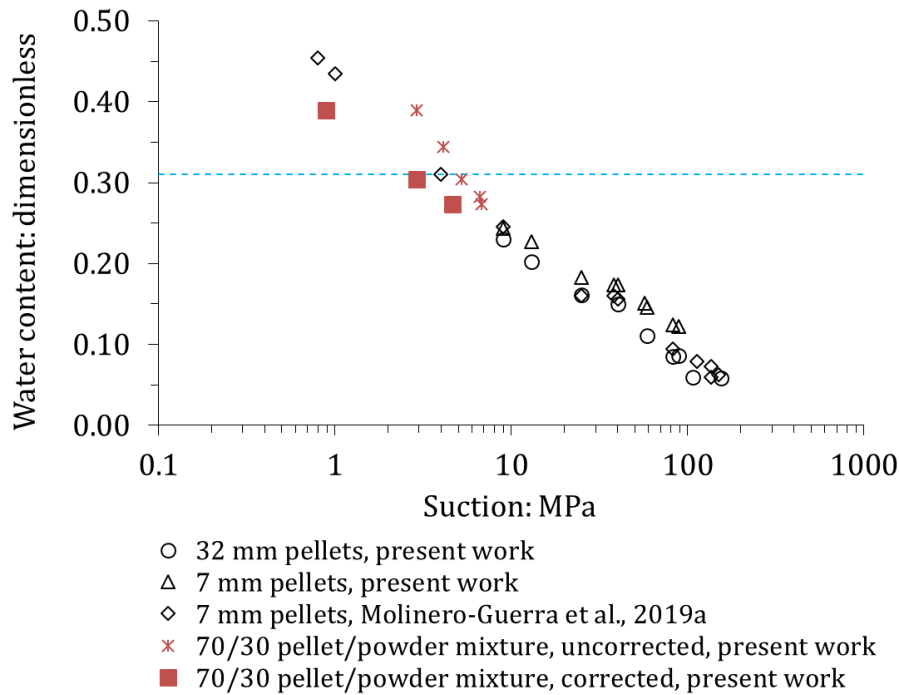


Figure 6-33: Water retention curve of the 70/30 mixture in the dismantled MU30 test compared with free-swelling pellets. Mixture values are obtained at different elevations. The dashed blue line represents the theoretical final water content.

6.2.5 Conclusions and perspectives

Mock-up imbibition tests have been performed on three different MX80 pellet-powder mixtures containing the same mass of pellets but different powder mass. Imbibition tests have been performed using a square-cuboid cells allowing the insertion of glass faces. In addition to traditional measurement of relative humidity, swelling pressure, and volume of infiltrated water, pictures of the samples have been taken at regular time intervals.

Experimental results allowed the influence of the initial granular structure, dominant saturation process, microstructural permeability and water retention behaviour of the mixture to be discussed. Main conclusions from this experimental study can be summarised as follow.

In 70/0 and 70/15 materials, the granular structure controlled the evolution of swelling pressure, characterised by an increase, reaching pellet strength, decrease and plateau of swelling pressure. In 70/0 material, the swelling pressure is expected to increase following further hydration. In 70/15 mixture, the swelling pressure increased again following the plateau as the powder contribution is considered to overcome the pellet assembly's. In 70/30 material, the influence of the granular structure was not clearly observable.

The dominant saturation process in the imbibition test is considered to be related to vapour diffusion in macropores. Indeed, it was shown that the liquid water front can be identified at approximately $z = 20$ mm in all samples as relative humidity was 100 % in the samples. Dry macropores were clearly identified in the 70/0 material after 1.5 year of imbibition, more than 1 year after measuring 100 % relative humidity in the sample.

Imbibition water flux displays a similar trend for all three samples. It is suggested that imbibition occurs through micropores in the homogenised layer at the bottom of the sample. It is proposed to

determine two distinct permeability coefficients to characterise micro-macro transfer and water transfer in the matrix.

Microstructural suction profile was measured following dismantling of the MU30 test. Results suggest that the release of stress upon dismantling can affect the measured suction. This latter may be corrected by removing the measured swelling pressure. Suction was higher at higher distance from the bottom (water inlet) and in all cases higher than 0 whereas relative humidity in macropores was 100 %.

The mechanical responses of the materials were consistent with the observed behaviour in swelling pressure tests described in Chapter 3. An interesting perspective arising from experimental results is the proposition of transfer laws able to describe water transfer from macropores to pellets, liquid water transfer in the matrix and vapour transfer in the matrix. These perspectives are addressed in the following section.

6.3 PROPOSITION OF TRANSFER LAWS

The present section focuses on the proposition of transfer laws suitable to describe relevant behaviour of the material. In the light of experimental results presented in the former section, parts 6.3.1 and 6.3.2 address microstructure permeability coefficient and water transfer between matrix (Table 5-2) and pellets, respectively. Then, part 6.3.3 suggests transfer laws suitable to describe transfer within the matrix. These laws can be implemented to perform FEM coupled simulations in which water transfer is described by laws proposed in part 6.3.3, and in which s_1 can be determined from s_2 and material properties using laws previously proposed in parts 6.3.1 and 6.3.2.

6.3.1 Apparent permeability of the microstructure

6.3.1.1 Introduction

It is proposed to determine a transfer law between pellets and matrix, based on a constant pellet permeability. In the present part, the method of determination of the pellet permeability is described. It is assumed that pellets are fully saturated and described by their microstructure. This hypotheses have been discussed in Chapter 4.

In MU30 test, initial microstructural suction is ~95 MPa. Following dismantling, the suction profile was determined and discussed in section 6.2. From initial and final (corrected) suction profile, it is proposed to determine pellet permeability using FEM simulations of a single pellet hydration in which boundary conditions are given by measured relative humidity in MU30 test.

An apparent permeability coefficient is proposed, assuming that Darcy's law is appropriate to describe water flux in the microstructure and that water flux is proportional to the gradient of suction. FEM simulations of water transfer can be repeated accounting for different intrinsic permeabilities to finally choose the one reducing quadratic error with respect to experimental results.

6.3.1.2 Method

The FEM problem accounts for liquid water transfer across a 1D geometry (line) with spherical symmetry. In the case of a saturated medium, increment of water mass is controlled by volumetric strain. This latter is described by equation 4-15. The length of the modelled line is set to the pellet equivalent radius r (determined from equation 4-16). Remeshing at each time step is avoided by normalising all length units to the pellet radius, thus indirectly taking into account swelling while using a single mesh along the entire hydration path. Boundary conditions in terms of suction are obtained from RH measurement through the Kelvin law.

In FEM simulations, the Richards equation is solved using Bil. Suction is modelled as a negative water pressure, neglecting atmospheric pressure. Suction at the centre of the modelled pellet is calculated from initial state to 235 days of hydration. Final value is compared to the experimental results.

6.3.1.3 Initial and boundary conditions

The following initial conditions for suction are used in the model:

- $s(t = 0) = 95 \text{ MPa}$ at $x = 0$;
- $s(t = 0) = 95 \text{ MPa}$ at $x = r$;

The boundary conditions used in the simulations are:

- $q = 0$ at $x = 0$;
- $s(x = r)$ is progressively decreased from 89 MPa to 0.1 MPa according to experimental results.

Gravity is not addressed in the simulation and gas pressure is taken equal to zero. The distance between two nodes in the mesh is defined by l_c . The ratio l_c/r is set to 0.05. Initial porosity is 0.31 (obtained from e_0 , Table 3-2). Water viscosity and density are considered equal to those of free water, $10^{-3} \text{ Pa}\cdot\text{s}$ and 1000 kg/m^3 respectively. In the model, suction is modelled as a negative water pressure. The mesh is presented in Figure 6-34.

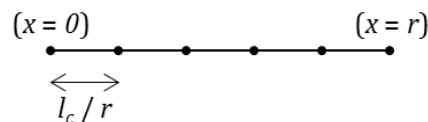


Figure 6-34: Mesh used for the FEM simulations of a single pellet hydration to determine microstructural permeability.

6.3.1.4 Numerical results

The permeability found to minimise the quadratic error in the simulations is $k_{int} = 10^{-23} \text{ m}^2$. Figure 6-35 presents numerical results of the evolution of microstructural suction in the pellet for $k_{int} = 10^{-23} \text{ m}^2$. This value is several order of magnitude lower than k_{int} values commonly obtained on saturated bentonites (Figure 2-39). It is however worth mentioning that in the present study, only the value of microstructural permeability is considered whereas, in Figure 2-39, results presented are apparent permeability coefficients accounting for both microstructure and macrostructure.

Permeability associated to the macrostructure is higher since water in the microstructure is more prone to adsorption phenomenon. In addition, it is commonly admitted that microstructure is not affected by compaction. Figure 2-39 can thus be considered as permeability values associated to the macrostructure.

In imbibition test conditions, the gradient of suction is considered the main mechanism inducing water transfer through the homogenised layer and water fluxes were not dry density dependent. In this respect, it is considered that a constant permeability coefficient is a reasonable assumption for the microstructure.

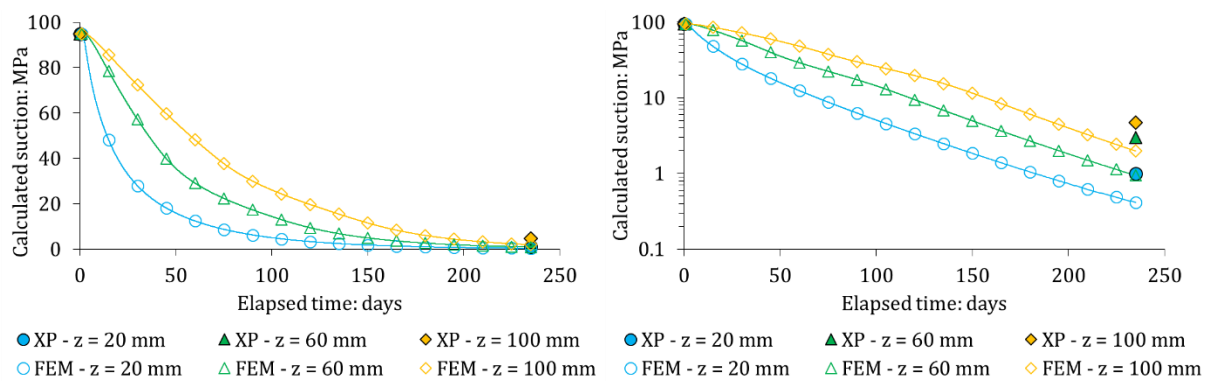


Figure 6-35: Numerical results of the evolution of microstructural suction in the pellet as a function of elapsed time, under boundary conditions of MU30 tests and with $k_{int} = 10^{-23} \text{ m}^2$, compared with experimental results.

Numerical results were obtained considering that the pellet behaves as determined in free-swelling conditions in the laboratory (Chapter 4). The pellet swelling behaviour as described in Chapter 4 and used in the FEM simulation was suggested to be valid for suction as low as 3 MPa but there is no certainty regarding its validity at lower suction. In the present simulations, final suction values are in this threshold range and the swelling of the pellet may be slightly underestimated. Higher swelling strain would result in higher k_{int} for the same suction decrease rate. Comparison of the water retention curves of the mixture and free-swelling pellets (Figure 6-33) are not significantly different and it is assumed that the hypothesis of free-swelling conditions in FEM simulations is reasonable.

Under fully saturated conditions and pressure gradients, water flow through the macrostructure would become the dominant water transfer mechanism. Under partially saturated conditions, owing to the very low permeability of the microstructure, vapour diffusion in the macroporosity would overcome “pellet-pellet” transfer through microstructure governed by suction gradient.

For larger scale modelling, it is proposed to use the microstructural permeability to describe pellet-matrix water transfer. It is considered from these results and discussions that $k_{int} = 10^{-23} \text{ m}^2$ is a reasonable estimation of the microstructure *apparent* permeability.

6.3.2 Pellet-matrix transfer law

6.3.2.1 Introduction

In the present part, a simplified transfer law describing water exchange between pellets and matrix is determined. It is proposed to write this latter as:

$$\frac{\partial m_1}{\partial t} = \frac{\beta_{Mm}}{\tau} (s_1 - s_2) \quad 6-1$$

Where m_1 is the pellet mass, β_{Mm} is a water transfer parameter, τ is a characteristic time, s_1 and s_2 are respectively the suction in pellet and the suction in the matrix. It is proposed to consider β_{Mm} and τ as functions of s_1 .

An advantage of this approach, apart from its simplicity, is that τ can be expressed as a function of material properties leaving β_{Mm} the only parameter controlling the water mass exchanges between pellet and matrix to be determined.

β_{Mm} is determined by FEM simulation of a pellet hydration and τ from the mass conservation equation. The following sub-parts focus on the determination of β_{Mm} and τ , considering the pellet permeability constant.

6.3.2.2 Characteristic time of transfer

Under a suction gradient from pellet to matrix, water transfer from the pellet surface to the pellet centre would occur. The mass conservation equation is written:

$$\frac{\partial}{\partial t} (\rho_w \phi_1 S_{r1}) = -\rho_w \nabla \cdot \mathbf{q} \quad 6-2$$

Where ϕ_1 is the pellet porosity, S_{r1} the pellet degree of saturation and \mathbf{q} the water advective flux.

Owing to the material particular features, equation 6-2 is equivalent to:

$$\frac{\partial}{\partial t} s_1 = -\frac{1}{\frac{\partial \varepsilon_{V1}}{\partial s_1}} \nabla \cdot \left(-\frac{k_{int1}}{\mu_w} \nabla s_1 \right) \quad 6-3$$

Where μ_w is the water dynamic viscosity, considered constant. Since k_{int1} is also considered constant, equation 6-3 is equivalent to:

$$\frac{\partial}{\partial t} s_1 = C(s_1) \Delta s_1 \quad 6-4$$

Where Δ is the Laplacian operator and C is a transfer coefficient:

$$C(s_1) = \frac{k_{int\ 1}}{\mu_w \frac{\partial \varepsilon_{V1}}{\partial s_1}} \quad 6-5$$

The characteristic time is then expressed as the ratio of the square of a characteristic length of transfer to the transfer coefficient. It is proposed to use r , the equivalent pellet radius, as the characteristic length of transfer. The initial value of r is written r_0 . Thus:

$$\tau = \tau(s_1) = \frac{r_0^2 (1 + \varepsilon_{V1})^{2/3}}{\frac{k_{int\ 1}}{\mu_w \frac{\partial \varepsilon_{V1}}{\partial s_1}}} \quad 6-6$$

Figure 6-36 presents the evolution of τ for two values of $k_{int\ 1}$ as a function of suction.

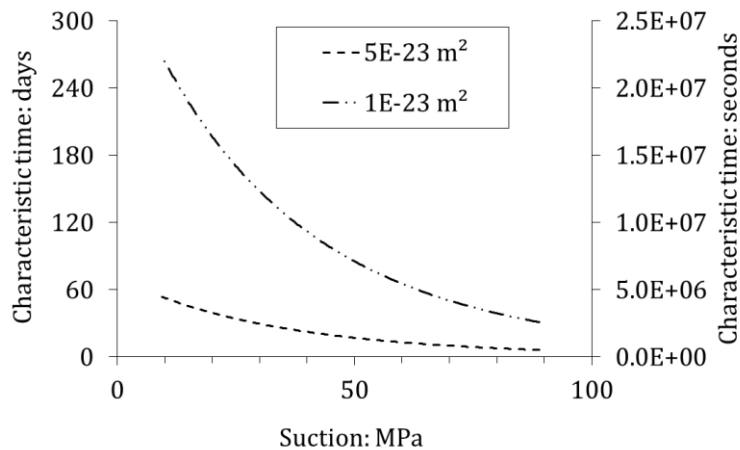


Figure 6-36: Characteristic time of transfer as a function of suction for two values of k_{int} .

6.3.2.3 Determination of the transfer coefficient

The transfer coefficient is determined from FEM simulation of the hydration of a pellet. The pellet is modelled by a 1D geometry (line). The line length is the pellet equivalent radius. The same method as in part 6.3.1 is used for the simulation of the pellet hydration.

Compared to simulations performed to obtain the pellet permeability, hydration is not performed on a single step over a defined time. Here, hydration of the pellet is performed in N small steps of suction decrease. Each suction step lasts for a time higher than τ . At each suction steps, the exchanged mass at $t = \tau$ is computed.

Considering that hydraulic equilibrium is reached when $t = \tau$, it is proposed, following equation 6-1, to determine β_{Mm} as the ratio of the variation of pellet mass to the variation of suction, during a time

equal to τ (*i.e.* equation 6-1 becomes $\Delta m_1/\tau = \beta_{Mm}/\tau \Delta s_1$). The value of β_{Mm} associated to each suction step is thus computed as:

$$\beta_{Mm} = \frac{m_1(t = \tau) - m_1(t = 0)}{s_1(t = \tau) - s_1(t = 0)} \quad 6-7$$

β_{Mm} is determined for a suction range of 90 MPa to 9 MPa.

6.3.2.4 Initial and boundary conditions

The following initial conditions for suction are used in the model:

- $s(t = 0, x = 0) = 90$ MPa, for the first step, then for each calculation step is equal to the last applied suction at $x = r$;
- $s(t = 0, x = r)$ depends on the number of calculation steps, N. Its value is always lower than $s(t = 0, x = 0)$ and at the final step is 9 MPa;

The boundary conditions used in the simulations are:

- $q = 0$ at $x = 0$;
- $s(x = r)$ is constant during each suction step.

Gravity is not addressed in the simulation and gas pressure is taken equal to zero. The ratio l_c/r is taken equal to 0.01. Initial porosity is 0.31 (obtained from e_0 , Table 3-2). Water viscosity and density are considered equal to those of free water, 10^{-3} Pa.s and 1000 kg/m³ respectively. In the model, suction is modelled as a negative water pressure. The mesh used for the FEM simulations is presented in Figure 6-37.

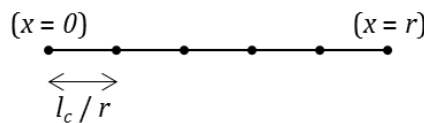


Figure 6-37: Mesh used for the FEM simulations of the hydration of a single pellet to determine the transfer coefficient.

6.3.2.5 Numerical results

Numerical results are presented in this part. Several calculations are performed to address the eventual β_{Mm} dependency on N, l_c/r , or k_{int1} .

Figure 6-38 and Figure 6-39 present the results of the simulation of a suction decrease from 66.6 to 65.0 MPa (N = 50), for $k_{int1} = 10^{-23}$ m² ($\tau = 4.76 \times 10^6$ s) and $l_c/r = 0.01$. From these results, it is highlighted

that the suction profile at $t = \tau$ is homogeneous (Figure 6-38). It is besides highlighted that this latter could be considered homogeneous at $t < \tau$ to some extent (Figure 6-39). In this respect, the β_{Mm} determined using this method may be slightly underestimated.

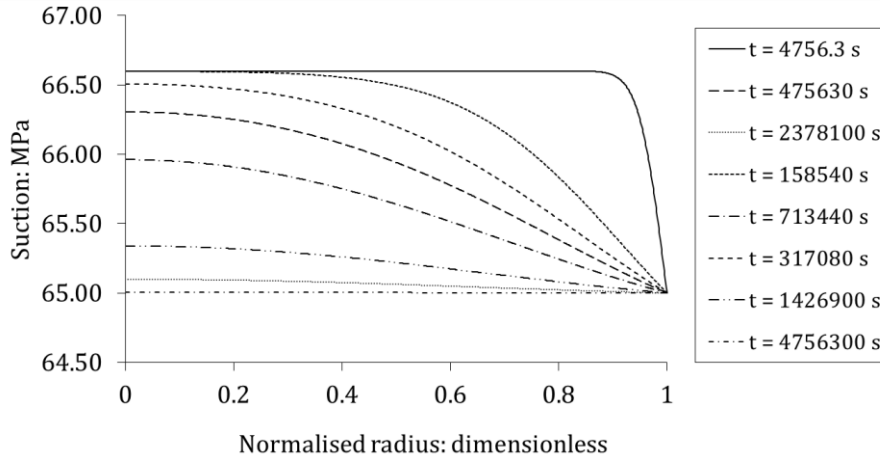


Figure 6-38: Evolution of the profile of suction in the pellet with time. The profile is homogeneous at $t = \tau$ (4756300 s).

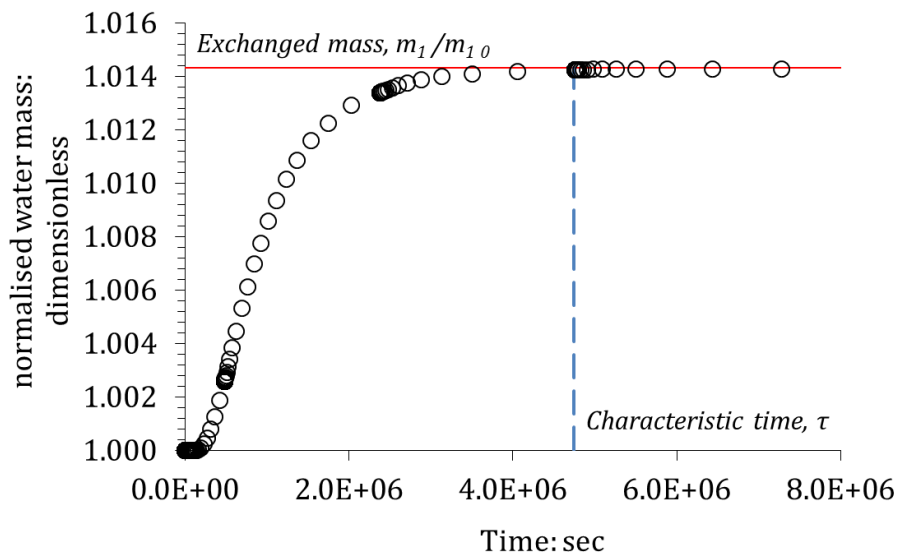


Figure 6-39: Mass exchange as a function of time during a step of suction decrease. It is highlighted that the equilibrium can be reached before $t = \tau$.

Using the proposed method, β_{Mm} is obtained for values of s_i in the range 90 MPa – 9 MPa. Five simulation types have been performed to address the influence of N , l_c/r , and k_{int1} . An overview of the types of calculations performed is presented in Table 6-4.

Table 6-4: Summary of the five types of FEM simulations performed. $k_{int 1}$ is given in m^2 .

	N = 50	N = 500
$l_c/r = 0.1$	$k_{int 1} = 1 \times 10^{-23}$	
$l_c/r = 0.01$	$k_{int 1} = 1 \times 10^{-23}$	$k_{int 1} = 1 \times 10^{-23}$ $k_{int 1} = 5 \times 10^{-23}$
$l_c/r = 0.001$	$k_{int 1} = 1 \times 10^{-23}$	

β_{Mm} is determined from the mass variation over a time τ . If the pellet has reached hydraulic equilibrium at $t = \tau$, β_{Mm} is obtained from the mass variation at equilibrium, which does not depend on the mesh. For instance, Figure 6-40 presents the results obtained for the evolution of β_{Mm} as a function of suction for different values of N, l_c/r and $k_{int 1}$. It is highlighted that, in the simulations performed, results do not depend on the mesh and $k_{int 1}$. N can have an influence on the results since the initial τ is used to determine β_{Mm} . In Figure 6-40c), it is highlighted that N = 50 is high enough to obtain consistent results.

Results obtained allow the transfer coefficient to be determined as a function of suction. Influence of the material properties can be associated to τ , which leaves β_{Mm} as the only parameter to fit to characterise pellet-matrix exchanges.

Numerical results suggest that β_{Mm} is a function of ε_{V1} . However, it is suggested in Figure 6-39 that β_{Mm} can be underestimated if determined at $t = \tau$ and that $\beta_{Mm} = \beta_{Mm}(\varepsilon_{V1})$ is a limit case. In addition, the present law aims at simplifying the implementation of water exchanges, and it is proposed to keep a single expression for both granular and continuous domains. As a consequence, it is proposed not to express β_{Mm} as a function of ε_{V1} , since equation 4-15 is no longer valid in the continuous domain, and at full homogenisation there should be no longer a delay between matrix and pellet phases hydration. β_{Mm} therefore should tend to infinity when suction tends to zero. It is proposed to express β_{Mm} as a power law of suction, such that the law may fit numerical results at high suction, and progressively tends to infinity as suction approaches zero:

$$\beta_{Mm} = \beta_H s_1^{-\gamma} \quad 6-8$$

Where β_H and γ are model parameters to be calibrated.

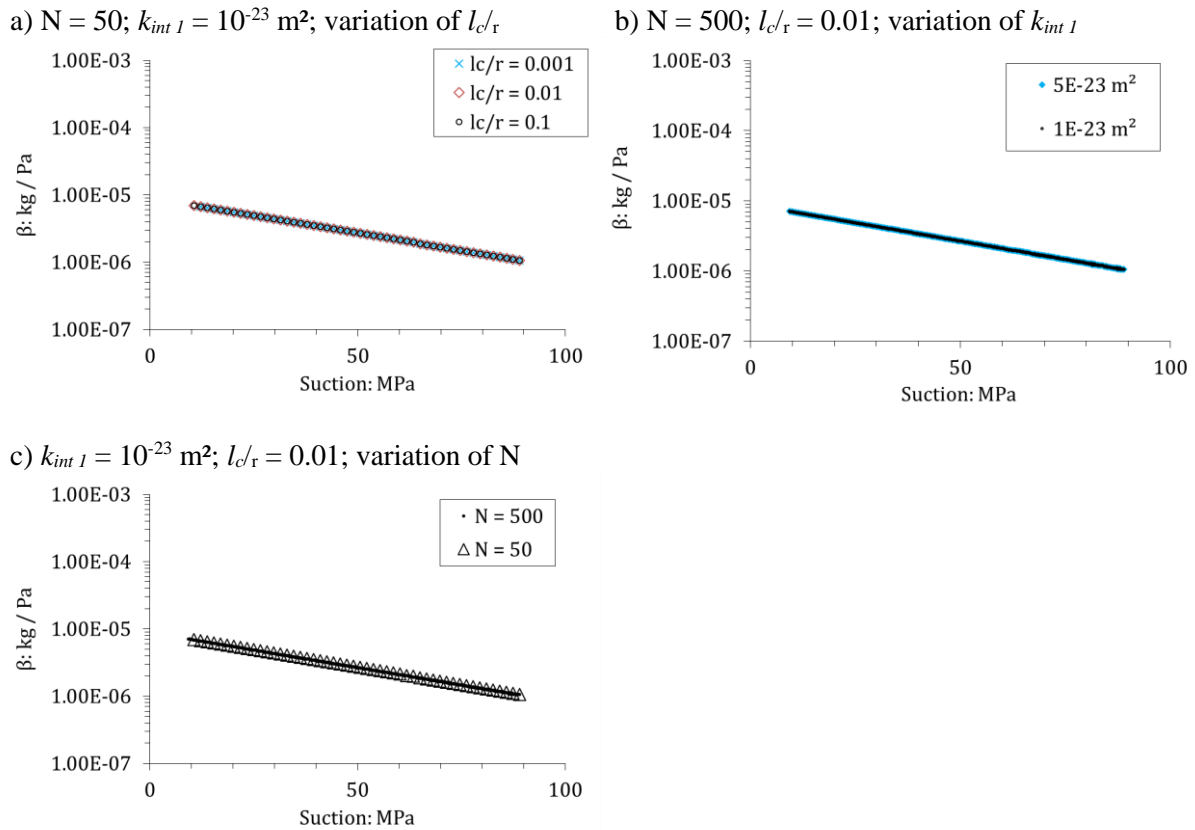


Figure 6-40: Evolution of β_{Mm} as a function of suction for varying $l_{c/r}$ (a), varying $k_{int l}$ (b), and varying N (c).

A value of $\gamma = 1.5$ is found to provide the best fit for the slope in the $\ln(\beta_{Mm})$ - s plane. It is proposed to set $\gamma = 1.5$ constant. Then, a value of $\beta_H = 5 \times 10^5 \text{ kg}^{-1} \text{ Pa}^{-0.5}$ is found to fit most of the numerical results and conveniently let β_{Mm} tend to infinity as suction approaches zero. Higher values of β_H may be suitable to describe the material behaviour since equation 6-7 may underestimate β_{Mm} . It is suggested however that lower values of β_H are not appropriate. Figure 6-41 presents a comparison between equation 6-8 for different values of β_H and the β_{Mm} trend obtained from FEM simulations, for $\gamma = 1.5$.

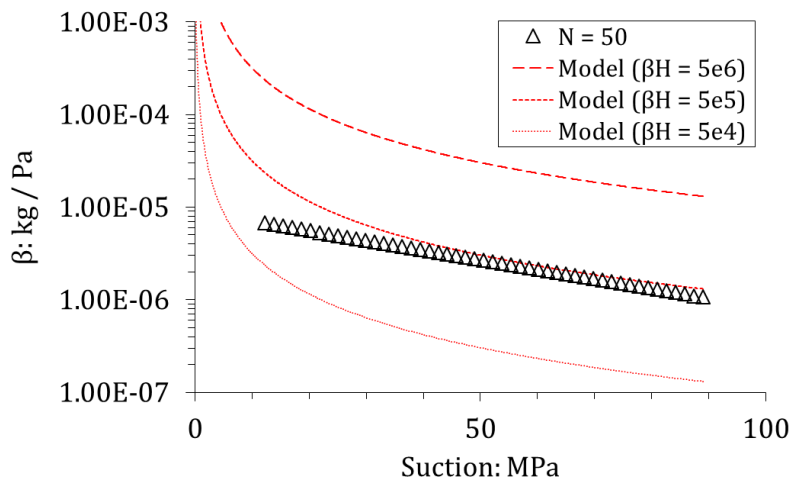


Figure 6-41: Comparison of β_{Mm} obtained in FEM simulations and values obtained from equation 6-8.

Equations 6-1 and 6-8 provide a simple way of describing water exchanges between pellets and matrix. Transition from granular to continuous domains is taken into account by allowing β_{Mm} to tend to infinity at low suction. β_H can be obtained directly from the simulation results. Higher value of β_H may be suitable since the values obtained by FEM simulations can be slightly underestimated as the $\Delta m_I/\Delta t$ slope in Figure 6-39 is slightly higher than $\Delta m_I/\tau$.

6.3.3 Water transfer within the matrix

6.3.3.1 Introduction

In the present part, equations describing water transfer in the pellet-powder mixtures are proposed. From experimental results presented in section 6.2, it seems appropriate to describe water transfer in the material as (Figure 6-42):

- liquid and vapour transfers in the matrix;
- liquid transfer between pellets and matrix, counted as a sink/source term;
- hydraulic equilibrium in the matrix between powder grains and macropores.

The sink/source term affecting water transfer in the matrix is related to pellet-matrix exchanges and has been described in part 6.3.2. Liquid and vapour transfer laws are suggested in the present part and constitute sub-part 6.3.3.2. The permeability of the matrix is discussed in 6.3.3.3. The degree of saturation of the macropores is briefly addressed in sub-part 6.3.3.4.

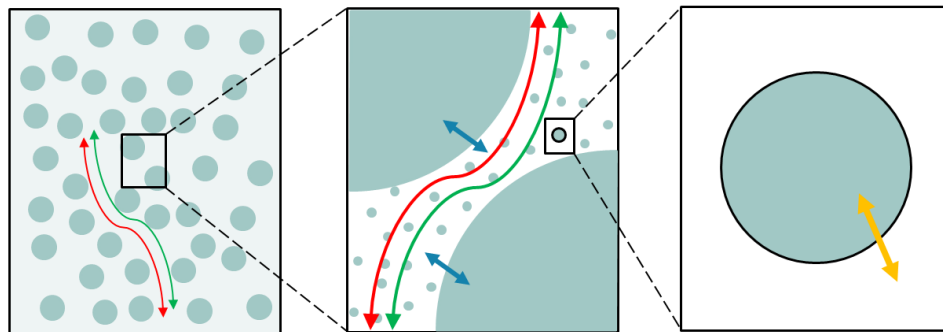


Figure 6-42: Sketch of water transfer in pellet-powder mixtures described in the present section. Red arrows represent vapour transfer, Green arrows represent liquid transfer, blue arrows represent pellet-matrix exchanges, and yellow arrow represents powder-macropores transfer (equilibrium). Left: mixture scale; Centre: pellet scale; Right: powder grain scale.

6.3.3.2 Liquid and vapour water transfer

The water mass in the material matrix phase (subscript *mat*) can be divided into liquid water mass, m_l , and vapour mass, m_{vap} :

$$m_{w\ mat} = m_{l\ mat} + m_{vap\ mat} \quad 6-9$$

The water mass balance equation in the matrix is written as:

$$\frac{\partial m_{l\ mat}}{\partial t} + \rho_w \nabla \cdot \mathbf{q}_l + \frac{\partial m_{vap\ mat}}{\partial t} + \rho_{vap} \nabla \cdot \mathbf{i}_{vap} = -\frac{\partial m_1}{\partial t} \quad 6-10$$

Where $\frac{\partial m_1}{\partial t}$ is the sink/source term, given by equation 6-1; \mathbf{q}_l and \mathbf{i}_{vap} are the flux vector of liquid water and vapour, respectively; ρ_w and ρ_{vap} are the liquid water and vapour densities, respectively.

\mathbf{q}_l is described by Darcy's law:

$$\mathbf{q}_l = \frac{k_{int\ mat} k_{r\ mat}}{\mu_w} \nabla s_2 \quad 6-11$$

Where $k_{int\ mat}$ and $k_{r\ mat}$ are the intrinsic and relative permeability to water of the matrix, respectively. These latter are described in the following sub-part.

\mathbf{i}_{vap} is described by Fick's law:

$$\mathbf{i}_{vap} = \tau_g \Phi_M (1 - S_{r\ mat}) D_{vap} \nabla \rho_{vap} \quad 6-12$$

Where $S_{r\ mat}$ is the matrix degree of saturation. ρ_{vap} is determined using equation 2-35, in which p_{vap} is determined from RH . At $T = 293\ K$, $D_{vap} = \sim 2.7 \cdot 10^{-5}\ (m^2/s)$ (Philip and de Vries, 1957) and $p_{vap} = 2.34 \cdot 10^{-3}\ RH\ (MPa)$. τ_g is lower or equal to 1 and is generally assumed. For instance, Olivella and Gens (2000) assumed $\tau_g = 1$ in a low permeability clayey soil and Kröhn (2005) assumed $\tau_g = 0.4$ in compacted MX80 bentonite.

6.3.3.3 Permeability of the matrix

The relative permeability to water is a function of the degree of saturation. It is equal to the ratio of permeability at a given degree of saturation to the saturated permeability. It is usually expressed as a power law of the degree of saturation. This approach is applied to pellet mixtures, thus yielding:

$$k_{r\ mat} = (S_{r\ mat})^\zeta \quad 6-13$$

With:

$$S_{r\ mat} = \frac{S_{rM} \Omega_M + S_{r2} \Omega_{v2}}{\Omega_M + \Omega_{v2}} \quad 6-14$$

Where ζ is a parameter relating the matrix degree of saturation to the matrix relative permeability. For pellet-powder mixtures, values of 1.5 (Alonso et al., 2011) and 3 (Gens et al., 2011; Sanchez et al., 2016; Mokni et al., 2019) for ζ are found in the literature. S_{rM} is the degree of saturation of macropores, S_{r2} is the degree of saturation of the powder.

In Chapter 2, experimental results of the evolution of MX80 bentonite intrinsic permeability have been presented (Figure 2-39). As previously discussed, the permeability plotted in this graph can be considered the permeability of the macrostructure. It is suggested from these results that $k_{int\ mat}$ is an exponentially decreasing function of the dry density. Transfers take place within the matrix. An apparent dry density of the matrix, $\rho_{d\ mat}$, is determined as:

$$\rho_{d\ mat} = \frac{x_{S0} \rho_d}{\Phi_2 + \Phi_M} \quad 6-15$$

Where x_{S0} is the initial dry mass proportion of powder in the mixture and ρ_d is the mixture dry density.

The following equation is then proposed to fit experimental data while allowing the minimal value of $k_{int\ mat}$ to be equal to the microstructure intrinsic permeability, k_{int1} , as determined in part 6.3.2:

$$k_{int\ mat} = k_{int\ 1} [1 + k_B (\exp(-k_A \rho_{d\ mat}))] \quad 6-16$$

Where k_A and k_B are model parameters. $k_A = 7 \text{ m}^3/\text{Mg}$ and $k_B = 7.5 \times 10^7$ are found to satisfactorily reproduce experimental data (Figure 6-43).

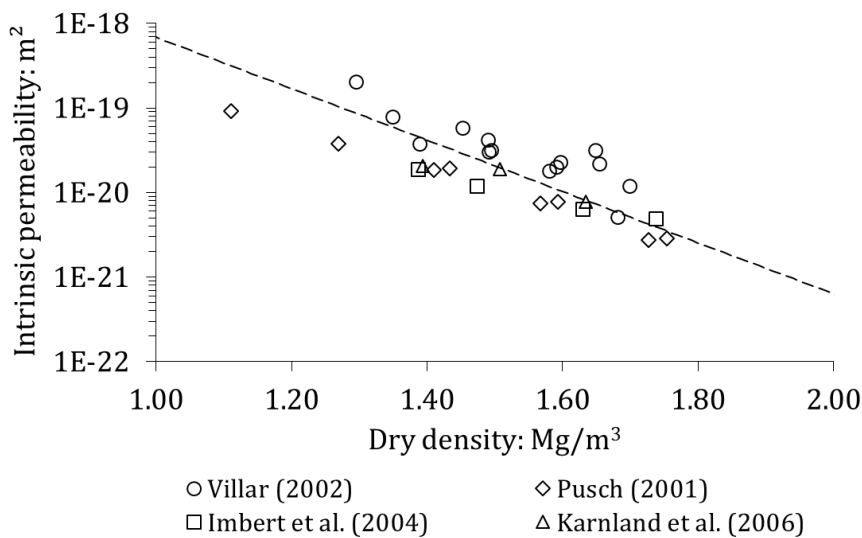


Figure 6-43: Comparison of experimental data for bentonite intrinsic permeability and model prediction for the matrix using $k_{int1} = 10^{-23} \text{ m}^2$; $k_A = 7 \text{ m}^3/\text{Mg}$ and $k_B = 7.5 \times 10^7$. Dashed line represents model predictions.

6.3.3.4 Degree of saturation of the macropores

It is suggested to describe the degree of saturation of the macropores using a model based on the van Genuchten model, as in Hoffmann et al. (2007); Gens et al. (2011); Alonso et al. (2011); Sanchez et al. (2016); Mokni et al. (2019):

$$S_{rM} = \left(1 + \left(\frac{S_2}{n} \right)^{\frac{1}{1-m}} \right)^m \quad 6-17$$

Where m and n are water retention model parameters.

From discussion regarding water retention domains in Chapter 2 and experimental evidence from Sun et al. (2019), it is considered that macropores may remain dry until low values of suction. It is suggested that suitable values of n and m should account for this feature.

6.4 IMPLEMENTATION OF PELLET-MATRIX TRANSFER LAW

6.4.1 Implementation in Bil

Transfer laws described in part 6.3.2 are implemented in Bil to model swelling pressure tests accounting for two different suctions in the pellet and matrix phases. From equation 6-1, at each time step $t + \Delta t$, suction in the pellet $s_{1\ t+\Delta t}$ is computed as:

$$s_{1\ t+\Delta t} = s_{1\ t} - C_{tr} (s_{2\ t+\Delta t} - s_{1\ t}) \quad 6-18$$

Where C_{tr} is a transfer coefficient determined from β_{Mm} , τ , and the derivative of volumetric strain with respect to s_j :

$$C_{tr} = \frac{\Delta t}{\Delta t - \rho_w \Phi_{10} \frac{\partial \varepsilon_{V1}}{\partial s_{1t}} \frac{\tau_t}{\beta_{Mm t}}} \quad 6-19$$

Where $\frac{\partial \varepsilon_{V1}}{\partial s_{1t}}$ is determined from equations 5-48 or 5-55 depending on the material state. $\beta_{Mm t}$ and τ_t are computed as:

$$\beta_{Mm t} = \beta_H s_{1t}^{-1.5} \quad 6-20$$

And

$$\tau_t = \frac{r_0^2 (1 + \varepsilon_{V1t})^{2/3}}{\frac{k_{int1}}{\mu_w \frac{\partial \varepsilon_{V1}}{\partial s_{1t}}}} \quad 6-21$$

In equation 6-21, r_0 is associated to the granular domain. In this respect, as suction reaches low values and the material is no longer granular, equation 6-21 may no longer be an appropriate estimation of τ_t . It is reminded that this phenomenon is indirectly taken into account by choosing a power law for β_{Mm} , thus allowing C_{tr} to progressively tend to 1 as suction decreases. At low suction, hydraulic equilibrium is thus reached regardless of the expression of τ_t .

6.4.2 Simulation of swelling pressure tests

6.4.2.1 Introduction

In the present part, swelling pressure tests simulated in Chapter 5 are simulated using the same geometry, initial conditions and boundary conditions, except that s_2 only is imposed instead of a single value of s . s_1 is determined at each time step from s_2 using the procedure described in 6.4.1. All the material parameters remain unchanged.

6.4.2.2 Geometry of the problem

The geometry and mesh are similar to FEM simulations of Chapter 5. Mesh is presented in Figure 5-23.

6.4.2.3 Initial and boundary conditions

The following initial conditions for the displacement field, \mathbf{u} , initial stress state and suction are used in all the model, for the three simulated tests:

- $\mathbf{u} = 0$;
- $s_{20} = 89$ MPa;
- $s_{10} = 89$ MPa;
- $\sigma_{xx0} = 10^{-5}$ MPa;
- $\sigma_{yy0} = 10^{-5}$ MPa;
- $\sigma_{zz0} = 10^{-5}$ MPa.

Compression are positive. The initial stress state is isotropic. Initial mean stress is taken greater than zero to avoid numerical issues associated to zero stress.

The boundary conditions used in the simulations are:

- $u_y = 0$ on the top boundary ($y = 0.030$);
- $u_y = 0$ on the bottom boundary ($y = 0$);
- $u_x = 0$ on the left boundary ($x = 0$);
- $u_x = 0$ on the right boundary ($x = 0.030$).

s_2 is progressively decreased from 89 MPa to 0.1 MPa by step according to experimental results. The same boundary conditions as in the vapour equilibrium technique are applied (see Chapter 3). Gravity is not addressed in the simulation and gas pressure is taken equal to zero.

Two simulations are performed for the three swelling pressure tests. β_H is taken equal to $5 \times 10^5 \text{ kg}^{-1} \text{ Pa}^{-0.5}$ and $5 \times 10^6 \text{ kg}^{-1} \text{ Pa}^{-0.5}$. The first value is the one identified as the best fit with respect to FEM simulations of pellet hydration in 6.3.2, while the second value is a higher one accounting for the eventual underestimation of β_{Mm} discussed in 6.3.2.

6.4.2.4 Comparison of numerical and experimental results

Figure 6-44 presents the comparison between FEM results and experimental results for the 70/0 material. The lower value of β_H induces a slower increase of swelling pressure at the beginning of hydration. Following water hydration, increase of swelling pressure also is slower for the lower value of β_H . However, the two trends in the swelling pressure-suction plane are close (Figure 6-45). Compared to results at hydraulic equilibrium, results taking into account two different suction values are characterised by a delayed transition for the 70/0 material since s_1 reaches 3 MPa later following the s_2 decrease to 0.1 MPa (Figure 6-44). A comparable final swelling pressure is obtained.

Figure 6-46 presents the evolution of s_1 as a function of elapsed time in the simulation for hydraulic equilibrium, for $\beta_H = 5 \times 10^6 \text{ kg}^{-1} \text{ Pa}^{-0.5}$, and for $\beta_H = 5 \times 10^5 \text{ kg}^{-1} \text{ Pa}^{-0.5}$. It is highlighted that hydraulic equilibrium is reached at the end of each suction decrease step for $\beta_H = 5 \times 10^6 \text{ kg}^{-1} \text{ Pa}^{-0.5}$, while this latter is only reached for $s_2 = 0.1 \text{ MPa}$ after ~ 650 days for $\beta_H = 5 \times 10^5 \text{ kg}^{-1} \text{ Pa}^{-0.5}$ which explains for instance the late increase of swelling pressure following imposition of $s_2 = 0.1 \text{ MPa}$ for $\beta_H = 5 \times 10^5 \text{ kg}^{-1} \text{ Pa}^{-0.5}$.

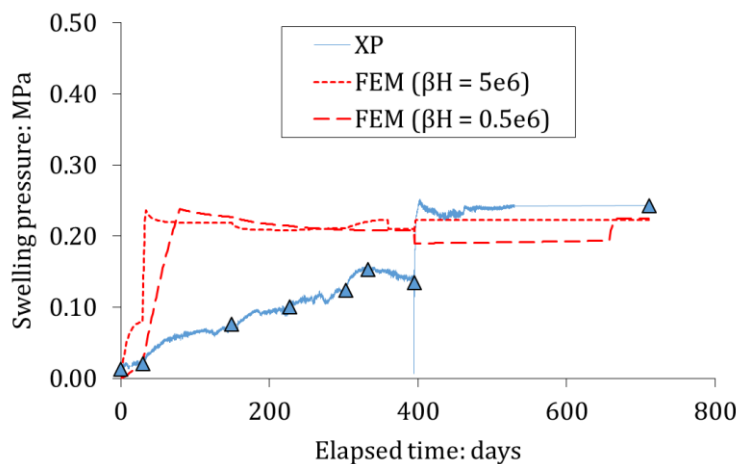


Figure 6-44: Comparison of FEM results and experimental results for the 70/0 material and two values of β_H .

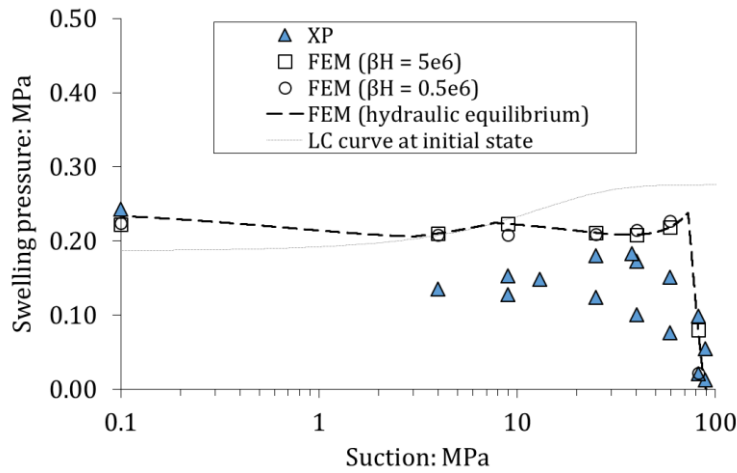


Figure 6-45: Comparison of FEM results and experimental results in the swelling pressure-suction (s_2) plane for $\beta_H = 5 \times 10^5 \text{ kg}^{-1} \text{ Pa}^{-0.5}$, $\beta_H = 5 \times 10^6 \text{ kg}^{-1} \text{ Pa}^{-0.5}$, and $\beta_H \rightarrow \infty$ for the 70/0 material.

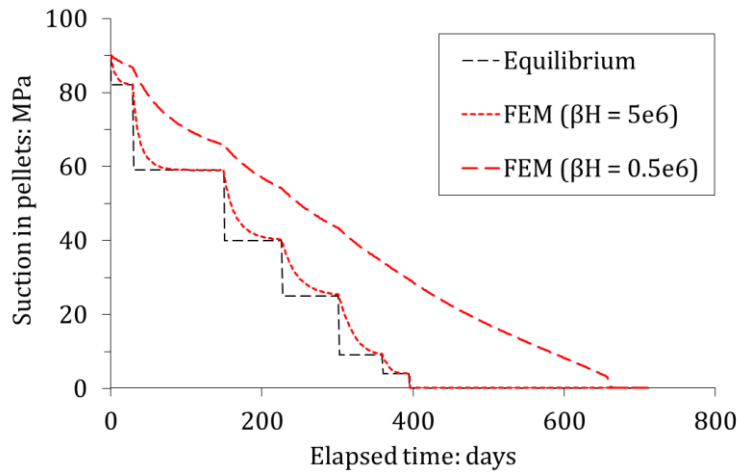


Figure 6-46: Evolution of pellet suction as a function of elapsed time in the simulation for $\beta_H = 5 \times 10^6 \text{ kg}^{-1} \text{ Pa}^{-0.5}$, $\beta_H = 5 \times 10^5 \text{ kg}^{-1} \text{ Pa}^{-0.5}$ and $\beta_H \rightarrow \infty$ for the 70/0 material.

Figure 6-47 presents the comparison between FEM results and experimental results for the 70/15 mixture. Both values of β_H provide satisfactory prediction of experimental results. At low suction however, the delay of pellet hydration associated to $\beta_H = 5 \times 10^6 \text{ kg}^{-1} \text{ Pa}^{-0.5}$ is overestimated. $\beta_H = 5 \times 10^6 \text{ kg}^{-1} \text{ Pa}^{-0.5}$ provides a reasonable prediction of the material behaviour with respect to elapsed time as s_2 is decreased from 4 MPa to 0.1 MPa for the 70/15 mixture. Figure 6-48 highlights that the swelling pressure suction relationship is satisfactorily reproduced by both values of β_H nevertheless. The main difference between results are obtained at low suction. It is related to the delay in the “granular”-“continuous” transition for $\beta_H = 5 \times 10^5 \text{ kg}^{-1} \text{ Pa}^{-0.5}$.

As for the 70/0 material, Figure 6-49 evidences that hydraulic equilibrium is reached at the end of each suction decrease step for $\beta_H = 5 \times 10^6 \text{ kg}^{-1} \text{ Pa}^{-0.5}$, while this latter is only reached for $s_2 = 0.1 \text{ MPa}$ after ~ 500 days for $\beta_H = 5 \times 10^5 \text{ kg}^{-1} \text{ Pa}^{-0.5}$. It is besides highlighted that reaching “granular”-“continuous” transition also induces hydraulic equilibrium.

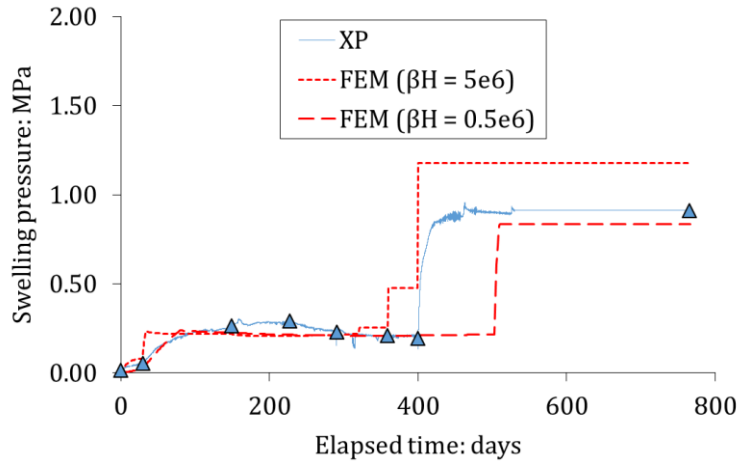


Figure 6-47: Comparison of FEM results and experimental results for the 70/15 material and two values of β_H .

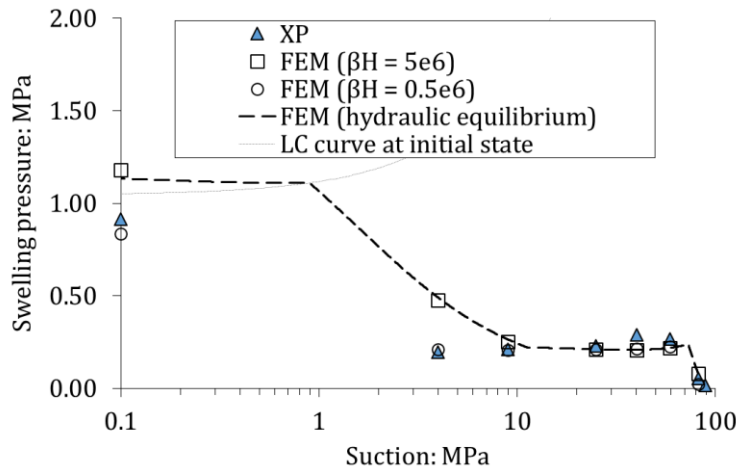


Figure 6-48: Comparison of FEM results and experimental results in the swelling pressure-suction (s_2) plane for $\beta_H = 5 \times 10^5 \text{ kg}^{-1} \text{ Pa}^{-0.5}$, $\beta_H = 5 \times 10^6 \text{ kg}^{-1} \text{ Pa}^{-0.5}$, and $\beta_H \rightarrow \infty$ for the 70/15 material.

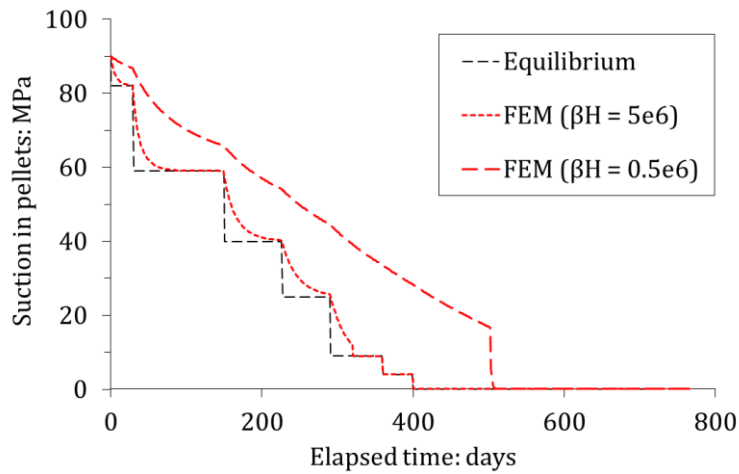


Figure 6-49: Evolution of pellet suction as a function of elapsed time in the simulation for $\beta_H = 5 \times 10^6 \text{ kg}^{-1} \text{ Pa}^{-0.5}$; $\beta_H = 5 \times 10^5 \text{ kg}^{-1} \text{ Pa}^{-0.5}$ and $\beta_H \rightarrow \infty$ for the 70/15 material.

Figure 6-50 presents the evolution of swelling pressure as a function of elapsed time for experiments and FEM simulations accounting for $\beta_H = 5 \times 10^6 \text{ kg}^{-1} \text{ Pa}^{-0.5}$ and $\beta_H = 5 \times 10^5 \text{ kg}^{-1} \text{ Pa}^{-0.5}$ for the 70/30 mixture. It is reminded that in this sample, the r_{vf} ratio at initial state is close to the threshold value. In this respect, most of the mixture hydration occurs in the continuous domain. In this case, Figure 6-50 highlights that the lower estimation of β_H (fitted with respect to results obtained on free-swelling pellet) provides low swelling pressure results compared to experimental results. Figure 6-51 besides highlight that the swelling pressure-suction relationship is better estimated using $\beta_H = 5 \times 10^6 \text{ kg}^{-1} \text{ Pa}^{-0.5}$ than $\beta_H = 5 \times 10^5 \text{ kg}^{-1} \text{ Pa}^{-0.5}$. Still, swelling pressure at $s_2 = 25 \text{ MPa}$ and $s_2 = 13 \text{ MPa}$ is slightly underestimated by the model. Compared to hydraulic equilibrium assumption, the swelling pressure accounting for hydration delay is lower until low suction values. Final values are very close for $\beta_H = 5 \times 10^6 \text{ kg}^{-1} \text{ Pa}^{-0.5}$ nevertheless. Figure 6-52 highlights that, as for 70/0 and 70/15 materials, hydraulic equilibrium is reached following the “granular”-“continuous” transition.

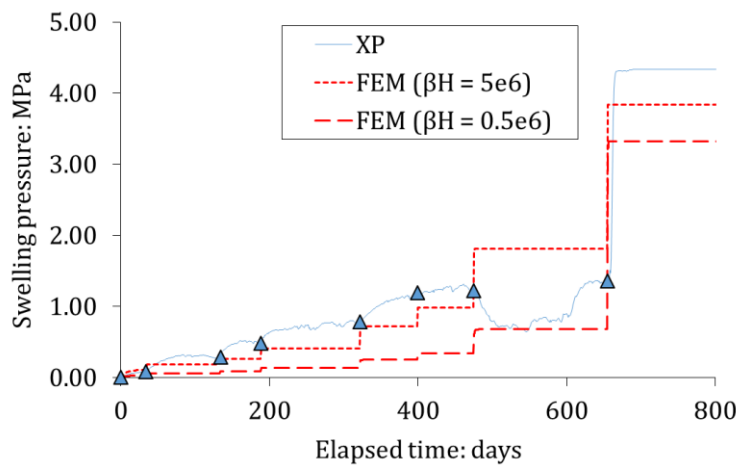


Figure 6-50: Comparison of FEM results and experimental results for the 70/30 material and two values of β_H .

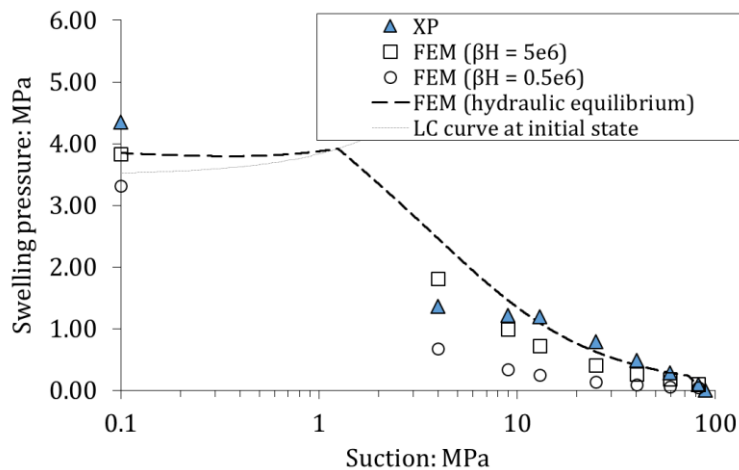


Figure 6-51: Comparison of FEM results and experimental results in the swelling pressure-suction (s_2) plane for $\beta_H = 5 \times 10^5 \text{ kg}^{-1} \text{ Pa}^{-0.5}$, $\beta_H = 5 \times 10^6 \text{ kg}^{-1} \text{ Pa}^{-0.5}$, and $\beta_H \rightarrow \infty$ for the 70/30 material.

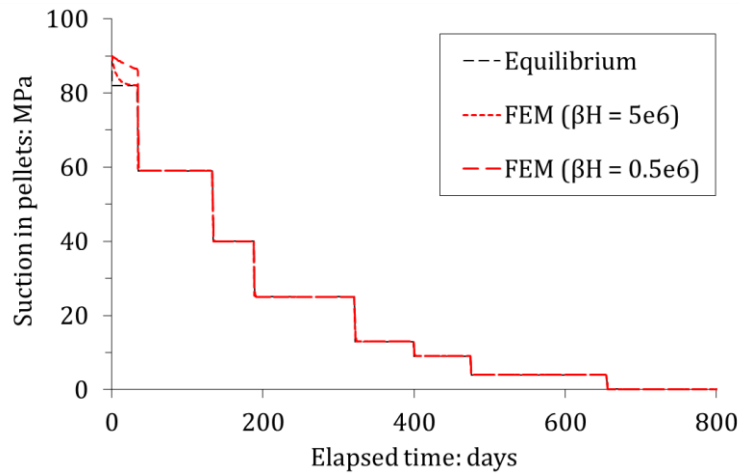


Figure 6-52: Evolution of pellet suction as a function of elapsed time in the simulation for $\beta_H = 5 \times 10^6 \text{ kg}^{-1} \text{ Pa}^{-0.5}$; $\beta_H = 5 \times 10^5 \text{ kg}^{-1} \text{ Pa}^{-0.5}$ and $\beta_H \rightarrow \infty$ for the 70/30 material.

Some differences between experimental results and FEM results arise when a hydration delay is accounted for in the simulations. These latter have however been shown not to be significant when considering $\beta_H = 5 \times 10^6 \text{ kg}^{-1} \text{ Pa}^{-0.5}$. Compared to the numerical study presented in 6.3.2, this value is higher than the initially proposed best fit. However, as previously discussed, this latter may be slightly underestimated. Still, Figure 6-39 evidences that the $\Delta m_I / \Delta t$ effective slope is not an order of magnitude higher than the proposed estimation ($\beta_H = 5 \times 10^5 \text{ kg}^{-1} \text{ Pa}^{-0.5}$). $\beta_H = 5 \times 10^6 \text{ kg}^{-1} \text{ Pa}^{-0.5}$ is still proposed because, as shown in the present numerical study, it does not induce significant differences for the low powder content and no powder samples (70/15 and 70/0 materials), whereas it provides better estimation for high powder content samples (70/30 material). Numerically, the better estimation for the 70/30 material is a consequence of a transition to continuous domain at higher mean stress.

It is reminded that the present approach aims at proposing a framework able to describe the mechanical behaviour of pellet-powder mixtures using the same parameters for all mixtures. In this respect, even if $\beta_H = 5 \times 10^6 \text{ kg}^{-1} \text{ Pa}^{-0.5}$ is likely to be higher than the real value, this latter allows a better overall prediction of experimental results for the three mixtures.

6.5 CONCLUSION AND PERSPECTIVES

6.5.1 Mock-up imbibition tests

The present Chapter presented the realisation of imbibition mock-up tests on three pellet-powder mixtures with exact same pellet mass and varying powder contents. Compared to traditional infiltration tests, the present test was performed using a square cuboid cell which allowed a glass face to be installed. Evolution of the material texture along with swelling pressure and relative humidity in macroporosity were determined in the course of imbibition. Hydration was performed using Bure site water under conditions in which the gradient of suction is considered to control the water intake.

Vapour transfer was identified as the dominant saturation process under these testing conditions. Slow hydration allowed the influence of granular structure of the mixture to be observed in low powder content sample and no powder sample.

6.5.2 Proposition of transfer laws

From experimental observations from the present study and literature, transfer laws were proposed to characterise liquid and vapour water fluxes within the matrix. Water exchanges between matrix and pellet phases are described using a simplified law proposed from experimental observations and FEM simulation of a pellet hydration. An apparent microstructural permeability coefficient is proposed to describe transfers within the microstructure and a traditional approach, considering density dependency of the permeability, was adopted for macrostructure. An empirical law is proposed for the macrostructure permeability. It is proposed to describe the degree of saturation of the macropores using a van Genuchten-based model, considering that experimental observations suggest that macropores remain dry until a low suction.

Pellet-matrix transfer law is implemented in Bil and swelling pressure tests performed in Chapter 4 are simulated. The main approach of the present work, considering a single set of parameters to describe the behaviour of all the mixtures, leads to the choice of a transfer coefficient higher than that suggested from FEM simulations of a pellet. Nevertheless, even if some differences arise between experimental and numerical results, the overall evolution of swelling pressure as a function of both elapsed time and suction is satisfactorily reproduced by this simple approach, for all mixtures, using a single set of parameters.

6.5.3 Large scale modelling

It is proposed from these results that the present approach is suitable to describe the behaviour of pellet-powder mixtures, taking into account the granular nature of the material and eventual heterogeneities of density in the material.

The main perspective arising from the study presented in Chapter 6 is the realisation of coupled simulations accounting for water transfer within the matrix. Laws proposed to describe these features are commonly used to describe water transfer in porous materials. Their calibration can be performed against the mock-up imbibition tests presented in Chapter 6.

Then, predictive simulations at the structure scale, over long hydration time, representative of repository conditions, can be performed using the proposed approach.

7 GENERAL CONCLUSION

In this final Chapter, an overview of the context is first reminded. Then, a summary of the conclusions of each Chapter of the present work is presented. Finally, perspectives for future work on this subject are proposed.

7.1 OVERVIEW OF THE CONTEXT

In radioactive waste disposal concepts, compacted bentonite-based materials are candidate materials for the engineered barriers. These materials are characterised by a low permeability, good radionuclide retention capacity, and high swelling potential. These properties would allow the engineered barrier to prevent polluted fluid migration in the repository, fill the technological voids upon hydration and subsequent swelling, then apply a swelling pressure against the gallery walls and contribute to the sealing of fractures in the excavation damaged zone.

In this framework, bentonite pellet-powder mixtures have been envisaged owing to operational convenience and reduction of technological voids. Mixtures are laid in a dry state as a granular assembly and progressively homogenise upon hydration, resulting of water flow from the host rock. Before homogenisation, the granular structure of the material controls its mechanical behaviour. Following homogenisation, mixtures behave as traditional compacted blocs.

Challenges exist in the characterisation of the hydromechanical behaviour of pellet-powder-based engineered barriers in the course of hydration. Before homogenisation, large inter-pellet voids and loose powder phase can leave this latter in free-swelling conditions while the pellet assembly is in constant-volume conditions. In addition, local heterogeneities can arise during installation, inducing variation in the powder content in inter-pellet voids in the buffer. In this respect, the present work has focused on the proposition of a model able to address these features.

7.2 CONTRIBUTIONS OF THE PRESENT WORK

7.2.1 Overview of the thesis

The present work aimed at characterising the behaviour of pellet-powder mixtures, accounting for the initial granular structure, eventual heterogeneities of density, and transition toward a continuous state. The first two Chapters of the thesis respectively consisted in a general introduction and a literature review. This latter mainly focused on the hydromechanical behaviour of bentonite materials, with highlights regarding granular materials. Fundamental aspects of the material behaviour as well as missing information in the literature were identified, allowing an experimental and numerical program to be proposed to address the problematic of the present work. An experimental characterisation of the material was carried out at the pellet scale, REV scale and mock-up scale. A numerical study using both DEM and FEM was performed to study and model the material behaviour from initial dry state to final saturated state.

Chapter 3 presented suction-controlled swelling pressure tests performed in the laboratory on pellet-powder mixtures with the same pellet mass and different powder contents. It was evidenced that the

pellet assembly can control the mechanical response of the mixture at high suction. The macroscopic response of loose powder samples was not significantly different from no powder samples at suction higher than 4 MPa. Liquid water hydration was performed from 4 MPa to reach full saturation. The transition to an apparent “continuous material” behaviour appeared related to the density of the powder phase and suction. Eventual occurrence of peak swelling pressure was highlighted to be related to either the pellet strength in the granular domain or the rearrangement of the material fabric in the continuous domain. Both phenomena could be observed in the course of hydration for a pellet assembly. Recommendations regarding the testing procedure of pellet materials were formulated. In particular, it was suggested that initial pressure following the cell closure can affect the material response and that fast wetting using liquid water at the REV scale would not allow the influence of the granular structure to be observed.

Chapter 4 presented a DEM modelling framework suitable to describe pellet assemblies. From pellet-scale experimental characterisation in the laboratory, a simple model describing the behaviour of a pellet was proposed and implemented in a DEM code. In DEM, the behaviour of each particle is described by the model for a pellet. Interactions at contacts between particles are described by the Hertz law and Coulomb friction. Swelling pressure tests were simulated using DEM. The material behaviour was satisfactorily reproduced. Results highlighted that the swelling pressure develops in two phases: an elastic increase of contact forces, followed by a plateau or decrease of swelling pressure as contact forces reach the elastic limit. Pellet stiffness and strength were identified as the parameters controlling the swelling pressure evolution. Using DEM, it was highlighted that the isochoric cell used in swelling pressure tests was not a true REV. Results suggested that the material behaviour is influenced by the wall as a result of the small size of the cell. In addition, the variability resulting from the ratio of sensor diameter to pellet diameter was quantified and found to be significant for low ratios. It was suggested from these results that the intrinsic behaviour of pellet assemblies can be addressed by DEM simulations of large samples with no influence of the wall.

Chapter 5 presented the development, implementation and validation against experimental results of a conceptual modelling framework suitable to describe the mechanical behaviour of pellet-powder mixtures upon hydration. It was proposed to consider two distinct domains. The material was considered either “granular” and controlled by the pellet assembly, or “continuous” and considered to behave as traditional compacted blocs. Constitutive laws describing the material behaviour in the granular domain were proposed from results of DEM simulations of large, periodic, pellet assemblies of 4000 particles. Transition to continuous state was described in terms of pellet suction and solid fraction of the powder phase. The material behaviour in the continuous domain was described in the framework of the BBM, modified to account for two levels of structure. Following the model implementation in Bil, swelling pressure tests performed in the laboratory were simulated using a single set of parameters for the three tested mixtures. Although the material behaviour is simplified in the proposed conceptual framework, the model was able to reproduce the main features of the material response observed in the laboratory. The swelling pressure evolution as a function of decreasing suction is satisfactorily reproduced for the three simulated mixtures.

Chapter 6 presented mock-up imbibition tests performed on the same three pellet-powder mixtures as described in Chapter 3. The cells were square-cuboids to allow the insertion of a glass face, which in turn allowed pictures to be taken at regular time intervals. Relative humidity and swelling pressure were measured at different elevations. Test results suggested that vapour transfer is the dominant process in the saturation of the material in the test conditions. The initial granular structure influence on the material response was highlighted in no powder and loose powder phase samples. In the loose powder phase sample, the transition from a pellet assembly controlled response to a response influenced by the powder phase was identified. The influence of initial granular structure was not observed on the dense powder phase sample. Inlet water fluxes were identical for all samples, suggesting that imbibition is controlled by an apparent coefficient of permeability independent on dry density, likely to be related to

microporosity. From experimental results and FEM simulations of a pellet hydration, a transfer law describing water exchanges between pellets and macropores was proposed. This latter was implemented in Bil and swelling pressure tests performed in the laboratory were simulated accounting for micro-macro water exchanges. Evolution of swelling pressure as a function of both elapsed time and decreasing suction was satisfactorily reproduced.

7.2.2 Limitations of the proposed model

The model proposed and implemented in the FEM code Bil was able to reproduce the main features of the material response. However, some hypotheses and simplifications have been made in the description of the mechanical behaviour.

In the granular domain, a constant value of the f_e parameter, relating dimensionless pressure parameter m_g to the total volumetric strain ε_v , was considered constant for simplicity. This assumption may induce an overestimation of the apparent stiffness of the granular assembly at low solid fraction and an underestimation at high solid fraction. A constant value of the f_{Mm} parameter, relating pellet volumetric strain ε_{vI} to ε_v , was considered regardless of the m_g value, which may progressively overestimate ε_v as contact forces reach plasticity.

In the continuous domain, the model is based on the BBM modified to consider different levels of porosity. Features often considered in the literature such as plastic macrostructural strains resulting of elastic microstructural strains are not taken into account. Irreversibility can only arise upon reaching the LC yield surface.

Transition from granular to continuous domain was assumed to be related to suction and relative solid fraction of the pellet and powder phases. Because of lack of available data, two distinct domains were considered, whereas the actual transition is likely to be a progressive mechanism.

In spite of these assumptions, the model was able to satisfactorily reproduce the macroscopic response of the material under constant-volume hydration or oedometer loading. Under complicated stress paths, for instance wetting-drying cycles, the model is likely to be too simplified.

7.3 PERSPECTIVES FOR FUTURE WORK

7.3.1 Large-scale modelling

In the present work, transfer laws have been proposed to describe water transfer within the matrix. These latter are based on free water flux (Darcy's law), vapour diffusion (Fick's law), and van Genuchten water retention model, traditionally used to describe water transfer in porous continua. An empirical permeability law for the matrix was proposed from experimental results in the literature. These laws have been implemented in Bil. Performing FEM simulations of mixture hydration at scales larger than the REV is thus an interesting and direct perspective of the present work.

Transfer parameters can be determined from simulations of the three mock-up tests, performed on three different pellet-powder mixtures. Predictive simulations at the structure scale using the model and accounting for hydromechanical couplings could then be performed.

7.3.2 Macrostructural swelling dependency on the dry density

Experimental results in the literature highlight that the swelling potential of bentonite materials increases with increasing dry density. In the present work, the ratio e_m/e was used to allow κ_s to increase/decrease depending on the material dry density while avoiding the introduction of an additional parameter. Still, this assumption is not directly supported by an experimental characterisation.

Few experimental data are available in the literature regarding the influence of dry density on the swelling behaviour of compacted bentonite. Characterisation of the volumetric strain-suction relationship upon hydration at different dry density, under free-swelling and under constant stress, would provide valuable information.

7.3.3 Water retention behaviour and water transfer

Results of mock-up imbibition tests suggested that water preferentially go through microporosity under conditions where gradient of suction is the main transfer mechanism. The dominant transfer mechanism at the cell scale was considered to be vapour diffusion. Free liquid water was considered to remain at low elevation while all relative humidity sensors measured 100% *RH* in all macroporosity. Dry macropores could be observed on the sample containing no powder (*i.e.* characterised by the lowest dry density and *a priori* the highest intrinsic permeability) after 1.5 year of imbibition. Consistently, SEM observations from Sun et al. (2019) suggest that bentonite macroporosity can remain dry until low suction. Experimental results concerning the saturated permeability in the literature evidence that this latter is dependent on the dry density, thus related to macroporosity.

The dominance of either vapour diffusion or liquid flux is likely to depend on the material saturation state and importance of macroporosity. The characterisation of the dominant transfer mechanism can provide valuable information in the calibration of transfer laws. Still, only qualitative information are available from the imbibition test performed. An interesting perspective is the use of magnetic resonance imaging experiments to determine with better accuracy the evolution of adsorbed and free water profiles in the samples. This method was successfully used on wood imbibition by Zhou et al. (2018). Associated to measurement such as total volume of water entering the sample and *RH* profile, it could provide valuable information on the saturation of compacted bentonite materials at large scale.

7.3.4 Characterisation of the state transition

Experimental results highlighted that the mechanical behaviour of samples containing no powder or a loose powder phase in inter-pellet voids is controlled by the pellet assembly at high suction. In samples containing a dense powder phase, this phenomenon was not observed.

It was considered that pellet-powder mixtures are binary granular mixtures. In this respect, the concept of dominant phase can define a proportion of fine particles at which these latter start influencing the mechanical behaviour of the mixture. For the mixture studied in the present work, this proportion was found to be slightly higher than 0.30. However, compared to traditional binary granular mixtures, for instance sand-silt mixtures, particles in pellet-powder mixtures are allowed to swell in a constant total volume. Transition from a behaviour controlled by the assembly of large particles to a behaviour influenced by small particles therefore occurs at relative proportions close to initial state. Additional criteria were thus necessary to describe the transition.

For simplicity, it was assumed in the proposition of the model that the material is either granular or continuous. Indeed, the material behaviour is more complicated. DEM simulations of binary granular mixtures suggested that influence of small particles on the macroscopic response progressively increases with increasing value of r_{vf} . However, the particle ratio in the simulations (1/6) was not really representative of the pellet-powder mixture. Transition was described by $r_{vf} = 1$, corresponding to small particle assembly having the same solid fraction as large particle assembly. In addition, literature review highlighted that a change in water retention behaviour associated to a significant fabric rearrangement occurs at low suction in bentonite materials. It is considered that following fabric rearrangement at low suction, initial granular structure would no longer influence the material macroscopic behaviour. A second suction criterion was thus introduced.

The proper characterisation of the transition from granular to continuous state constitutes an interesting perspective of the present work. The description of a smooth, progressive, transition from a state controlled by the pellet assembly toward the continuous state should be proposed. For this purpose, using DEM to study binary mixtures of pellet and powder with appropriate diameter ratio could provide interesting insight into their intrinsic behaviour. Experimental tests simultaneously performed on compacted blocks, mixtures of same average densities as the compacted blocks, and pellet assemblies with no powder could also provide valuable information. To this end, traditional experiments such as vapour hydration under constant stress, loading at constant suction or swelling pressure tests could be performed.

LIST OF REFERENCES

- AFNOR. (2000). NF P 94-059. Détermination des masses volumiques minimale et maximale des sols non cohérents, Reconnaissance et essais.
- Agnolin, I., & Roux, J. N. (2007a). Internal states of model isotropic granular packings. I. Assembling process, geometry, and contact networks. *Physical Review E - Statistical, Nonlinear, and Soft Matter Physics*, 76(6), 1–27. <https://doi.org/10.1103/PhysRevE.76.061302>
- Agnolin, I., & Roux, J. N. (2007b). Internal states of model isotropic granular packings. III. Elastic properties, 76(6), 1–22. <https://doi.org/10.1103/PhysRevE.76.061304>
- Agus, S. S., & Schanz, T. (2005). Effect of Shrinking and Swelling on Microstructures and Fabric of a Compacted Bentonite-Sand Mixture. *Proceedings of International Conference on Problematic Soils*, 25-27 May 2005, Eastern Mediterranean University, Famagusta, N. Cyprus.
- Agus, S. S., Arifin, Y. F., Tripathy, S., & Schanz, T. (2013). Swelling pressure-suction relationship of heavily compacted bentonite-sand mixtures. *Acta Geotechnica*, 8(2), 155–165. <https://doi.org/10.1007/s11440-012-0189-0>
- Aitchison, G. D., Russam, K., & Richards, B. G. (1965). Engineering concepts of moisture equilibria and moisture changes in soils. *Road Research Laboratory Report*, 38.
- Al-Mukhtar, M., Qi, Y., Alcover, J.-F., & Bergaya, F. (1999). Oedometric and water-retention behaviour of highly compacted unsaturated smectites. *Canadian Geotechnical Journal*, 36(4), 675–684. <https://doi.org/10.1139/t99-035>
- Alonso, E. E., Gens, A., & Josa, A. (1990). A constitutive model for partially saturated soils G”. *Géotechnique*, 40(3), 405–430. <https://doi.org/10.1680/geot.1990.40.3.405>
- Alonso, E. E., Hoffmann, C., & Romero, E. (2010). Pellet mixtures in isolation barriers. *Journal of Rock Mechanics and Geotechnical Engineering*, 2(1), 12–31. <https://doi.org/10.3724/SP.J.1235.2010.00012>
- Alonso, E. E., Pereira, J.-M., Vaunat, J., & Olivella, S. (2010). A microstructurally based effective stress for unsaturated soils. *Géotechnique*, 60(12), 913–925. <https://doi.org/10.1680/geot.8.P.002>
- Alonso, E. E., Romero, E., & Hoffmann, C. (2011). Hydromechanical behaviour of compacted granular expansive mixtures: experimental and constitutive study. *Géotechnique*, 61(4), 329–344. <https://doi.org/10.1680/geot.2011.61.4.329>
- Alonso, E. E., Romero, E., Hoffmann, C., & García-Escudero, E. (2005). Expansive bentonite-sand mixtures in cyclic controlled-suction drying and wetting. *Engineering Geology*, 81(3), 213–226. <https://doi.org/10.1016/j.enggeo.2005.06.009>
- Alonso, E. E., Vaunat, J., & Gens, A. (1999). Modelling the mechanical behaviour of expansive clays. *Engineering Geology*, 54(1–2), 173–183. [https://doi.org/10.1016/S0013-7952\(99\)00079-4](https://doi.org/10.1016/S0013-7952(99)00079-4)
- Andra (2005). Evaluation of the feasibility of a geological repository in an argillaceous formation. Andra, Chatenay-Malabry, France, 2005.
-

List of References

- Baille, W., Tripathy, S., & Schanz, T. (2010). Swelling pressures and one-dimensional compressibility behaviour of bentonite at large pressures. *Applied Clay Science*, 48(3), 324–333. <https://doi.org/10.1016/j.clay.2010.01.002>
- Baker, R., & Frydman, S. (2009). Unsaturated soil mechanics. Critical review of physical foundations. *Engineering Geology*, 106(1–2), 26–39. <https://doi.org/10.1016/j.enggeo.2009.02.010>
- Basma, A. A., Al-Homoud, A. S., & Husein, A. (1995). Laboratory assessment of swelling pressure of expansive soils. *Applied Clay Science*, 9(5), 355–368. [https://doi.org/10.1016/0169-1317\(94\)00032-L](https://doi.org/10.1016/0169-1317(94)00032-L)
- Bennethum, L. S., Murad, M. A., & Cushman, J. H. (1997). Modified Darcy's law, Terzaghi's effective stress principle and Fick's law for swelling clay soils. *Computers and Geotechnics*, 20(3–4), 245–266. [https://doi.org/10.1016/S0266-352X\(97\)00005-0](https://doi.org/10.1016/S0266-352X(97)00005-0)
- Bian, X., Cui, Y., & Li, X. (2016). Voids effect on the swelling behaviour of compacted bentonite. <https://doi.org/10.1680/jgeot.17.P.283>
- Bishop, A. W. (1959). The principle of effective stress. *Teknisk ukeblad*, 39, 859–863.
- Blatz, J. A., Cui, Y. J., & Oldecop, L. (2008). Vapour equilibrium and osmotic technique for suction control. In *Laboratory and Field Testing of Unsaturated Soils* (pp. 49–61). Springer, Dordrecht.
- Blatz, J. A., Graham, J., & Chandler, N. A. (2002). Influence of suction on the strength and stiffness of compacted sand–bentonite. *Canadian Geotechnical Journal*, 39(5), 1005–1015. <https://doi.org/10.1139/t02-056>
- Bolton, M. D., Nakata, Y., & Cheng, Y. P. (2008). Micro- and macro-mechanical behaviour of DEM crushable materials. *Géotechnique*, 58(6), 471–480. <https://doi.org/10.1680/geot.2008.58.6.471>
- Börgesson, L., Karnland, O., & Johannesson, L. E. (1996). Modelling of the physical behaviour of clay barriers close to water saturation. *Engineering Geology*, 41(1–4 SPEC. ISS.), 127–144.
- Bourg, I. C., Bourg, A. C. M., & Sposito, G. (2003). Modeling diffusion and adsorption in compacted bentonite: A critical review. *Journal of Contaminant Hydrology*, 61(1–4), 293–302. [https://doi.org/10.1016/S0169-7722\(02\)00128-6](https://doi.org/10.1016/S0169-7722(02)00128-6)
- Carrier, B., Vandamme, M., Pellenq, R. J. M., Bornert, M., Ferrage, E., Hubert, F., & Van Damme, H. (2016). Effect of Water on Elastic and Creep Properties of Self-Standing Clay Films. *Langmuir*, 32(5), 1370–1379. <https://doi.org/10.1021/acs.langmuir.5b03431>
- Castellanos, E., Gens, A., Lloret, A., & Romero, E. (2006). Influence of water chemistry on the swelling capacity of a high-density bentonite. *Unsaturated Soils 2006*, 962–972.
- Castellanos, E., Villar, M. V., Romero, E., Lloret, A., & Gens, A. (2008). Chemical impact on the hydro-mechanical behaviour of high-density FEBEX bentonite. *Physics and Chemistry of the Earth*, 33(SUPPL. 1), 516–526. <https://doi.org/10.1016/j.pce.2008.10.056>
- Cheng, Y. P., Bolton, M. D., & Nakata, Y. (2004). Crushing and plastic deformation of soils simulated using DEM. *Géotechnique*, 54(2), 131–141. <https://doi.org/10.1680/geot.2004.54.2.131>
- Christoffersen, J., Mehrabadi, M. M., & Nemat-Nasser, S. (1981). A micromechanical description of granular material behavior. *Journal of applied mechanics*, 48(2), 339–344.
-

-
- Clark, G. L., Grim, R. E., & Bradley, W. F. (2014). A Study of the Behavior of Montmorillonite upon Wetting. *Zeitschrift Für Kristallographie - Crystalline Materials*, 97(1–6), 216–222. <https://doi.org/10.1524/zkri.1937.97.1.216>
- Coussy, O., Pereira, J. M., & Vaunat, J. (2010). Revisiting the thermodynamics of hardening plasticity for unsaturated soils. *Computers and Geotechnics*, 37(1–2), 207–215. <https://doi.org/10.1016/j.compgeo.2009.09.003>
- Coussy, O. (1995). *Mechanics of porous continua* (Vol. 1016). Chichester: Wiley.
- Croney, D., Coleman, J. D., & Black, W. P. M. (1958). Movement and distribution of water in soil in relation to highway design and performance. *Water and Its Conduction in Soils*, Highway Res Board, Special Report, Washington, DC, (40), 226–252.
- Cui, Y. J. (2017). On the hydro-mechanical behaviour of MX80 bentonite-based materials. *Journal of Rock Mechanics and Geotechnical Engineering*, 9(3), 565–574. <https://doi.org/10.1016/j.jrmge.2016.09.003>
- Cui, Y. J., Tang, A. M., Loiseau, C., & Delage, P. (2008). Determining the unsaturated hydraulic conductivity of a compacted sand-bentonite mixture under constant-volume and free-swell conditions. *Physics and Chemistry of the Earth*, 33(SUPPL. 1), 462–471. <https://doi.org/10.1016/j.pce.2008.10.017>
- Cui, Y. J., Yahia-Aissa, M., & Delage, P. (2002). A model for the volume change behaviour of heavily compacted swelling clays. *Engineering Geology*, 64(2–3), 233–250. [https://doi.org/10.1016/S0013-7952\(01\)00113-2](https://doi.org/10.1016/S0013-7952(01)00113-2)
- Cui, Y., Loiseau, C., & Delage, P. (2002). Microstructure changes of a confined swelling soil due to suction controlled hydration. *Proc 3rd Int Conf on Unsaturated Soils UNSAT. 2002.*, 2002(2), 593–598.
- Cuisinier, O., & Laloui, L. (2004). Fabric evolution during hydromechanical loading of a compacted silt. *International Journal for Numerical and Analytical Methods in Geomechanics*, 28(6), 483–499. <https://doi.org/10.1002/nag.348>
- Cuisinier, O., & Masrouri, F. (2005). Hydromechanical behaviour of a compacted swelling soil over a wide suction range. *Engineering Geology*, 81(3), 204–212. <https://doi.org/10.1016/j.enggeo.2005.06.008>
- Cundall, P., & Strack, O. (1979). A discrete numerical model for granular assemblies. *Géotechnique*, 29(1), 47–65.
- Davy, C. A., Skoczylas, F., Barnichon, J. D., & Lebon, P. (2007). Permeability of macro-cracked argillite under confinement: gas and water testing. *Physics and Chemistry of the Earth, Parts A/B/C*, 32(8-14), 667-680.
- De Larrard, F. (2014). *Concrete mixture proportioning: a scientific approach*. CRC Press.
- Delage, P., & Cui, Y. (2000). L'eau dans les sols non saturés. *Techniques de L'ingénieur. Construction*, C301.1-C320.20.
- Delage, P., & Cui, Y. J. (2008). An evaluation of the osmotic method of controlling suction. *Geomechanics and Geoengineering*, 3(1), 1–11. <https://doi.org/10.1080/17486020701868379>
-

List of References

- Delage, P., & Lefebvre, G. (1984). Study of the structure of a sensitive clay and of its evolution during consolidation. *Canadian Geotechnical Journal*, 21, 21–35.
- Delage, P., & Pellerin, F. M. (1984). Influence de la lyophilisation sur la structure d'une argile sensible du Québec. *Clay Minerals*, 19, 151–160.
- Delage, P., Audiguier, M., Cui, Y. J., & Howat, M. D. (1996). Microstructure of a compacted silt. *Canadian Geotechnical Journal*, 33, 150–158.
- Delage, P., Howat, M. D., & Cui, Y. J. (1998). The relationship between suction and swelling properties in a heavily compacted unsaturated clay. *Engineering Geology*, 50(1–2), 31–48. [https://doi.org/10.1016/S0013-7952\(97\)00083-5](https://doi.org/10.1016/S0013-7952(97)00083-5)
- Delage, P., Marcial, D., Ruiz, X., & Cui, Y. J. (2006). Ageing effects in a compacted bentonite: a microstructure approach. *Géotechnique*, 56(5), 291–304. <https://doi.org/10.1680/geot.2006.56.5.291>
- Delage, P., Romero, E., & Tarantino, A. (2008). Recent developments in the techniques of controlling and measuring suction in unsaturated soils. *Unsaturated Soils: Advances in Geo-Engineering - Proceedings of the 1st European Conference on Unsaturated Soils, E-UNSAT 2008*, 33–52.
- Della Vecchia, G., Dieudonné, A. C., Jommi, C., & Charlier, R. (2015). Accounting for evolving pore size distribution in water retention models for compacted clays. *International Journal for Numerical and Analytical Methods in Geomechanics*, 39, 702–723. <https://doi.org/10.1002/nag.2326>
- Dieudonne, A. C., Della Vecchia, G., & Charlier, R. (2017). Water retention model for compacted bentonites. *Canadian Geotechnical Journal*, 54(7), 915–925. <https://doi.org/10.1139/cgj-2016-0297>
- Dieudonné, A. C. (2016). Hydromechanical behaviour of compacted bentonite: from micro-scale analysis to macro-scale modelling. PhD thesis, Université de Liège, Belgium.
- Dixon, D. A. (1996). Swelling and hydraulic properties of bentonites from Japan, Canada and the USA. In *Proceedings of the Second International Congress on Environmental Geotechnics (IS-Osaka)*, 1996 (Vol. 1, pp. 43-48).
- Dixon, D. A., Graham, J., & Gray, M. N. (1999). Hydraulic conductivity of clays in confined tests under low hydraulic gradients. *Canadian Geotechnical Journal*, 36(5), 815–825. <https://doi.org/10.1139/t99-057>
- Fleureau, J. M., Kheirbek-Saoud, S., Soemitro, R., & Taibi, S. (1993). Behavior of clayey soils on drying-wetting paths. *Canadian Geotechnical Journal*, 30(2), 287–296. <https://doi.org/10.1139/t93-024>
- Fredlund, D. G., & Morgenstern, N. R. (1977). Stress state variables for unsaturated soils. *Journal of Geotechnical and Geoenvironmental Engineering*, 103(ASCE 12919).
- García-Gutiérrez, M., Mingarro, M., Missana, T., Martín, P. L., Sedano, L. A., & Cormenzana, J. L. (2004). Diffusion experiments with compacted powder/pellets clay mixtures. *Applied Clay Science*, 26(1–4 SPEC. ISS.), 57–64. <https://doi.org/10.1016/j.clay.2003.09.014>
-

-
- García-Sineriz, J. L., Villar, M. V., Rey, M., & Palacios, B. (2015). Engineered barrier of bentonite pellets and compacted blocks: State after reaching saturation. *Engineering Geology*, 192, 33–45. <https://doi.org/10.1016/j.enggeo.2015.04.002>
- Gatabin, C., Talandier, J., Collin, F., Charlier, R., & Dieudonné, A. C. (2016). Competing effects of volume change and water uptake on the water retention behaviour of a compacted MX-80 bentonite/sand mixture. *Applied Clay Science*, 121–122, 57–62. <https://doi.org/10.1016/j.clay.2015.12.019>
- Gens, A. (2010). Soil–environment interactions in geotechnical engineering. *Géotechnique*, 60(1), 3–74. <https://doi.org/10.1680/geot.9.P.109>
- Gens, A., & Alonso, E. E. (1992). A framework for the behaviour of unsaturated expansive clays. *Canadian Geotechnical Journal*, 29, 1013–1032.
- Gens, A., Valleján, B., Sánchez, M., Imbert, C., Villar, M. V., & Van Geet, M. (2011). Hydromechanical behaviour of a heterogeneous compacted soil: experimental observations and modelling. *Géotechnique*, 61(5), 367–386. <https://doi.org/10.1680/geot.SIP11.P.015>
- Gens, A., Valleján, B., Zandarín, M. T., & Sánchez, M. (2013). Homogenization in clay barriers and seals: Two case studies. *Journal of Rock Mechanics and Geotechnical Engineering*, 5(3), 191–199. <https://doi.org/10.1016/j.jrmge.2013.04.003>
- Gouy, M. (1910). Sur la constitution de la charge électrique à la surface d'un électrolyte. *Journal de Physique Théorique et Appliquée*, 9(1), 457–468. <https://doi.org/10.1051/jphystap:019100090045700>
- Hendricks, S. B., Nelson, R. A., & Alexander, L. T. (1940). Hydration Mechanism of the Clay Mineral Montmorillonite Saturated with Various Cations. *Journal of the American Chemical Society*, 62(6), 1457–1464. <https://doi.org/10.1021/ja01863a037>
- Hoffmann, C., Alonso, E. E., & Romero, E. (2007). Hydro-mechanical behaviour of bentonite pellet mixtures. *Physics and Chemistry of the Earth*, 32(8–14), 832–849. <https://doi.org/10.1016/j.pce.2006.04.037>
- Imbert, C., & Villar, M. V. (2006). Hydro-mechanical response of a bentonite pellets/powder mixture upon infiltration. *Applied Clay Science*, 32(3–4), 197–209. <https://doi.org/10.1016/j.clay.2006.01.005>
- Imbert, C., Billaud, P., Touzé, G. & Dang, K. D. (2004). Acquisition des paramètres de comportement hydraulique et hydromécanique de base de l'argile MX80 à l'état saturé. Technical report, Commissariat à l'Énergie Atomique (CEA).
- Jacinto, A. C., Villar, M. V., & Ledesma, A. (2012). Influence of water density on the water-retention curve of expansive clays. *Géotechnique*, 62(8), 657–667. <https://doi.org/10.1680/geot.7.00127>
- Johnson, K. L. (1985). *Contact Mechanics*. Cambridge, UK: Cambridge University Press.
- Jommi, C. (2000). Remarks on the constitutive modelling of unsaturated soils. *Experimental Evidence and Theoretical Approaches in Unsaturated Soils*, (1968), 139–153.
-

List of References

- Karnland, O., Nilsson, U., Weber, H., & Wersin, P. (2008). Sealing ability of Wyoming bentonite pellets foreseen as buffer material - Laboratory results. *Physics and Chemistry of the Earth*, 33(SUPPL. 1), 472–475. <https://doi.org/10.1016/j.pce.2008.10.024>
- Karnland, O., Olsson, S., & Nilsson, U. (2006). Mineralogy and sealing properties of various bentonites and smectite-rich clay materials. SKB Technical Report, (06–30). Retrieved from <http://www.skb.se/publication/1419144/TR-06-30.pdf>
- Kaufhold, S., Baille, W., Schanz, T., & Dohrmann, R. (2015). About differences of swelling pressure - dry density relations of compacted bentonites. *Applied Clay Science*, 107, 52–61. <https://doi.org/10.1016/j.clay.2015.02.002>
- Keller, L. M., Seiphoori, A., Gasser, P., Lucas, F., Holzer, L., & Ferrari, A. (2014). The pore structure of compacted and partly saturated MX-80 bentonite at different dry densities. *Clays and Clay Minerals*, 62(3), 174–187. <https://doi.org/10.1346/CCMN.2014.0620302>
- Khalili, N., Geiser, F., & Blight, G. (2004). Effective Stress in Unsaturated Soils: Review with New Evidence. *International Journal of Geomechanics*, 4(2), 115–126. [https://doi.org/doi:10.1061/\(ASCE\)1532-3641\(2004\)4:2\(115\)](https://doi.org/doi:10.1061/(ASCE)1532-3641(2004)4:2(115))
- Komine, H. (2004). Simplified evaluation on hydraulic conductivities of sand-bentonite mixture backfill. *Applied Clay Science*, 26(1–4 SPEC. ISS.), 13–19. <https://doi.org/10.1016/j.clay.2003.09.006>
- Komine, H. (2008). Theoretical equations on hydraulic conductivities of bentonite-based buffer and backfill for underground disposal of radioactive wastes. *Journal of Geotechnical and Geoenvironmental Engineering*, 134(4), 497–508. [https://doi.org/10.1061/\(ASCE\)1090-0241\(2008\)134:4\(497\)](https://doi.org/10.1061/(ASCE)1090-0241(2008)134:4(497))
- Komine, H. (2010). Predicting hydraulic conductivity of sand-bentonite mixture backfill before and after swelling deformation for underground disposal of radioactive wastes. *Engineering Geology*, 114(3–4), 123–134. <https://doi.org/10.1016/j.enggeo.2010.04.009>
- Komine, H., & Ogata, N. (2003). New equations for swelling characteristics of bentonite-based buffer materials. *Canadian Geotechnical Journal*, 40(2), 460–475. <https://doi.org/10.1139/t02-115>
- Kröhn, K. P. (2004). Modelling the re-saturation of bentonite in final repositories in crystalline rock. Final report.
- Kröhn, K. P. (2005). New evidence for the dominance of vapour diffusion during the re-saturation of compacted bentonite. *Engineering Geology*, 82(2), 127–132. <https://doi.org/10.1016/j.enggeo.2005.09.015>
- Laloui, L., & Nuth, M. (2009). On the use of the generalised effective stress in the constitutive modelling of unsaturated soils. *Computers and Geotechnics*, 36(1–2), 20–23. <https://doi.org/10.1016/j.compgeo.2008.03.002>
- Langmuir, I. (1917). The constitution and fundamental properties of solids and liquids. *Journal of the American Chemical Society* 39, 1848–1906.
- Langmuir, I. (1938). The role of attractive and repulsive forces in the formation of tactoids, thixotropic gels, protein crystals and coacervates. *The Journal of Chemical Physics*, 6(12), 873–896. <https://doi.org/10.1063/1.1750183>
-

-
- Lawrence, G. P. (1978). Stability of soil pores during mercury intrusion porosimetry. *Journal of Soil Science*, 29(3), 299-304.
- Liu, H. H., Li, L., & Birkholzer, J. (2012). Unsaturated properties for non-Darcian water flow in clay. *Journal of Hydrology*, 430–431, 173–178. <https://doi.org/10.1016/j.jhydrol.2012.02.017>
- Liu, H., Zou, D., & Liu, J. (2008). Particle Shape Effect on Macro-and Micro Behaviours of Monodisperse Ellipsoids. *International Journal for Numerical and Analytical Methods in Geomechanics*, 32(March 2007), 189–213. <https://doi.org/10.1002/nag>
- Lloret, A., & Villar, M. V. (2007). Advances on the knowledge of the thermo-hydro-mechanical behaviour of heavily compacted “FEBEX” bentonite. *Physics and Chemistry of the Earth*, 32(8–14), 701–715. <https://doi.org/10.1016/j.pce.2006.03.002>
- Lloret, A., Villar, M. V., Sanchez, M., Gens, A., Pintado, X., & Alonso, E. (2003). Mechanical behaviour of heavily compacted bentonite under high suction changes. *Geotechnique*, 53(1), 27–40. <https://doi.org/10.1680/geot.53.1.27.37258>
- Low, P. F. (1979). Nature and properties of water in montmorillonite-water systems. *Soil Science Society of America Journal* 43, No. 4, 651–658.
- Madsen, F. T., & Müller-Vonmoos, M. (1989). The swelling behaviour of clays. *Applied Clay Science*, 4(2), 143–156. [https://doi.org/10.1016/0169-1317\(89\)90005-7](https://doi.org/10.1016/0169-1317(89)90005-7)
- Marcial, D. (2003). Comportement hydromécanique et microstructural des matériaux de barrière ouvragée, Doctoral dissertation, École nationale des ponts et chaussées (France).
- Masin, D., & Khalili, N. (2016). Swelling phenomena and effective stress in compacted expansive clays. *Canadian Geotechnical Journal*, 53, 134–147. <https://doi.org/10.1139/cgj-2014-0479>
- Massat, L., Cuisinier, O., Bihannic, I., Claret, F., Pelletier, M., Masrouri, F., & Gaboreau, S. (2016). Swelling pressure development and inter-aggregate porosity evolution upon hydration of a compacted swelling clay. *Applied Clay Science*, 124–125, 197–210. <https://doi.org/10.1016/j.clay.2016.01.002>
- Mayor, J. C., García-Siñeriz, J. L., Alonso, E., Alheid, H. J., & Blumbling, P. (2005). Engineered barrier emplacement experiment in Opalinus Clay for the disposal of radioactive waste in underground repositories (No. ENRESA--02/05). Empresa Nacional de Residuos.
- Meunier, A. (2005). *Clays*. Springer Science & Business Media.
- Mokni, N., Barnichon, J. D., Dick, P., & Nguyen, T. S. (2016). Effect of technological macro voids on the performance of compacted bentonite/sand seals for deep geological repositories. *International Journal of Rock Mechanics and Mining Sciences*, 88, 87–97. <https://doi.org/10.1016/j.ijrmms.2016.07.011>
- Mokni, N., Molinero-Guerra, A., Cui, Y.-J., Delage, P., Aïmediou, P., Bornert, M., & Tang, A. M. (2019). Modelling the long-term hydro-mechanical behaviour of a bentonite pellet/powder mixture with consideration of initial structural heterogeneities. *Géotechnique*, 1–61. <https://doi.org/10.1680/jgeot.18.p.110>
-

- Molinero-Guerra, A., Mokni, N., Delage, P., Cui, Y. J., Tang, A. M., Aïmedieu, P., Bernier, F., & Bornert, M. (2017). In-depth characterisation of a mixture composed of powder/pellets MX80 bentonite. *Applied Clay Science*, 135, 538–546. <https://doi.org/10.1016/j.clay.2016.10.030>
- Molinero-Guerra, A., Aïmedieu, P., Bornert, M., Cui, Y. J., Tang, A. M., Sun, Z., Mokni, N., Delage, P., & Bernier, F. (2018a). Analysis of the structural changes of a pellet/powder bentonite mixture upon wetting by X-ray computed microtomography. *Applied Clay Science*, 165(August), 164–169. <https://doi.org/10.1016/j.clay.2018.07.043>
- Molinero-Guerra, A., Cui, Y. J., Mokni, N., Delage, P., Bornert, M., Aïmedieu, P., Tang, A. M., & Bernier, F. (2018b). Investigation of the hydro-mechanical behaviour of a pellet/powder MX80 bentonite mixture using an infiltration column. *Engineering Geology*, 243(January), 18–25. <https://doi.org/10.1016/j.enggeo.2018.06.006>
- Molinero-Guerra, A., Delage, P., Cui, Y.-J., Mokni, N., Tang, A. M., Aïmedieu, P., Bernier, F., & Bornert, M. (2019a). Water retention properties and microstructure changes of a bentonite pellet upon wetting/drying; application to radioactive waste disposal. *Géotechnique*, 1–41. <https://doi.org/10.1680/jgeot.17.p.291>
- Molinero-Guerra, A., Cui, Y. J., He, Y., Delage, P., Mokni, N., Tang, A. M., Aïmedieu, P., Bornert, M., & Bernier, F. (2019b). Characterization of water retention, compressibility and swelling properties of a pellet/powder bentonite mixture. *Engineering Geology*, 248(April 2018), 14–21. <https://doi.org/10.1016/j.enggeo.2018.11.005>
- Montes-Hernandez, G., Duplay, J., Martinez, L., & Mendoza, C. (2003). Swelling-shrinkage kinetics of MX80 bentonite. *Applied Clay Science*, 22(6), 279–293. [https://doi.org/10.1016/S0169-1317\(03\)00120-0](https://doi.org/10.1016/S0169-1317(03)00120-0)
- Norrish, K. (1954). The swelling of montmorillonite. *Discussions of the Faraday Society*, 18, 120–134. <https://doi.org/10.1039/DF9541800120>
- Nowamooz, H., & Masrouri, F. (2008). Hydromechanical behaviour of an expansive bentonite/silt mixture in cyclic suction-controlled drying and wetting tests. *Engineering Geology*, 101(3–4), 154–164. <https://doi.org/10.1016/j.enggeo.2008.04.011>
- Nowamooz, H., & Masrouri, F. (2009). Density-dependent hydromechanical behaviour of a compacted expansive soil. *Engineering Geology*, 106(3–4), 105–115. <https://doi.org/10.1016/j.enggeo.2009.03.010>
- Nuth, M., & Laloui, L. (2008). Advances in modelling hysteretic water retention curve in deformable soils. *Computers and Geotechnics*, 35(6), 835–844. <https://doi.org/10.1016/j.compgeo.2008.08.001>
- O’Brien, F. E. M. (1948). The Control of Humidity by Saturated Salt Solutions. *Journal of Scientific Instruments*, 25(3), 73–76. <https://doi.org/10.1088/0950-7671/25/3/305>
- Olivella, S., & Gens, A. (2000). Vapour transport in low permeability unsaturated soils with capillary effects. *Transport in Porous Media*, 40(2), 219–241. <https://doi.org/10.1023/A:1006749505937>
- Palacios, B., Rey, M., Garcia-Siñeriz, J. L., Villar, M. V., Mayor, J. C., & Velasco, M. (2013). Engineered Barrier Emplacement Experiment in Opalinus Clay “EB” Experiment. As-built of dismantling operation. Long-term Performance of Engineered Barrier Systems PEBS. European Commission, 7th Euratom Framework Program for Nuclear Research and Training Activities (2007-2011). Report number: D2. 1, 4.
-

-
- Pereira, J. M., Wong, H., Dubujet, P., & Dangla, P. (2005). Adaptation of existing behaviour models to unsaturated states: Application to CJS model. *International Journal for Numerical and Analytical Methods in Geomechanics*, 29(11), 1127-1155.
- Philip, J. R., & de Vries, D. A. (1957). Moisture movements in porous materials under temperature gradients. *Transactions, American Geophysical Union*, 38(2), 222-232.
- Pusch, R. (1979). Highly Compacted Sodium Bentonite for Isolating Rock-Deposited Radioactive Waste Products. *Nuclear Technology*, 45(2), 153-157. doi:10.13182/nt79-a32305
- Pusch, R., & Yong, R. N. (2006). *Microstructure of smectite clays and engineering performance*. CRC Press.
- Push, R. (2001). *The Buffer and Backfill Handbook part 2: Materials and techniques (SKB Technica 1 Report TR-02-20)*. Sweden: Swedish Nuclear Fuel and Waste Management Co.
- Radjai, F. & Dubois, F. (2011). *Discrete-element modeling of granular materials*. Wiley-ISTE, ISBN 978-1-84821-260-2.
- Richards, L. A. (1941). A pressure-membrane extraction apparatus for soil solution. *Soil Science*, 51(5), 377-386. <https://doi.org/10.1097/00010694-194105000-00005>
- Romero, E. (2013). A microstructural insight into compacted clayey soils and their hydraulic properties. *Engineering Geology*, 165, 3-19. <https://doi.org/10.1016/j.enggeo.2013.05.024>
- Romero, E., & Simms, P. H. (2008). Microstructure investigation in unsaturated soils: A review with special attention to contribution of mercury intrusion porosimetry and environmental scanning electron microscopy. *Geotechnical and Geological Engineering*, 26, 705-727. https://doi.org/10.1007/978-1-4020-8819-3_8
- Romero, E., Della Vecchia, G., & Jommi, C. (2011). An insight into the water retention properties of compacted clayey soils. *Géotechnique*, 61(4), 313-328. <https://doi.org/10.1680/geot.2011.61.4.313>
- Romero, E., Gens, A., & Lloret, A. (1999). Water permeability, water retention and microstructure of unsaturated compacted boom clay. *Engineering Geology*, 54, 117-127. [https://doi.org/10.1016/S0013-7952\(99\)00067-8](https://doi.org/10.1016/S0013-7952(99)00067-8)
- Romero, E., Gens, a., & Lloret, a. (2003). Suction effects on a compacted clay under non-isothermal conditions. *Géotechnique*, 53(1), 65-81. <https://doi.org/10.1680/geot.2003.53.1.65>
- Romero, E., Villar, M. V., & Lloret, A. (2005). Thermo-hydro-mechanical behaviour of two heavily overconsolidated clays. *Engineering Geology*, 81(3), 255-268. <https://doi.org/10.1016/j.enggeo.2005.06.011>
- Roquier, G. (2015). *Etude théorique des effets de paroi et de desserrement dans les mélanges granulaires*. Thèse de Doctorat, Ecole Nationale Des Ponts et Chaussées, France, 614 pp.
- Roux, J.-N. (2000). Geometric origin of mechanical properties of granular materials. *Physical Review E - Statistical, Nonlinear, and Soft Matter Physics*, 61(6), 1-35.
- Roux, J.-N., & Chevoir, F. (2005). Généralités sur la simulation numérique discrète des matériaux granulaires, 254, 109-138.
-

List of References

- Roux, J.-N., Chevoir, F., & Toussaint, F. (2007). Etats de compacité maximale pour les mélanges binaires de grains sphériques : étude par simulation numérique. *Bulletin Des Laboratoires Des Ponts et Chaussées*, 268–269, 141–152.
- Saba, S., Barnichon, J. D., Cui, Y. J., Tang, A. M., & Delage, P. (2014a). Microstructure and anisotropic swelling behaviour of compacted bentonite/sand mixture. *Journal of Rock Mechanics and Geotechnical Engineering*, 6(2), 126–132. <https://doi.org/10.1016/j.jrmge.2014.01.006>
- Saba, S., Cui, Y., Tang, A. M., & Barnichon, J. (2014b). Investigation of the swelling behaviour of compacted bentonite-sand mixtures by mock-up tests. *Canadian Geotechnical Journal*, 51(April), 1399–1412.
- Saiyouri, N., Hicher, P. Y., & Tessier, D. (2000). Microstructural approach and transfer water modelling in highly compacted unsaturated swelling clays. *Mechanics of Cohesive-Frictional Materials*, 5, 41–60.
- Saiyouri, N., Tessier, D., & Hicher, P. Y. (2004). Experimental study of swelling in unsaturated compacted clays. *Clay Minerals*, 39(4), 469–479. <https://doi.org/10.1180/0009855043940148>
- Sánchez, M., Gens, A., do Nascimento Guimarães, L., & Olivella, S. (2005). A double structure generalized plasticity model for expansive materials. *International Journal for Numerical and Analytical Methods in Geomechanics*, 29(8), 751–787. <https://doi.org/10.1002/nag.434>
- Sánchez, M., Gens, A., Villar, M. V., & Olivella, S. (2016). Fully Coupled Thermo-Hydro-Mechanical Double-Porosity Formulation for Unsaturated Soils. *International Journal of Geomechanics*, D4016015. [https://doi.org/10.1061/\(ASCE\)GM.1943-5622.0000728](https://doi.org/10.1061/(ASCE)GM.1943-5622.0000728)
- Schneider, A. (1960). Neue diagramme zur bestimmung der relativen luftfeuchtigkeit über gesättigten wasserigen salzlosungen und wasserigen schwefelsaurelosungen bei verschiedenen temperaturen. *Holz als Rohund Werkstoff* 18, 269-272.
- Schofield, R. K. (1935). The pF of water in soil. In *Trans. of the Third International Congress on Soil Science*, 2, Plenary Session Papers, 30 July-7 August, 1935 Oxford, UK (pp. 37-48).
- Seiphoori, A., Ferrari, A., & Laloui, L. (2014). Water retention behaviour and microstructural evolution of MX-80 bentonite during wetting and drying cycles. *Géotechnique*, 64(9), 721–734. <https://doi.org/10.1680/geot.14.P.017>
- Sellin, P., & Leupin, O. X. (2014). The use of clay as an engineered barrier in radioactive-waste management - A review. *Clays and Clay Minerals*, 61(6), 477–498. doi:10.1346/CCMN.2013.0610601.
- Sheng, D., Gens, A., Fredlund, D. G., & Sloan, S. W. (2008). Unsaturated soils: From constitutive modelling to numerical algorithms. *Computers and Geotechnics*, 35(6), 810–824. <https://doi.org/10.1016/j.compgeo.2008.08.011>
- Sheng, D., Sloan, S. W., & Gens, A. (2004). A constitutive model for unsaturated soils: Thermomechanical and computational aspects. *Computational Mechanics*, 33(6), 453–465. <https://doi.org/10.1007/s00466-003-0545-x>
- Sposito, G., & Prost, R. (1982). Structure of Water Adsorbed on Smectites. *Chemical Reviews*, 82(6), 553–573. <https://doi.org/10.1021/cr00052a001>
-

-
- Sun, D., Zhang, L., Li, J., & Zhang, B. (2015). Evaluation and prediction of the swelling pressures of GMZ bentonites saturated with saline solution. *Applied Clay Science*, 105–106, 207–216. <https://doi.org/10.1016/j.clay.2014.12.032>
- Sun, H., Mašín, D., Najser, J., Nedela, V., & Navrátilová, E. (2019). Bentonite microstructure and saturation evolution in wetting-drying cycles evaluated using ESEM, MIP and WRC measurements. *Geotechnique*, 69(8), 713–726. <https://doi.org/10.1680/jgeot.17.P.253>
- Sweijen, T., Chareyre, B., Hassanizadeh, S. M., & Karadimitriou, N. K. (2017). Grain-scale modelling of swelling granular materials; application to super absorbent polymers. *Powder Technology*, 318, 411–422. <https://doi.org/10.1016/j.powtec.2017.06.015>
- Tang, A.-M., & Cui, Y.-J. (2005). Controlling suction by the vapour equilibrium technique at different temperatures and its application in determining the water retention properties of MX80 clay. *Canadian Geotechnical Journal*, 42(1), 287–296. <https://doi.org/10.1139/t04-082>.
- Tang, A.-M., & Cui, Y.-J. (2009). Modelling the thermomechanical volume change behaviour of compacted expansive clays. *Géotechnique*, 59(3), 185–195. <https://doi.org/10.1680/geot.2009.59.3.185>
- Tang, A. M., Cui, Y. J., & Le, T. T. (2008). A study on the thermal conductivity of compacted bentonites. *Applied Clay Science*, 41: 181–189.
- Tarantino, A. (2009). A water retention model for deformable soils. *Geotechnique*, 59(9), 751–762. <https://doi.org/10.1680/geot.7.00118>
- Tarantino, A., Gallipoli, D., Augarde, C. E., De Gennaro, V., Gomez, R., Laloui, L., Mancuso, C., El Mountassir, G., Munoz, J. J., Pereira, J. M., Peron, H., Pisoni, G., Romero, E., Raveendraraj, A., Rojas, J. C., Toll, D. G., Tombolato, S., & Wheeler, S. (2011). Benchmark of experimental techniques for measuring and controlling suction. *Geotechnique*, 61(4), 303–312. [doi:10.1680/geot.2011.61.4.303](https://doi.org/10.1680/geot.2011.61.4.303).
- Terzaghi, K. V. (1936). The shearing resistance of saturated soils and the angle between the planes of shear. In *First international conference on soil Mechanics*, 1936 (Vol. 1, pp. 54–59).
- Tessier, D. (1984). *Etude expérimentale de l'organisation des matériaux argileux. Hydratation, gonflement et structuration au cours de la dessiccation et de la réhumectation*. Thèse de Doctorat. Université de Paris VII, Paris, France.
- Tessier, D., Lajudie, A., & Petit, J. C. (1992). Relation between the macroscopic behavior of clays and their microstructural properties. *Applied Geochemistry*, 7(I), 151–161. [https://doi.org/10.1016/S0883-2927\(09\)80071-1](https://doi.org/10.1016/S0883-2927(09)80071-1)
- Thornton, C., & Ning, Z. (1998). A theoretical model for the stick/bounce behaviour of adhesive, elastic-plastic spheres. *Powder Technology*, 99(2), 154–162. [https://doi.org/10.1016/S0032-5910\(98\)00099-0](https://doi.org/10.1016/S0032-5910(98)00099-0)
- Thornton, C., Cummins, S. J., & Cleary, P. W. (2017). On elastic-plastic normal contact force models, with and without adhesion. *Powder Technology*, 315, 339–346. <https://doi.org/10.1016/j.powtec.2017.04.008>
-

List of References

- Tuller, M., Dani, O., & Dudley, L. M. (1999). Adsorption and capillary condensation in porous media: Liquid retention and interfacial configurations in angular pores. *Water Resources Research*, 35(7), 1949–1964. <https://doi.org/10.1029/1999WR900098>
- Ueda, T., Matsushima, T., & Yamada, Y. (2011). Effect of particle size ratio and volume fraction on shear strength of binary granular mixture. *Granular Matter*, 13(6), 731–742. <https://doi.org/10.1007/s10035-011-0292-1>
- Vallejo, L. E. (2001). Interpretation of the limits in shear strength in binary granular mixtures. *Canadian Geotechnical Journal*, 38(5), 1097–1104.
- van Geet, M., Volckaert, G., & Roels, S. (2005). The use of microfocus X-ray computed tomography in characterising the hydration of a clay pellet/powder mixture. *Applied Clay Science*, 29(2), 73–87. <https://doi.org/10.1016/j.clay.2004.12.007>
- van Genuchten, M. T. (1980). A Closed-form Equation for Predicting the Hydraulic Conductivity of Unsaturated Soils1. *Soil Science Society of America Journal*. <https://doi.org/10.2136/sssaj1980.03615995004400050002x>
- Vargas, W. L., & McCarthy, J. J. (2007). Thermal expansion effects and heat conduction in granular materials. *Physical Review E - Statistical, Nonlinear, and Soft Matter Physics*, 76(4), 1–8. <https://doi.org/10.1103/PhysRevE.76.041301>
- Vaunat, J., & Casini, F. (2017). A procedure for the direct determination of Bishop's χ parameter from changes in pore size distribution. *Géotechnique*, 67(7), 631–636. <https://doi.org/10.1680/jgeot.15.T.016>
- Vaunat, J., & Gens, A. (2005). Analysis of the hydration of a bentonite seal in a deep radioactive waste repository. *Engineering Geology*, 81(3), 317–328. <https://doi.org/10.1016/j.enggeo.2005.06.014>
- Villar, M. V. (1999). Investigation of the behaviour of bentonite by means of suction-controlled oedometer tests. *Engineering Geology*, 54(1–2), 67–73. [https://doi.org/10.1016/S0013-7952\(99\)00062-9](https://doi.org/10.1016/S0013-7952(99)00062-9)
- Villar, M. V. (2000). Caracterización termo-hidro-mecánica de una bentonita de Cabo de Gata. Ph.D. Thesis, Universidad Complutense de Madrid. 396 Pp.
- Villar, M. V. (2005). MX80 bentonite. Thermo-Hydro-Mechanical Characterisation Performed at CIEMAT in the Context of the Prototype Project. *Informes Técnicos Ciemat*, 1053.
- Villar, M. V. (2007). Water retention of two natural compacted bentonites. *Clays and Clay Minerals*, 55(3), 311–322. <https://doi.org/10.1346/CCMN.2007.0550307>
- Villar, M. V., & Lloret, A. (2008). Influence of dry density and water content on the swelling of a compacted bentonite. *Applied Clay Science*, 39(1–2), 38–49. <https://doi.org/10.1016/j.clay.2007.04.007>
- Villar, M. V., Martín, P. L., & Barcala, J. M. (2005a). Modification of physical, mechanical and hydraulic properties of bentonite by thermo-hydraulic gradients. *Engineering Geology*, 81(3), 284–297. <https://doi.org/10.1016/j.enggeo.2005.06.012>
-

-
- Villar, M. V., García-Siñeriz, J. L., Bárcena, I., & Lloret, A. (2005b). State of the bentonite barrier after five years operation of an in situ test simulating a high level radioactive waste repository. *Engineering Geology*, 80(3–4), 175–198. <https://doi.org/10.1016/j.enggeo.2005.05.001>
- Villar, M.V., (2008). Thermo-hydro-mechanical characterisation of a bentonite from Cabo de Gata. A Study Applied to the Use of Bentonite as Sealing Material in High Level Radioactive Waste Repositories. *Publicación Técnica ENRESA 01/2002*, Madrid (258 pp.).
- Volckaert, G., Bernier, F., Alonso, E., Gens, A., Samper, J., Villar, M. V., Martín, P.L., Cuevas, J., Campos, R., Thomas, H.R., Imbert, C., & Zingarelli, V. (1996). Thermal-hydraulic-mechanical and geochemical behaviour of the clay barrier in radioactive waste repositories (model development and validation). *Nuclear Science and Technology*. EUR 16744. Commission of the European Communities, Luxembourg. 722 pp.
- Wang, Q., Tang, A. M., Cui, Y. J., Delage, P., & Gatmiri, B. (2012). Experimental study on the swelling behaviour of bentonite/claystone mixture. *Engineering Geology*, 124(1), 59–66. <https://doi.org/10.1016/j.enggeo.2011.10.003>
- Wang, Q., Tang, A. M., Cui, Y. J., Delage, P., Barnichon, J. D., & Ye, W. M. (2013a). The effects of technological voids on the hydro-mechanical behaviour of compacted bentonite-sand mixture. *Soils and Foundations*, 53(2), 232–245. <https://doi.org/10.1016/j.sandf.2013.02.004>
- Wang, Q., Cui, Y. J., Tang, A. M., Barnichon, J. D., Saba, S., & Ye, W. M. (2013b). Hydraulic conductivity and microstructure changes of compacted bentonite/sand mixture during hydration. *Engineering Geology*, 164, 67–76. <https://doi.org/10.1016/j.enggeo.2013.06.013>
- Wang, Q., Tang, A. M., Cui, Y. J., Barnichon, J. D., & Ye, W. M. (2013c). A comparative study on the hydro-mechanical behavior of compacted bentonite/sand plug based on laboratory and field infiltration tests. *Engineering Geology*, 162, 79–87. <https://doi.org/10.1016/j.enggeo.2013.05.009>
- Wang, Q., Minh, A., Cui, Y., Barnichon, J., & Ye, W. (2013d). Investigation of the hydro-mechanical behaviour of compacted bentonite / sand mixture based on the BExM model. *Computers and Geotechnics*, 54(October 2013), 46–52. Elsevier Ltd. doi:10.1016/j.compgeo.2013.05.011.
- Warr, L., & Berger, J. (2007). Hydration of bentonite in natural waters: Application of “confined volume” wet-cell X-ray diffractometry. *Physics and Chemistry of the Earth*, 32(1–7), 247–258. <https://doi.org/10.1016/j.pce.2006.02.048>
- Westman, A. E. R., & Hugill, H. R. (1930). the Packing of Particles. *Journal of the American Ceramic Society*, 13(10), 767–779. <https://doi.org/10.1111/j.1151-2916.1930.tb16222.x>
- Wiacek, J., Molenda, M., Horabik, J., & Ooi, J. Y. (2012). Influence of grain shape and intergranular friction on material behavior in uniaxial compression: Experimental and DEM modeling. *Powder Technology*, 217, 435–442. <https://doi.org/10.1016/j.powtec.2011.10.060>
- Wiebe, B., Graham, J., Tang, G. X., & Dixon, D. (1998). Influence of pressure, saturation, and temperature on the behaviour of unsaturated sand-bentonite. *Canadian Geotechnical Journal*, 35, 194–205. <https://doi.org/10.1139/t97-093>
- Wieczorek, K., Gaus, I., Mayor, J. C., Schuster, K., García-Siñeriz, J. L., & Sakaki, T. (2017). In-situ experiments on bentonite-based buffer and sealing materials at the Mont Terri rock laboratory (Switzerland). *Swiss Journal of Geosciences*, 110(1), 253–268. <https://doi.org/10.1007/s00015-016-0247-y>
-

List of References

- Williams, J., & Shaykewich, C. F. (1969). An evaluation of polyethylene glycol (P.E.G.) 6000 and P.E.G. 20,000 in the osmotic control of soil water matric potential. *Canadian Journal of Soil Science*, 49, 397–401.
- Xu, L., Ye, W. M., Chen, B., Chen, Y. G., & Cui, Y. J. (2016). Experimental investigations on thermo-hydro-mechanical properties of compacted GMZ01 bentonite-sand mixture using as buffer materials. *Engineering Geology*, 213, 46–54. <https://doi.org/10.1016/j.enggeo.2016.08.015>
- Ye, W. M., Cui, Y. J., Qian, L. X., & Chen, B. (2009). An experimental study of the water transfer through confined compacted GMZ bentonite. *Engineering Geology*, 108(3–4), 169–176. <https://doi.org/10.1016/j.enggeo.2009.08.003>
- Yerazunis, S., Cornell, S. W., & Wintner, B. (1965). Dense random packing of binary mixtures of spheres. *Nature*, 207(4999), 835.
- Yigzaw, Z. G., Cuisinier, O., Massat, L., & Masrouri, F. (2016). Role of different suction components on swelling behavior of compacted bentonites. *Applied Clay Science*, 120, 81–90. <https://doi.org/10.1016/j.clay.2015.11.022>
- Zhao, S., Evans, T. M., Zhou, X., & Zhou, S. (2017). Discrete element method investigation on thermally-induced shakedown of granular materials. *Granular Matter*, 19(1), 1–11. <https://doi.org/10.1007/s10035-016-0690-5>
- Zhou, M., Caré, S., Courtier-Murias, D., Faure, P., Rodts, S., and Coussot, P. (2018). Magnetic resonance imaging evidences of the impact of water sorption on hardwood capillary imbibition dynamics. *Wood Science and Technology*, 52(4), 929–955. Springer Berlin Heidelberg. doi:10.1007/s00226-018-1017-y.

